TU Delft

Delft University of Technology

Document Version
Final published version

Citation (APA)
Christoforidou, A. (2025). *Fatigue behavior of steel reinforced resin connectors for fibre-polymer composite bridge decks.* [Dissertation (TU Delft), Delft University of Technology]. https://doi.org/10.4233/uuid:4aa40c38-d549-4386-8635-a425fffe4f36

Important note
To cite this publication, please use the final published version (if applicable).
Please check the document version above.

Copyright
In case the licence states “Dutch Copyright Act (Article 25fa)”, this publication was made available Green Open Access via the TU Delft Institutional Repository pursuant to Dutch Copyright Act (Article 25fa, the Taverne amendment). This provision does not affect copyright ownership.
Unless copyright is transferred by contract or statute, it remains with the copyright holder.

Sharing and reuse
Other than for strictly personal use, it is not permitted to download, forward or distribute the text or part of it, without the consent of the author(s) and/or copyright holder(s), unless the work is under an open content license such as Creative Commons.

Takedown policy
Please contact us and provide details if you believe this document breaches copyrights.
We will remove access to the work immediately and investigate your claim.

This work is downloaded from Delft University of Technology.

FATIGUE BEHAVIOR OF STEEL REINFORCED RESIN CONNECTORS FOR FIBRE-POLYMER COMPOSITE BRIDGE DECKS

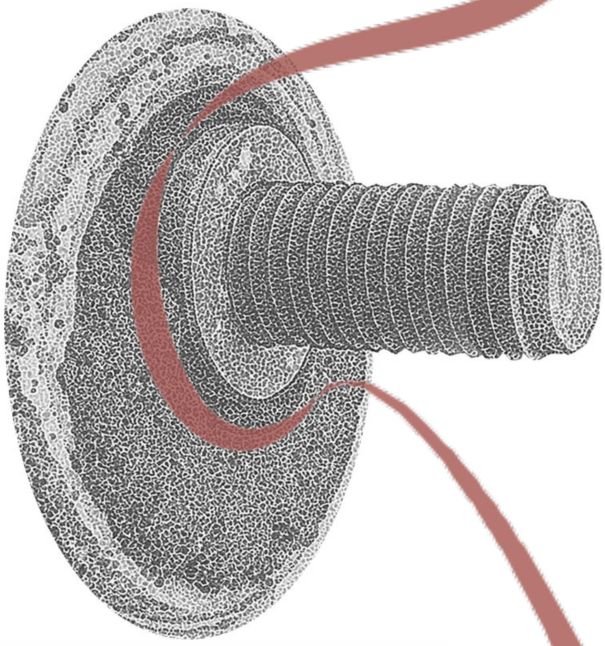



ANGELIKI CHRISTOFORIDOU

Fatigue behavior of steel reinforced resin connectors for fibre-polymer composite bridge decks

Fatigue behavior of steel reinforced resin connectors for fibre-polymer composite bridge decks

Dissertation

for the purpose of obtaining the degree of doctor
at Delft University of Technology,
by the authority of the Rector Magnificus Prof.dr.ir. T.H.J.J. van der Hagen,
chair of the Board for Doctorates,
to be defended publicly on
Friday 4 July 2025 at 12:30 o'clock

by

Angeliki CHRISTOFORIDOU

Master of Science in Civil Engineering,
Delft University of Technology, Delft.

This dissertation has been approved by the promotors.

Composition of the doctoral committee:

Rector Magnificus,	chairperson
Prof.dr. M. Veljkovic,	Delft University of Technology, promotor
Dr. M. Pavlovic	Delft University of Technology, copromotor

Independent members:

Prof.dr. M.A.N. Hendriks,	Delft University of Technology
Dr. V.A. Popovich,	Delft University of Technology
Em.prof.dr. J.T. Mottram,	University of Warwick, United Kingdom
Prof.dr. M. Schäfer,	University of Luxembourg, Luxembourg
Prof.dr.ir. H.E.J.G. Schlangen,	Delft University of Technology, reserve member

This work is financed by the *Dutch Minstry of Infrastructure and Water Management*.





Rijkswaterstaat
Ministerie van Infrastructuur en Waterstaat

Keywords: fatigue of connectors, fibre-polymer composite decks, GFRP-steel bridge decks, steel reinforced resin, fatigue, shear resistance, finite element analysis, continuum damage mechanics

Printed by: JouwBoek Uitgeverij U2pi - The Hague, the Netherlands

Cover design: Elissavet Markozani

Copyright © 2025 by A. Christoforidou

ISBN 978-94-6518-069-4

An electronic version of this dissertation is available at
`https://repository.tudelft.nl/`.

There is a crack in everything,
that's how the light gets in…

— Leonard Cohen, *Anthem*, from the album *The Future* (1992), Columbia Records.

Contents

Summary xi

Preface xiii

Εισαγωγικό σημείωμα xv

I Prologue 1

1 Introduction 3
- 1.1 Background information on bridges . . . 3
- 1.2 Fibre-polymer composites in infrastructure . . . 4
- 1.3 Development of the iSRR connector . . . 5
- 1.4 Understanding damage in iSRR connector . . . 7
- 1.5 Scope and research questions . . . 10
- 1.6 Experimental program . . . 13
- 1.7 Numerical modeling . . . 13
- 1.8 Thesis outline . . . 14

2 Literature review 17
- 2.1 Fatigue behavior of bulk resin materials . . . 17
- 2.2 Development of Steel Reinforced Resin (SRR) . . . 18
- 2.3 Testing of composite materials with granular constituents . . . 19
- 2.4 Pressure dependency of SRR and other granular composites . . . 20
- 2.5 Shear connectors for composite decks . . . 20
- 2.6 Numerical modeling of bolted connectors for composite decks . . . 25
- 2.7 Summary of knowledge gaps . . . 25

II Static and Fatigue Behavior of (Steel-Reinforced) Resin material 27

3 Tensile behavior of steel reinforced resin 29
- 3.1 Resin systems considered . . . 29
- 3.2 Resin preparation and production of specimens . . . 30
- 3.3 Test set-up for SRR tensile experiments . . . 31
- 3.4 Tensile strength of SRR material at various temperatures . . . 33
- 3.5 Stiffness and Poisson's ratio of SRR material under tension . . . 33
- 3.6 Cyclic response of SRR in tension including temperature effects . . . 39
- 3.7 Water absorption of pure and steel-reinforced resins . . . 43
- 3.8 Conclusions . . . 46

4 Compressive behavior of steel-reinforced resin **49**
4.1 Specimen preparation and test set-ups for compressive behavior of SRR . . 49
4.2 Uniaxial compressive behavior of SRR under static loading 52
4.3 Triaxial compressive behavior of SRR under static loading 55
4.4 Uniaxial compressive behavior of SRR under cyclic loading 58
4.5 Conclusions 60

III Fatigue Behavior of iSRR Connectors in Joint Experiments **63**

5 Design of experiments for connector's shear behavior **65**
5.1 Development of the test set-up 66
5.2 Development of FE models for designing the test set-up 70
5.3 Influence of boundary conditions, gaps and steel stiffeners 73
5.4 Stress analysis at web-to-skin junction of GFRP deck 76
5.5 Final connector test set-up and specimen design 78
5.6 Development of experimental and full-size bridge models 82
5.7 Validation of experimental and full-size bridge models 87
5.8 Conclusions 89

6 Behavior of connectors under cyclic shear loading **91**
6.1 Test matrix, specimens and instrumentation 91
6.2 Cyclic behavior under fully reversed load ratio and various load ranges . . . 94
6.3 Cyclic behavior under different load ratios 96
6.4 Cyclic behavior under different temperatures 98
6.5 Cyclic behavior under the influence of moisture and water 99
6.6 Remaining stiffness and static resistance 102
6.7 Residual fatigue behavior with fully reversed cyclic loading 106
6.8 Conclusions 107

7 Fatigue life of connectors loaded in shear **109**
7.1 Extrapolation methods for F-N curve prediction 109
7.2 Influence of the load level 112
7.3 Influence of the load ratio 116
7.4 Influence of temperature 121
7.5 Influence of environmental exposure 126
7.6 Reliability and conservatism in prediction methods 128
7.7 Conclusions 129

IV Analysis and Prediction of Fatigue Behavior of iSRR Connector **131**

8 Damage mechanisms of iSRR connector **133**
8.1 Decomposition of damage mechanisms of the connector 133
8.2 Description of numerical analysis 134
8.3 Numerical results 135
8.4 Influence of single and combined damage components 136
8.5 Model validation 138
8.6 Conclusions 140

9 Computational prediction of steel reinforced resin behavior **141**
9.1 Micro-mechanical modeling of SRR material 141
9.2 Continuum Damage Mechanics approach 148
9.3 FE model set-up for subroutine implementation 152
9.4 Implementation of CDM fatigue model using subroutine. 155
9.5 Meso-scale modeling of SRR material under cyclic tension and compression loading. 158
9.6 Connector-level cyclic FE model and discussion 161
9.7 Conclusions 163

V Epilogue **165**

10 Conclusions and recommendations **167**
10.1 Conclusions 167
10.2 Recommendations for future research 169

List of Acronyms **169**

Bibliography **173**

Acknowledgements **183**

Curriculum Vitæ **187**

Publications **189**

Summary

The need to renovate many European road bridges due to end-of-life conditions, fatigue, corrosion, and increasing traffic loads drives the demand for innovative solutions. The Dutch Ministry of Infrastructure and Water Management (Rijkswaterstaat (RWS)) estimates that 50 bridges in the Netherlands will require renovation annually over the next three decades. Lightweight, fatigue-resistant fiber-polymer composite panels have emerged as a promising solution for deck replacement in steel bridges. However, the adoption of this technology is hindered by the lack of a reliable connection method.

This research, conducted at Delft University of Technology in collaboration with RWS, develops and evaluates the novel injected Steel Reinforced Resin (iSRR) connector to enable the use of glass fibre-polymer composite decks, often termed as GFRP. Initial tests demonstrate that the iSRR connector offers superior static, fatigue, and creep performance compared to existing GFRP-steel connection technologies.

The main objective of this PhD project is to understand the fatigue behavior of iSRR connectors and provide prediction methods for their performance that can be used for efficient design in engineering practice. The research pursues two specific goals: (1) characterizing the fatigue behavior of iSRR connectors under realistic GFRP panel configurations and load conditions, and (2) evaluating the effects of environmental conditions, such as moisture and temperature, on connector performance.

The research involves extensive fatigue testing at both material and connector levels, together with finite element analysis. A specialized test set-up is developed in the Stevin 2 laboratory to apply cyclic shear loads, replicating realistic boundary conditions and load transfer. Temperature and moisture tests are also conducted to assess the impact of environmental conditions on the connectors.

At the material level, coupon experiments are carried out to evaluate the SRR properties, and detailed finite element models are developed to better understand the mechanical behavior and failure mechanisms of SRR material and iSRR connectors.

This dissertation identifies the fatigue mechanisms that lead to degradation in iSRR connectors for GFRP decks on steel girders. It establishes a fatigue detail that characterizes iSRR connectors, enabling the design of reliable connections between GFRP decks and steel girders. Furthermore, it provides a methodology to describe the fatigue degradation of iSRR connectors using a phenomenological model that builds upon existing Continuum Damage Mechanics (CDM) principles.

The findings of this research fill a significant knowledge gap in understanding the behavior of iSRR connectors, offering a practical and sustainable solution for the upcoming bridge renovations in engineering practice. This project bridges theoretical understanding and practical application, aiming to enhance the performance and longevity of GFRP-steel bridge systems under growing traffic and environmental challenges.

Preface

In July 2017, I found myself sitting in the ceremony hall of Aristotle University of Thessaloniki, waiting for my name to be called so I could receive my Civil Engineering diploma. At that moment, despite knowing I had already been admitted to TU Delft, I mistakenly thought this was the end of my academic journey. I remember thinking, *"Oh enjoy, you're done now"*. Of course, I was not. Not only did I push myself through a Master's in Structural Engineering at TU Delft, but I also stayed on for several more years to pursue a PhD.

During my studies, I took one course on fatigue, but the real lessons in fatigue came from observing my own. Over almost eight years in the Netherlands, always affiliated with TU Delft, I learned more about myself than anything else. Both in my MSc thesis and PhD dissertation, I worked on structural connections, but the irony of my PhD was its focus on fatigue characterization. Writing this book was challenging. The thought that I was incapable often crossed my mind. Yet, unlike the connectors I tested, I proved to myself that I could survive without failing under high stress levels. Or more accurately, I often felt as though I had failed, but each time I found a way to begin again, ultimately leading me to this book, which I am now proudly sharing with you.

In the following chapters, I won't be discussing my own struggles with fatigue. Instead, we will explore the fatigue behavior of a novel type of a slip-resistant connector, capable of efficiently joining together two different materials: the fiber-reinforced polymer of a deck with the steel girders of a bridge.

As I write these final words, I again believe that this book will officially mark the end of my studies. But now, I'm not entirely certain, and maybe that's okay. What I say now to you, just starting to read this book, and to myself, having finished writing it, is: *"Oh enjoy, you are just beginning now"*.

Angeliki Christoforidou
Delft, January 2025

Εισαγωγικό σημείωμα

Τον Ιούλιο του 2017 βρέθηκα να κάθομαι στην αίθουσα τελετών του Αριστοτελείου Πανεπιστημίου Θεσσαλονίκης, περιμένοντας να ακουστεί το όνομά μου για να παραλάβω το δίπλωμά μου ως Πολιτικός Μηχανικός. Εκείνη τη στιγμή, παρόλο που ήξερα ότι είχα ήδη γίνει δεκτή στο Πανεπιστήμιο του Ντελφτ, νόμιζα λανθασμένα πως αυτό ήταν το τέλος της ακαδημαϊκής μου πορείας. Θυμάμαι να σκέφτομαι, *"Ω απόλαυσέ το, τώρα τελείωσες"*. Φυσικά, δεν είχα τελειώσει. Όχι μόνο πίεσα τον εαυτό μου για ένα μεταπτυχιακό στη Δομοστατική Μηχανική στο Πανεπιστήμιο του Ντελφτ, αλλά παρέμεινα εκεί για αρκετά χρόνια ακόμα, συνεχίζοντας με διδακτορική έρευνα.

Κατά τη διάρκεια των σπουδών μου, παρακολούθησα ένα μάθημα για την κόπωση, αλλά τα πραγματικά μαθήματα κόπωσης τα έλαβα παρατηρώντας τη δική μου. Σχεδόν οκτώ χρόνια στην Ολλανδία, πάντα συνδεδεμένη με το Πανεπιστήμιο του Ντελφτ, έμαθα περισσότερα για τον εαυτό μου από οτιδήποτε άλλο. Τόσο στη μεταπτυχιακή μου εργασία όσο και στη διδακτορική μου διατριβή ασχολήθηκα με δομικές συνδέσεις, αλλά η ειρωνεία του διδακτορικού μου ήταν η εστίαση του στον χαρακτηρισμό της κόπωσης. Η συγγραφή αυτού του βιβλίου ήταν μια πρόκληση για μένα. Η σκέψη ότι ήμουν ανίκανη να τα καταφέρω περνούσε συχνά από το μυαλό μου. Ωστόσο, σε αντίθεση με τις συνδέσεις που δοκίμασα, απέδειξα στον εαυτό μου ότι μπορούσα να επιβιώσω χωρίς να αποτύχω κάτω από υψηλά επίπεδα έντασης. Ή, πιο σωστά, συχνά ένιωθα σαν να είχα αποτύχει, αλλά κάθε φορά έβρισκα έναν τρόπο να ξεκινήσω ξανά, οδηγώντας με τελικά σε αυτό το βιβλίο, το οποίο τώρα με περηφάνια μοιράζομαι μαζί σας.

Στα επόμενα κεφάλαια, δεν θα μιλήσω για τις προσωπικές μου δυσκολίες με την κόπωση. Αντίθετα, θα διερευνήσουμε τη συμπεριφορά κόπωσης ενός καινοτόμου τύπου αντιολισθητικού συνδετήρα, ικανού να ενώνει αποτελεσματικά δύο διαφορετικά υλικά: το ενισχυμένο με ίνες πολυμερές ενός καταστρώματος με τις χαλύβδινες δοκούς μιας γέφυρας.

Καθώς γράφω αυτές τις τελευταίες λέξεις, πιστεύω και πάλι ότι αυτό το βιβλίο θα σηματοδοτήσει επίσημα το τέλος των σπουδών μου. Αλλά αυτή τη φορά, δεν είμαι απολύτως σίγουρη, και ίσως αυτό να είναι εντάξει. Αυτό που λέω τώρα σε σένα, που μόλις ξεκινάς να διαβάζεις αυτό το βιβλίο, και σε εμένα, που μόλις τελείωσα τη συγγραφή του, είναι: *"Ω απόλαυσέ το, μόλις τώρα αρχίζεις"*.

Αγγελική Χριστοφορίδου
Ντελφτ, Ιανουάριος 2025

I

Prologue

1

Introduction

1.1. Background information on bridges

Since ancient times, humans have demonstrated an innate ability to solve challenges, driven by the need not only to survive but to improve their quality of life. One of the earliest manifestations of this problem-solving instinct was the creation of pathways to traverse difficult terrain. Initially, simple rows of stones were laid to form rudimentary paths. As engineering knowledge advanced, these pathways evolved into elevated structures, ultimately leading to the development of bridges.

Early bridges were constructed using natural materials such as stone, wood, and rope, reflecting the technological capabilities of their time. Over the centuries, advancements in materials and construction techniques allowed for longer spans, increased load capacities, and improved durability. The introduction of iron and steel during the Industrial Revolution, followed by the widespread use of reinforced concrete, transformed bridge engineering, enabling more resilient and efficient designs.

Bridges play a fundamental role in modern infrastructure, providing essential connectivity and supporting economic activities. However, as these structures age, they are subjected to increasing demands due to traffic growth and environmental exposure. Repeated loading over time leads to fatigue, a primary concern in bridge engineering, as it can cause progressive damage and, in severe cases, structural failure. The collapse of the Silver Bridge in 1967, attributed to a fatigue crack in an eyebar, underscored the significance of fatigue assessment in ensuring the long-term safety of bridges. Since then, extensive research has been dedicated to understanding and mitigating fatigue-related deterioration.

In the Netherlands, many bridges were constructed in the decades following World War II, designed according to standards that did not anticipate current traffic loads. For instance, the tandem system and uniformly distributed loads specified in Eurocode EN1992-1 represent increases of 100% and 125%, respectively, compared to the standards in use during the 1960s [1, 2]. As a result, fatigue and corrosion have become increasingly prevalent issues, necessitating frequent inspections and maintenance interventions [3].

To address these challenges, infrastructure managers are shifting towards renovation

strategies that extend the lifespan of existing structures rather than opting for full replacement. This approach aligns with sustainability objectives and the principles of a circular economy, emphasizing the need to reinforce or replace critical components rather than decommission entire bridges [4]. Consequently, a significant number of steel bridges with orthotropic, timber, or concrete decks are scheduled for renovation, with estimates indicating that approximately 50 bridges per year will require repair over the coming decades [3], as illustrated in Figure 1.1.

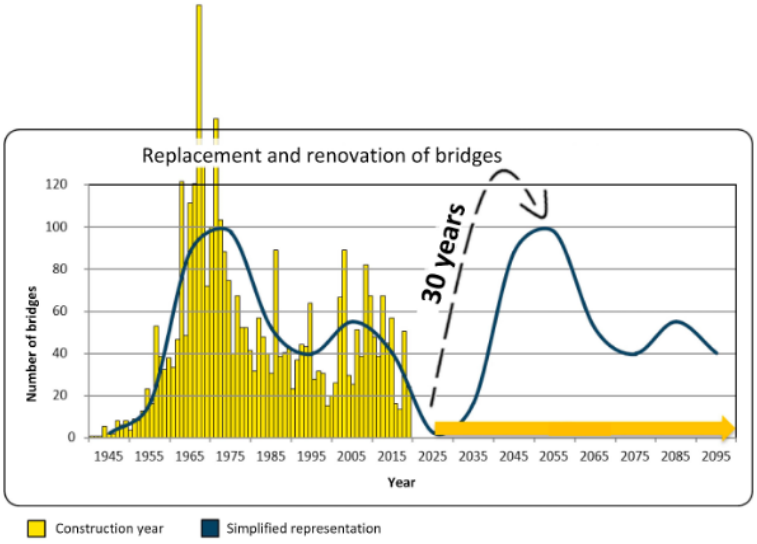

Figure 1.1: Overview of replacement and renovations that Rijkswaterstraat will be facing [5].

This status quo presents excellent opportunities for fostering research initiatives in many directions. New studies are performed on implementing an infrastructure-for-service approach [6] or utilizing a potential synergy program by bundling the renovation projects [7]. Apart from developing efficient project management strategies, researchers are dealing with crack prediction models that can allow for accurate determination of maintenance and repair duration [8]. Several ideas are also explored to retrofit concrete decks, such as applying external prestressing, composite, also termed as GFRP, laminas or advanced cementitious materials [9, 10].

1.2. Fibre-polymer composites in infrastructure

Similarly to the approaches mentioned above, this research will target to tackle the increasing demand for bridge renovation from another perspective. More specifically, the use of composite panels as a replacement for the existing deteriorated steel, concrete or timber bridge decks will be proposed since it is emerging to be one of the most attractive solutions [11].

In recent years, fiber-polymer composite (also known as GFRP), sandwich panels with either foam core or other core material (e.g. balsa wood), and with or without internal

stiffening webs, have revolutionized numerous high-performance applications due to their unique lightweight yet robust construction. Encapsulating a lightweight porous (foam, balsa, etc.) core between resilient GFRP composite outer and inner skins, these panels offer superior thermal and acoustic insulation properties, proving advantageous across various sectors. Their versatile use extends from serving as effective materials in residential to industrial construction, to enabling lightweight design in the shipbuilding, aerospace and automotive sectors, and enhancing the resilience of wind turbine blades in the renewable energy industry [12, 13]. Building on their broad applications, in mid 1990s the use of GFRP sandwich foam core panels has permeated the field of bridge construction and renovation [14, 15].

Fiber-polymer composite decks are lightweight, and as a result, the well-preserved steel substructure in many bridges does not need to be strengthened in the future because of the reduced permanent load from the deck. Additionally, GFRP is a durable material that can act as a barrier for the steel girders, protecting them from exposure to harsh environmental conditions. Most importantly, the high strength-to-weight ratio and the tailor-made nature of composite elements make them highly fatigue resistant [16]. Nevertheless, one of the main factors limiting their widespread implementation is the lack of a generic, robust, and practical connection technology.

1.3. Development of the iSRR connector

While materials and bridge designs have evolved, so too have the methods for connecting structural components, ensuring stability and effective load transfer. The development of shear connectors has paralleled advancements in bridge construction, beginning with simple dowels and fasteners and progressing to innovative solutions designed for hybrid structures like GFRP and steel.

Currently, the most prevalent solutions for structural connections between composite and steel are bolted and bonded solutions. Bolted connections are exposed to slip due to bolt-to-hole clearances and, therefore, have insufficient initial stiffness [17]. Their relatively poor fatigue and creep behavior due to localized bearing stresses around the hole in the composite material has limited their application [18]. Bonded connections can be a viable solution but can have a very unpredictable brittle failure and their susceptibility to environmental influences is insufficiently known [19]. Additionally, such connections are generally not demountable or reusable, posing limitations for sustainable structural designs.

A less frequently employed approach involves the use of injection materials to embed mechanical connectors within composite structural elements. Presently, polymer resins or cementitious grouts serve this purpose, albeit with certain limitations. Shear stud connections embedded in cement-based grout have exhibited satisfactory performance in static and fatigue tests [20]. However, their effectiveness is contingent upon the degree of confinement within the composite member and the relatively low tensile strength of the grout, raising the need for local spiral reinforcement around connectors. Moreover, the creep behavior and environmental durability of grout-injected connections can be suspected and have yet to be thoroughly investigated.

Injection bolts could be beneficial in terms of execution efficiency, demountability and have shown improved level of fatigue performance vs. non-injected bolts. However, the fatigue performance of this type of bolt remains constrained due to the small hole

diameter in the composite material, which generates high bearing stresses. These stresses progressively weaken the connector, undermining both its short-term effectiveness and long-term durability [21].

In light of the aforementioned, a novel type of connector, the injected steel reinforced resin connector (iSRR), has been developed for GFRP deck panels in hybrid steel-GFRP bridges. Figure 1.2a illustrates how the iSRR connectors are conceptually embedded within a generic composite deck panel. This connector uses standard bolts or rods surrounded by a steel-reinforced resin (SRR) matrix. The SRR injection material was originally developed by Nijgh [22]. It consists of high-carbon, round, hardened steel balls (type S390) with diameters between 1–2 mm and a hardness of 40–50 HRC, chosen for their stiffness, mechanical stability, and long-term deformation resistance [23]. The steel balls are impregnated with a polymeric resin to encapsulate the mechanical connector.

The SRR material is injected into a large, nearly cylindrical hole in the composite deck, enclosing the bolt or rod (see Figure 1.2b). Here, the injected material is directly surrounded by the bottom GFRP facing and the foam of the sandwich web-core panel. This connection concept could also be applied to other soft materials, such as solid or cross-laminated timber panels, or other GFRP-based structural elements like lock gates. The performance and behavior of this shear connector system in GFRP bridge decks are the focus of the present thesis.

By using a relatively large hole diameter filled with SRR material, bearing stress concentrations seen with traditional injected bolts in GFRP are alleviated. The SRR material also provides superior stiffness and creep behavior compared to pure resin, and the large hole diameter enhances assembly tolerances for multiple connectors. The design includes either a steel rod with nuts mimicking a bolt head or an actual bolt, secured with nuts or couplers as needed. Slip resistance is ensured by preloading the steel connector against the steel flange, while preload loss due to the presence of the GFRP composite laminate is mitigated by excluding the bottom facing and the SRR material from the preloading package and relying on the SRR injection piece for the shear and pull-out transfer.

At TU Delft, the Steel and Composite Structures research group within Engineering Structures Department, with support from RWS, investigated innovative connection methods for hybrid bridge systems. The iSRR connector demonstrated outstanding static, fatigue and creep performance compared to other connection solutions available for composites, such as injected or blind-bolts. From static push-out tests, the iSRR connector with an M20 bolt diameter illustrated a comparable stiffness and shear resistance with the steel-concrete hybrid structures connected with same bolts' diameter [24]. Tests on a glass fibre composite-to-steel single-lap joint (SLJ) configuration revealed that iSRR connectors yielded a 42% lower creep deformation compared to injected bolts with conventional resin [21].

Moreover, under a fully reversed cyclic shear load of ±40 kN (R = -1), iSRR connectors withstand 2.31E+06 cycles without failure, compared to 2.37E+04 cycles for traditional resin-injected bolts and only 8E+03 for blind bolts, which fail prematurely due to GFRP bearing deformation and bolt loosening [21, 25]. The exceptional fatigue performance of iSRR connectors is attributed to their load-transferring mechanism, which preloads the bolt to prevent shear stress cycles. In contrast, blind bolts exhibit significant displacement increases and delamination under cyclic loading, making them unsuitable for high-cycle fatigue scenarios.

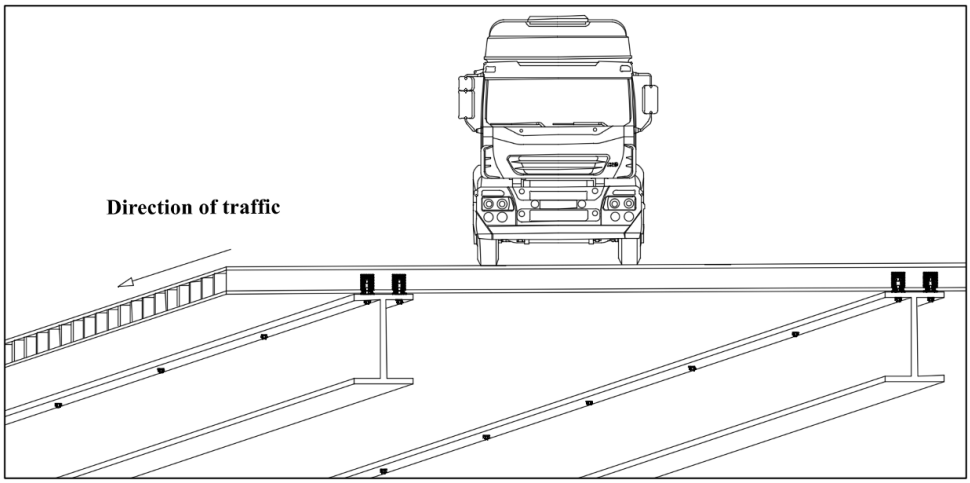

(a)

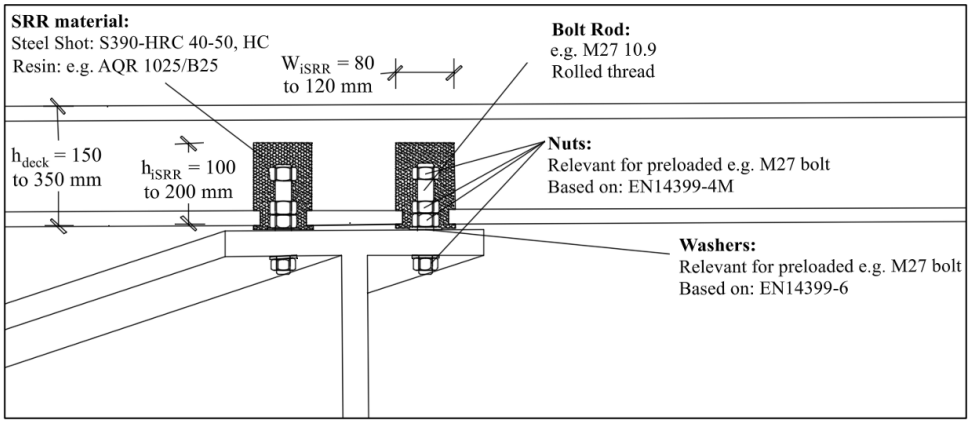

(b)

Figure 1.2: Cross section of a bridge with iSRR bolted connections between composite deck panel and steel girder: (a) Global view, (b) Close-up view of iSRR connectors.

1.4. Understanding damage in iSRR connector

To understand the potential damage mechanisms during cyclic loading of an iSRR connector, it is crucial to examine the dominance of shear loads generated by the hybrid interaction between the GFRP deck and the steel girder. Allowing for hybrid interaction ensures that the primary load transferred through the iSRR connector is shear, rather than compressive or tensile forces. These shear loads are introduced by wheel traffic and are conveyed through the GFRP top facing to the webs, and then to the bottom facing. The load is subsequently transferred through the SRR material to the bolt rod and, ultimately, to the steel girder. Understanding this load transfer mechanism is critical to evaluating the fatigue performance of the iSRR connector.

From preliminary cyclic testing on the iSRR connector, the development of a crack reaching the surface of the SRR injection piece was reported, as shown in Figure 1.3. This crack initiated and propagated within the first few thousand cycles without leading to failure, emphasizing the importance of understanding the behavior of the SRR material under cyclic loading. Literature highlights that in such connectors, cracks predominantly develop within the SRR material. Gaining this understanding is critical for predicting crack initiation and progression, which are important for the long-term durability of the iSRR connector.

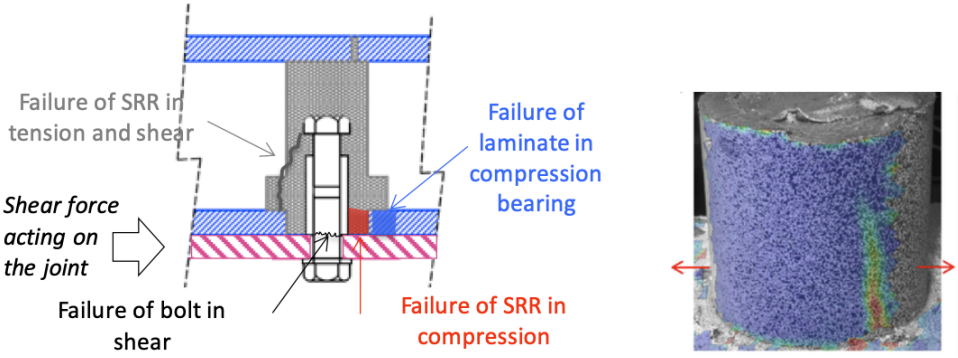

Figure 1.3: Load transfer mechanism and crack through SRR injection piece found in fatigue experiment [21].

Throughout this research, the iSRR connector is studied exclusively in combination with a GFRP sandwich deck. Both experimental and numerical investigations are conducted using this specific composite structure as the host material. No other embedding materials, such as concrete, are considered within the scope of this work. This decision ensures consistency and enables a focused evaluation of the connector's mechanical performance in hybrid GFRP-steel systems. While the potential application of the iSRR connector in alternative deck materials (e.g., concrete or timber) may be explored in future studies, the current research is confined to configurations where load transfer occurs directly through the GFRP sandwich panel to the steel substructure. Therefore, understanding the possible damage mechanisms in the iSRR connector must be interpreted in the context of its embedding in the GFRP sandwich deck, as this host material fundamentally influences the connector's stress distribution, crack development, and long-term performance.

More specifically the GFRP sandwich deck panel to be analyzed in this work is produced by FiberCore Europe using vacuum infusion, following a method aimed at minimizing delamination risk and ensuring robustness near connection zones [26]. The deck is manufactured upside down to yield a wavy bottom surface (against the vacuum bag) and a smooth top surface (against the mold), which is relevant to this research. The panel is fabricated from continuous 1.27 m wide fabrics and foam blocks without splices to avoid resin accumulation and reduce distortion during testing.

As illustrated in Figure 1.4, the production process involves multiple steps: each PUR foam core is first wrapped three times with a $[+45/-45]_{33}$ fabric (Figure 1.4a), promoting shear continuity across the web zone. This is followed by the application of three UD layers $[90]_3$ across four adjacent cores (Figure 1.4b), and subsequently by Z-layers

$[0_2/90_2/+45/-45]$ applied from top to bottom over a five-core region (Figure 1.4c). These steps are repeated until each core is covered with four UD layers and five Z-layers (Figure 1.4d). This combination of overlapping layers ensures structural integrity and minimizes interfacial discontinuities. A centralized injection channel is incorporated to reduce distortion during infusion. Once complete, the full-size panel was cut into 300×600 mm specimens in a single operation to ensure dimensional consistency.

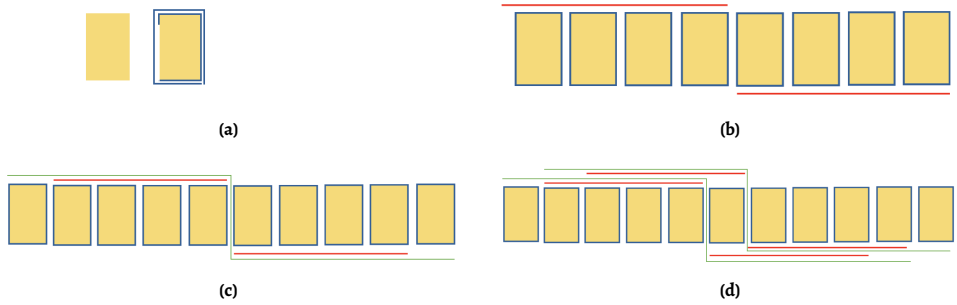

Figure 1.4: Production method of GFRP sandwich panel deck with integrated webs: (a) Wrapping of each core three times with a $[+45/-45]_3$ fabric, (b) Application of three UD layers $[90]_3$ with a four-core overlay, (c) Application of Z-layer $[0_2/90_2/+45/-45]$ with five-core overlay, (d) Repetition of steps 2 and 3 until full coverage is achieved with 4 UD layers and 5 Z-layers.

Due to the continuity of fabrics from the top skin, through the web, to the bottom skin, the stacking sequence is constrained and the result of a manual iterative process. Three fabric types are employed in the laminate: unidirectional (UD), bidirectional 0°/90°, and ±45°. All fabrics have an areal weight of 1200 gsm. For a fibre volume fraction of 54% in the skins, this corresponds to an approximate layer thickness of 0.838 mm (or 0.419 mm when using 600 gsm). In contrast, the webs exhibit a lower fibre content of 27%, for which a 1200 gsm fabric translates to a nominal thickness of 1.676 mm.

The final stacking sequence, summarized in Table 1.1, is selected to comply with CUR recommendations and to provide a balanced distribution of fibre orientations around the connection zones [27]. The facings consist of 62.5% 0°, 12.5% +45°, 12.5% −45°, and 12.5% 90°, while the integrated webs follow a lay-up optimized for shear transfer. The facing thickness is set at 25 mm, and the webs are placed at 150 mm center-to-center spacing with a 10 mm thickness, in accordance with the mechanical requirements for the selected 3-meter span. This span length represents the most probable cross-girder spacing, based on an inventory study of Dutch bridges conducted by Koetsier [28], as shown in Figure 1.5. These design decisions ensure that the specimens meet stiffness and hybrid interaction demands under the expected loading conditions.

Table 1.1: Stacking sequence of laminates of GFRP deck.

Facings (skins)	[45/-45/45/-45/45/-45/0_2/90_2/45/-45/90_3/0_2/90_2/45/-45/90_3/0_2/90_2/45/-45 /90_3/0_2/90_2/45 /-45/90_3/0_2/90_2/45/-45]
Webs	[-45/45/-45/45/-45/45/-45/45/90_2/0_2/-45/45/-45/45/-45/45]

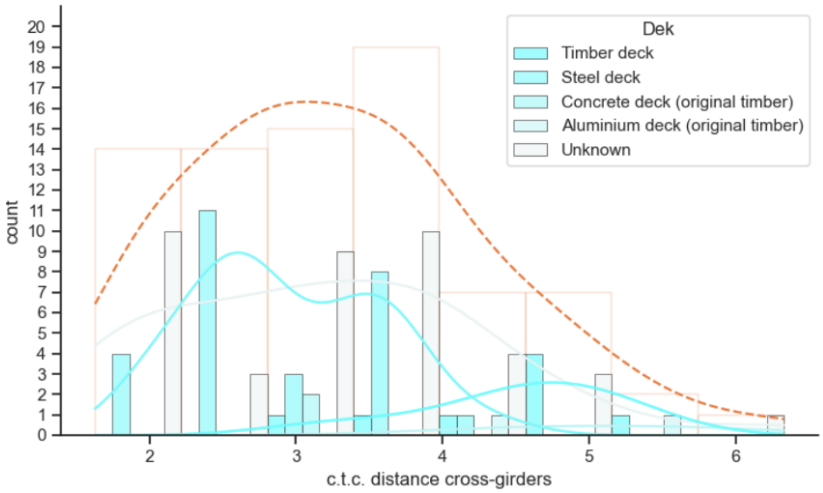

Figure 1.5: Distribution of center-to-center distances between cross-girders in existing RWS bridges, grouped by deck material [28].

1.5. Scope and research questions

Lightweight and fatigue-resistant composite panels offer a competitive solution for deck replacement on steel bridges. However, the integration of these relatively new materials into one of the most critical structural elements i.e., the connection between the deck and the girder, has presented significant challenges. The joints in this region are particularly critical, as they largely govern the fatigue performance of the overall structural system. The lack of a generic, reliable, and predictable connection technology has historically hindered the widespread application of composites in bridge construction.

Although the preliminary research performed at TU Delft [24, 21, 25], concluded that the novel iSRR connectors have potential for connecting composite decks on steel girders, systematic understanding of the connectors' behavior and ability to predict its performance in cyclic load regime is still lacking. The primary goal of this thesis is to advance understanding of the fatigue behavior and performance of shear connection technologies for composite-to-steel hybrid highway bridges. This goal is pursued through a combined focus on both the material-level properties of SRR and the structural performance of the iSRR connector.

To achieve these objectives, the research incorporates systematic experimental testing and numerical modeling. The work begins with characterizing the mechanical and fatigue behavior of the SRR material under compressive and tensile loading to establish a detailed understanding of its properties. The optimal resin composition for the SRR material is selected based on its mechanical and durability properties, ensuring improved long-term performance.

At the connector level, representative test set-ups are designed for fatigue characterization of the iSRR connector under shear loading. Experimental investigations include static and cyclic loading tests, as well as the evaluation of environmental factors such as

moisture and temperature. These tests are complemented by numerical models that provide insights into failure mechanisms and guide design modifications to enhance connector performance.

Based on the aforementioned, the following research questions are defined:

1. What are the mechanical characteristics of SRR material under monotonic (static) loading in both uniaxial (unconfined) and triaxial (confined) conditions, and how do these conditions influence its deformation capacity and failure mechanisms?

2. How does SRR material behave under compressive and tensile cyclic loading, and what are the key factors governing its fatigue life (σ-N curves) and ultimate failure mode?

3. What are the dominant failure modes of the iSRR connector within the GFRP deck under cyclic shear loading, and what is the expected fatigue life under various load ratios as well as the remaining static resistance?

4. How do variations in environmental conditions, such as temperature and moisture, affect the high-cycle fatigue performance and service life of the iSRR connector within a GFRP deck under cyclic shear loading?

5. How accurately can the damage progression observed in material-level experiments be captured through a Continuum Damage Mechanics (CDM), to accurately predict stiffness degradation, dominant failure modes, and fatigue life of the iSRR connector within a GFRP deck?

The objectives of this thesis will be approached through a combined methodology of experimental and numerical studies, which are outlined in the following sections. Complementary, Figure 1.6 gives holistic view on interplay between research scope and methodology that combines: i) short-term and long-term testing; at ii) material and connector (component) level; within iii) experimental and numerical approaches.

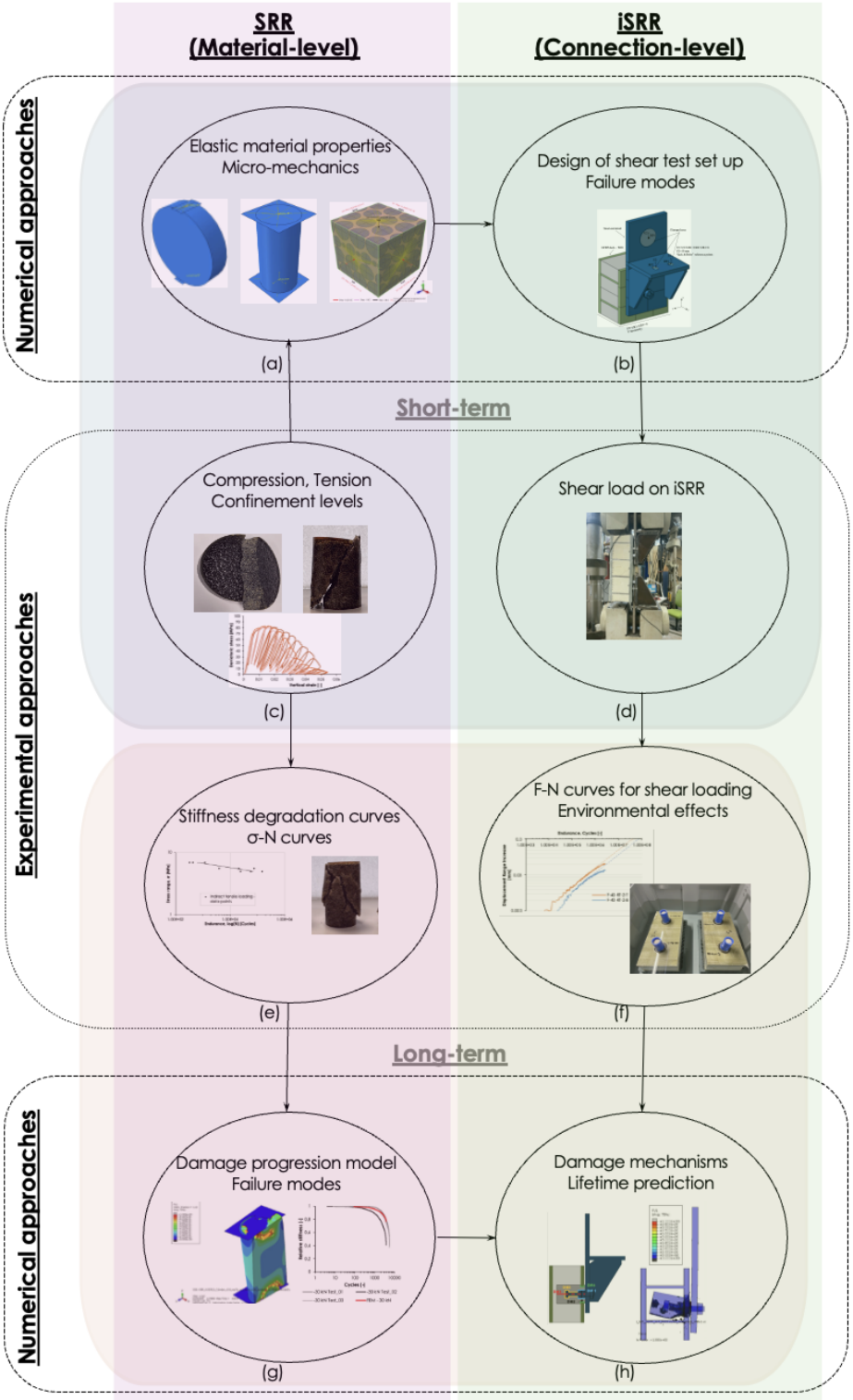

Figure 1.6: Visualization of methodology.

1.6. Experimental program

The experimental approach for SRR aims to characterize its short-term and long-term material properties to enhance understanding of its behavior and fatigue damage modeling. Standardized tests, frequently used for other granular materials (concrete, asphalt, etc.), will be employed to assess the material's performance in compression and tension. The stress-strain behavior and strength of SRR will be examined under different confinement levels, including unconfined conditions. Cylindrical and disk specimens are hypothesized to be effective for compressive and tensile testing, respectively. Incremental loading tests will be done under compression to derive the relation between plasticity and damage, as shown in Figure 1.6c. Finally, fatigue tests will also be performed for SRR under both compression and tension in the unconfined state to evaluate its behavior under cyclic loading, as illustrated in Figure 1.6e. Additionally, the tensile and water absorption tests will be conducted with three variations in SRR resin composition to ensure optimized material selection following a coupled mechanical-durability criterion. These experiments will provide critical insights into the mechanical, fatigue, and durability properties of SRR.

The fatigue resistance of iSRR connections will be evaluated through a series of customized tests under both static and cyclic loading conditions, shown in Figure 1.6d. The primary objective is to assess the shear behavior of the iSRR connections (Chapter 6 and 7) under various load ranges, ratios, temperatures, and moisture conditions. At first, three different alternating load levels (R = -1) and two temperature conditions (25 and 55 °C) will be applied. These tests aim to establish F-N curves (force vs. number of cycles until failure) and stiffness degradation curves, illustrated in Figure 1.6f, providing insight into the connection's performance over time for this most severe load scenario. Since the fatigue life of iSRR connectors is fundamentally governed by progressive stiffness degradation, rather than sudden failure, these curves will help quantify how stiffness loss evolves with cyclic loading. Experimental observations have shown that while crack formation may occur during cyclic loading, it is the gradual reduction in stiffness that dictates the remaining service life of the connector.

Additionally, the influence of the R-ratio (the ratio of minimum to maximum load in a fatigue load cycle) on the fatigue behavior will be investigated using the same type of specimens. To simulate real-world environmental effects, a set of specimens for shear experiments will be exposed to aging by moisture exposure. This includes submerging some samples in water baths, while others will be placed outdoors for a year to experience natural weathering. Understanding stiffness degradation in these different conditions will provide essential insights into the long-term fatigue resistance of the iSRR connectors, ensuring their reliability under real-world operational conditions.

1.7. Numerical modeling

Due to its granular nature, the performance of SRR material in compression is highly pressure dependent. The influence of different confinement levels and the material's failure behavior in compression will also be numerically evaluated. Central to this understanding are micro-mechanical FE models, where small representative volume of the material is modeled with actual steel balls surrounded by resin and considering nonlinear behavior of the interface between the resin and the steel balls as well as friction between steel balls.

Results of the micro-mechanical modeling will be validated against the experimental data previously gathered. The micro-mechanical model will provide critical insights into the Poisson's ratio and Young's modulus under both tensile compressive and loading conditions with various confinements, helping to understand material's elastic properties (see Figure 1.6a but also true failure mechanism. Additionally, homogenized meso-scale model based on continuum damage mechanics will be developed to simulate fatigue driven stiffness degradation of the SRR material obtained in compressive and tensile cyclic load experiments on coupon cylinders and disks as shown in Figure 1.6g. These models will be key in predicting the cyclic behavior of SRR, both at the material and connection levels.

The iSRR connector assembly will be modeled numerically on a component level to provide an in-depth understanding interaction of multiple materials: steel connector, SRR injection piece, GFRP composite panel and interaction between those. Detailed FE models of the complete specimens used in the shear connection experiments will be analyzed in ABAQUS® using advanced dynamic explicit solver [29]. At first the model of the connector loaded in shear will be utilized with mainly linear material properties and contact conditions, as shown in Chapter 5 and illustrated in Figure 1.6c, to properly design the test set-up for single connector testing scenario that best reflects the connector's load conditions arising from hybrid interaction between GFRP deck and steel girder in a bridge. In next instance the connector model will be used in Chapter 8 to characterize the individual and coupled impact of components of the failure mechanism of the connector loaded in shear, see Figure 1.6h. Non-linear contact interactions and alterations of material stiffness will be introduced at this stage of modeling in quasi-static analysis. At last, the continuum damage mechanics model of SRR material developed in Chapter 9 will be implemented in the connector model with all accompanying contact interactions between SRR, steel bolt, steel flange and GFRP laminate, as illustrated in Figure 1.6h. The aim is to offer valuable insights into the complex behavior of the connector under cyclic loading.

1.8. Thesis outline

This thesis is divided into five parts and ten chapters and one appendix. The structure of the thesis is presented below to guide the reader.

The first part includes this introduction, followed by a literature review in the second chapter, which focuses on both material- and connector-level experimental and numerical research. Firstly, the fatigue behavior of resins and the development of reinforced resin solutions is addressed. It then examines testing methods for composites with granular constituents, emphasizing parameters such as pressure that affect their mechanical performance. The review subsequently shifts to the connection level, discussing how composite decks are connected to steel girders, and how their fatigue behavior is tested and modeled. Finally, the chapter concludes with an exploration of continuum damage modeling for granular composites, providing insights into the long-term performance of these materials in structural applications.

The second part addresses the mechanical properties and behavior of SRR and includes two chapters. Chapter 3 presents an experimental study on three variants of resin used in SRR material focusing on the static and fatigue behavior, as well as hygroscopic performance., The indirect tensile set-up is utilized to analyze the mechanical properties of the granular composite material. The water absorption characteristics of three different

resins are briefly discussed based on experimental findings. From these results, a resin type is selected for use in all iSRR connectors and SRR coupons fabricated for the subsequent experimental campaigns in this thesis.

Chapter 4 presents the experimental investigation of the fatigue behavior of SRR material under compressive loading. The study evaluates the mechanical performance of SRR under monotonic loading in both unconfined and confined conditions. Next to monotonic loading, the incremental loading tests are utilized to derive direct correlation between plasticity and damage development towards the material failure. Furthermore, the chapter characterizes and provides insights into the long-term cyclic compressive behavior of SRR, contributing to a deeper understanding of its fatigue performance.

The third part shifts its focus from the material level to the fatigue behavior of iSRR connectors, based on the connector experiments. In order to experimentally characterize the fatigue behavior of iSRR connectors, Chapter 5 presents the design of a test set-up for evaluating the connectors' shear behavior. Various test set-ups are numerically modeled, and the influence of boundary conditions, steel flange stiffness, and the web direction of the composite deck are assessed. Based on stress concentration analyses, a test set-up is selected and compared to a more representative experimental configuration, which simulates a full deck subjected to wheel loading, generating shear forces on the connector due to deck-to-girder hybrid interaction. The representative set-up is selected followed by description of the final test design to be used for all subsequent shear loading experiments on the iSRR connectors.

Chapter 6 examines the cyclic and post-cyclic static shear performance of the iSRR connector. Utilizing the test set-up developed in Chapter 5, segments of composite sandwich web core panels are employed to assess the fatigue performance of the connections under shear loading. Three different load levels and several load ratios are tested. Complementary tests are conducted to evaluate the fatigue behavior of the iSRR connector under varying moisture conditions. Finally, post-cyclic static tests are performed to assess the connectors' residual stiffness, resistance, and ductility.

In Chapter 7, the focus is on extrapolating and integrating the fatigue degradation behavior to establish the fatigue life model of iSRR connectors subjected to shear loading. This investigation builds upon the experimental data delineated in Chapter 6. Statistical analysis is conducted resulting in the construction of two F-N curves that define the fatigue life of the connectors for both ambient and elevated temperature conditions. This chapter focuses on extrapolating the influence of various parameters, such as load level, load ratio, temperature, and moisture, on the fatigue life of the iSRR connectors.

To further understand and support the experimental observations from the iSRR connectors' campaign, numerical modeling work is imperative in order to comprehend the failure/damage mechanisms. For that purpose, the fourth part of this dissertation presents the numerical analysis and prediction of the SRR material and iSRR connector and it consists of two chapters. More specifically, Chapter 8 delves into numerical simulations that lead to understanding the mechanics of cyclic failure of the iSRR connector.

Chapter 9 starts with a computational prediction of SRR material based on damage modeling. Specifically, micro-mechanical models are constructed to predict the Young's modulus and Poisson's ratio of SRR under both compression and tension. The model is also employed to further investigate the influence of confinement and pressure dependency.

Finally, a nonlinear material model for SRR is developed, which accounts for damage progression under cyclic loading using compressive and tensile principal stresses as driving force in a continuum damage mechanics model. This model is validated using experimental results from the compression and tensile tests performed on the SRR material. Finally, the damage accumulation per cycle relationship is used to predict the cyclic behavior of the iSRR connector under shear loading.

The final, firth part of this dissertation consists solely of Chapter 10, which provides a summary of the key findings presented throughout the thesis. It synthesizes the results and conclusions drawn from the experimental and numerical studies, offering a consolidated overview of the contributions made in this research. Specifically, the chapter highlights two main findings: (1) the understanding of crack initiation and propagation under cyclic loading in the SRR material and its more complex behavior within the iSRR connector, and (2) the establishment of endurance criteria, represented by the F-N curve, for the design of connectors in structural applications. Finally, the chapter outlines recommendations for future research, emphasizing areas where further investigation could advance the understanding and application of SRR materials and iSRR connectors.

2

Literature review

This chapter is divided into seven sections and provides a comprehensive review of relevant literature. Section 2.1 introduces the fatigue behavior of bulk resin materials, followed by Section 2.2, which outlines the SRR material. Section 2.3 and Section 2.4 discuss testing techniques and the pressure sensitivity of SRR and other granular composites. Section 2.5 examines the use of shear connectors in composite deck systems, while Section 2.6 addresses numerical modeling approaches for bolted connections. Finally, Section 2.7 summarizes the identified knowledge gaps that motivate the current research.

2.1. Fatigue behavior of bulk resin materials

In engineering practice, resins are essentially used either as a thick structural bonding layer conversely to the traditional mechanical joining techniques or as an injected substance for bolts, studs, and void fillings. Additionally, polymeric materials are one of the two main ingredients to make fibrous composites. Many of these structural applications, such as in bridge construction, have to undergo a high number of fatigue cycles due to fluctuating loads. In that respect, extensive research on adhesive joints or fibre-polymer composite coupons has been conducted.

However, the influence of joint configuration on adhesives' stress state response [30] and the role of polymer matrices in composites' fatigue behavior [31, 32] has prompted increasing interest in investigating the fatigue resistance of bulk adhesive coupons [33]. Consequently, research dating back to the 1960s revealed that the crack initiation and propagation rates differ among the various types of resins, resulting in significant fatigue life variations [34]. Beyond the influence of resin type, a dependency on fatigue endurance was demonstrated by alternating the testing frequency, the magnitude of cyclic load, the R ratio, and the environmental effects [35].

One key discovery was the inverse relationship between the fatigue life of resins and testing frequency. More specifically, increasing the frequency results in elevated temperature levels within the resin, ultimately degrading its mechanical properties [36, 35] and impairing fatigue performance. Regarding the R ratio, it has been proved that the slope of the σ-N

curve is steeper for reversed loading than for tensile-tensile or compression-compression fatigue loadings [37].

In addition to these factors, environmental conditions represent another important parameter in the fatigue behavior of resins. Despite resins often being shielded from detrimental external influences in most applications, the long operation lifetime means it cannot be guaranteed that the resins will not be exposed to moisture or even water. Their high sensitivity to temperature is another concern, as their material properties tend to degrade owing to thermal effects such as softening [38, 39]. Recent studies have demonstrated the significant influence of environmental conditions, such as immersion in tap water and seawater, as well as associated thermal effects, on the mechanical properties of epoxy resins [40, 41]. From fatigue experiments conducted on aged and unaged coupons, it was observed that exposure to water induced plasticization and softening of the material [42]. Thus, the slopes of the σ-N curves were, yet again, greatly increased, indicating a detrimental effect on the material's fatigue performance.

2.2. Development of Steel Reinforced Resin (SRR)

Aiming to improve the durability of the resins, polymer matrix composite materials were invented. In particular, several researchers suggested modifications to the resin's composition by introducing various inclusions. Among these alterations, the incorporation of carbon nanofibers into the bulk resin system has received widespread attention due to its potential to enhance the mechanical and thermal properties, as well as fracture toughness, of the resulting composite material [43]. Later it was proved beneficial also in terms of durability and fatigue resistance [44]. Apart from randomly shaped fillers, nano, and micro-spherical particles are also used as reinforcement [45]. In particular, a swift of the σ-N curve with higher fatigue lifetime and the same slope was reported in the polymers with rubber and silica nanoparticles [46].

Besides the nano or micro inclusions, Nijgh [22] proposed reinforcing commercially available resins using macro steel particles i.e., steel balls of a few millimeters in diameter. The steel particles were selected for their easy workability, immediate availability, and cost-effectiveness. More importantly, they have been demonstrated to enhance the stiffness and creep resistance of the resulting composite material [22]. However, up until now, there is no literature available on the fatigue performance and water resistance of such SRR.

Initially, SRR was investigated as an injection material for composite floor systems using an epoxy resin system [47]. Later studies employed SRR as a cavity filler in GFRP decks for highway bridges using an unsaturated polyester polyurethane hybrid system (UPE+PU) [24, 21]. Despite its successful application in various structures, there is still no data on SRR performance under different environmental conditions. However, material properties at room temperature are available (see Table 2.1) and show variation based on resin composition, hardener type, specimen geometry, and steel balls percentage. This highlights the importance of optimizing these parameters for SRR composite materials.

Table 2.1: Collection of mechanical properties of SRR at room temperature from literature.

Type of SRR	Property	Methodology	Reference
40% epoxy, RenGel SW 404 + HY 2404 60% steel balls	E=15.7 GPa	5 compression tests on unconfined specimens D26.3x50 mm	[48]
	fu=120.3 MPa	5 compression tests on unconfined specimens D26.3x50 mm	[48]
	ν=0.22	1 compression test on unconfined specimens D26.3x50 mm	[48]
	ν=0.19	Numerically determined	[47]
	E=17.6 GPa	5 compression tests on unconfined specimens D22x22 mm	[48]
40% epoxy, RenGel SW 404 + HY 2404 60% steel balls	E=21.9 GPa	3 compression tests on unconfined specimens D22x22 mm	[49]
	fc=136.2 MPa	3 compression tests on unconfined specimens D22x22 mm	[49]
	ν=0.22	Assumed based on a test with another hardener HY 2404	[49]
	ν=0.20	Numerically determined	[47]
20% UPE+PU, AQR 1025/B25	E = 9.3 GPa	3 compression tests on unconfined cylinders D62x130 mm	[50]
	fc = 74.3 MPa	3 compression tests on unconfined cylinders D62x130 mm	[50]
	ft = 10.1 MPa	3 tensile splitting tests on unconfined cylinders D62x130 mm	[50]

Concerning the cyclic performance of SRR material, previous experiments focused only on a connection level [21]. However, in a recent publication, it has been suggested that the fatigue performance of these connections is predominantly dictated by the stresses experienced within the SRR component [51]. Hence, there's an imperative need to examine the fatigue response of the SRR material itself, particularly its susceptibility to varying environmental conditions.

2.3. Testing of composite materials with granular constituents

Composite materials consist of at least two distinct constituents, combined to create a new material with properties that are superior to those of the individual components. When one of the components is a granular material, the result is a non-homogeneous product with significant potential for structural applications. For example, the combination of bitumen and aggregates produces asphalt, while cement mixed with aggregates forms concrete, both of which are widely used in civil engineering due to their enhanced strength and durability. In the case of steel-reinforced resin, which incorporates granular inserts as well, its characterization can be conducted using methodologies adapted from those applied to other well-established construction granular composites.

More specifically, unlike homogeneous materials such as steel, the characterization of composite materials with granular components cannot rely on standard methods like dog-bone coupons. Instead, the compressive strength of these materials is typically measured using cylindrical specimens, which are better suited for capturing the unique mechanical behavior of composites with granular constituents. Research in concrete has demonstrated that the size and shape of specimens can significantly influence test outcomes. Additionally, for both concrete and asphalt, the effect of friction at the end surfaces of specimens has been explored, highlighting its impact on test accuracy [52, 53].

To evaluate the tensile behavior of these materials, the most commonly used test set-up is the indirect tensile splitting test, also known as the Brazilian test. The term "Brazilian test" is typically used in the context of concrete, whereas in asphalt research, it is mainly referred to as the indirect tensile test (IDT). In both cases, disk-shaped specimens are placed between two loading plates, and tensile stress is indirectly applied through diametrical compression to assess the material's tensile strength. In 1978, the Society for Rock Mechanics officially proposed the indirect tensile splitting test as the standard method for determining the tensile strength of rocks [54]. Many studies have since focused on the influence of the loading

plates, with several suggesting modifications to either flatten the surfaces of the coupon or apply the load using arc-shaped plates.

Triaxial test methods are widely used to evaluate the shear resistance and strength of granular composites under various conditions of axial loading and confining pressure. Initially developed for soil research, triaxial testing gained popularity for asphalt mixtures in the 1950s. In 1969, the exploration of biaxial and triaxial stress states was extended to normal-strength concrete [55]. In granular composite materials, it is well established that lateral confinement increases both compressive strength and deformation capacity [56]. Furthermore, shear strength is enhanced under confinement, as the tighter contact between particles reduces their ability to rearrange or slide, thereby increasing overall stability and resistance to shear forces.

2.4. Pressure dependency of SRR and other granular composites

Research has also focused on understanding the influence of confinement, particularly in the compressive behavior of SRR. Since this type of resin is reinforced with steel balls, it is classified as a granular composite, leading to the hypothesis that it exhibits pressure-dependent material behavior. In fact, M. Nijgh, the inventor of the SRR material, modeled SRR under pressure using the Drucker-Prager model, which is commonly applied to pressure-sensitive materials [47].

The application of confinement to the SRR material has not yet been studied using a triaxial test set-up. Instead, lateral confinement was passively applied by both Nijgh and Pedrosa using a 4 mm thick steel tube, while the load was introduced to the SRR cylindrical specimen through a solid steel pin [47, 49]. Static tests conducted by Nijgh and quasi-static cyclic tests by Pedrosa both demonstrated that full confinement increases the stiffness of SRR. Pedrosa particularly noted that this effect becomes more pronounced after a larger number of cycles, once the material undergoes settlement and densification [49]. However, this test set-up proved insufficient for assessing compressive strength, as the steel tube used to confine the specimen yielded once the axial load increased further.

In its initial application, SRR was used as an injection material for injection bolts and it was surrounded by metallic components, where the confining pressure was considered to be very high. In the present study, the injected material is surrounded by the composite bottom facing and the foam core of the sandwich panel web. The contribution of the foam core to load transfer is considered negligible, while the composite bottom facing offers less rigid boundary conditions compared to steel-to-steel confinement. Therefore, in the context of GFRP-to-steel applications, the injected SRR is considered to be in a semi-confined state.

2.5. Shear connectors for composite decks

The connections of composite decks can be categorized into three levels: component-level, panel-level, and system-level connections [57] Component-level connections are typically made in the factory, using adhesive bonding or mechanical fastening methods to form individual panels. Panel-level connections, on the other hand, are made on-site, where panels are joined using adhesives, tongue-groove joints, or mechanical fasteners. This type of connection presents challenges such as curing time and quality control during installation. Finally, system-level connections secure the deck to the girders, either by either with or

without composite (hybrid) action. These system-level connections are the most complex and have attracted significant research attention, as they are critical to the overall structural performance of the composite deck system. The following review focuses on the various approaches and research surrounding shear connectors, examining three primary types: traditional bolted fasteners, adhesive bonding systems, and shear stud connections, as seen in Figure 2.1.

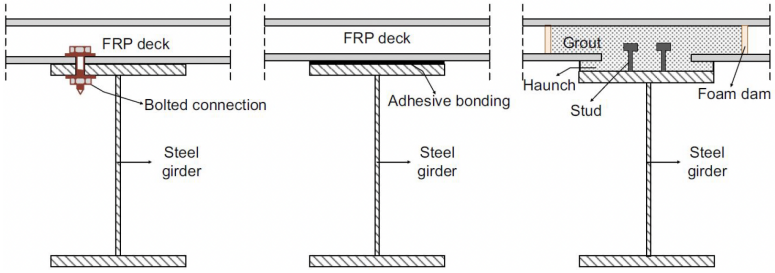

Figure 2.1: System-level connection types in steel-GFRP bridges [58].

Shear connectors play a critical role in composite decks by ensuring effective load transfer between the deck and the supporting steel girders. In cases where composite action is not achieved, the connectors are only required to prevent vertical separation and lateral displacement between the deck and the girder. In such configurations, bolts or blind fasteners are typically utilized. However, in systems designed to enable composite action, the role of the connectors becomes more critical, as they must not only resist transverse movements and uplift of the deck but also transfer shear forces between the deck and the girder, ensuring effective load-sharing and mechanical integration between the two components.

Bolted fasteners are one of the simplest and most commonly used connection methods in steel-GFRP bridges. These connectors involve inserting long bolts through pre-drilled holes in the GFRP deck and securing them to the steel girders below. Traditional bolts provide a mechanical fastening method that allows for easy assembly and disassembly, making them ideal for modular structures where maintenance and part replacement are priorities. Temeles and Lesko utilized a long shaft similar to the one later used by Park et al. but modified the connection by incorporating a steel sleeve around the shaft, as shown in Figure 2.2a, which was partially preloaded [59]. Park studied the composite behavior of long traditional bolts (Figure 2.2b), demonstrating that the bolts' performance is largely dependent on the interval between fasteners, which governs the degree of load sharing between the GFRP deck and the steel girders [17].

Blind bolts are a subtype of bolted fasteners that require access to only one side of the deck, making them more practical for installation in difficult-to-reach areas, such as the underside of bridge decks. This feature provides a significant advantage during on-site assembly, reducing construction time and labor costs. Blind bolts are particularly beneficial in cases where traditional long bolts cannot be used due to limited access to the top side of the deck after production. Studies by Satasivam and Bai confirmed that blind bolts offer similar structural performance to traditional bolts under service load levels, making them a viable alternative for steel-GFRP deck connections [60]. Csillag and Pavlović investigated

the static of blind bolts, specifically the Ajax (Figure 2.2c) and Lindapter connectors (Figure 2.2d), and found that both exhibited significant ductility and sufficient ultimate shear resistances [24]. The failure mode of both bolt types was a combination of local bearing of the laminate and yielding of the bolts.

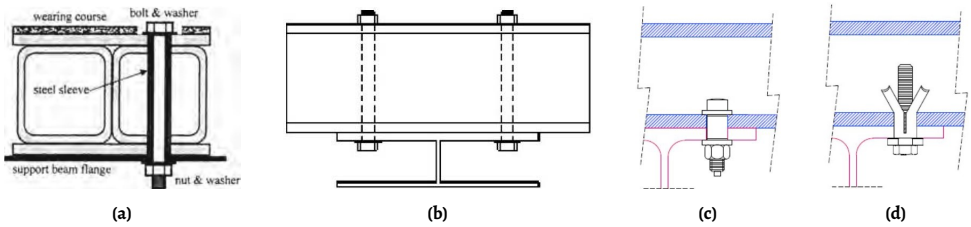

Figure 2.2: Traditional and blind bolts used in GFRP-steel bridges: (a) Long shaft with sleeve, (b) Long shaft, (c) Ajax bolt and (d) Lindapter bolt [50].

Although the blind bolts tested by Csillag demonstrated good initial shear and ductility performance, later research by Olivier evaluated the fatigue performance of blind bolts and revealed their insufficiency [25]. In general, the potential for slip at the bolt interfaces exacerbates the fatigue issues, making bolted connections less suitable for applications where long-term fatigue performance is critical, as demonstrated in [25]. The constant slip observed in these connections can lead to unexpected fatigue failure, especially when bolts are required to carry both shear and tension loads.

While bolted fasteners offer simplicity, they have notable limitations, primarily due to the high localized stress concentrations introduced around the drilled holes in the GFRP deck, which can result in fatigue issues and delamination over time. Therefore, as an alternative adhesive bonding is used, providing a more uniform stress distribution across the interface between the GFRP deck and steel girders. Adhesives are applied over large surface areas, allowing shear forces to be transferred smoothly without the concentrated stress peaks that are common in bolted connections. This feature makes adhesive bonding particularly attractive for hybrid bridges, where the lightweight nature of the adhesive and its excellent fatigue performance can enhance the longevity of the structure.

Gürtler conducted large-scale experiments on adhesively bonded pultruded GFRP bridge decks connected to steel girders, demonstrating excellent static performance under four-point bending tests [61]. Full shear load transfer between the deck and girders was achieved for two different types of pultruded decks. Schollmayer identified that the tensile (peeling) stress distribution was uneven, with the highest stress concentrations occurring beneath the webs of the GFRP panel [62]. Jiang, Kolstein, and Bijlaard performed experiments on adhesively bonded sandwich panels, showing shear strengths of up to 70 kN when proper surface preparation techniques, such as sandblasting, were employed [63].

Research on both mechanically connected and adhesively bonded joints highlights the significant influence of thermal conditions on their performance. Studies by Turvey and Wang, Wu et al., and Xue et al. demonstrated that single- or double-bolted pultruded composite profiles experienced strength reductions and changes in failure modes when subjected to high temperatures [64–66]. Similar findings were observed in adhesively bonded joints, where temperature variations accelerated fatigue failure, as evidenced in

the works of Liu et al. and Ashcroft et al. [67, 68]. Heshmati identified moisture and temperature as key factors affecting the long-term performance of adhesively bonded steel-GFRP joints, significantly reducing strength and stiffness [69]. The combined effects of these environmental conditions can be more damaging than each individually, highlighting the need for careful consideration in design.

Due to durability concerns of purely adhesive systems, many modern bridge designs employ hybrid systems that combine adhesive bonding with mechanical fasteners to enhance performance. This combination allows for both the smooth load transfer of adhesive bonds and the added mechanical security of bolts, reducing the risk of sudden failure. Keller and Gürtler explored the use of a hybrid system, bonding GFRP decks to steel girders with an adhesive layer between 6 and 10 mm thick, supplemented by mechanical fasteners [70]. Their experiments showed that this hybrid system exhibited ductile failure modes during static loading tests and performed exceptionally well in fatigue tests, with no signs of damage after 10 million load cycles.

Despite the advantages of hybrid adhesive-bolted systems, the need for additional design and construction effort limits their widespread use. The combination of adhesives and fasteners complicates the installation process, as careful coordination is required to ensure proper curing of the adhesive while maintaining the integrity of the mechanical connection. Furthermore, hybrid systems are not easily disassembled, which can pose challenges for maintenance and retrofitting of the bridge.

Shear studs, commonly used in steel-concrete composite structures, have been adapted for steel-GFRP decks, where they are welded to the steel girders and connected to the GFRP deck through cut-outs. After positioning the deck, the studs are typically secured with grout or similar bonding materials. Moon et al. tested shear stud connections in GFRP decks and reported excellent shear resistance with negligible stiffness degradation after 10 million load cycles, indicating their suitability for high-cycle fatigue environments such as road bridges [20].

Davalos et al. introduced an innovative shear connector design featuring a welded threaded stud surrounded by steel sleeves, which helps reduce shear and compressive stresses on the GFRP deck [71]. This replaceable connection minimizes damage to the composite material. Push-out tests showed a shear strength of 114 kN before yielding, with no fatigue deterioration after 10.5 million load cycles, though it achieved only partial composite action (around 25%). Further studies by Davalos and Righman revealed that displacement was primarily due to stud deformation, with stiffness improving once the bottom flange of the sleeve contacted the stud. Despite limited composite action, the connector showed durability under cyclic loading, equivalent to a 75-year bridge service span.

However, shear stud connections present significant challenges. The installation is labor-intensive, requiring large cut-outs in the GFRP deck, which leads to stress concentrations around the grout pockets, raising concerns about fatigue damage and delamination. Additionally, the grouting process is time-consuming and must be performed with precision to avoid voids or leaks. Furthermore, the durability of the grout under fatigue loading has been questioned, and some studies suggest that shear stud connectors may not always provide full composite action in GFRP applications, with researchers presenting conflicting results on their effectiveness [20, 71].

Instead of embedding a mechanical connector in bonding material, another option is to use injection bolts. These bolts are specifically designed to reduce slip in shear connections by injecting a two-component epoxy resin through the bolt head. Once the resin cures, it takes on a load-bearing role, reducing slip to below 0.3 mm over the connection's service life. The resin facilitates shear load transfer through both bearing and the bolt itself, making injection bolts ideal for applications where minimal slip is essential.

Injection bolts have been used in several studies for connecting composites. For example, van Wingerde [72] investigated the fatigue performance of injection bolts in pultruded GFRP joints, finding that while fatigue life showed minimal improvement under standard loading conditions ($R = 0.1$), it increased significantly—by 100 times—under reversed cyclic loading ($R = -1$). Additionally, a study by Zafari on resin injected bolted joints in pultruded GFRP observed promising results in slip and fatigue resistance [73]. The study suggested that the 0.3 mm lifetime slip limit outlined for steel structures might be too conservative for GFRP applications due to the viscoelastic nature of polymeric materials, proposing a higher limit of 0.75 mm over 100 years. These findings highlight the effectiveness of injection bolts in composite bridge engineering.

Despite their advantages, injection bolts come with certain disadvantages. The installation process is labor-intensive and requires precise application, leading to higher time demands during on-site construction. Additionally, the curing process makes these bolts sensitive to environmental conditions, such as temperature and humidity, which can affect their performance.

To address the challenges associated with the traditional connection technologies, recent innovations have focused on reducing stress concentrations and improving fatigue performance. One such innovation is the development of the iSRR connector. This connector, introduced by Csillag [50], combines a mechanical shear stud with a steel-reinforced resin, which fills the cavity inside the GFRP deck. The SRR provides additional strength and rigidity, significantly reducing slip in the connection and improving fatigue performance.

While the iSRR connector has shown excellent performance under short- and long-term loading conditions, it has not yet been tested under elevated temperatures. All current testing has been conducted under favorable laboratory conditions, with perfectly flat panels and ambient temperatures between 20–25 °C. The potential influence of higher temperatures, which could accelerate fatigue and creep failure, has not been explored. Given the findings from studies on both bolted and adhesively bonded joints, future research should investigate the effects of thermal conditions on the iSRR connector to ensure its durability in a wider range of environmental conditions.

In conclusion, shear connectors are essential for the efficient transfer of forces in composite steel-GFRP decks, and their design plays a significant role in determining the bridge's overall performance. Traditional bolted fasteners offer simplicity and ease of installation but can cause stress concentrations that may lead to fatigue issues. Adhesive bonding systems provide smooth load transfer but are sensitive to environmental factors, necessitating careful design considerations. Shear stud connections offer excellent shear and fatigue resistance but are labor-intensive and can introduce stress concentrations around grout pockets. Recent innovations, such as the iSRR connector, demonstrate promising advancements in shear connection technology, improving fatigue performance and sustainability. Each method has its specific strengths and limitations, and the choice of connector must be

tailored to the specific requirements of the bridge design, considering factors such as load transfer, durability, and ease of maintenance.

2.6. Numerical modeling of bolted connectors for composite decks

Regardless of connection type, physical testing has been the conventional practice to analyze the joint cyclic behavior in both composite and non-composite structures. This approach has significantly enhanced the understanding of the interactions between various structural elements. However, the reliance on physical testing is limited by the availability of comprehensive and relevant test data. The extensive variety of joint types, along with the nuances within each category, poses challenges in achieving a holistic understanding through empirical testing alone. These limitations underscore the necessity for alternative or supplementary methodologies to fully comprehend the complexities in joint behaviors, with a specific emphasis on understanding their fatigue characteristics.

While significant strides have been made in understanding and predicting fatigue behavior in bonded joints [74], the same cannot be said for bolted joints, particularly within fibre-polymer composite contexts. This area remains relatively under-explored, as evidenced by the limited literature. A common thread across these studies is the identification of stiffness degradation within composite laminates as the primary damage mechanism driving fatigue degradation in bolted joints. This understanding simplifies the damage mechanism analysis, allowing predictions of cyclic performance to focus predominantly on this aspect. However, this approach does not extend to the iSRR connection, where conspicuous failure in the GFRP bottom laminate facing is absent, both during cyclic testing and post-cyclic static testing.

2.7. Summary of knowledge gaps

Based on the discussions throughout this chapter and with a focus on the material- and connection-level performance of SRR and iSRR, several key gaps in the existing literature have been identified. These gaps highlight critical areas that need further investigation to enhance the understanding and practical application of SRR materials and iSRR connectors. The following conclusions can be drawn:

- There is a lack of comprehensive studies on the fatigue resistance of SRR materials under varying environmental conditions (e.g., moisture, temperature). Attention should be given to long-term durability and fatigue testing in real-world conditions.
- Current testing methodologies for SRR, particularly under cyclic shear and triaxial stress states, are insufficient. Triaxial and shear testing set-ups need to be developed to better understand SRR's pressure-dependent behavior.
- The iSRR connector has not been adequately tested under high temperatures, humidity, and other real-world environmental factors. The long-term performance under these conditions, especially regarding fatigue should be explored.
- Existing numerical models for bolted connectors lack complexity in addressing the interaction of materials within the iSRR connector. More advanced models should be developed to capture the effects of cyclic loading.

II

Static and Fatigue Behavior of (Steel-Reinforced) Resin material

3

Tensile behavior of steel reinforced resin

The primary objective of this study is to evaluate the performance of various SRR types considering the application-oriented requirements such as resistance to cyclic loading and environmental conditions, like moisture and increased temperature. Elevated temperatures are considered because they simulate the service conditions experienced by bridges due to their sunlight exposure and high ambient temperatures. Through a series of tests, the static mechanical properties and fatigue performance of SRR material will be assessed at both ambient and elevated temperatures.

This chapter is structured as follows: Section 3.1 provides a description of the three distinct resin types considered in this study. Sections 3.2 and 3.3 detail the experimental procedures, focusing on the preparation of the samples and the description of the test set-up, respectively. Section 3.4 presents an evaluation of the tensile properties of the three SRR types under both room and elevated temperatures using indirect tensile splitting test configurations. In Section 3.5, the elastic properties of the SRR materials are calculated. Section 3.6 shifts the focus to the fatigue performance of these materials, presenting stress-cycle (σ-N) diagrams derived from indirect tensile fatigue tests conducted at ambient temperature, along with additional fatigue experiments performed at elevated temperatures. Section 3.7 assesses the long-term practicality of SRR materials by examining their susceptibility to aging. This includes water absorption tests conducted on all three resin compositions, both with and without the inclusion of steel balls. Finally, Section 3.8 consolidates the main points, elaborates on the key findings of the study, and concludes with the selection of one resin system for further research on SRR material and connector-level applications.

3.1. Resin systems considered

Epoxy resins are widely used due to their excellent mechanical properties, versatility, low shrinkage on curing, and ease of use. However, they often require post-curing to achieve

Parts of this chapter have been published in Christoforidou et al. [75].

optimal mechanical and thermal properties, which can add complexity to the manufacturing process. Additionally, their high viscosity has led to challenges in molding and injection processes, prompting interest in alternative resin types such as vinyl ester or polyurethane resins. vinyl ester resins, with their low hydrophobic features, have demonstrated superior hydrothermal aging resistance compared to epoxies [76]. With regard to polyurethane resins, although they have been used in various structural applications due to their versatile properties, certain types with a weak elastomeric nature and high thermal expansion coefficient are initially deemed unsuitable for larger structural forms [77]. The introduction of unsaturated polyester as an additional reactive polymer led to the development of UPE+PU, effectively eliminating the deficits of polyurethane resin [78].

Three resin systems from the main categories described above are investigated. More specifically, an infusion epoxy resin commercially available as Resoltech 1080S/ Hardener 1083, the vinyl ester resin Atlac 430LV and the UPE+PU resin referred to as AQR 1025/B25 are considered in this work. The main characteristic that all three have in common is their high glass transition temperature ($Tg > 100\ ^\circ C$) when subjected to complete curing conditions. This information together with their Young's modulus (E), maximum tensile strength (f_u), and viscosity (η) at 23 °C are reported in Table 3.1, based on technical data provided by the resin supplier [79–81].

Table 3.1: Nominal properties of the investigated resins.

Type	Name	E [GPa]	f_u [MPa]		η [mPa.s]	Tg.max [°C]
Post cure		Fully[1]	5 hr 60 °C	Fully[1]		Fully[1]
Infusion epoxy	Resoltech 1080S/ Hardener 1083	2.91	77	116	1100	110
UPE+PU	AQR 1025/B25	3.53	77	95	150 – 220	135
Vinyl ester	Atlac 430LV	3.13	67	95	440 – 500	130

[1] Fully post-cured: 4h at peak tan delta temperature

3.2. Resin preparation and production of specimens

All resins are prepared at room temperature, adhering to the supplier-recommended mixing ratios [79–81]. The epoxy resin is created using a 100/20 mixing ratio between the Resoltech 1080S and the hardener 1083, respectively. For the UPE+PU system, a three-component resin, 2 grams of a catalyst system, supplied as PerkadoxCH50, are dissolved into 100 grams of AQR 1025/B25 (2% wt) followed by the addition of 25 grams of Lupranate M20R+29 after thorough stirring. Lastly, the vinyl ester resin is prepared by mixing 100 grams of Atlac 430LV and 2 grams of PerkadoxCH50, representing 2% of the Atlac 430LV weight. Each mixture is stirred for at least 1 minute to ensure proper dissolution.

SRR disks are produced by mixing polymer resin with high-carbon steel balls and casting the mixture into cylindrical acrylic molds. The steel balls used is spherical, type S390, with an average diameter of approximately 1 mm, and occupies roughly 80% of the total volume. This high packing fraction ensures that the balls remain in contact with one another, creating a mechanically interlocked network that governs the composite's stiffness and load transfer capacity. The steel balls' properties are based on manufacturer specifications provided by Airblast [23]. All the coupons are manufactured the same way with proportions of both

ingredients being: 830 g of steel balls and 65 g of resin. This ratio yields an average thickness of 23 mm for the SRR specimens, while the diameter is set to 100 mm as shown in 3.1. To allow extraction of air bubbles created during mixing, the specimens are placed on a vibrating table for five minutes. Following a one-day curing period at ambient temperature, the samples are post-cured at 60 °C for five hours as specified in [81].

3.3. Test set-up for SRR tensile experiments

Depending on the specific mechanical property under investigation, varying loading protocols and instrumentation are employed. These are further detailed in Table 3.2. For the investigation of strength and Poisson's ratio, the force is applied using a 50 kN MTS actuator and measured with a Lebow 50 kN load cell. This actuator is managed by an Instron test controller, featuring a frequency range of 0.001 - 30 Hz and a strain rate range of 0.001 - 5% per second. The experimental set-up is placed in a Weiss Enet temperature cabinet with internal dimensions of 1.0x1.0x1.0 m. This cabinet allows precise control of internal temperature, ranging from -40 to 60 °C, through electrical heating control with an accuracy of 0.1 °C.

When determining stiffness, a pneumatic Universal Testing Machine (UTM) is utilized, equipped with a load cell of a maximum capacity equal to 5 kN. This set-up is positioned within a temperature cabinet with internal dimensions of 0.5x0.8x1.0 m, capable of sustaining a temperature range between 0 and 60 °C. Solartron Linear Variable Displacement Transducers (LVDTs) are employed to monitor the horizontal displacements during stiffness tests, offering a maximum capacity of ±1 mm. Lastly, during the tests for determining the Poisson's ratio, a Canon EOS 5DS DSLR camera is used to capture photos of the specimen.

Table 3.2: Description of experiments for determining mechanical properties of SRR material under tension.

Property	Loading	Instrumentation	Temperatures	Coupons	Machine
Strength	25 mm/min	Machine	25, 40, 55 °C	3	MTS-50
Stiffness	5 compressive pulses	LVDTs	25, 40, 55 °C	3	UTM-5
Poisson's ratio	0.01 mm/sec	Camera	25 °C	3	MTS-50

The heterogeneous composition of composite materials with granular additions complicates the determination of their tensile strength via dog-bone tensile coupons, which is the regular procedure for determining bulk properties of adhesives and resins. Thus, the strength of the SRR material is assessed by applying compressive force in the vertical plane of cylindrical coupons, generating horizontal tensile stresses that lead to fracture (a.k.a. Brazilian test). Indirect tensile splitting tests are performed at room and elevated temperatures e.g., 25 °C, 40 °C, and 55 °C, and the set-up is shown in Figure 3.1.

The load is applied at a constant rate of 25 mm/min using two 12 mm thick steel loading strips in contact with the disk-shaped SRR coupon. To determine the indirect tensile splitting strength, the specimens are loaded until failure. A tensile crack at the centre of the disks is observed, as displayed in Figure 3.1. The average force versus the recorded stroke curves from the three tests performed for each type of SRR are presented in Figure 3.2. The initial straight line, observed until 0.4 mm for the case of UPE+PU, is attributed to the absence of contact between the specimen and the loading blade. Subsequently, a nonlinear

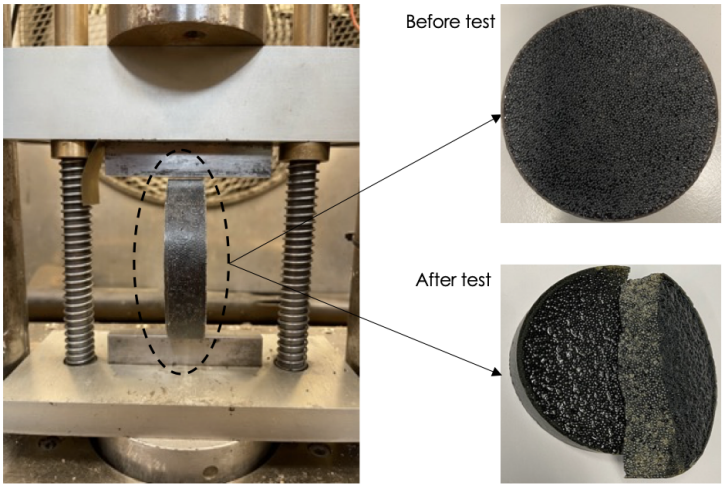

Figure 3.1: Indirect tensile strength test set-up and coupon prior and after testing; epoxy based SRR.

section, noticeable up until approximately 10 kN of applied load arose from plotting the external force against the total displacement. This displacement incorporates the settlement of the specimens in the apparatus or the localized crushing near the loading areas. This nonlinearity has also been attributed to densification in the case of asphalt concrete mixtures under indirect tensile loading [82], or to the bedding-in effect for anisotropic rocks under the indirect tensile splitting test arrangement [83].

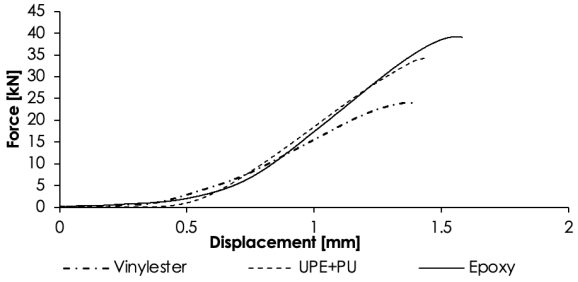

Figure 3.2: Average tensile splitting force versus displacement at 25 °C from stroke of the machine.

The resulting tensile splitting stress (horizontal) $\sigma_{x,max}$ at the centre of the specimen in (MPa) is calculated using the conventional formula for homogeneous and linear elastic materials tested as outlined in [84]. In particular, the vertically applied force is divided by the corresponding tensile area as follows:

$$\sigma_{x,max} = \frac{2 \cdot F}{\pi \cdot D \cdot t} \tag{3.1}$$

where F represents the vertically applied loading (N); D is the diameter of the test specimen (mm); and t is the thickness of the test specimen (mm).

3.4. Tensile strength of SRR material at various temperatures

The results of the tensile strengths of the three types of resins under varying temperatures are shown in Table 3.3. The maximum strength is observed for the SRR produced with epoxy resin at room temperature, equating to 11.6 MPa which diminished by 13% and 22% once temperature rose to 40 °C and 55 °C, accordingly. For the vinyl ester based SRR, the ultimate tensile strength of the coupon is not affected by temperature changes. However, it consistently exhibited the lowest strength value, approximately 6.8 MPa, across all three temperature conditions. Regarding the UPE+PU based SRR specimens, the 10 MPa tensile strength at room temperature aligns with the tabulated results in Table 2.1, reported in literature [50]. The strength reduction due to temperature increase follows a similar trend to that observed for the epoxy resin, as depicted in Figure 3.3. Lastly, under the same post-curing conditions, the addition of steel reinforcement in the pure resin matrix led to an approximately 85% reduction in their tensile strength, as tabulated in Table 3.1 and Table 3.3.

Table 3.3: Average strength values for various temperatures and types of resins.

SRR Type	Strength [MPa]		
	at 25 °C	at 40 °C	at 55 °C
Epoxy (COV%)	11.6 (2.7%)	10.1 (3.6%)	9.0 (2.0%)
UPE+PU (COV%)	10.0 (3.9%)	8.9 (2.2%)	7.5 (9.9%)
Vinyl ester (COV%)	6.8 (2.2%)	7.1 (8.6%)	6.6 (5.6%)

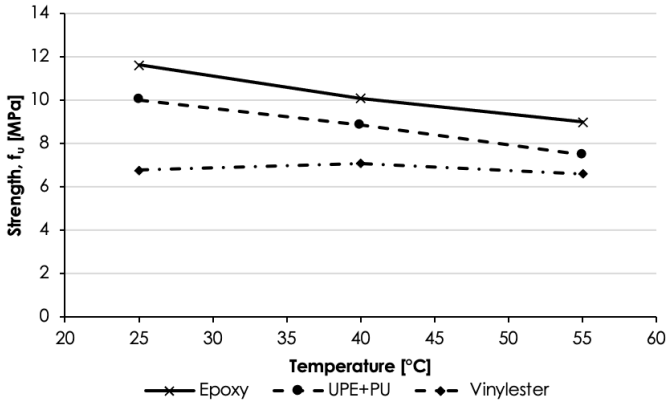

Figure 3.3: Average indirect tensile splitting strength variation under various temperatures.

3.5. Stiffness and Poisson's ratio of SRR material under tension

To accurately determine the indirect tensile modulus of granular materials, it is essential to measure their Poisson's ratios. In the subsequent sections, the Poisson's ratios are deduced through a combination of numerical and experimental approach. Initially, the horizontal

and vertical extensions will be derived, followed by the establishment of a numerical model designed to correlate the horizontal-to-vertical proportion with the material's Poisson's ratio. The results presented focus on the two SRRs with the highest static strength, specifically the epoxy and the UPE+PU resin systems.

A set-up analogous to the one used for the indirect tensile strength tests described in Section 3.3 is employed, with the primary difference being the incorporation of a single camera to perform the Digital Image Correlation (DIC) technique to quantify the surface planar deformations. Sequential digital images are captured for two SRR coupons that are loaded up to 20 kN of force at a loading rate of 0.01 mm/sec. The image acquisition is synchronized with the load from the test frame through a data acquisition system.

A fine speckled pattern is applied to the coupons, as shown in Figure 3.4a. From the DIC analysis performed on an SRR disk made with epoxy and UPE + PU resin, the ratio between the vertical and the horizontal strain, as depicted in Figures 3.5a and 3.5b, is equal to 0.1312 and 0.129, respectively. These extensions are calculated via virtual extensometers positioned at least 10 mm away from the edges and loading points to avoid local effects, as sketched in Figure 3.4b.

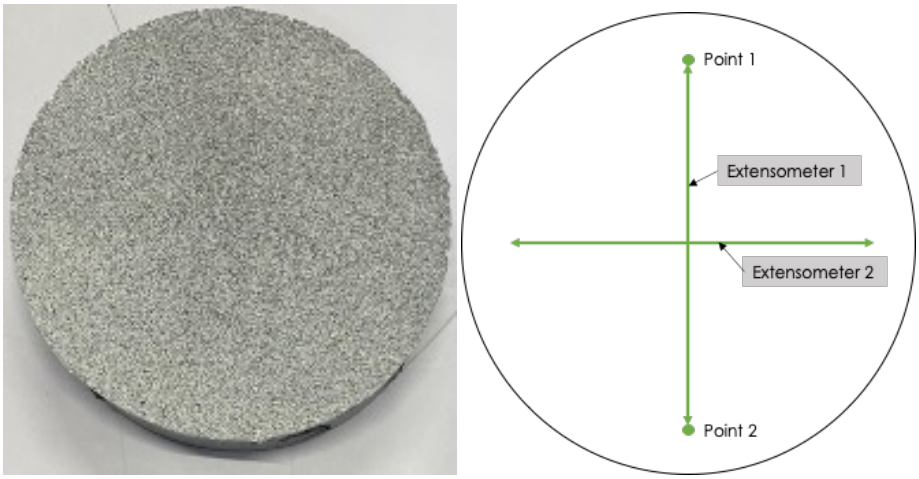

Figure 3.4: DIC based displacement measurement: (a) Speckled pattern on UPE+PU based SRR disk, (b) Location of virtual extensometers.

Two-dimensional plane-stress FE models of the complete steel-reinforced disk geometry are developed in the commercial software ABAQUS®/CAE 2021 [29]. The diameter and thickness of the disk are set equal to 100 and 23 mm, respectively, corresponding to the sample size used in the physical tests. The built-in 2D plane stress elements of four or three nodes (CPS4R and CPS3) from ABAQUS®/Standard are chosen to mesh the circular geometry (Figure 3.6a). An approximate element size of 0.3 mm with a quad-dominated shape, an advancing front algorithm and a free technique are applied. This results in a total number of elements equal to 104674 for the linear quadrilateral elements of type CPS4R and 3194 for the linear triangular elements of type CPS3.

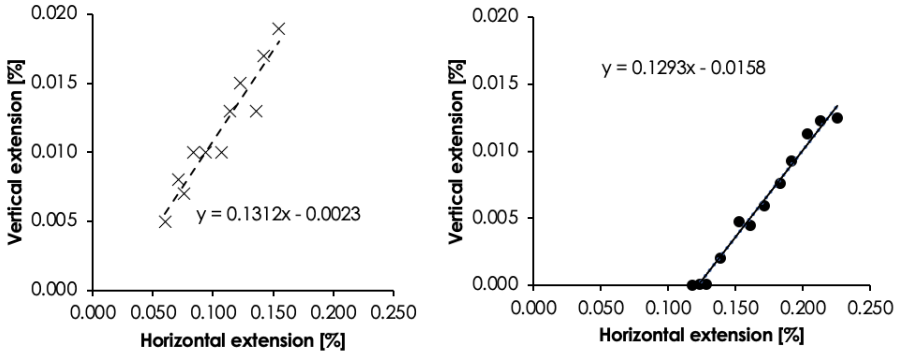

Figure 3.5: Horizontal versus vertical extension from DIC of SRR coupons loaded from 5 kN until 15 kN: (a) Epoxy, (b) UPE+PU.

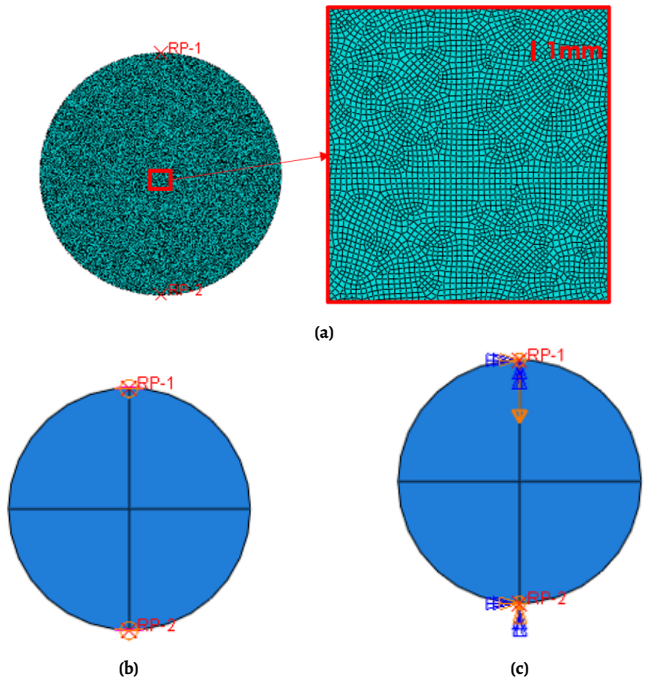

Figure 3.6: Description of FE model of the disk: (a) mesh, (b) reference point coupled to the arc, (c) boundary conditions for the disk.

Steel loading strips are not explicitly modeled; instead, the two contact areas of the blades are kinematically constrained i.e., coupled to the reference points (RP1, RP2), as shown in Figure 3.6b. Displacement-controlled loading is prescribed to the reference point on the upper part of the disk, RP1 (Figure 3.6c), with a maximum vertical displacement of

0.5 mm. Additionally, a fully fixed boundary condition is applied in the reference point RP2 in the lower part of the disk.

The purpose of the two FE models is to determine the correlation between the ratio of horizontal to vertical deformation and the Poisson's ratio of the SRR based on two resin systems. The SRR material is approximated on a meso-level as a linear, isotropic, and homogeneous material. Given that the FE models are exclusively utilized at this phase to establish a connection between the vertical and horizontal extensions and the Poisson's ratio, a preliminary Young's modulus value of 20 GPa is assumed, with the Poisson's ratio ranging between 0.1 and 0.5.

The proportion of vertical to horizontal displacements is extracted from a series of 2D linear elastic and homogeneous material models, each exhibiting varying Poisson's ratios. Figure 3.7 shows the relation between the Poisson's ratio and the proportion of vertical versus horizontal extension. Based on the vertical-to-horizontal deformation ratios determined by DIC in the experiments, the Poisson's ratio of 0.13 is found to be fairly similar for epoxy and UPE+PU based SRR (refer to the red markers in Figure 3.7).

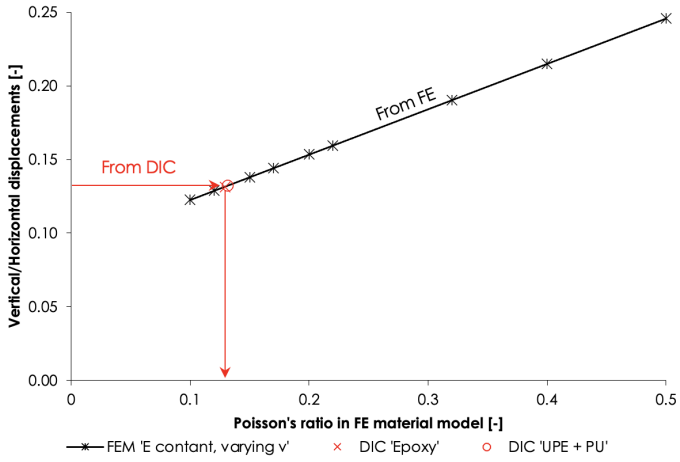

Figure 3.7: Poisson's ratio versus ratio between vertical and horizontal displacement.

A non-destructive test took place to obtain the Young's modulus of the same SRR coupons, which are used later to determine the indirect tensile strength. In accordance with [85], five compressive pulses are applied, ensuring a peak transient horizontal deformation of 5 μm gauged by LVDTs, as depicted in Figure 3.8. The relationship to obtain the Young's modulus is as follows:

$$E_t = \frac{F}{\Delta l \cdot t} \cdot (\nu + 0.27) \tag{3.2}$$

where F denotes the vertically applied loading (N); Δl is the peak horizontal diametral deformation (mm); t represents the thickness of the test specimen (mm); and ν is the Poisson's ratio of the SRR material.

The vertical load, measured by a load cell, ranged from 4.6 kN to 5 kN for the prescribed horizontal deformation. The experimental temperatures encompassed a range of 25, 40, and 55 °C.



Figure 3.8: Set-up of indirect tensile Young's modulus test.

Utilizing Equation 3.2, the Young's modulus for the SRR based on three types of resins is calculated at three different temperatures, as tabulated in Table 3.4. A total of three specimens are tested for each resin type. From this table, it can be concluded that the stiffness of the UPE+PU based SRR exhibits no significant reduction in response to temperature increase from 25 °C to 40 °C. Conversely, the epoxy and vinyl ester based SRRs experienced stiffness reductions of 15% and 12% at 55 °C compared to 25 °C. The difference in the mean Young's modulus with respect to the variation of temperatures is illustrated in Figure 3.9. The stiffness of the epoxy based SRR experienced the most pronounced reduction.

Table 3.4: Average elastic moduli for various temperatures and types of resins.

SRR Type	Stiffness [GPa]		
	at 25 °C	at 40 °C	at 55 °C
Epoxy (COV%)	16.6 (7%)	14.0 (10%)	13.1 (9%)
UPE+PU (COV%)	16.2 (6%)	16.2 (16%)	14.9 (14%)
Vinyl ester (COV%)	14.7 (4%)	12.9 (0%)	13.1 (4%)

The determined stiffness from the splitting test is reliant on the Poisson's ratio. To validate the selected Poisson's ratio and the resulting stiffness of the SRR material, the combination of these two elastic properties is inputted into the FE model, see Table 3.5. Furthermore, the load-displacement and spatial displacements from the model are compared to DIC measurements from the experiments.

Table 3.5: Elastic material properties for SRR with epoxy and UPE+PU resin tested at 25 °C.

Resin	Strength [MPa]	Poisson's ratio [-]
SRR with Epoxy resin @25 °C	16.6	0.13
SRR with UPE+PU resin @25 °C	16.2	0.13

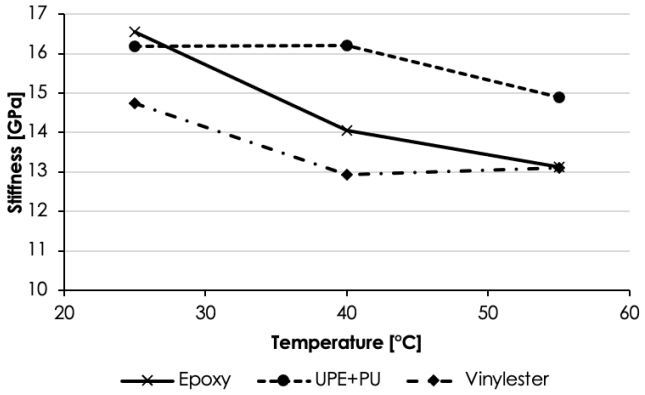

Figure 3.9: Average stiffness variation of SRR material under various temperatures.

The vertical displacements from DIC, extracted 10 mm beneath the loading point and above the support, are used to compare the vertical displacements from the model excluding the local indentation effects at load introduction. The load-displacement graphs are shown in Figure 3.10a and 3.10b. It should be noted that the initial non-linear part reported in Figure 3.2 is not evident in these graphs, primarily due to the fact that the DIC displacements are obtained from spatially remote points with respect to the load application points. This observation is consistent with findings reported in [86, 87], where the vertical or horizontal strains are extracted from the centre of the coupons using DIC.

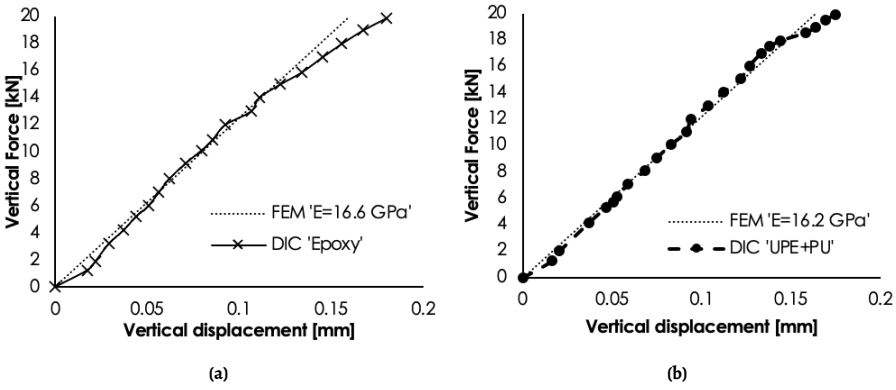

Figure 3.10: Force versus vertical displacements close to loading and support points: (a) Epoxy, (b) UPE+PU.

In a more detailed analysis, the distribution of vertical and horizontal displacements across the disk specimen are compared in Figure 3.11. Both load-displacement and spatial deformation results of the experiments and the models match well. This is an indirect justification that the determined combination of stiffness and Poisson's rations of the epoxy and UPE+PU based SRRs are valid.

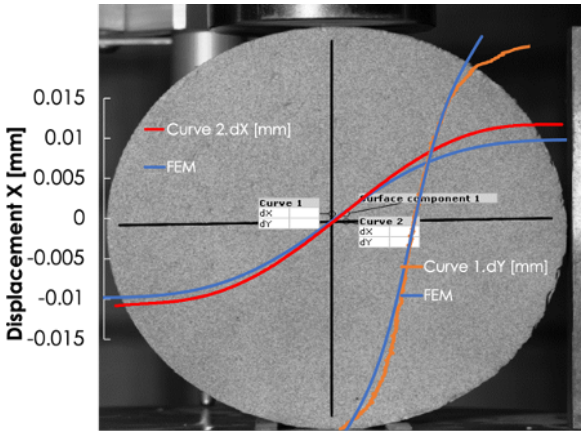

Figure 3.11: Vertical and horizontal displacements along the main lines; SRR with epoxy resin at 20 kN.

3.6. Cyclic response of SRR in tension including temperature effects

The fatigue performance of the epoxy and UPE+PE based SRR are characterized using an experimental set-up analogous to the one employed for the indirect tensile strength test. The cyclic loading is applied to SRR disk coupons of 100 mm diameter and 23 mm thickness. The fatigue endurance of the SRR disks is defined as the number of load cycles resulting in the full fracture of the specimens.

The constant load amplitude is applied to the SRR disks in a sinusoidal form with a frequency of 5 Hz (force-controlled). The load ratio, or R-value, for all specimens is maintained at 10, indicating that the specimens are subjected to compressive loading exclusively. However, this resulted in an indirect tensile splitting behavior. Therefore, indirectly, the stress ratio $R = 0.1$ is applied in these tensile splitting cyclic experiments. SRR of both resin systems are tested using the same stress ranges, specifically 7 MPa, 5.55 MPa, and 5 MPa. Since their maximum strengths at 25 °C under static loading differed, the applied cyclic stresses corresponded to different percentages of their respective maximum strengths. This apparently unorthodox decision for testing strategy is made to facilitate a comparison between the two resin systems in prospective injected connector applications where the SRR would experience identical bearing and splitting stress levels.

LVDTs are used to gauge the splitting deformation of the specimen. The indirect tensile modulus stiffness is acquired by dividing the constant force range with the accompanied range of horizontal displacement provided by the LVDTs. The stiffness degradation is then calculated at every load cycle as normalized to the initially acquired stiffness i.e., in the first load cycle. Figure 3.12 presents the normalized (relative) stiffness, degradation over the load cycles, of SRR produced with epoxy (Figure 3.12a) and UPE+PU (Figure 3.12b) resin at a stress level of 7 MPa, corresponding to 70% and 60% of the maximum strength for each resin, accordingly. For the UPE+PU specimen subjected to this loading scenario, the relative stiffness experienced a gradual reduction of approximately 80%. Subsequently, the degradation rate accelerated, leading to the final brittle fracture of the coupons across the

height (splitting) which is the same form of failure observed in static tests. In the case of the epoxy resin, an average stiffness degradation of 55% is recorded at the end of the coupons' fatigue life.

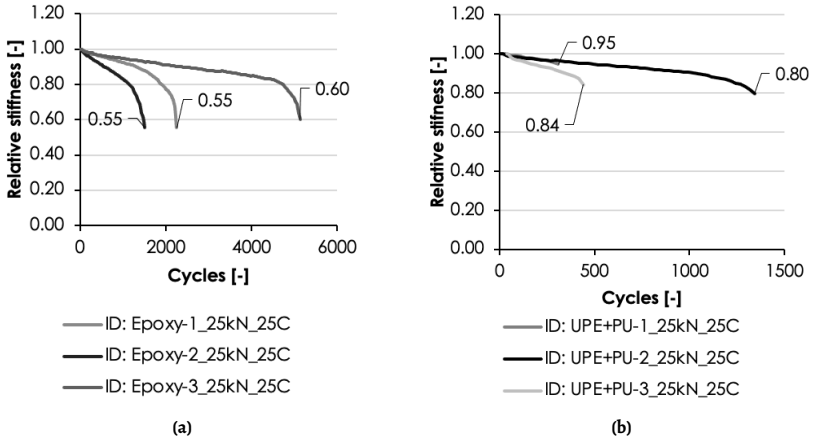

Figure 3.12: Normalized stiffness degradation at 25 °C and maximum stress range of 7 MPa (R=0.1): (a) Epoxy, (b) UPE+PU.

For the UPE+PU based SRR disks, the stiffness degradation curves of all nine failed specimens are illustrated in Figure 3.13. In this illustration, the black and grey lines designate the tests conducted at 7 MPa while the lowest ranges of 5.55 MPa and 5 MPa are denoted by orange and green color gradients, respectively. Dispersion of the results is more pronounced under medium stress levels, where the number of cycles to failure varies by a factor of approximately 25 between specimens. By contrast, at the lowest and highest loading conditions, the variation is smaller, ranging from a factor of 3 to 10 in the number of cycles to failure. Such dispersion in the number of cycles is typical in fatigue testing of granular materials. On average, a stiffness degradation of approximately 10% is observed before the complete failure of the coupons occurred.

Fatigue performance of the SRR material in the form of stress range versus the number of cycles to failure, the so-called σ-N curves, are constructed and displayed in Figure 3.14a and 3.14b. Average σ-N curves are calculated based on statistical analysis according to the ASTM E729 [88]. This method does not account for runouts i.e., the specimens that did not reach the failure criterion. A linear form is adopted for the double-logarithmic σ-N relationship, which is expressed as follows:

$$log(N) = A + B \cdot log(\sigma) \tag{3.3}$$

where N denotes the corresponding number of cycles to failure; σ is the stress range endured by the specimen (MPa); and A and B are the regression parameters determined using linear regression. Considering the $Y = \log(N)$ and the $X = \log(\sigma)$ as dependent and independent variables, respectively, Equation 3.3 can be rewritten as:

$$Y = A + B \cdot X \tag{3.4}$$

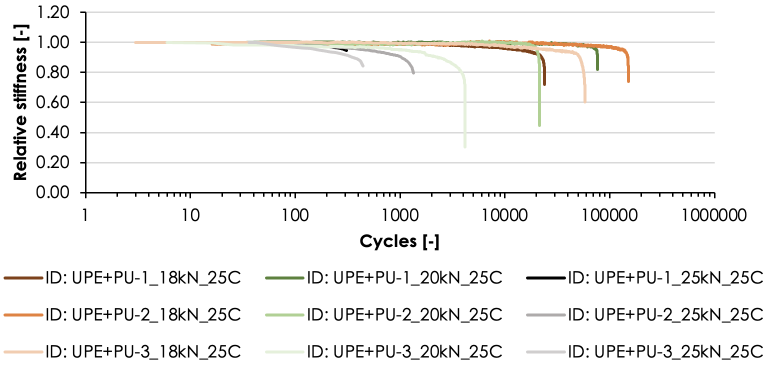

Figure 3.13: Normalized stiffness degradation at 25 °C across various load ranges for SRR with UPE+PU.

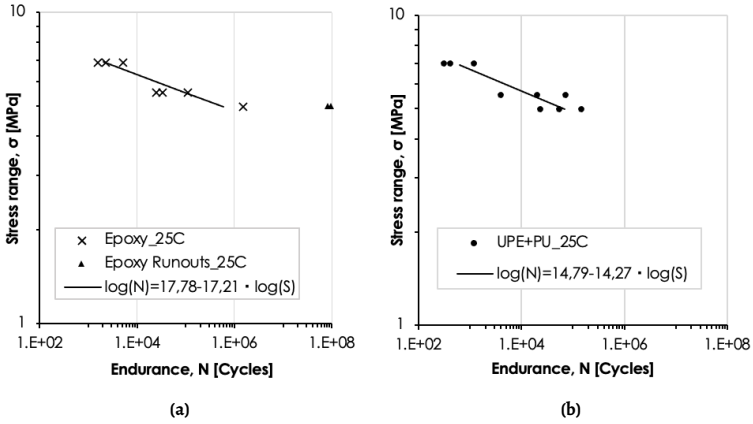

Figure 3.14: Preliminary σ-N curves (R=0.1) for SRR loaded in indirect tensile direction at 25 °C: (a) Epoxy, (b) UPE+PU.

The 95% upper and lower confidence bands are not analyzed as the number of coupons would not result in fatigue curves with statistical significance. Nonetheless, the preliminary A and B parameters are determined for both SRRs. Notably, the slope of the σ-N curve is found steeper for the UPE+PU based SRR (B = -14.27) compared to the epoxy variant (B = -17.21), suggesting better fatigue endurance of the epoxy variant. The corresponding A parameters are found equal to 14.79 and 17.78 for the UPE+PU and epoxy resin systems, respectively.

Regarding the failure mode of the investigated SRR systems under indirect tensile cyclic loading, complete splitting of the specimens along the vertical plane is observed for nearly every stress range and across all distinct temperature conditions. However, as previously stated, two epoxy based SRR specimens tested at the lowest stress levels withstood over 8 million cycles without fracturing or exhibiting plastic deformation. In these instances, localized deformations are observed at the loading strip edges, but no stiffness degradation is recorded.

Additionally, two cyclic load tests are performed under elevated temperature conditions. Stress range of 6.1 MPa is subjected at a temperature of 55 °C, and 5.55 MPa at 40 °C. A collection of the acquired data is provided in Figure 3.15, with the average curves obtained previously at room temperature displayed for comparison purposes.

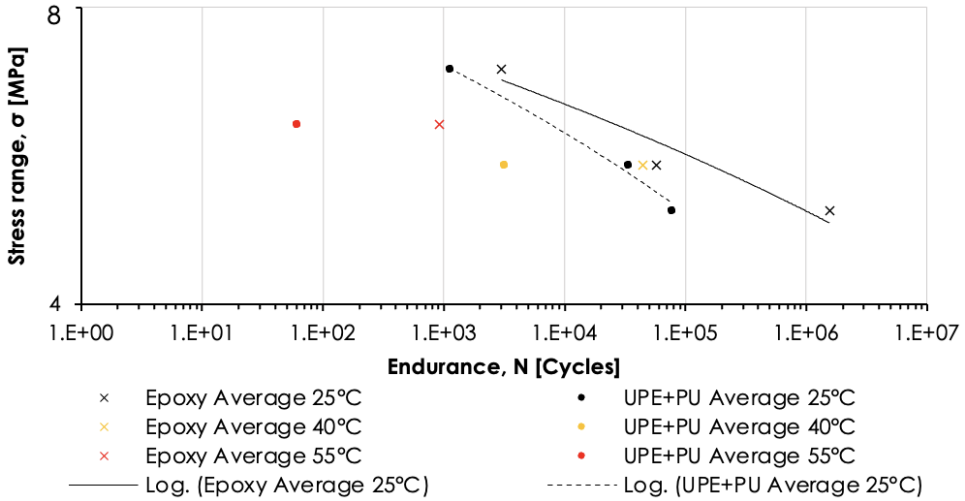

Figure 3.15: Endurance of SRR at 25 °C, 40 °C and 55 °C for epoxy and UPE+PU resin systems.

For a stress range equal to 5.55 MPa (48%·$\sigma_{max,epoxy}$, 55%·$\sigma_{max,UPE+PU}$), experimental results for both resins at room and elevated temperature of 40 °C are obtained. In particular, the average value of cycles leading to fracture in the epoxy SRR specimens is determined to be 58000 and 44500 at 25 °C and 40 °C, respectively. Conversely, the UPE+PU SRR samples failed after an average of 35500 cycles at room temperature which reduced by a factor of 10 when the temperature rose to 40 °C, resulting in 3200 cycles. Furthermore, the epoxy based SRR coupons persisted for a minimum of 10 times more cycles to failure compared to the UPE+PU SRR counterparts under elevated temperatures.

Figure 3.16 presents the normalized stiffness degradation curves for tests conducted at both elevated temperatures. Based on Figure 3.16a, at 40 °C, the fatigue endurance of the UPE+PU based SRR samples grouped around 3200 cycles, while the variability among the epoxy resin samples became more pronounced. The UPE+PU resin samples, subjected to testing at 55 °C and a stress range of 6.1 MPa, experienced premature failure which prevented the documentation of their progressive stiffness degradation. The scarcity of input data yielded linear lines, as illustrated in Figure 3.16b. Conversely, the epoxy based SRR coupons endured, on average, 1000 cycles before failure, with their nonlinear trend effectively captured. Minimal dispersion among the distinct coupons is observed for epoxy based SRR at 55 °C.

Based on the limited data, an approximate trend can be observed: the fatigue life of UPE+PU-based SRR decreases by a factor of 10 for every 15 °C increase in temperature. For epoxy-based SRR, the decrease is more gradual between 25 °C and 40 °C, while at 55 °C, the fatigue life of epoxy-based SRR drops significantly, indicating a more pronounced decline in

performance under extreme conditions. Under every condition, epoxy-based SRR materials exhibit superior fatigue resistance and durability compared to UPE+PU SRR materials.

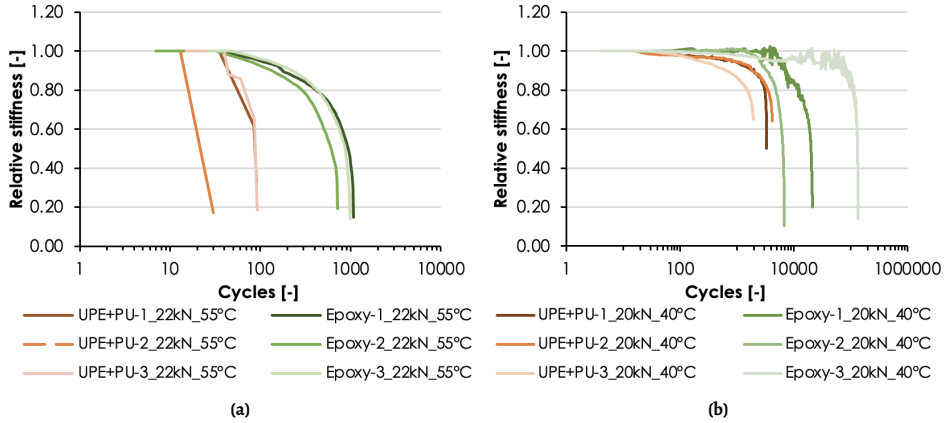

Figure 3.16: Normalized stiffness degradation at elevated temperatures: (a) at 5.55 MPa and 40 °C, (b) at 6.1 MPa and 55 °C.

3.7. Water absorption of pure and steel-reinforced resins

Water absorption tests are conducted on bulk resin and SRR specimens to evaluate moisture uptake and assess the corrosion susceptibility of the steel-polymer composite system. The objective is to determine which resin system is most suitable for injected connectors in environments with high moisture exposure.

Pure resin specimens (50×50×4 mm) are immersed in water at 20, 40, and 60 °C for six months, and their weight gain is recorded periodically. Figures 3.17a, 3.17b and 3.17c present the weight change versus the square root of immersion time for epoxy, UPE+PU, and vinyl ester resins, respectively. A red dashed line at 1.0% weight gain serves as a reference across all graphs.

All resins initially follow a linear moisture uptake trend, indicating Fickian diffusion behavior. Higher temperatures accelerate water absorption, reducing saturation time. Some resins deviate from Fickian behavior after prolonged exposure, potentially due to polymer degradation [89] or leaching effects [90]. Despite variations in weight gain, no visible surface degradation is observed in any specimens.

SRR specimens are fabricated with 80×80×8 mm molds, where steel balls are added first, followed by resin injection (Figure 3.18a). Unlike pure resin samples, SRR specimens contain only 20% resin by volume. To prevent water penetration from imperfections, the exposed side edges are coated with the same resin used in fabrication (Figure 3.18b).

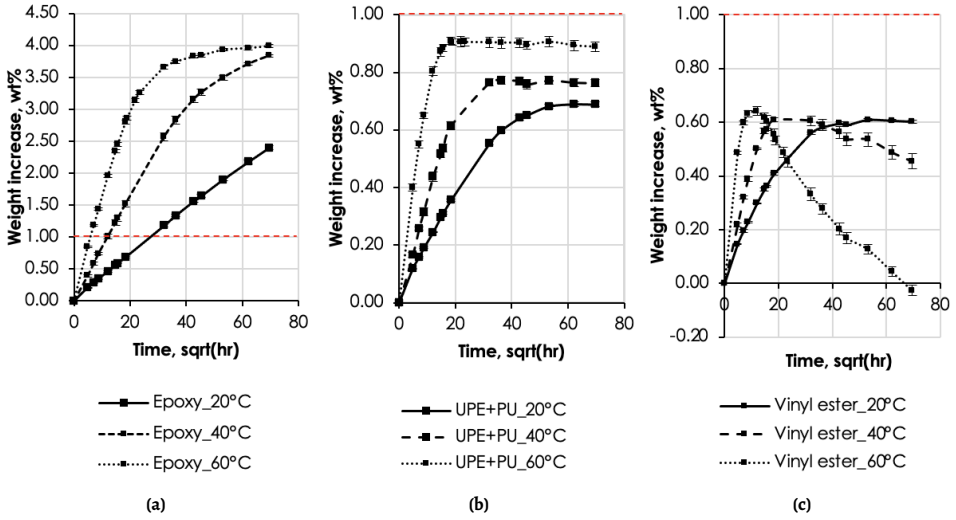

Figure 3.17: Weight change of pure resins versus square root of water immersion time, square(t) for temperatures varying from 20 °C to 60 °C (red dashed line included at 1.0% as a reference in all three graphs): (a) Epoxy, (b) UPE+PU, (c) Vinyl ester.



Figure 3.18: SRR coupons for water absorption: (a) Production set-up, (b) Final product.

The moisture uptake of SRR specimens is shown in Figure 3.19, with a 0.2% weight gain threshold (red dashed line) for comparison. Unlike pure resins, none of the SRR specimens reach saturation after 200 days.

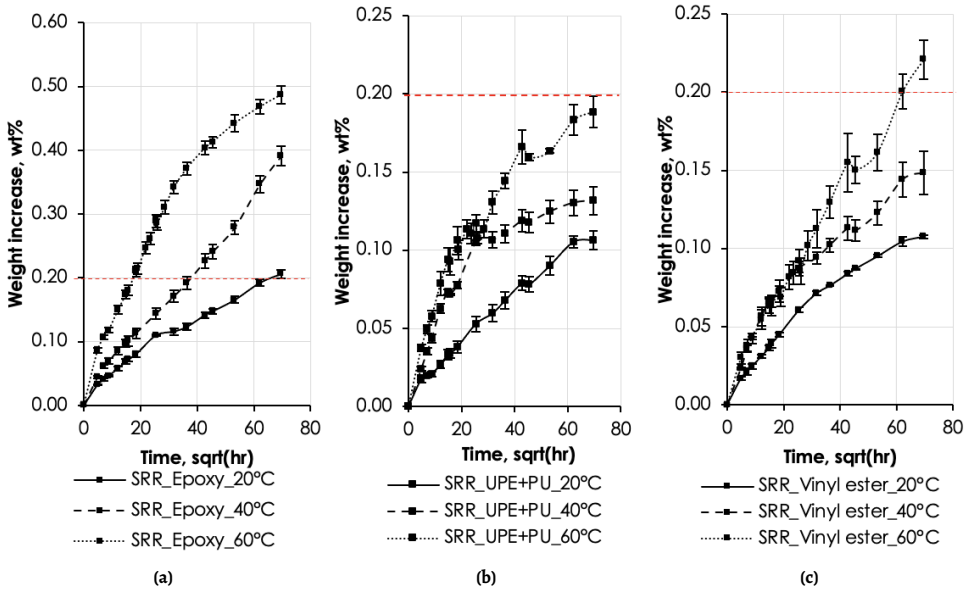

Figure 3.19: Weight change of SRR versus square root of water immersion time, square(t) for temperatures varying from 20 °C to 60 °C (red dashed line included at 0.2% as a reference in all three graphs): (a) Epoxy, (b) UPE+PU, (c) vinyl ester.

Moisture uptake remains continuous, indicating that saturation is not reached within the tested period. Epoxy-based SRR material, presented in Figure 3.19a, shows the highest weight increase (0.50% at 60 °C), while UPE+PU (Figure 3.19b) and vinyl ester (Figure 3.19c) exhibit lower values (60% and 56% lower, respectively). Water uptake in SRR is significantly lower than in pure resins due to the presence of steel balls reducing the resin fraction and increasing the diffusion path.

Upon examining the external surfaces, oxidation of steel balls is observed in UPE+PU and vinyl ester-based SRR, particularly at the edges (Figure 3.20c, 3.20d, 3.20e, 3.20f). However, epoxy-based SRR shows almost no visible corrosion, as shown in Figure 3.20a and 3.20b despite having the highest weight increase.

Top views of the specimens after 200 days of immersion at 40 °C (Figure 3.21) further reveal the distribution and intensity of corrosion at the surfaces. The epoxy-based SRR specimens (Figure 3.21a) show only minor localized spots of corrosion, while UPE+PU (Figure 3.21b) and vinyl ester specimens (Figure 3.21c) exhibit more extensive oxidation of the steel balls, consistent with the patterns observed at the edges. Notably, corrosion is also concentrated around the corners and additional resin-coated areas, suggesting moisture diffusion through these resin coatings.

The inclusion of steel balls significantly reduces water absorption, especially in epoxy-based SRR, which also exhibits the least corrosion. This suggests that epoxy provides superior barrier properties and metal adhesion, making it a strong candidate for moisture-exposed connectors. Further details on methodology and extended analysis can be found in [75].

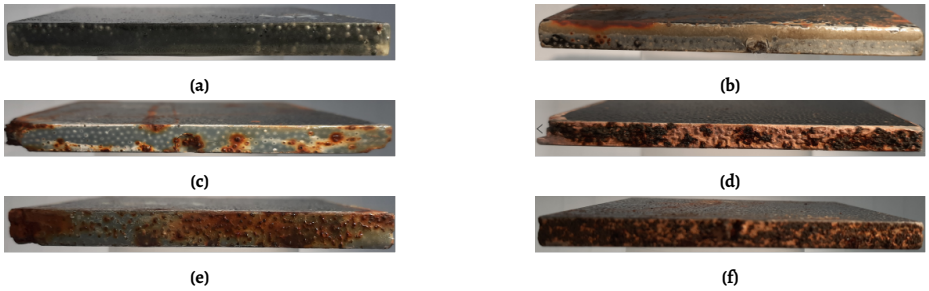

Figure 3.20: Edges of SRR specimens after 200 days of immersion at 20 and 60 °C: (a) SRR with epoxy at 20 °C, (b) SRR with epoxy at 60 °C, (c) SRR with UPE+PU at 20 °C, (d) SRR with UPE+PU at 60 °C, (e) SRR with vinyl ester at 20 °C, (f) SRR with vinyl ester at 60 °C.

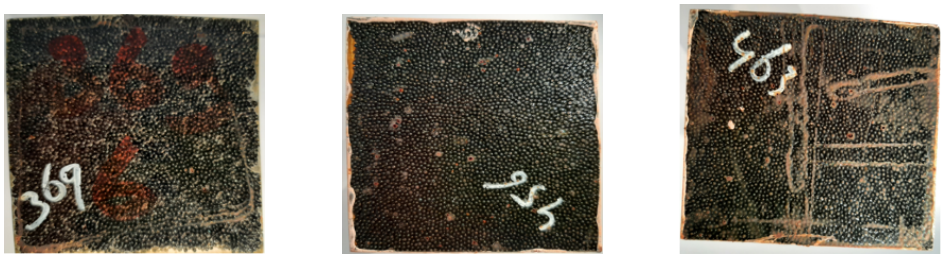

Figure 3.21: Top view of SRR specimens after 200 days of immersion at 40 °C: (a) SRR with epoxy, (b) SRR with UPE+PU, (c) SRR with vinyl ester.

3.8. Conclusions

Three different types of resins with Tg values exceeding 110 °C are used to fabricate unreinforced coupons and coupons reinforced with steel balls resin coupons. SRR disks with D100x23 mm geometry and cube specimens of 80x80x8 mm, featuring a volume fraction of steel balls equal to 80%, are created to determine their strength, modulus, Poisson's ratio, σ-N curves, and water absorption profiles under varying (room and increased) temperature conditions. The static and fatigue performance of the SRR is assessed through a series of cylinder splitting tests that are relevant for granular materials such as bituminous asphalt, concrete, or fractured rocks. The water uptake of the pure resin systems is obtained by immersing coupons of 50x50x4 mm in water compartments at 20, 40, and 60 °C. Susceptibility to corrosion of the steel balls within SRR made of three different resins in submerged condition is compared. The following conclusions can be deduced:

1. The average tensile splitting strength of SRR made with epoxy is found equal to 11.6 MPa at 25 °C. A lower value of 10.0 MPa and 6.8 MPa is obtained for UPE+PU and vinyl ester resin, accordingly. The tensile moduli of SRR at room temperature are equal to 16.6 GPa, 16.2 GPa, and 14.7 GPa for epoxy, UPE+PU and vinyl ester-based SRR, respectively. The Poisson's ratio of the SRR coupons made with epoxy and UPE+PU resin is found equal to 0.13 using the indirect tensile test set-up.

2. The indirect tensile strength of the vinyl ester resin exhibited negligible sensitivity to elevated temperatures. In contrast, the respective strength reduction for epoxy and UPE+PU resin at 55 °C is 15% and 25%, respectively. The epoxy resin displayed the greatest sensitivity of tensile modulus to temperature increase, with a 21% modulus decrease observed at 55 °C.

3. Regarding fatigue endurance, the SRR coupons fabricated with epoxy resin withstood 1.6 million cycles at a stress range of 5 MPa, which is approximately 20 times greater than the cycles to failure observed with UPE+PU resin. Preliminary slopes of the σ-N curves are determined to be m = -15 for UPE+PU and m = -18 for epoxy resin.

4. The pure epoxy resin exhibited a peak water uptake of 4% after 200 days of immersion at 60 °C, while UPE+PU and vinyl ester resins showed lower maximum weight increases of 0.90% and 0.65%, respectively. The addition of steel balls reduced water absorption, both in saturation level and diffusion rate. At 20 °C, SRR coupons with epoxy resin absorbed 0.20% water, 12 times less than pure epoxy, while UPE+PU and vinyl ester SRRs absorbed 0.65% and 0.60%, reducing water uptake by factors of 6.5 and 5.5, respectively. Oxidation on the SRR surface is observed only along the edges of cubic specimens made with vinyl ester or UPE+PU systems.

4

Compressive behavior of steel-reinforced resin

The compressive stresses generated within the SRR material when applied in the injected SRR connector play a critical role in the joint's fatigue performance. The literature review highlighted the importance pressure dependency of granular composite materials, prompting an initial evaluation of the influence of confinement on the short-term performance of SRR. To further this investigation, incremental cyclic loading tests will be conducted under unconfined conditions to establish a direct correlation between plasticity and damage accumulation. Additionally, cyclic experiments at three different stress ratios will be performed to complete the testing matrix for the compressive behavior of unconfined SRR material, providing insights into material degradation and fatigue behavior with respect to load cycles.

Chapter 4 is organized into five sections and is structured as follows. The test set-up and an overview of the compressive experiments are presented in Section 4.1. Then, Section 4.2 evaluates the static mechanical properties of SRR in unconfined conditions. Section 4.3 assesses the influence of confinement (triaxial stress state) on the short-term performance of the SRR material. The long-term cyclic compressive behavior of SRR is characterized in Section 4.4. Finally, Section 4.5 summarizes the key findings of this chapter.

4.1. Specimen preparation and test set-ups for compressive behavior of SRR

Cylindrical specimens, each with an average diameter of 26.0 mm and length of 52.0 mm, are prepared by integrating high-carbon steel balls (type S390) with an average diameter of approximately 1 mm and a hardness range of 40-50 HRC [23] into an unsaturated polyester polyurethane resin, AQR 1025/B25 [80], as selected in Chapter 3. The mass ratio of steel balls to resin is maintained at 4:5. No mechanical compaction is applied during specimen

This chapter has been published in Christoforidou et al. [91].

fabrication, as it is deemed unnecessary due to the open cylindrical mold and a gravity-assisted top-to-bottom manufacturing process, similar to the method used for producing iSRR connectors.

In this process, the steel balls are first added into the mold, after which the resin is injected from the bottom upwards using a pressure gun. This technique promotes uniform resin distribution around the steel particles and reduces the risk of void formation. Once the mold is filled with steel balls up to the required specimen length, any excess resin that accumulates at the top is removed by laser cutting to ensure a flat and even surface, an essential condition for reliable compressive testing.

The experimental test matrix is presented in Table 4.1, summarizing the number of tests for each loading condition and confinement level applied in this study. All tests are done under room temperature and moisture conditions. Three monotonic tests without confinement are conducted to determine the compressive strength. Following these destructive monotonic tests, three incremental cyclic loading tests are performed to generate the material's hysteresis loops. Finally, cyclic loading is applied at three different stress levels, with three specimens tested at each level.

Table 4.1: Overview of experiments for SRR material characterization under compression.

Loading	Minimum load	Confinement level	Coupons	Machine
Monotonic	NA	Unconfined	3	MTS-50
	NA	10 MPa	1	MTS-25
	NA	20 MPa	1	MTS-25
	NA	30 MPa	1	MTS-25
Incremental cyclic	NA	Unconfined	3	UTM-5
Cyclic (fatigue)	20 kN	Unconfined	3	MTS-50
	24 kN	Unconfined	3	MTS-50
	30 kN	Unconfined	3	MTS-50

The application of compressive force varies depending on the confinement conditions, necessitating the use of different machines (see Table 4.1 last column) and methods. For static tests conducted without confinement, the compressive strength of the specimens is evaluated using an MTS actuator with a capacity of 250 kN. The system is equipped with three LVDTs to accurately measure the average contraction of the specimens between the plates where load is applied. The experimental set-up, including the placement of the sensors, is illustrated in Figure 4.1a. All tests are performed under a displacement-controlled regime at a speed of 0.01 mm/s. This set-up is also employed for incremental cyclic loading tests, where the loading and unloading rates remained the same. The cycles of loading, unloading, and reloading are depicted in Figure 4.2.

This same set-up is further utilized for cyclic loading tests, where the load is applied in a sinusoidal form. Force control is regulated by a peak controller to maintain a constant peak force, even as the material properties degrade. These tests are conducted at a frequency of 4 Hz, under room temperature and dry environmental conditions. A stress ratio of $R = 10$ is used for all specimens, meaning they are subjected to compressive loading only, with no load relief during testing.

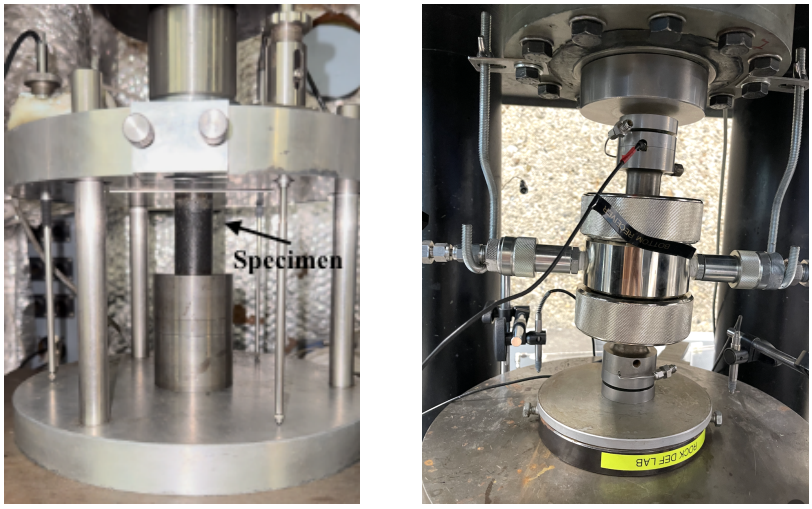

(a) (b)

Figure 4.1: Experimental set-ups used for characterizing the compressive behavior of SRR material: (a) Unconfined test set-up, (b) Triaxial test set-up.

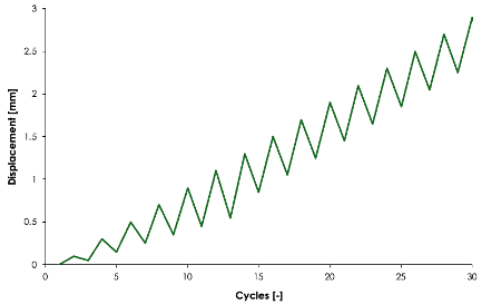

Figure 4.2: Incremental cyclic loading protocol.

The triaxial compression tests are conducted using a servo-controlled loading machine with a maximum capacity of 500 kN. The experiments take place at room temperature on intact samples, utilizing a Hoek cell embedded in the 500 kN machine to apply confining pressure using oil under load control without pore pressure. The testing system, as shown in Figure 4.1b, uses an external ISCO 65D syringe pump to control the confining pressure with an accuracy of 0.5%. Both the axial force and confining pressure are applied simultaneously, with a constant displacement ratio of 0.6, until reaching the desired confinement level of 10, 20, or 30 MPa. Once reached, the pressure is maintained constant, and only the compressive load is applied under strain control at an axial strain rate of 0.00005 s^{-1}.

During the tests, axial displacement, axial force, and confining pressure are logged at 1-second intervals, with vertical deformation measured using two highly accurate LVDTs. The tests continue until a displacement limit of 1.95 mm is reached, at which point the system

reaches its deformation capacity. Each confinement level is tested with one monotonic test, as preliminary trials show minimal variation at lower confinement pressures.

4.2. Uniaxial compressive behavior of SRR under static loading

The compressive strength of the cylindrical specimens is determined by dividing the applied force from the actuator by the initial cross-sectional area of the specimen, calculated as $A = \pi \cdot r^2$, where $r = 13.0$ mm, resulting in an area of 531 mm^2. Strain is calculated as the ratio of the specimen's contraction to its initial height. The Young's Modulus of the SRR material in compression is obtained from the slope of the initial linear portion of the stress-strain curve. For accuracy, it is consistently measured within the stress range of 40 MPa to 60 MPa, which lies below the onset of nonlinearity. This method ensures that the measurement is unaffected by any potential initial settling of the specimen during testing.

The stress-strain curves for the unconfined SRR specimens subjected to both monotonic and incremental cyclic loading are presented in Figure 4.3a and 4.3b. The maximum compressive strength recorded under monotonic loading was approximately 84.3 MPa, which decreased by only 2.85% under incremental loading. Under both loading conditions, neither the Young's modulus nor the stress at the onset of non-linearity and the ultimate compression strength vary significantly. A collection of the experimental results is given in Table 4.2.

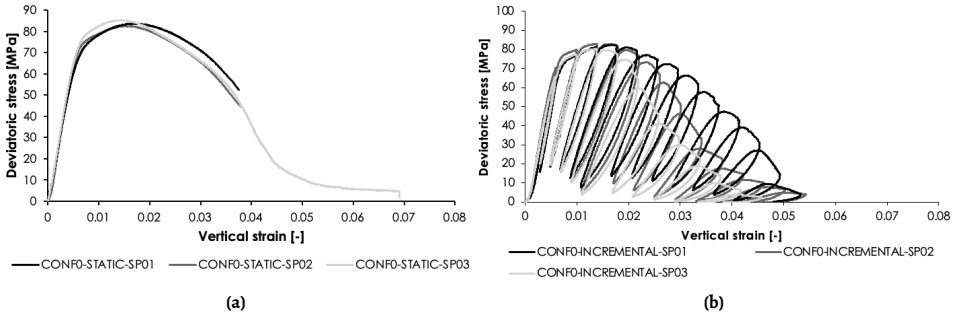

Figure 4.3: Stress strain curves under uniaxial compression of SRR material: (a) Monotonic loading, (b) Incremental loading.

The stress-strain curve for the monotonic loading test is fairly linear until 80 MPa of compressive stress. Then it shows a distinct peak followed by a gradual decrease in stress, indicating strain softening behavior after the material reaches its maximum compressive strength. This post-peak reduction suggests that the SRR material begins to lose its load-bearing capacity due to micro-cracking and localized damage. Similarly, during the incremental cyclic loading tests, an increase in residual strain is observed after each unloading cycle, further reinforcing the presence of strain softening. The progressive accumulation of residual strain and the change in the slope of the reloading loops in incremental cyclic tests highlight the dual nature of nonlinear behavior, attributed to both damage, resulting in a decrease in material stiffness, and plasticity, leading to permanent deformation.

The results from the incremental cyclic tests further highlight the progressive nature of damage and plastic deformation in the SRR material. As evident in Figure 4.4, plastic

Table 4.2: Experimental results of compression tests under monotonic loading in unconfined condition.

Loading	Specimen	Young's modulus (GPa)	Compression strength (MPa)
Monotonic	1	13.2	84.3
	2	13.0	83.9
	3	13.1	84.8
	Mean	13.0	84.3
Incremental cyclic	1	11.8	82.5
	2	11.4	82.9
	3	13.1	80.2
	Mean	12.1	81.9

strain remains negligible during the initial loading cycles, while the total strain accumulates. This suggests that damage is the dominant mechanism driving stiffness degradation at the early stages, as it correlates with the relatively linear increase in damage observed in Figure 4.5. The gradual onset of plasticity is evident later in the test, as ϵ_{pl} begins to grow more significantly, aligning with the progressive accumulation of permanent deformation. The early dominance of damage as the primary degradation mechanism supports the use of CDM models that emphasize stiffness reduction due to damage, while disregarding the effects of plasticity. Such an approach is partially validated by these findings, where stiffness degradation is initially governed by damage before plasticity becomes more pronounced in later cycles.

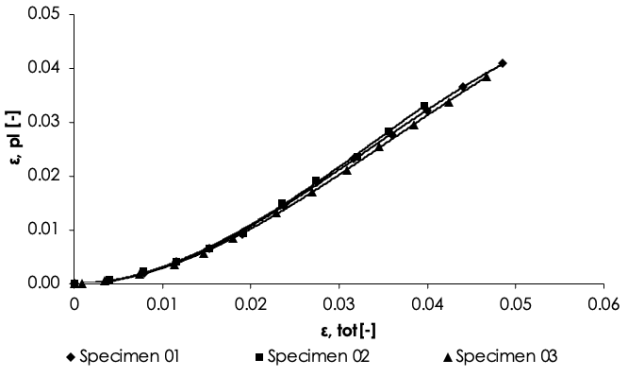

Figure 4.4: Plastic strain versus total strain of SRR material under compression and unconfined conditions.

Additionally, the hysteresis loops of the SRR material based on the incremental cyclic tests provide insights into energy dissipation due to material damage and micro-cracking. The area within the loops evolves with the number of cycles, reflecting the viscous behavior of the material. It should be noted that the incremental cyclic loading is applied at a relatively low rate (approximately 1.5 min/cycle), which may have introduced creep effects. This time-dependent deformation could contribute to the overall strain accumulation, potentially affecting the ratio between damage and plasticity contributing to the non-linear behavior

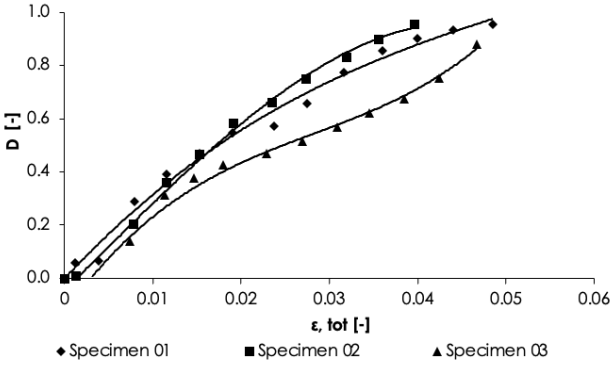

Figure 4.5: Damage progression versus total strain of SRR material under compression and unconfined conditions.

of the material. To better distinguish between damage caused by cyclic loading and creep, further analysis, such as tracking the evolution of residual strain or conducting dedicated creep tests, would be necessary. The damage versus plastic strain curves, constructed from these loops, provide an initial indication of how the material deforms plastically and accumulates damage over time, though a more comprehensive approach is required to fully isolate the impact of creep.

The relationship between damage, D, and plastic strain, ϵ_{pl}, for the three specimens, as demonstrated in Figure 4.6, reveals that damage accumulates steadily throughout the tests, with a nonlinear increase as plastic strain develops. The early stages are dominated by damage accumulation, as evidenced by the gradual slope in the figure for ϵ_{pl}<0.02. Beyond this threshold, the damage accelerates sharply, indicating a transition where plastic deformation begins to significantly contribute to the material's degradation.

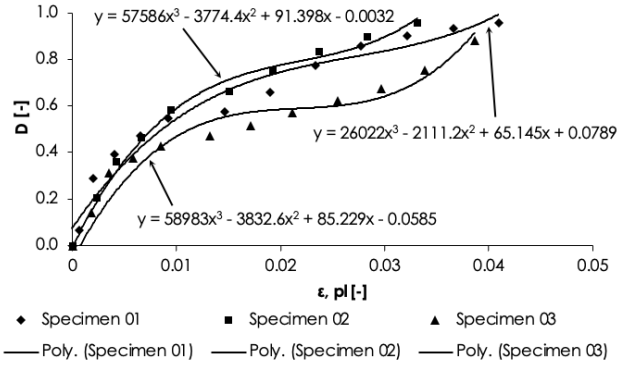

Figure 4.6: Damage progression versus plastic strain of SRR material under compression and unconfined conditions.

Despite some variations in the rate of damage progression between the specimens, all curves follow a third-degree polynomial trend, emphasizing a typical 3-stage development

form of interaction between plastic deformation and material degradation. The results suggest that softening is primarily driven by plastic strain in the second (steady) stage, with damage dominating in the primary and tertiary stage of softening. This consistency across the specimens tested under incremental (low-cycle loading) indicates that the SRR material may exhibit predictable fatigue behavior under high-cycle compressive loading.

The post-peak behavior of the monotonic and incremental cyclic loading tests varies among the tested specimens, which is to be expected. Specifically, the post-peak behavior exhibits noticeable variation due to the inherent heterogeneity of the SRR material, where the interaction between steel particles and resin leads to localized stress concentrations and varying failure mechanisms on a microscopic scale. Additionally, particle sliding, rearrangement, and dilatancy effects contribute to the observed differences, as the material undergoes micro-cracking and damage localization after reaching peak load. Regardless of the loading type applied, a consistent failure mode was observed across all specimens by the end of the test. As shown in Figure 4.7, the predominant failure involved mainly diagonal and some longitudinal cracks, culminating in the final fracture of the specimen through "explosive" spalling of some specimens.

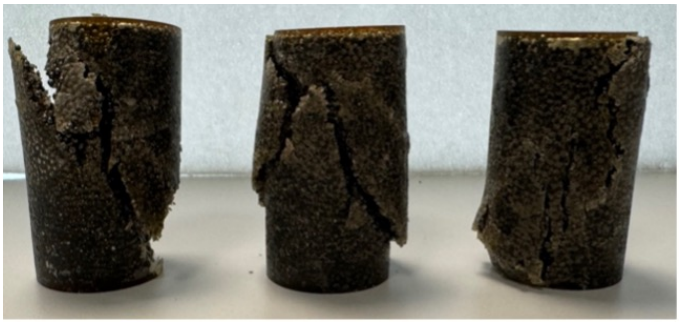

Figure 4.7: Failure mode of SRR material under monotonic uniaxial compression.

4.3. Triaxial compressive behavior of SRR under static loading

Three triaxial tests are performed, with the confining pressure varying from 10 MPa to 30 MPa. During each test, an increasing longitudinal compressive load is applied alongside the confining pressure until the desired confining pressure (σ_3) is reached. Once this target confining lateral pressure is achieved, it is held constant, and only the axial load (F) is progressively increased during what is considered the shearing (deviatoric) phase of the test. The additional stress from the load is applied solely in the axial direction and is calculated by dividing the axial force by the initial cross-sectional area (A) of the cylindrical specimen (Figure 4.8a). The total axial stress experienced by the SRR material is equivalent to the major principal stress (σ_1) and can be expressed as:

$$\sigma_1 = \sigma_3 + \frac{F}{A} \tag{4.1}$$

The deviatoric stress component (q) for the confined SRR specimens is determined by subtracting the applied confining pressure (minor principal stress, σ_3) from the vertical

stress (major principal stress, σ_1). The deviatoric stress component is progressively increased until either the specimen experiences failure, typically through cracking or spalling, or until a plateau is reached, indicating that the material has undergone plastic deformation or strain softening. The loading stages, highlighting the sequential application of cell pressure and axial force, are illustrated in Figure 4.8b.

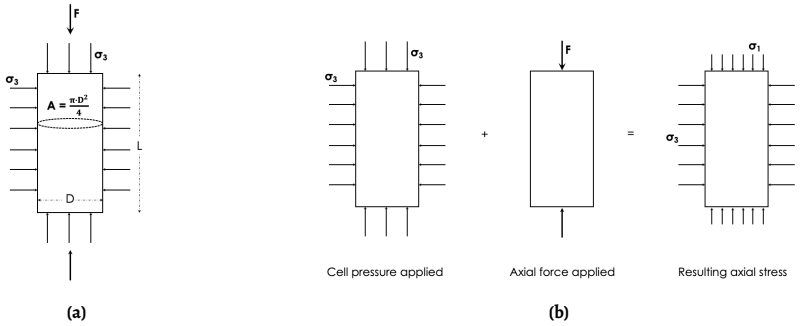

Figure 4.8: Principals of triaxial compression test: (a) Cylindrical specimen under triaxial compression, (b) Loading stages of triaxial test.

The deviatoric stress component versus axial strain curves are presented in Figure 4.9. A clear trend of increasing deviatoric stress with higher applied confining pressure is observed, aligning with conclusions drawn from the literature. All three specimens exhibit only slight variation in initial stiffness. The stiffness for 10, 20 and 30 MPa of confinement pressure is 10.5, 11.3 and 12.1 GPa, respectively, showing a slight increase with rising pressure. However, given the minor variations between the different confinement levels, this change is more likely attributed to statistical variability rather than a significant shift in material behavior.

The most significant change occurs at the onset of nonlinearity, which directly impacts the maximum deviatoric stress that the SRR material experiences and confirms that the SRR material benefits from confinement, as it enhances its load-bearing capacity. The transition from the elastic to nonlinear region is smooth, indicating that the SRR material gradually absorbs energy and deforms plastically and is not exhibiting a sharp yield point. This gradual transition highlights the ductile nature of the material under confinement.

Notably, none of the specimens exhibit failure; instead, they reach a plateau in deviatoric stress, which is maintained until the test is manually stopped. This plateau behavior suggests that the SRR material under confinement can sustain a high level of stress without immediate failure, potentially indicating stable plastic flow or strain hardening. This behavior has important implications for the material's application in structures, where maintaining stress without failure could enhance safety and durability.

Even though failure is not reached in any of the tests, the plateau phase suggests that micro-cracking or particle rearrangement is occurring at the micro-structural level, delaying complete failure. To better understand the nonlinear behavior and the plateau observed in the experimental tests, micro-mechanics modeling, conducted in Chapter 9, is used to investigate the underlying mechanisms. The modeling provides insights into how the interaction between the steel particles and the resin matrix contributes to the material's overall response, particularly the transition to nonlinearity and the stable plateau phase.

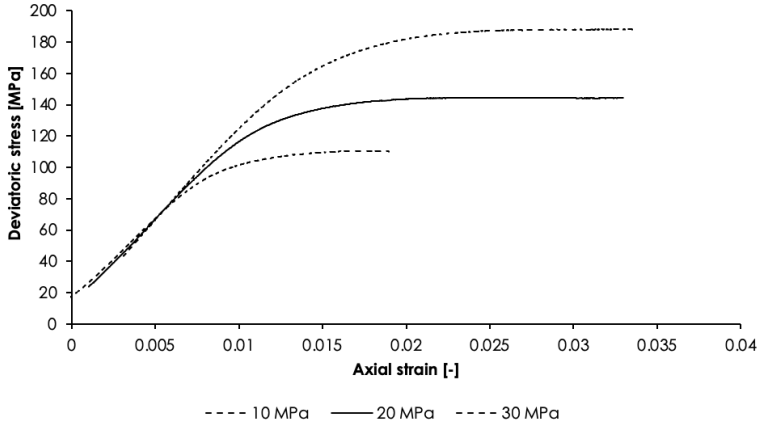

Figure 4.9: Deviatoric stress versus axial strain curves for SRR material during the shearing phase of triaxial compression tests at varying confining pressures.

Comparing the triaxial test results with the unconfined monotonic tests on the SRR material highlights the significant improvement in load-bearing resistance under confinement, as shown in Figure 4.10. It is also clear that confining pressure generally enhances the ductility of the SRR material. This behavior is typical for granular composites, suggesting that confinement plays a crucial role in restricting lateral expansion and delaying the onset of failure, thereby improving both the material's strength and ductility. The increased confining pressure allows the SRR to sustain higher deviatoric stresses without experiencing announced failure, making it particularly suited for applications where lateral confinement or triaxial stress states are present. Such a scenario is expected in the application of SRR as an injection material for connectors in composite decks. In these cases, the SRR material is surrounded by the composite material of the deck facing, which can provide mild confinement conditions.

An important point of attention is the difference in the slope of the deviatoric stress versus axial strain curve, which reflects the Young's modulus. The stiffness of the unconfined SRR material appears to be higher than that observed under the three confinement levels. This discrepancy is attributed to the use of different testing apparatus for the two sets of tests, with different machines and LVDTs potentially leading to measurement variations. Despite this experimental outcome, it is hypothesized that the SRR material being evaluated in this thesis, with its 80% steel particle volume fraction, should exhibit a similar Young's modulus under both unconfined and confined conditions. This is because the material's elastic behavior is primarily governed by the densely packed steel particles, which dominate the load-bearing mechanism in both scenarios. Further insights into this hypothesis will be explored through micro-mechanics modeling in Chapter 9, which aims to shed light on the underlying mechanisms contributing to the stiffness in these tests.

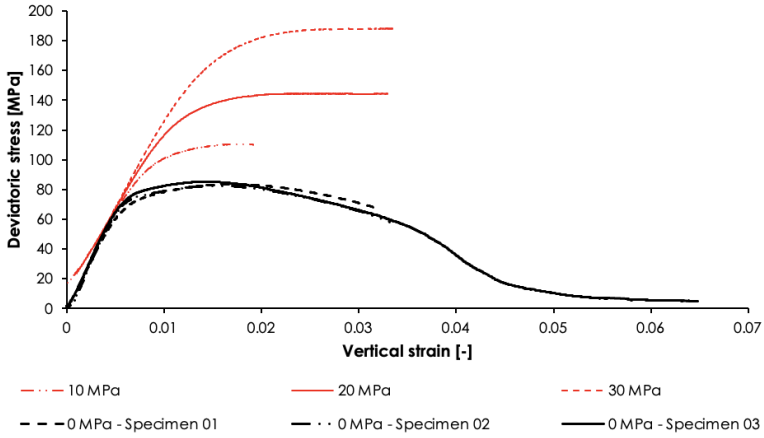

Figure 4.10: Comparison of deviatoric stress versus axial strain curves for SRR material for unconfined and confined conditions.

4.4. Uniaxial compressive behavior of SRR under cyclic loading

In this section, the fatigue behavior of the SRR material under uniaxial compression is examined. These tests are conducted without confinement, as the applied stresses are maintained within controlled levels to evaluate the material's response. The focus on unconfined conditions aims to capture the high-cycle fatigue behavior of the SRR material and to predict its performance in applications with mild confinement, such as when applied in the iSRR connector.

As previously mentioned, the unconfined test set-up is used for this series of cyclic experiments, with three minimum force levels of -20, -24, and -30 kN applied to cylindrical SRR specimens. The stiffness values of the specimens are computed for each cycle by dividing the force range by the corresponding LVDTs displacement range. Figure 4.11a, 4.11b and 4.11c present the normalized stiffness values for all specimens over their fatigue life. The pattern is consistent across most specimens: stiffness gradually decreases in a roughly linear manner until approximately 40% of the specimen's life, at which point the degradation rate accelerates exponentially until failure.

In the monotonic loading tests, the main failure mode of the SRR material is a diagonal crack, which is a typical failure mode under such conditions due to the high stress concentration along the shear plane. In contrast, during the cyclic loading tests, the failure mode was more complex, resembling a clepsydra (hourglass) pattern, where the specimen fractured into several pieces.

The clepsydra-shaped failure observed in the cyclic loading tests is a result of cyclic fatigue damage, leading to multiple crack initiation at stress concentration zones near the top and bottom of the specimen. These cracks propagate in a triangular pattern, eventually constricting the midsection and causing the specimen to break into several pieces, forming the characteristic hourglass shape, as depicted in Figure 4.12. The failure mechanism is driven by the progressive weakening of the material under cyclic stress, resulting in distributed damage rather than a single failure plane.

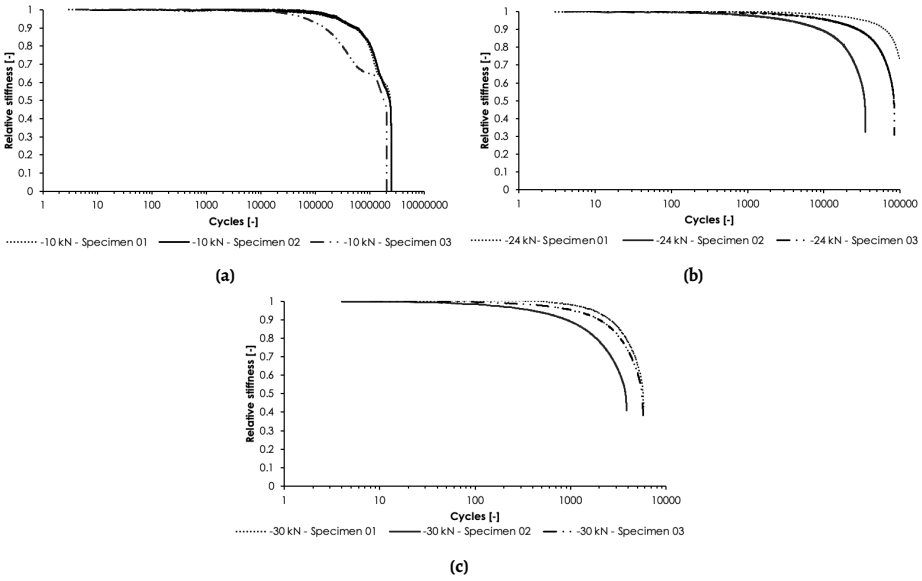

Figure 4.11: Normalized stiffness values for SRR material under uniaxial compression over their fatigue life: (a) Minimum load of -20 kN, (b) Minimum load of -24 kN, (c) Minimum load of -30 kN.

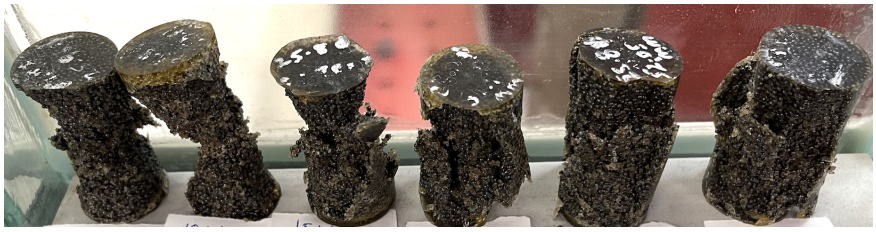

Figure 4.12: Failure mode of SRR material under cyclic uniaxial compression (fatigue).

The same statistical analysis approach applied to the fatigue data in the previous chapter is employed here. However, in this chapter, the confidence bands for the upper and lower bounds of the characteristic S-N curve are computed in accordance with the procedure outlined in ASTM standards. The end-of-life criterion is defined as the point at which the specimen experiences failure.

Interestingly, during fatigue tests conducted under indirect tensile loading on the same SRR material, the slope of the S-N curve was calculated to be 14.27 (see Figure 3.14), which is very close to the value of 14.63 obtained in the compressive fatigue tests. The similarity in the slope across different testing methods indicates a consistent relationship between stress and fatigue life for the SRR material, regardless of the loading mode.

This close agreement suggests that the material exhibits similar fatigue sensitivity in both tensile and compressive fatigue scenarios. Specifically, in both cases, even slight in-

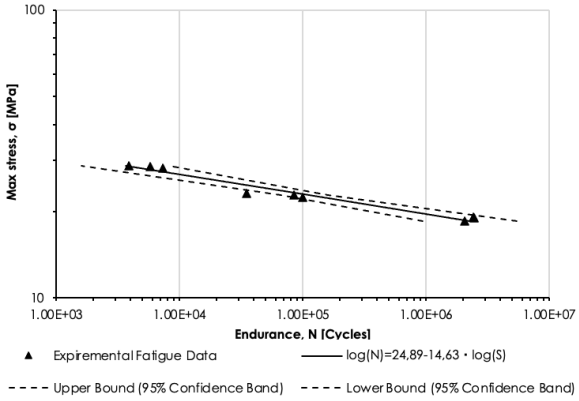

Figure 4.13: Preliminary σ-N curves ($R = 10$) for SRR loaded in compression at 25 °C.

creases in stress lead to a significant reduction in fatigue life. This consistency highlights the material's inherent fatigue behavior, which can be useful when designing components subjected to various loading conditions, as the fatigue life predictions across different loading modes are comparable. In addition, such steep slope of the fatigue behavior indicates that cut-off limit for connectors may exist. In other words, with a proper design of the connection (e.g. appropriate connector diameter) the load level can be replicated to a sufficiently low stress level that in turn will result in an infinite life of the connector.

4.5. Conclusions

This chapter presented a comprehensive evaluation of the compressive behavior of SRR material under both unconfined and confined conditions, using monotonic, incremental (low-cycle), and high-cycle fatigue tests. The experimental results provided valuable insights into the material's load-bearing capacity, stiffness, and failure modes under various stress conditions. Additionally, the impact of confinement on the SRR material's mechanical performance was assessed, highlighting its role in improving ductility and delaying failure. Despite minor stiffness variations between confined and unconfined tests, further micromechanics modeling is needed to fully understand these differences and their implications for SRR performance. Based on these findings, several key conclusions can be drawn:

- In the unconfined monotonic tests, the SRR material exhibited strain softening after reaching its maximum compressive strength (approximately 84.3 MPa). This was evidenced by a gradual post-peak stress reduction. Incremental cyclic load tests exhibited a stress-strain behavior nearly identical to that observed in monotonic tests, characterized by ductile strain-softening behavior. These tests highlighted the dual nature of the nonlinear response, attributed to the combined effects of plasticity and damage.
- The triaxial tests demonstrated that confining pressure significantly enhances the load-bearing capacity of the SRR material. The material exhibited a smoother transition to peak strength under confinement, which delayed the onset of failure and

improved ductility. Confinement restricts lateral expansion, delays micro-cracking, and distributes deformation more uniformly. Specifically, the confined SRR showed a maximum deviatoric stress of 190 MPa at a confining pressure of 30 MPa, compared to 84.3 MPa compressive strength in unconfined conditions.

- The failure modes differed significantly between monotonic and cyclic loading. Under monotonic conditions, the SRR material consistently failed along a diagonal shear plane, splitting the specimen into two pieces. In contrast, cyclic loading induced a more complex failure mode, forming a clepsydra (hourglass) shape, with specimens fragmenting into several pieces. This clepsydra failure mode was attributed to the progressive accumulation of fatigue damage, leading to multiple crack initiation and distributed damage across several planes.
- Stiffness values from the tests showed only minor differences between confined and unconfined conditions. The measured stiffness for unconfined specimens was approximately 13.1 GPa, while confined specimens had stiffness values of 10.5 to 12.5 GPa for confinement levels between 10 and 30 MPa. These small variations are likely due to statistical differences in testing rather than intrinsic material behavior. It is hypothesized that SRR, with its 80% steel volume fraction, should exhibit similar stiffness under both confined and unconfined conditions due to the dominance of the steel phase in governing elastic behavior. However, further micro-mechanics modeling is needed to better understand the factors contributing to these variations in stiffness, especially how the resin and steel interact at the micro-scale.
- The fatigue data from the unconfined compressive experiments show a slope in the σ-N curve, which aligns with the slope observed in the tension fatigue tests, around 14. This consistent steep slope suggests that a cut-off limit may exist for the iSRR connectors and indicates that with appropriate design, stress levels can be reduced to ensure infinite fatigue life. Finally, the stiffness degradation prior to failure under compressive load cycles is quantified at approximately 50%, highlighting the progressive damage accumulation in the SRR material.

III

Fatigue Behavior of iSRR Connectors in Joint Experiments

5

Design of experiments for connector's shear behavior

Chapters 3 and 4 have focused on understanding and characterizing the behavior of the SRR material. It is now time to upscale the focus to the behavior of the connectors, where SRR is utilized as the injection material. This chapter centers on designing an appropriate set-up to experimentally characterize the fatigue shear behavior of the iSRR connector. The emphasis on developing a test set-up for shear loading arises from the lack of designated standards for shear characterization of GFRP-steel joints and the unique design of the iSRR connector, which prevents slip. By preloading the bolt and injecting resin between the rod and the GFRP facing, the iSRR connector ensures a slip-resistant connection. The adoption of iSRR connectors enhances the collaborative behavior between the GFRP deck and a steel superstructure, resulting in improved hybrid interaction. While this interaction enhances the structure's bending stiffness, leading to lower overall stresses and more efficient material usage, it also increases shear stresses at the connection's interface.

This chapter is subdivided into eight sections. Section 5.1 presents the development of the test set-up, outlining the rationale behind selecting specific configurations to replicate realistic shear loading conditions. Section 5.2 introduces numerical models used to design and optimize the test set-up, exploring different configurations for effective shear load transfer. Section 5.3 evaluates the influence of boundary conditions, gaps, and steel stiffeners on stress distribution in the iSRR connector, identifying the most representative set-up for fatigue testing. Section 5.4 focuses on the stress analysis at the web-to-skin junction of the GFRP deck, identifying potential fatigue-prone locations. Section 5.5 describes the final connector test set-up and specimen design, detailing the fabrication of the iSRR connectors and test conditions. Section 5.6 extends the study to the global bridge system by developing experimental and full-size bridge models, validating the laboratory test results against realistic bridge behavior. Section 5.7 focuses on the validation of the experimental and full-size numerical models, assessing their ability to capture the realistic shear response of the iSRR connector. Finally, Section 5.8 summarizes the key findings, highlighting the rationale for the selected experimental configuration.

5.1. Development of the test set-up

To precisely characterize the shear behavior of the iSRR connector, the most realistic approach involves testing a complete bridge deck with the connectors installed in a laboratory facility. However, this method requires substantial resources, including time, funding, specialized personnel, and a large laboratory space, which are beyond the scope of this project. Consequently, it is decided to perform tests at the connector level. This decision, while pragmatic, introduces its own set of challenges due to the lack of standardized methods for testing injected bolted connectors, particularly under high-cycle fatigue loading. To address this, a comprehensive numerical study is initiated to explore various possibilities for conducting cyclic shear loading tests.

The main goal is to design a test set-up that leads to a test configuration representative for characterizing the fatigue life of the injected SRR connectors. The experiments at the joint level are conducted under cyclic loading, and it is hypothesized that the generation of high principal stresses in the injected piece will govern the joint's performance. Stress concentration analyses are performed using the commercial finite element software ABAQUS® to estimate the magnitude of stresses when alternating the geometries and boundary conditions of the test set-up.

Push-out tests, as detailed in Annex B of Eurocode 4 [92], are commonly used for evaluating the performance of shear connectors in composite structures. These tests typically involve two pairs of connectors placed on opposite sides of a steel web and embedded in concrete blocks. A schematic representation of a conventional push-out set-up is provided in Figure 5.1. While well-established for static testing, this method is not standardized for fatigue loading. Moreover, the configuration introduces averaging across multiple connectors, making it difficult to isolate individual cyclic responses. Additional uncertainties arise from friction effects at the concrete supports and from the requirement for larger and more complex specimen geometries.

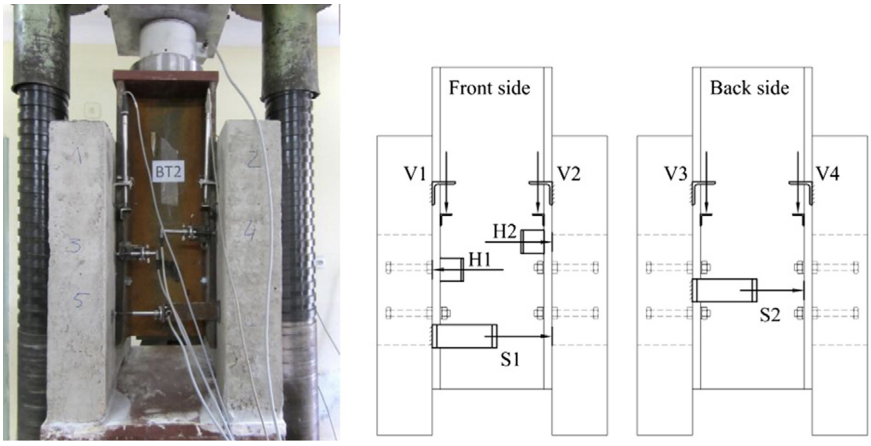

Figure 5.1: Traditional push-out test set-up, consisting of a steel girder and eight connectors embedded in concrete. Left: experimental configuration. Right: schematic representation [93].

To address these limitations, a single-connector test set-up was developed in this study. By focusing on one or two symmetrically placed connectors, the set-up enables a more direct and precise evaluation of cyclic load behavior. This approach increases the frequency of testing, minimizes variations due to asymmetric force distribution, and improves the repeatability of fatigue results. Each test with two connectors yields two independent measurements, in contrast to the single averaged result obtained from a traditional push-out test.

The experimental set-ups include several configurations, each designed to examine specific aspects of the iSRR connector's performance under shear loading. Each set-up systematically alters parameters such as boundary conditions, the presence of gaps between the steel flange and the composite facing, and the stiffness of steel stiffeners, evaluating their impact on the connector behavior. These configurations help determine an optimal set-up that replicates realistic conditions while remaining practical for laboratory testing. Specifically, the set-ups are categorized as SINGLE and SYMMETRIC configurations, representing a range from realistic bridge boundary conditions to simplified experimental models for ease of testing. Variations also include incorporating STIFF to stiffen the steel plate and reduce eccentricity in the SINGLE and SYMMETRIC set-ups. Due to the non-flat surfaces of both the GFRP plate (shown in Figure 5.2) and the steel girder, modifications in the iSRR connector design are explored, referred to as "GAP."

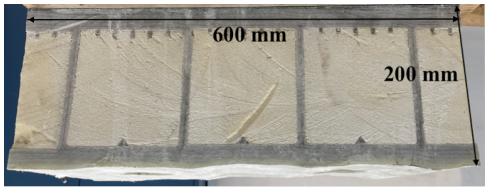

Figure 5.2: Realistic bottom facing of glass fibre composite sandwich web core panel used for testing.

The connector geometry and installation method of the iSRR system is based on prior experimental studies to allow for comparison and model validation, and follows the implementation proposed by Olivier et al. [21]. M20 bolts are used in this work, consistent with Olivier's configuration, which results in an 60 mm diameter hole in the bottom facing of the GFRP deck to accommodate the injected SRR material and ensure proper encapsulation. The SRR material itself is assumed to consist of the same components used in Chapters 3 and 4, namely high-carbon steel shot (S390, HRC 40–50) embedded in AQR 1025/B25 resin. The steel shot properties are based on the manufacturer's datasheet provided by Airblast [23], while the resin characteristics follow the technical documentation supplied by AOC Resins [80]. This material combination was also adopted in the studies by Csillag and Olivier [24, 21], ensuring consistency across modeling and experimental investigations. In the current numerical models, the SRR injection volume is modeled to extend up to the top facing of the deck, simulating full vertical encapsulation of the connector within the GFRP panel.

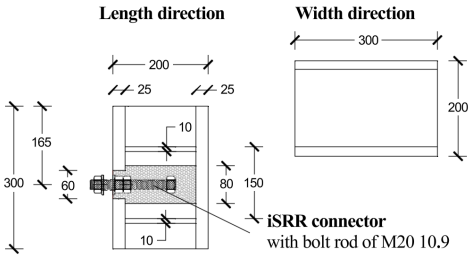

Figure 5.3: Dimensions of GFRP deck and iSRR connector in millimeters used for numerical modeling.

Figures 5.4a to 5.4i illustrate the nine specimens considered as candidates for evaluating the iSRR connector's performance under several conditions. The set-ups include combinations of configurations with and without gaps, steel stiffeners, and the GFRP deck, designed to assess the effects of boundary conditions, flexural stiffness, imperfections (gaps), and the presence of the deck. Each set-up is meticulously configured to isolate the effect of a particular parameter, allowing for a comprehensive understanding of how each factor, such as flange stiffness or the introduction of imperfections, impacts the overall structural performance.

The first set-up, named SINGLE and shown in Figure 5.4a, aims to replicate the boundary conditions representative of a bridge. In this set-up, the GFRP deck and steel plate are tested without additional gaps or stiffeners, representing the simplest configuration to evaluate the direct shear behavior of the iSRR connector. By focusing on single-sided loading, this set-up avoids complexities such as averaging results from multiple connectors, making it ideal for capturing clear cyclic load behavior.

The SINGLE + GAP set-up (Figure 5.4ib) introduces gaps between the steel girder and the GFRP facing to investigate how imperfections, like non-flat surfaces, influence the shear behavior. This scenario mimics realistic field conditions where perfect contact may not always be achieved. Such gaps could lead to differential movements or stress concentrations, affecting the connector's fatigue life.

In the SINGLE + STIFF configuration, presented in Figure 5.4ic, stiffeners are introduced to the set-up to increase the flexural stiffness of the steel plate and address local bending, which originates from the inherent single-lap joint nature of the set-up. This modification aims to understand how additional stiffness in the connected steel elements influences the overall performance of the connector, potentially minimizing stress concentrations and improving load distribution between the connector and GFRP deck. Notably, connectors in actual bridge applications are less exposed to local bending due to the flexural rigidity provided by the deck and the web of the steel girder.

The SINGLE + GAP + STIFF set-up combines both the presence of gaps and steel stiffeners, incorporating every possible condition seen in real-life installations, as illustrated in Figure 5.4id. This comprehensive set-up helps determine the combined effects of gaps and increased flexural stiffness, providing insights into the worst-case and best-case boundary conditions for the connector.

Similarly, several set-ups involve symmetric configurations. The SYMMETRIC set-up in Figure 5.4ie focuses on the boundary conditions of a simplified specimen without explicit external restraining of the GFRP deck, making it easier and faster to test. This set-up is

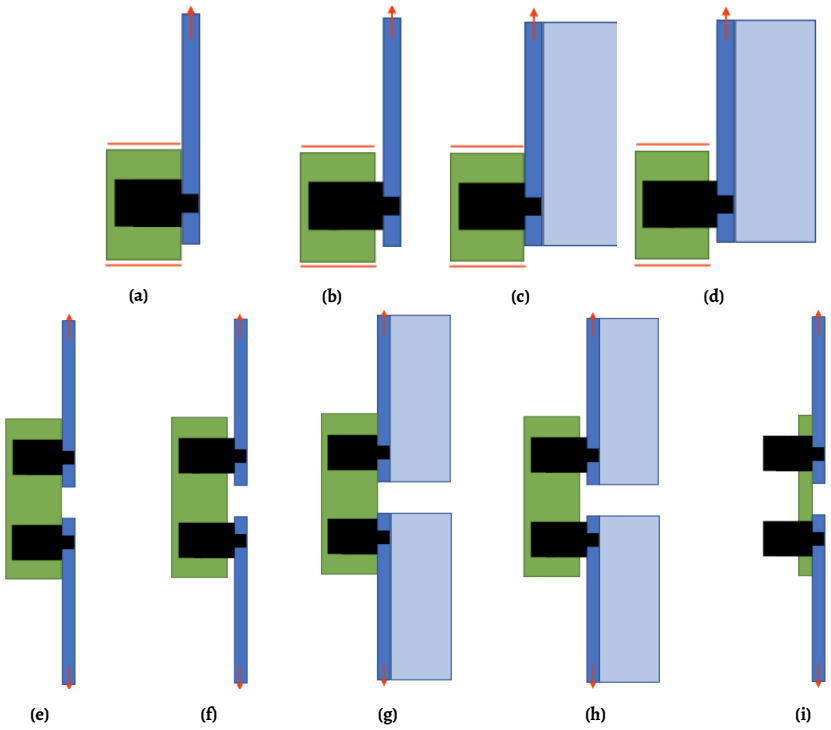

Figure 5.4: Test set-up design variants considered in the numerical modeling (green: GFRP deck, blue: steel end detail, black: iSRR connector, red lines: pinned boundary conditions, and red arrows: load direction): (a) SINGLE, (b) SINGLE+GAP, (c) SINGLE+STIFF, (d) SINGLE+GAP+STIFF, (e) SYMMETRIC, (f) SYMMETRIC+GAP, (g) SYMMETRIC+STIFF, (h) SYMMETRIC+GAP+STIFF, (i) SYMMETRIC-DECK.

particularly efficient, as it allows two independent fatigue results to be obtained from a single test, providing valuable data while requiring fewer test resources compared to the SINGLE configuration.

SYMMETRIC + GAP (Figure 5.4if) and SYMMETRIC + STIFF (Figure 5.4ig) have the same configuration as the SINGLE variations, incorporating either a gap or stiffener to evaluate the specific impacts of each factor independently. The SYMMETRIC + GAP + STIFF set-up includes both features, allowing the combined effects of boundary condition variations to be assessed with the GFRP deck present, as shown in Figure 5.4ih.

Lastly, Figure 5.4ii presents the SYMMETRIC - DECK set-up which excludes the GFRP deck entirely and substitutes it by only the composite plate that represents the bottom facing of the deck panel, thereby directly observing the shear behavior of the SRR piece itself. This test set-up is the fastest and least expensive to fabricate, also offering a direct insight into the SRR behavior without the influence of the GFRP deck, making it a valuable tool for isolating and understanding the connector's fundamental properties.

Out of all these test set-ups, the SINGLE + GAP + STIFF configuration (Figure 5.4ih) is considered the most representative because it closely simulates the conditions that an iSRR connector would experience when installed in a bridge. This includes fixed displace-

ment boundary conditions that provide a realistic representation of the external constraints acting on the GFRP deck and steel girder. Specifically, all exterior faces of the GFRP deck are restrained from moving in the thickness and the vertical loading direction, while displacement in the transverse direction, parallel to the GFRP webs, remains unconstrained. Additionally, in an actual bridge installation, imperfections such as gaps between the steel girder and the GFRP deck can occur, affecting the load transfer. Finally, the presence of steel stiffeners reflects the structural elements that increase stiffness, reducing eccentricity, and providing a more realistic representation of the boundary conditions encountered in the field. This configuration includes all critical factors that influence the connector's performance.

Although the SINGLE + GAP + STIFF configuration is considered the most representative of real bridge conditions, the exploration of other test set-ups is considered essential. Firstly, the other set-ups allow for isolating the influence of specific variables, such as gaps or stiffeners, thereby providing insights into how each factor individually affects the connector's performance. Understanding the behavior under simpler configurations also helps in validating numerical models and developing a baseline for performance comparison. Moreover, simpler set-ups like symmetric configurations can be tested more quickly and cost-effectively, which is particularly important in fatigue testing, where multiple results are needed to understand long-term behavior. These exploratory models will ensure that the final representative configuration is selected based on the localized (peak) principal stresses in the SRR, leading to more reliable and optimized design solutions.

5.2. Development of FE models for designing the test set-up

The FE models are developed in ABAQUS®, including a GFRP deck with an embedded iSRR bolted connector and a steel end detail. These analyses are conducted as a preliminary investigation, focusing primarily on selecting an appropriate experimental set-up, based on the magnitude of stresses generated within the SRR injection piece. From prior research, it is evident that non-linear behavior occurs only after the slip resistance of the joint is exceeded [21]. Therefore, for loads up to 50 kN, it is reasonable to assume linear elastic behavior since these loads remain within the elastic region of an injected SRR connector with an M20 bolt rod. This phase is intended to understand and compare stress distributions across different configurations.

The iSRR connector's 3D geometry is explicitly modeled, incorporating bolts, nuts, and washers while excluding threaded details. Due to high geometric and contact nonlinearities, the ABAQUS®/Explicit solver is chosen to avoid convergence issues present in the Standard solver. In every analyses, two steps are performed, with the first one corresponding to the preloading of the bolts and the second one to the application of the loading. Nonuniform semi-automatic mass-scaling is used across the model to reduce computation time, with time periods of 500 s and 2500 s set for the preloading and loading steps, respectively, and a target time increment of 0.003 s.

The bolts are preloaded by thermally contracting the bolt rod using the predefined field option as in [94, 95]. Then, the load is applied as a prescribed displacement on the reference point in the steel end detail kinematically coupled to its corresponding surface. Both steps are assigned with a smooth amplitude curve, i.e., a gradual time-dependent load application, to prevent the creation of inertia forces.

To precisely represent varying boundary conditions, a deck model with a single connector is developed, allowing the application of constraints to either simulate the SINGLE or SYMMETRIC scenario. In the SINGLE model, all four facings of the GFRP deck are restrained in the x-direction and y-direction (U1 = U2 = 0), while displacement in the z-direction (U3) is left unconstrained, as depicted in Figure 5.5a. This constraint configuration represents the realistic boundary conditions of bridge decks, where lateral and vertical movements are restricted, but out-of-plane compliance is allowed. No rotational degrees of freedom (UR1, UR2, UR3) are constrained, allowing the facings to rotate freely to simulate realistic deformation behavior.

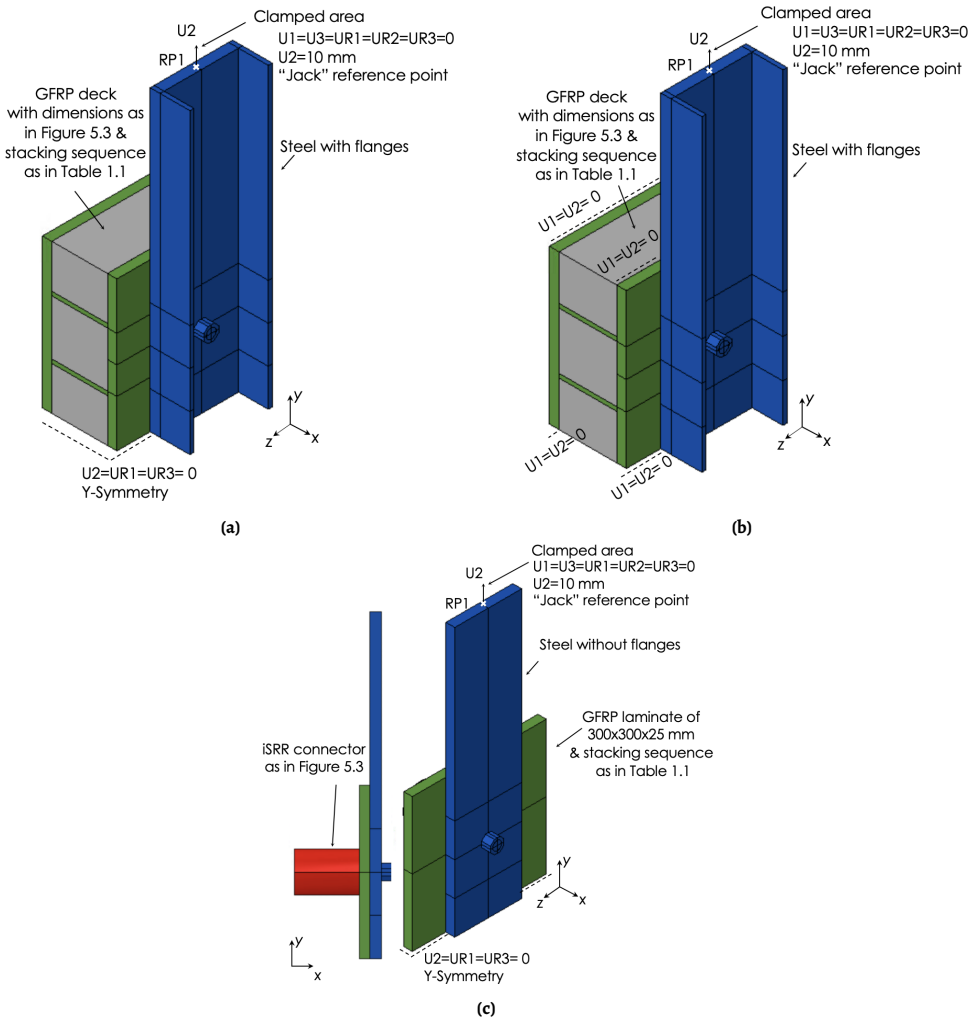

Figure 5.5: Model set-up with different boundary conditions: (a) SINGLE+STIFF, (b) SYMMETRIC+STIFF, and (c) SYMMETRIC-DECK.

In the SYMMETRIC models, symmetry is applied along the cross-sectional surface normal to the y-direction, enforcing the condition U2 = UR1 = UR3 = 0. For the SYMMETRIC model with the deck, this includes both facings and the foam core, as shown in Figure 5.5b. In the SYMMETRIC-DECK model, presented in Figure 5.5c, only the GFRP laminate is present instead of the full deck, and the same translational symmetry condition is applied to its corresponding face to replicate consistent support and deformation constraints.

The materials used in the FE models are described as linear elastic, reflecting the hypothesis that the stresses will remain within the elastic range at a load level of 50 kN. The steel components are modeled as linear elastic with an Young's modulus (E) of 210 GPa and Poisson's ratio (ν) of 0.3, assuming isotropic behavior without fracture definition. The bolt rod, required to achieve the desired prestress, is modeled as an orthotropic material incorporating thermal expansion properties. The SRR material properties are sourced from Chapter 3. The foam core of the GFRP deck is modeled using compressive test results for low-density foams reported by Tuwair [96]. The composite laminates used in the finite element model are assumed to behave in a linear elastic manner, consistent with the expectation that cyclic stresses remain within the elastic range under the applied load levels (up to 50 kN). The detailed stacking sequence, fabric types, fiber volume fractions, and laminate build-up reflect the actual lay-up applied by the manufacturer, FiberCore Europe [26], as described in Section 1.4. Homogenized orthotropic engineering constants are assigned based on values reported in [50], representative of the unidirectional plies used in the deck's facings and webs. A comprehensive overview of the mechanical properties used for all components in the finite element models is provided in Table 5.1.

Table 5.1: Material indexes for every utilized component.

Component	Mechanical properties
UD laminate [50]	$E_1 = 31450$ MPa, $E_2 = E_3 = 8459$ MPa, $G_{12} = G_{13} = 4838$ MPa $G_{23} = 3021$ MPa, $\nu_{12} = \nu_{13} = 0.272$, $\nu_{23} = 0.4$, $\rho = 1873$ kg/m^3
Foam [96]	$E = 2.1$ MPa, $\nu = 0.3$, $\rho = 32$ kg/m^3
Steel shot [23]	S390, HRC 40-50, $\rho = 7400$ kg/m^3
Resin [80]	$\eta = 150 - 220$ [mPa.s], $E = 3530$ MPa, $T_g = 135$ °C
SRR [Chapter 3]	$E_t = 16181$ MPa, $f_t = 10$ MPa, $\nu = 0.13$ and $\rho = 4955$ kg/m^3
Bolt rod	Grade 10.9, $E = 210000$ MPa, $\nu = 0.3$, S355
Nuts	Grade 10.9, $E = 210000$ MPa, $\nu = 0.3$, S355
Washers	Grade 10.9, $E = 210000$ MPa, $\nu = 0.3$, S355

The assembly comprising the bolt rod, four nuts, two washers, and the SRR material is modeled to precisely capture the complex geometry and contact interactions within the connection (Figure 5.6). The bolt rod, nuts, and washers are meshed with linear eight-noded solid elements (C3D8R) with a 3 mm global element size. The SRR injection material is meshed with ten-noded modified tetrahedral elements (C3D10M) using a uniform element size of 3 mm to represent the curved geometry and internal stress gradients accurately. The surrounding foam layer is also modeled using C3D8R elements, with a global mesh size of 8 mm and 3 mm refinement near the bolt holes. The steel end detail, including the clamping plate and flange stiffeners where applicable, is modeled with C3D8R elements and a global size of 10 mm and a refined mesh close to the bolt hole equal to 3 mm.

The GFRP composite deck is modeled using eight-noded continuum shell elements (SC8R), commonly referred to as 2.5D elements [97]. A global mesh size of 8 mm is used throughout the deck, with local refinement to 3 mm around the connector holes to improve accuracy in the stress concentration regions. Owing to the nature of continuum shell elements, one element is used through the thickness, providing an efficient yet sufficiently detailed representation of the layered composite behavior.

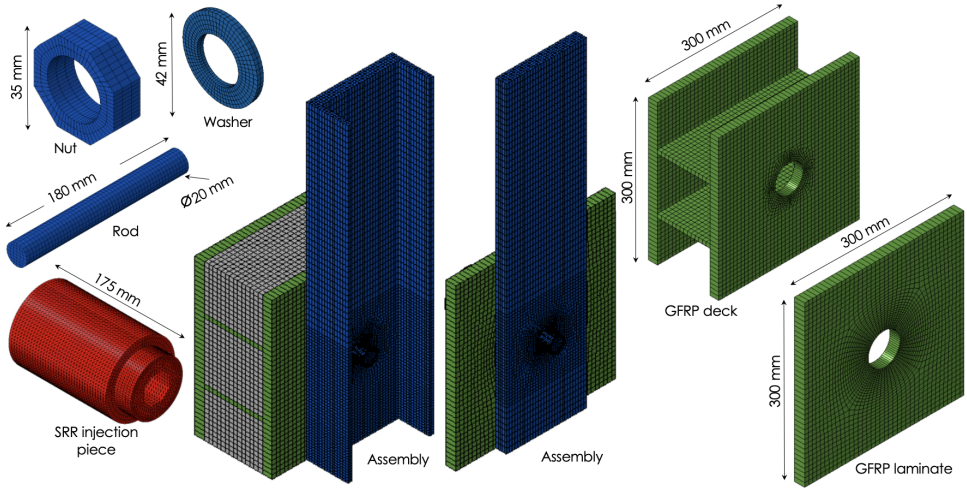

Figure 5.6: Details of FE mesh.

Contact interactions between the SRR material and surrounding components—including the bolt, nuts, washers, and GFRP deck—play a critical role in accurately simulating load transfer. In actual fatigue testing, the connection is initially undamaged, and the injected SRR material is expected to remain fully bonded to the surrounding surfaces for a significant number of cycles. To reflect this physical condition in the early stages of loading, the numerical model assumes a perfectly bonded interface at the onset of cyclic loading. This is implemented using tie constraints, which prevent any relative displacement between the SRR material and its adjoining surfaces during this initial phase. The assumption is that damage initiation, such as interface debonding or cracking, will only occur after substantial fatigue degradation has accumulated. At the remaining interfaces, tangential contact is modeled using a penalty formulation with a friction coefficient of 0.2, representative of steel-FRP interface behavior [98, 99]. In the normal direction, hard contact is applied to allow separation under tension while preventing penetration under compression [29].

5.3. Influence of boundary conditions, gaps and steel stiffeners

The exaggerated deformed shapes of the tested configurations, as shown in Figures 5.7a to 5.7i, highlight the influence of added features such as gaps and stiffeners on structural stiffness and deformation behavior. In the SINGLE configurations, presented in Figures 5.7a to 5.7d, the inclusion of gaps leads to increased deformation in the steel plate, indicating the negative effect of imperfections. The addition of steel stiffeners, however, improves

the stiffness of the system by reducing deformation and limiting deflection in the steel plate. The SYMMETRIC configurations, shown in Figures 5.7e to 5.7i, exhibit similar trends, with the presence of steel plate stiffeners notably reducing visible deformation. Among all configurations, the SINGLE + GAP + STIFF and SYMMETRIC + GAP + STIFF set-ups, presented in Figure5.7d and Figure 5.7h respectively, show reduced deformation, indicating the combined benefits of increased flexural stiffness and minimized load eccentricity. These observations suggest that including stiffeners is crucial for enhancing the performance of the connectors by controlling deformation under loading, making the configurations with stiffeners more representative of realistic, effective structural conditions.

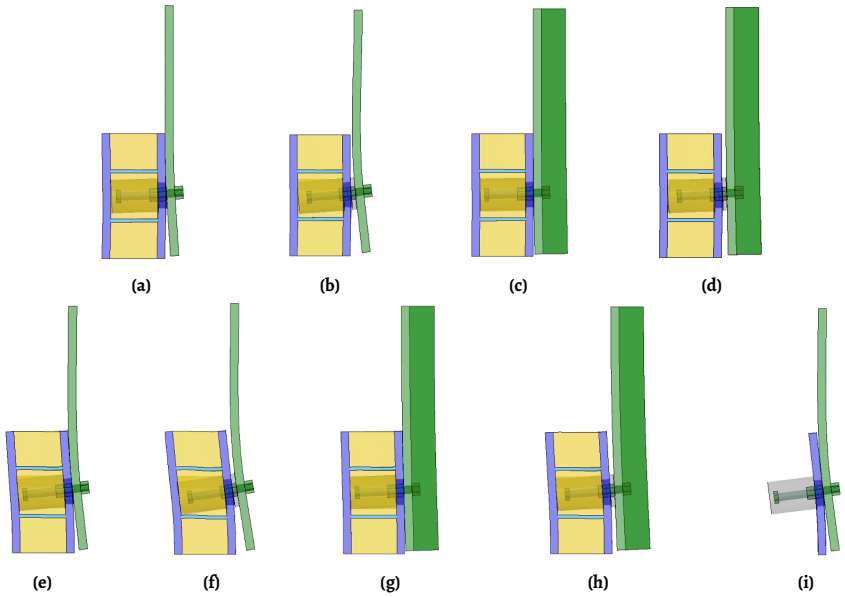

Figure 5.7: Deformed shapes of the different test set-ups at 50 kN exaggerated by a factor of ten: (a) SINGLE, (b) SINGLE+GAP, (c) SINGLE+STIFF, (d) SINGLE+GAP+STIFF, (e) SYMMETRIC, (f) SYMMETRIC+GAP, (g) SYMMETRIC+STIFF, (h) SYMMETRIC+GAP+STIFF, (i) SYMMETRIC-DECK.

In the SYMMETRIC - DECK configuration, which only includes the connector and the facing without the GFRP deck, the deformation behavior is more pronounced compared to configurations that incorporate a deck. The absence of the deck results in reduced constraints on the connector, leading to increased flexibility. This set-up highlights the essential role of the GFRP deck in providing stability and stiffness to the connector assembly. Without the deck, the system experiences greater deformation, indicating that the deck significantly contributes to the overall structural performance and resistance to shear forces.

Another important aspect to be investigated is the influence of the boundary conditions to the maximum principal stresses in the SRR material at a load level equal to 50 kN. Figure 5.8 presents the distribution of maximum principal stresses within the injected SRR material for various configurations under a spectrum of stresses ranging from +95 MPa to -30 MPa. The stress distributions are fairly similar but with different peak value, indicating the effect of different boundary conditions and features such as gaps and stiffeners. Overall,

the configurations in Figures 5.8d and 5.8h, which include both stiffeners and gaps, consistently provide the lowest stress levels, suggesting that these features help distribute loads more effectively, reduce stress concentrations, and therefore enhance the overall fatigue performance of the iSRR connector.

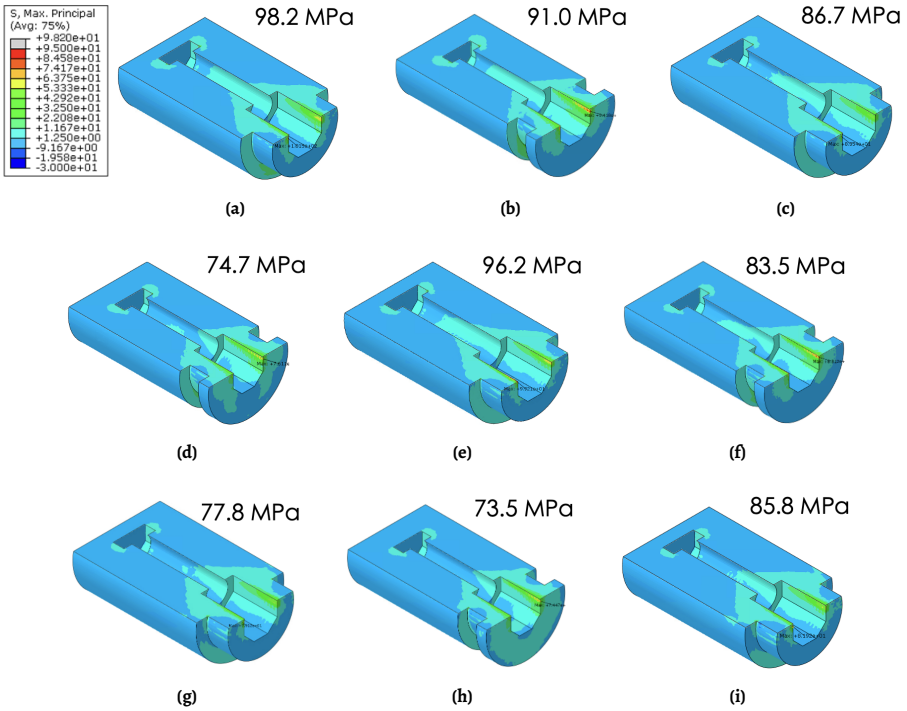

Figure 5.8: Peak value of maximum principal stresses in an cut-through of SRR injection piece forming the iSRR connector for a load of 50 kN: (a) SINGLE, (b) SINGLE+GAP, (c) SINGLE+STIFF, (d) SINGLE+GAP+STIFF, (e) SYMMETRIC, (f) SYMMETRIC+GAP, (g) SYMMETRIC+STIFF, (h) SYMMETRIC+GAP+STIFF, (i) SYMMETRIC-DECK.

The results demonstrate that each design modification contributes to a reduction in peak stress, highlighting the importance of geometric and structural enhancements to the connector set-up. A key observation is that shifting from a SINGLE to a SYMMETRIC configuration consistently reduces peak stress across all tested cases. The base SYMMETRIC set-up (Figure 5.8e) exhibits a slightly lower peak stress of 96.2 MPa, compared to 98.2 MPa in the SINGLE configuration (Figure 5.8a), indicating that symmetric loading conditions help distribute stresses more evenly. Although the stress reduction is marginal (1.8 MPa), it can be attributed to the elimination of asymmetric boundary conditions and secondary bending effects present in the SINGLE configuration. However, the benefit of symmetry alone is limited unless combined with additional design modifications. Significantly lower peak stresses are achieved only when symmetry is combined with additional design features such as a gap between the deck and the steel flange and/or the inclusion of stiffeners, which reduce constraint-induced stress concentrations and promote a more uniform shear load

transfer in the SRR piece.

Further reductions in stress are observed when a GAP is introduced, as it alleviates constraints in the load path. In the SINGLE set-up, the incorporation of a gap decreases the peak stress from 98.2 MPa to 91.0 MPa (Figure 5.8b), while in the SYMMETRIC set-up, the stress drops from 96.2 MPa to 83.5 MPa, as shown in Figure 5.8f. Similarly, adding stiffeners enhances structural rigidity and reduces stress concentrations. The SINGLE + STIFF configuration achieves a lower peak stress of 86.7 MPa (Figure 5.8c), while its SYMMETRIC counterpart further decreases stress to 77.8 MPa (Figure 5.8g). When both stiffeners and a gap are included, the reduction becomes even more pronounced. The SINGLE + GAP + STIFF configuration results in a stress level of 74.7 MPa, as shown in Figure 5.8d, whereas the SYMMETRIC + GAP + STIFF set-up achieves the lowest peak stress of 73.5 MPa (Figure 5.8h), representing a 25% reduction compared to the baseline SINGLE configuration.

Finally, a distinct trend is observed in the SYMMETRIC - DECK set-up, where the absence of the deck leads to an increased peak stress of 85.8 MPa, as illustrated in Figure 5.8i. This suggests that deck constraints play a crucial role in stress distribution and must be considered in the final design. Overall, transitioning from a fully encased, flexible SINGLE connector to the optimized SYMMETRIC + GAP + STIFF configuration results in a significant stress reduction of 24.7 MPa (from 98.2 MPa to 73.5 MPa). This substantial decrease in stress concentration is essential for enhancing fatigue resistance and ensuring the long-term performance of the SRR connector.

The absence of imperfections (gaps) and stiffeners in the experimental set-ups can lead to overly conservative results, potentially giving an imprecise depiction of the connector's performance. This conservatism, while ensuring safety, might be too pessimistic, thus affecting the feasibility of practical applications. It can be seen that the most simplistic test set-up (SYMMETRIC-DECK), used in the past by Olivier [21], would lead to a 10–15% overestimation of peak stress (85.8 MPa vs. 74.7 MPa) compared to the most realistic variant representing connectors in a bridge (SINGLE + GAP + STIFF). On the other hand, the SYMMETRIC + GAP + STIFF set-up provides a very comparable peak stress to the SINGLE + GAP + STIFF configuration.

Therefore, the SYMMETRIC + GAP + STIFF configuration is selected for further experimental testing. This set-up strikes a balance between realistic stress concentrations and practicality in laboratory testing, allowing for two results to be obtained per experiment, which is crucial in fatigue testing. This approach ensures that the results are neither overly optimistic, which could compromise safety, nor excessively conservative, which could be unsustainable in real-world applications. The SYMMETRIC + GAP + STIFF configuration ultimately provides a realistic, efficient, and representative experimental scenario for evaluating fatigue life.

5.4. Stress analysis at web-to-skin junction of GFRP deck

This section investigates the stress distribution in the GFRP composite deck, with a particular focus on the web-to-skin junction, a critical region where high local stresses may lead to failure and compromise the fatigue performance of the iSRR connector. To assess the risk of such failure, the normal stress component S_{22} in the Y-direction is analyzed across various test configurations. This component reflects tensile stresses that develop at the web-to-skin

corner under loading, and its evaluation helps identify areas susceptible to crack initiation or fatigue-driven degradation.

This analysis requires accurate resolution of local stress concentrations in a geometrically complex region. Therefore, the model is constructed using fully 3D solid elements, in contrast to the 2.5D continuum shell elements used in previous sections. This shift is essential to capture the three-dimensional nature of the stress field and the geometric discontinuities at the web-skin interface. The GFRP facings and webs are modeled using equivalent orthotropic engineering constants, derived from the stacking sequence, fiber volume fractions, and material properties introduced earlier in the thesis.

To enable clear visualization of the stress field at the web-to-skin junction, selected components, specifically the foam core, the bottom facing in contact with the iSRR connector, and half of the internal webs, are hidden in the post-processing phase. The results, shown in Figures 5.9a to 5.9h, indicate that the inclusion of stiffeners and gaps significantly influences stress localization. Set-ups with stiffeners tend to exhibit reduced stress peaks (Figures 5.9c, 5.9d, 5.9g, 5.9h) suggesting improved load transfer and reduced risk of failure. These findings emphasize the importance of connector detailing and local reinforcement strategies in improving the structural performance of GFRP-steel hybrid joints.

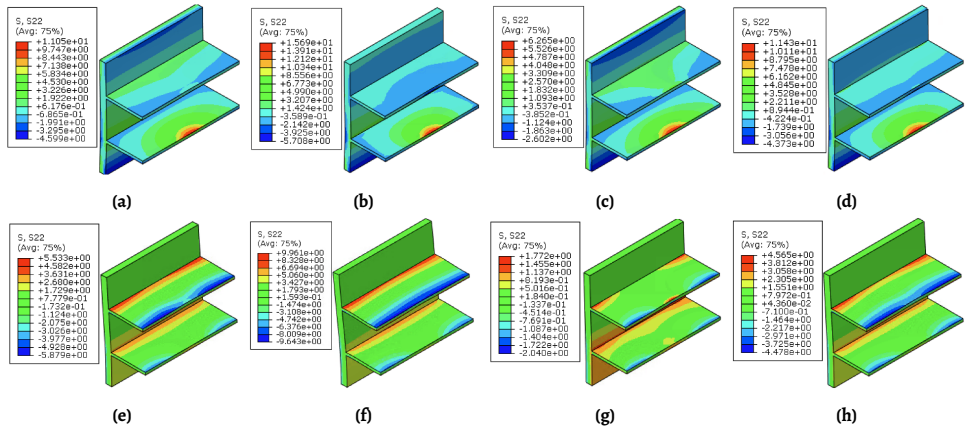

Figure 5.9: Stress concentrations around web-to-skin corner in GFRP deck at 50 kN: (a) SINGLE, (b) SINGLE+GAP, (c) SINGLE+STIFF, (d) SINGLE+GAP+STIFF, (e) SYMMETRIC, (f) SYMMETRIC+GAP, (g) SYMMETRIC+STIFF, (h) SYMMETRIC+GAP+STIFF.

In comparing the SINGLE + GAP + STIFF (Figure 5.9d) and SYMMETRIC + GAP + STIFF (Figure 5.9h) set-ups, there are clear differences in the stress distribution of the S_{22} component at the web-to-skin junction. In the SINGLE + GAP + STIFF configuration, the peak S_{22} stress reaches approximately 11.1 MPa, and the stress is highly localized near the connection area, indicating a concentration that may trigger fatigue damage. In contrast, the SYMMETRIC + GAP + STIFF configuration shows a lower peak value of around 4.7 MPa, with the stress more evenly distributed along the junction. This suggests that symmetric boundary conditions and the presence of stiffeners help reduce the severity of local stress buildup.

While the observed S_{22} values remain well below the transverse tensile strength of

the GFRP laminate (173.7 MPa, as documented by [21]), this strength alone does not fully represent the failure mechanisms that may develop at the web-to-skin interface. In reality, localized debonding, delamination, or interlaminar damage are likely to occur at much lower stress levels, particularly under cyclic loading where fatigue degradation accumulates over time. Although the current linear elastic model does not simulate such failure modes directly, it is valuable for identifying stress concentrations that may lead to premature degradation of the GFRP deck. In this context, the absolute magnitude of the stress is less important than its distribution and localization. These insights are essential not for predicting failure of the deck itself, but for ensuring that the chosen test set-up does not promote early damage at the web-to-skin junction, which would interfere with the goal of the experimental campaign. This focus aligns with the design of the test program, which aims to characterize the fatigue performance of the iSRR connector rather than the fatigue degradation of the GFRP deck. Ensuring that stress concentrations in the deck remain low and well-distributed allows the connector to be the dominant source of fatigue damage in the experiments, enabling meaningful evaluation of its performance.

5.5. Final connector test set-up and specimen design

The SYMMETRIC + GAP + STIFF configuration is selected for experimental testing due to its comparable stress concentrations to the SINGLE + GAP + STIFF set-up, while offering increased efficiency in the testing process. In the SYMMETRIC set-up, two connectors can be tested concurrently, allowing for faster data collection. This efficiency is particularly advantageous in fatigue testing, where the number of load cycles is significant, and minimizing experimental time is crucial.

The full-size GFRP sandwich deck panel, described in Section 1.4, is subsequently cut into smaller composite panels measuring 600x300x200 mm, with the integrated webs positioned perpendicularly to the loading direction. The segments from the vacuum-infused glass fibre composite sandwich web-core panel and the two steel end details are shown in Figure 5.10a.

The full connector configuration is illustrated in Figure 5.10b and consists of an M27 bolt rod, embedded nuts, washers, and a SRR injection piece. The selection of the M27 bolt is based on findings from the MSc thesis of Swinnen [100], which included an analysis of thermal load effects under serviceability conditions in a hybrid GFRP-steel bridge deck system. The study showed that high longitudinal forces near the cross- to main-girder connections led to an unsatisfactory unity check of 1.53 when using M24 bolt rods. As a solution, it was proposed to either redesign the connection layout or use bolts with a larger diameter. Thus, the current experiments involve M27 10.9 bolt rods, which were found to be sufficient to resist the expected shear forces in these critical locations. To accommodate the larger bolt diameter, the hole in the bottom GFRP facing is enlarged from 60 mm to 80 mm to ensure sufficient clearance between the bolt and the GFRP, allowing the SRR material to fully surround the bolt without direct contact with the facing. All components used in the experimental campaign, along with their corresponding material indexes, are listed in Table 5.1.

The SRR injection piece is deliberately designed not to reach the top facing of the sandwich panel. This decision addresses two key concerns. First, contact between the SRR material and the top facing could promote local heat transfer to the connection region,

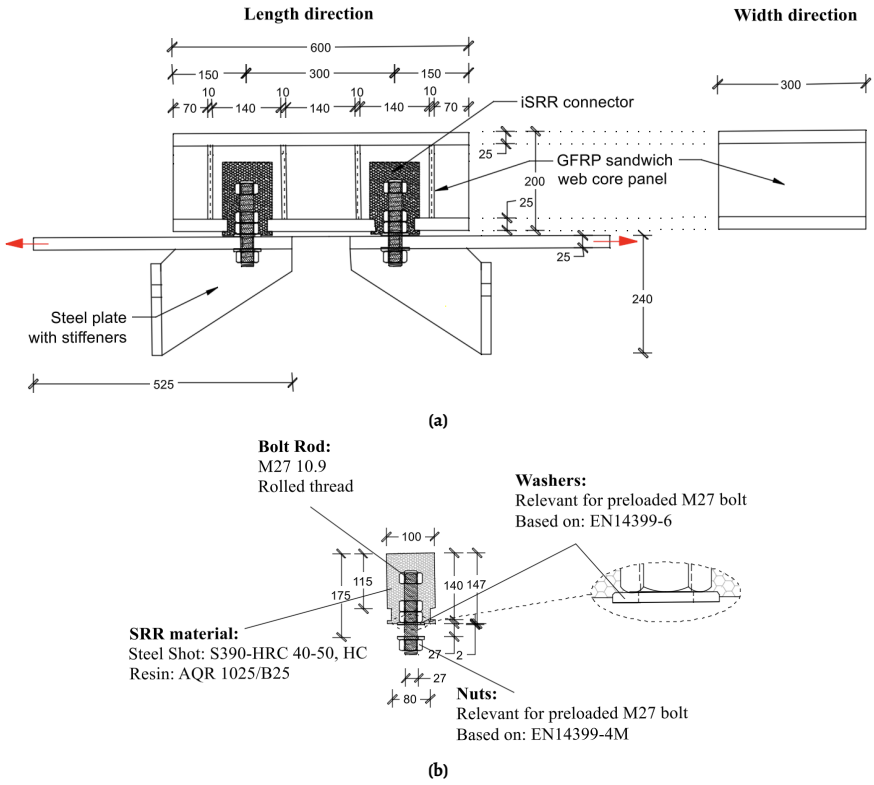

Figure 5.10: iSRR connectors in composite-steel single-lap shear joint specimens (dimensions in mm): (a) Detailed view of configuration (red arrows indicate loading direction), (b) Details of the connector.

especially under elevated ambient or surface temperatures. Second, avoiding contact with the top facing prevents unwanted stiffening or disruption of the structural response in regions subjected to wheel loading. In practice, both the connector and the surrounding deck may be exposed to elevated service temperatures, such as through solar radiation on bridge surfaces. Measurements from previous studies indicate that GFRP bridge decks in the Netherlands can reach surface temperatures exceeding 54 °C [101].

Therefore, a testing temperature of 55 °C was selected as a realistic extreme-case scenario for evaluating the connector's thermal performance. This value represents a conservative upper bound for service conditions likely to be encountered in practice. While Chapter 3 used this temperature to assess water absorption of the SRR material, in this chapter it is used to simulate elevated thermal exposure for mechanical and durability evaluation. Since the critical load transfer occurs at the root of the iSRR connector (near the bottom facing), the actual temperature in this region is expected to be lower; however, testing at 55 °C ensures a conservative assessment of the structural integrity and long-term performance of the connector system.

The selected test set-up includes a gap in the design of the iSRR connector, requiring specific modifications to retain preloading. To achieve this, rubber rings (8 mm thick and

100 mm in diameter) are placed around the holes in the deck to facilitate controlled resin injection. Additionally, in prefabricated connectors, the surface of the SRR material is adjusted to be lower than the washer surface, preventing direct contact with the steel plates and ensuring that preloading is maintained throughout the service life. This separation ensures that the preloading assembly consists solely of metallic components, eliminating the inclusion of polymeric materials in the load path. These modifications are essential for achieving slip resistance and enabling a strong hybrid interaction between the composite deck and steel substructure.

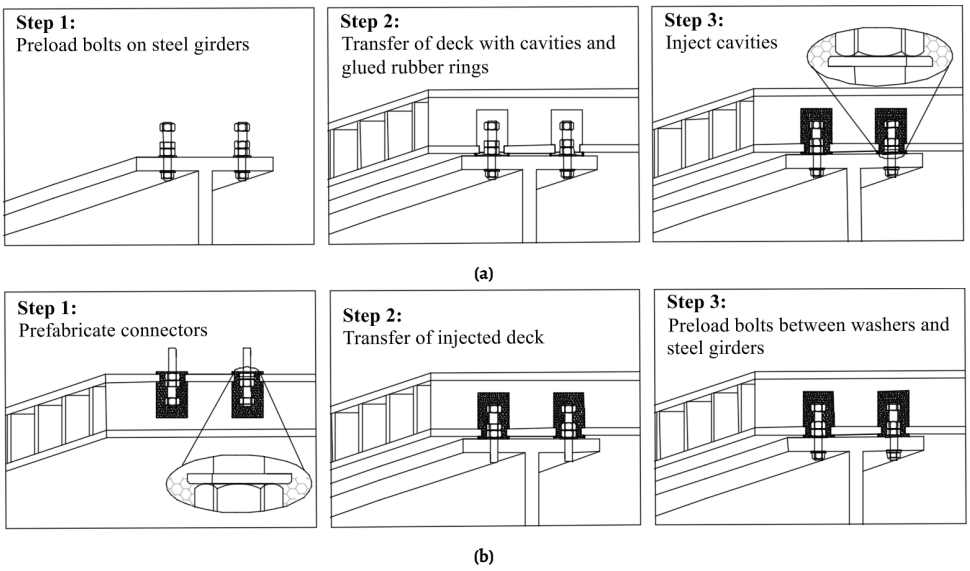

Figure 5.11: Procedures for producing iSRR connectors: (a) On-site fabrication, (b) Prefabricated.

The fabrication of iSRR connectors can be conducted either in a factory setting or directly on-site, as illustrated in Figure 5.11. In the on-site fabrication approach, the bolts are first preloaded into the steel girders, after which the GFRP deck with pre-drilled cavities is placed over them, and the cavities are injected from the top. This method ensures that the preloading of the bolts is fully completed before resin injection, preventing any loss of preload during the process. Since the resin does not permeate the preloading package, the SRR material fully fills the cavity, reaching the height of the washers.

In contrast, prefabricated iSRR connectors (Figure 5.11b) require a different adjustment to maintain preloading. In this case, the SRR material is intentionally set below the washer level to prevent direct contact with the steel girders. This configuration ensures that only the metallic components contribute to the preloading assembly, preventing potential relaxation effects from polymeric materials. Regardless of the chosen fabrication method, the preloading integrity and long-term performance of the connection are ensured.

In this study, the connectors are manufactured following the prefabricated procedure illustrated in Figure 5.11b, which is chosen for its simplicity, speed of execution, and the ability to easily reuse the steel loading end details across multiple tests. The bolt rods are

first positioned through a temporary steel plate of reduced width, which includes two holes to allow simultaneous placement of both connectors and ensure proper alignment. The surface of the plate in contact with the SRR was sprayed with a release agent to facilitate removal after curing. This plate is aligned above the rubber rings that define the cavities in the GFRP deck. Steel balls are then added around the bolts within each cavity, after which the two-part resin, selected in Chapter 3, is injected from the bottom up until the cavities are fully filled.

Once the resin has cured and solidified, the temporary steel plate is removed. Preload is then applied to the bolts using a calibrated torque gun after the specimen is placed within the steel loading frame. Torque levels of 900 Nm or 1350 Nm are applied for specimens tested at different load levels, as described in more detail in Section 6.1. Although direct verification of bolt tension is not performed during assembly, the applied torque provided repeatable and consistent preloading. Additional insights into the quality of the preload are inferred from the monotonic loading response during post-cyclic monotonic testing. In real bridge installations, direct preload verification could be achieved through the use of load-indicating washers or embedded strain gauges.

The experimental set-up, including the test specimen and the test rig, is depicted in Figure 5.12. All cyclic and static tests are executed in an Instron dual column testing equipment with a load cell capacity of 600 kN. Part of the steel end detail is clamped in the hydraulic jaws, whilst their horizontal elements are fastened to the upper and (movable) lower cross heads. To control the temperature at 55 °C, a custom-built chamber is constructed using insulating panels. The dimensions of the panels and a schematic representation of the chamber s provided in Figure 5.13a. Air circulation within the test chamber is facilitated by a fan and a motor. To ensure that the temperature remained constant at the specified level, two temperature sensors were positioned adjacent to the steel stiffeners, as illustrated in Figure 5.13b. The sensors' tips were specifically placed near the two bolt regions.

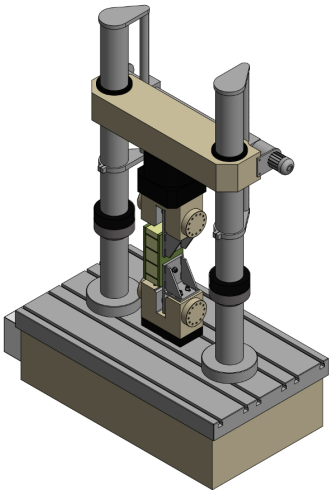

Figure 5.12: Test set-up of cyclic and static tests under ambient temperature.

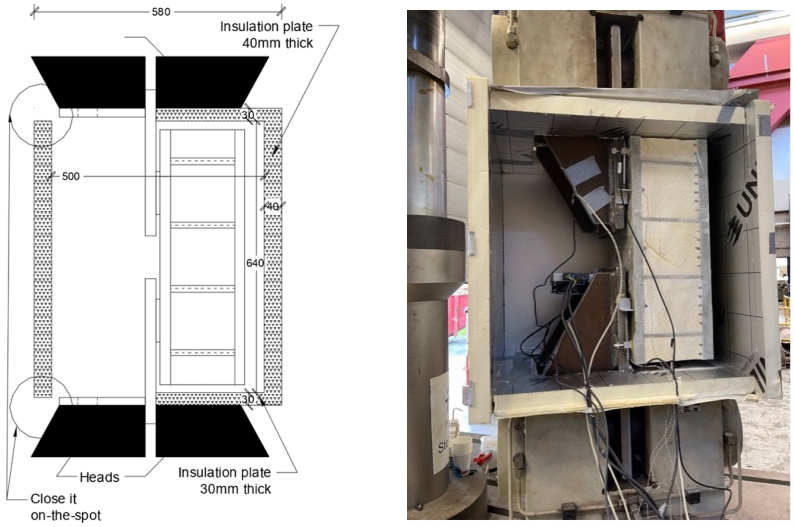

Figure 5.13: Test set-up of cyclic and static tests under elevated temperature: (a) Schematic view of the chamber, (b) Open chamber.

5.6. Development of experimental and full-size bridge models

Following the selection of the SYMMETRIC + GAP + STIFF test set-up for characterizing the cyclic response under shear loading of the iSRR connectors, it is essential to ensure that this set-up provides results that are representative of real-world bridge applications. To achieve this, two separate models are developed using ABAQUS®: one that precisely replicates the experimental test set-up and another that models a full-size bridge configuration. The goal is to validate the applicability of experimental results to practical bridge conditions and provide insight into the structural response of iSRR connectors at full-size conditions.

The full-size model represents a segment of a bridge deck supported on a girder system, a configuration commonly found in movable bridges and medium-span highway bridges recorded in the RWS database. In bridges with both main and cross girders, the deck can be considered either supported directly on the main girders (if the spacing is relatively small) or supported on cross girders (if the cross girders carry the deck as primary structural elements). In this model, the support condition is designed to align with feasible laboratory testing, while still maintaining the essential hybrid interaction between the deck and steel substructure seen in actual bridges.

The modeled deck segment represents a 10-meter span with a total width of 3 meters, approximating the typical spacing between main girders. To reflect the expected laboratory test setup, which is commonly based on a twin-girder bridge configuration, a transverse symmetry condition is applied at mid-span, modeling only half the bridge width (1.5 meters). Although not representative of repetitive interior spans between cross girders, the model includes 0.75 meter cantilever extensions. An overview of the applied boundary conditions, connector arrangement, and key geometric parameters is provided in Figure 5.14.

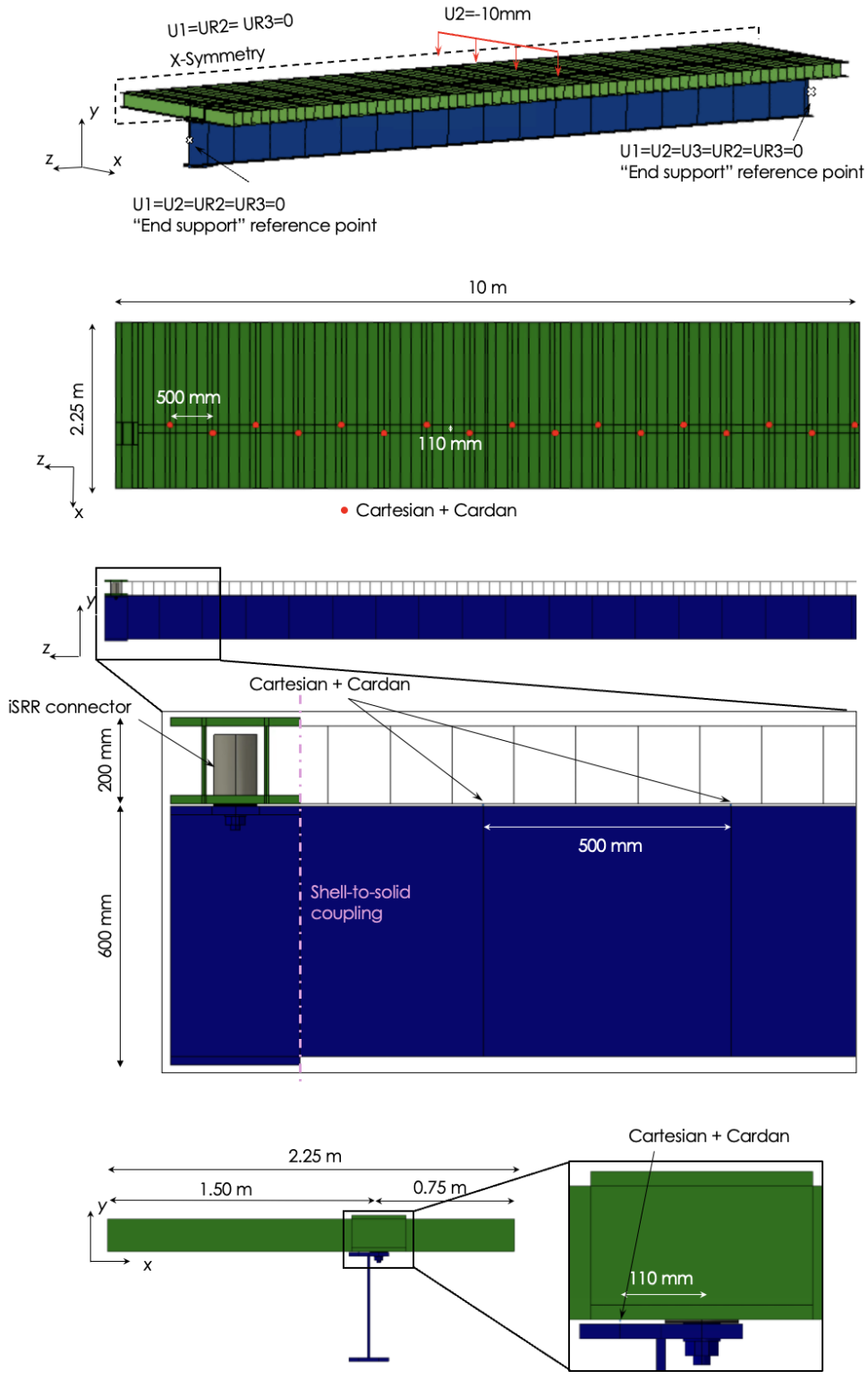

Figure 5.14: Boundary conditions and connector details of bridge model.

The iSRR connectors are modeled using a combination of detailed 3D geometry and simplified elements. One iSRR connector is fully represented in 3D to capture detailed stress distributions within the SRR injection material. The remaining connectors are modeled as translational springs, assigned axial and shear stiffness values of 1×10^6 kN/mm and 100 kN/mm, respectively, based on values reported in the literature [50]. The shear connectors are arranged in a staggered pattern at 500 mm longitudinal intervals, with a transverse offset of 110 mm to achieve alternating placement between rows, reflecting a typical layout in hybrid bridge design. The detailed 3D representation allows for precise stress analysis at critical locations, such as the midspan of the girder, where maximum shear effects are expected.

This model is built to serve a dual purpose: it is representative of real-world bridge configurations, whether the deck is supported on main girders or cross girders, while also being adaptable to laboratory testing. This approach ensures that findings from the experimental set-up can be confidently extrapolated to practical bridge applications.

Two types of interactions are addressed in the model. The first involves the connection between shell and solid elements, using ABAQUS®'s built-in 3D-to-2D connection capabilities. This shell-to-solid coupling is essential for accurately transferring forces between the full bridge deck, modeled with two-dimensional elements, and the localized connector region, modeled with three-dimensional elements. As shown in Figure 5.15a, the global mesh size for the shell deck model is 78 mm (S4R elements), with refinement in the connection area. The full 3D version of the deck is modeled using SC8R elements, with a global mesh size of 8 mm and local refinement to 5 mm in the oversized hole near the connector region.

The steel girder is represented in two forms as well: a simplified shell model using S4R elements, and a more detailed 3D model using C3D8R elements with reduced integration, as seen in Figure 5.15b. The mesh around the hole of the three-dimensional girder is refined down to 1 mm, while the flange and web employ a mesh size of approximately 8–55 mm depending on the region. The SRR material forming the connector is meshed using tetrahedral C3D4 elements with an average size of 3 mm, as illustrated in Figure 5.15c.

The second type of interaction concerns the internal interfaces of the 3D connector model, including those between the SRR material, the bolt rod, embedded nuts, bottom GFRP facing, and washers. These interfaces are modeled using tie constraints to replicate fully bonded conditions, consistent with the assumption of no slip during the early stages of cyclic loading, as discussed in Section 5.2. The foam insert is excluded from the simulation, and the bolt, nut, and washer meshes are modeled as previously described in Figure 5.6

In terms of pretension, the iSRR connector is not explicitly preloaded. Instead, to ensure that comparable stresses are developed in the injection piece, tie constraints are applied between the surfaces of the washers and the steel plates. This approach effectively prevents any relative movement, allowing the iSRR connector to behave as if it were fully preloaded during the loading stage. The rest of the connectors are modeled as rigid wires with a Cartesian + Cardan connection type, as defined in ABAQUS®. This combination allows for translational freedom in Cartesian directions and rotational freedom about two axes, replicating a universal joint-like behavior.

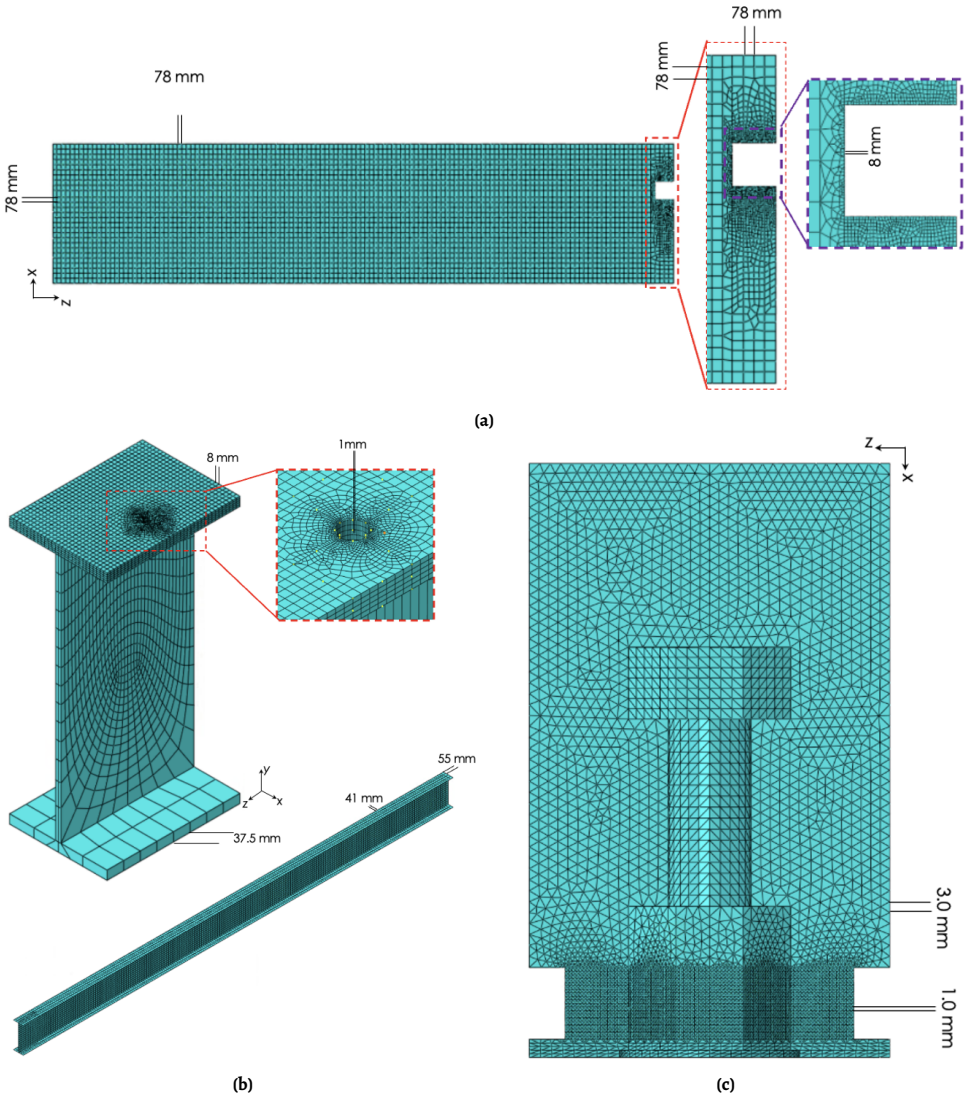

Figure 5.15: Details of mesh: (a) Shell elements of fibre-polymer deck, (b) Shell and solid elements for steel girder, (c) Solid elemeents in a cut-through of SRR injection block.

The iSRR connector is modeled using its precise geometry to reflect the conditions of prefabricated installation. Specifically, the SRR material is extended slightly beyond the bottom surface of the GFRP deck to account for the wavy, undulant pattern of the GFRP's top surface. The washers are positioned to extend beyond the SRR material, ensuring that only the metallic components are included in the preload package in a realistic setting. This configuration results in a gap between the GFRP deck and the steel girder, preventing direct contact under normal conditions. However, under high loading scenarios, the deck may

deflect sufficiently to come into contact with the steel girder. To account for this possibility, a general contact interaction is defined, incorporating normal behavior with a "hard contact" formulation and tangential behavior using a penalty friction formulation with a coefficient of 0.2. The same composite laminate properties and stacking sequence described in Section 1.4 are used. Likewise, the steel material properties follow the definitions provided in Section 5.2.

The second model replicates the lab test set-up, involving a 300 mm by 300 mm GFRP deck section, without the foam, connected to the actual steel stiffeners through an iSRR connector, as shown in Figure 5.16. To represent the complete deck specimen that is aimed to be used in the joint test, symmetry boundary conditions are applied along the end surface of the GFRP deck segment. Loading is applied on the steel end detail, using displacement-controlled conditions. Preloading is again not explicitly modeled; instead, tie constraints are used between washers and the steel plates to achieve comparable effects. To maintain consistency, the same mesh, material characteristics, and interaction properties are applied as in the 3D section of the full-size model. Frictional effects are also included with the same coefficient as in the bridge model to ensure consistent interaction conditions.

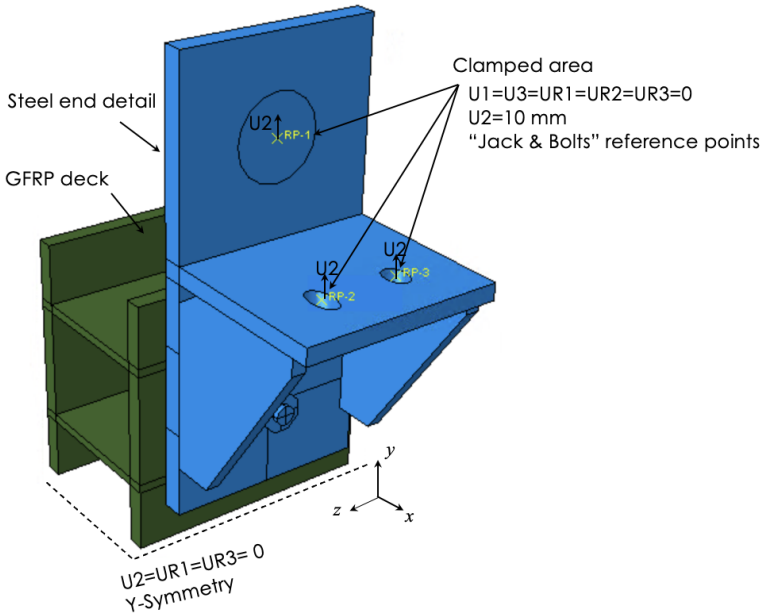

Figure 5.16: Assembly and boundary conditions of the proposed connector level experiment.

The validation process aims to ensure that the stress behavior in the connector-level experimental set-up is representative of real bridge conditions. This is achieved by comparing the maximum principal stresses within the SRR connector in both models in the same manner as it was done in Section 5.2. The use of both detailed 3D geometry and springs within the beam model enables capturing realistic stress distributions under cyclic shear loading, while also minimizing computational effort. By validating the experimental model

results against the bridge beam model, the accuracy and applicability of the small-scale experimental set-up are confirmed, ensuring that the results are both reliable and useful for practical bridge applications.

5.7. Validation of experimental and full-size bridge models

In this validation phase, a load level of 80 kN is adopted, which remains within the linear range of the joint due to the use of an M27 bolt rod. The larger bolt diameter increases the slip resistance of the connector, enabling higher applied loads before any relative displacement occurs between the bolt and the surrounding SRR material, compared to the analysis conducted in Section 5.2. This allows the linear elastic assumption to remain valid while aligning with the load levels applied in the experimental validation campaign.

The deformed shapes at an applied shear force of 80 kN shown in Figure 5.17 reveal significant differences between the SYMMETRIC model and the beam model due to the different boundary conditions and structural constraints applied in each case. In the beam model (Figure 5.17a), the downward deflection of the left side of the GFRP deck's bottom facing occurs due to the combined loading conditions and lack of symmetry constraints on the deck in that direction. Essentially, the beam set-up allows more freedom for downward displacement, especially as the load is transferred from the top through the iSRR connector to the deck and steel girder, resulting in asymmetric deformation of the bottom facing. The loading and the support condition applied along the beam span create a realistic scenario where the bottom facing bends downwards due to distributed load effects, typical of bridge set-ups. Additionally, the cantilever effect on the right side of the deck allows uplift because of rotational moments occurring in response to the overall load distribution.

In the SYMMETRIC model (Figure 5.17b), the left side of the deck is constrained by symmetry, meaning it cannot move sideways or rotate. Thus, the bottom facing on that side remains fixed without any uplift or deflection. This restriction forces the deformation to occur on the right side instead, where the applied load causes the bottom facing to bend upward. In contrast, in a bridge configuration, there are no such symmetry constraints, allowing in Figure 5.17a for more natural deformations on both sides of the deck.

As for the webs, the beam model shows a more pronounced bending of the webs compared to the SYMMETRIC model. This is due to the global hybrid interaction in the hybrid girder comprised of the GFRP deck and steel beam and how the deck interacts with the steel girder underneath. The webs in the beam model experience greater bending moments because through-thickness shear flexibility and "Vierendeel" effects lead to local bending at the web-skin junctions. While these effects suggest that in a bridge set-up, fatigue could be dominated by stresses and deformations in these web-to-skin junctions, the fatigue performance of the deck components is outside the scope of this thesis, which maintains its focus on the behavior of the iSRR connectors. Understanding the role of junctions, however, remains crucial for assessing overall fatigue performance in bridge applications, as highlighted by recent investigations into strain concentrations and damage at web-flange interfaces in pultruded GFRP decks [102, 103].

Analysis presented in Section 5.3 indicated that increased flexibility in the deck segment leads to reduced stresses in the SRR. This trend can be observed in Figure 5.8, where introducing a gap or removing stiffeners results in peak stress reduction. A similar behavior is evident when comparing the SYMMETRIC test set-up with the hybrid beam model.

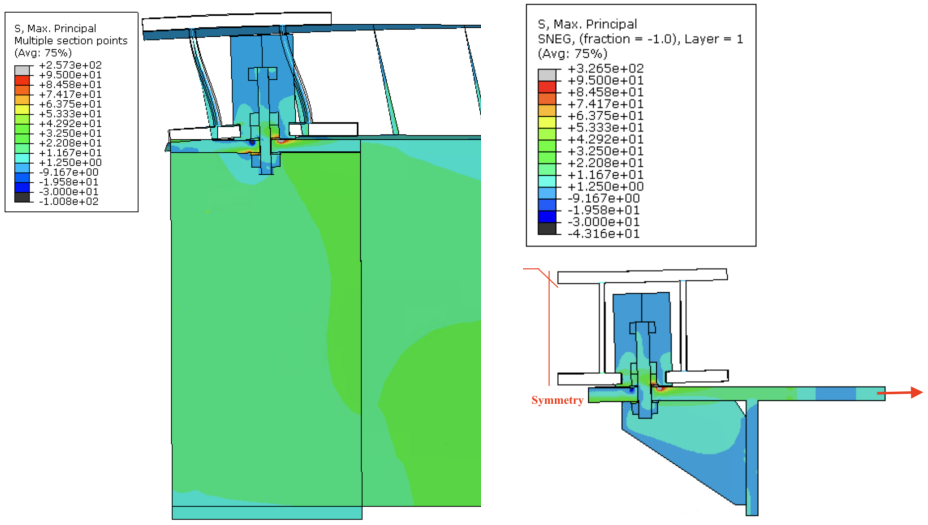

Figure 5.17: Maximum principal stress distribution with 20 times exaggerated deformed shape at 80 kN of shear force - tie constraints among SRR and other parts (red line indicates symmetric boundary conditions and red arrow indicates load application): (a) Beam model, (b) SYMMETRIC model.

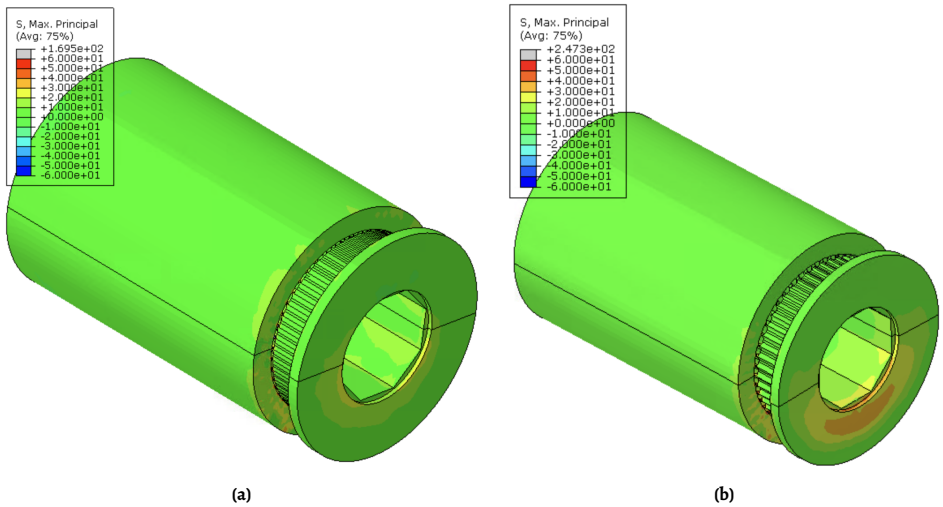

Figure 5.18: Maximum principal stress distribution in the SRR piece under 80 kN of applied shear force: (a) Beam model, (b) SYMMETRIC model (Fixed color scale between –60 MPa and +60 MPa, with stresses outside this range shown in gray).

More specifically, as shown in Figure 5.17, the deck in the hybrid beam model exhibits more flexibility, leading to lower stress concentrations in the SRR. This is further confirmed by the maximum principal stresses depicted in Figure 5.18, where the SYMMETRIC model (Figure 5.18a) reaches a peak of 247 MPa, whereas the beam model (Figure 5.18b) reaches 170 MPa. These results reinforce the conservative nature of the SYMMETRIC configuration, ensuring it represents a higher-stress scenario for fatigue assessment and thus captures critical performance limits of the connector. By this choice, if the SRR component can withstand the stresses generated in the SYMMETRIC set-up, it is likely to perform well in a real bridge scenario.

The SYMMETRIC set-up is chosen to isolate and accelerate the connector failure mechanism while minimizing the influence of the deck deformation on fatigue performance. This set-up allows for easier identification of failure characteristics related to the connector and avoids having to deal with complex damage propagation in the GFRP deck that could detract from the reliability of the iSRR connector's fatigue characterization.

5.8. Conclusions

In this chapter, the design and validation of an experimental test set-up were presented to characterize the fatigue shear behavior of the iSRR connector. The study focused on finding a practical yet representative test configuration that captures realistic bridge-like conditions while being feasible for laboratory testing. Various set-ups were examined to determine the optimal balance between accuracy and practicality. Based on these models, several key conclusions can be drawn:

- Adding stiffeners in the steel end detail and incorporating the gap between the GFRP deck and the steel girders reduced peak stresses in the iSRR connector.
- The SYMMETRIC set-up represents a conservative and efficient method for capturing early-phase fatigue behavior. Maximum principal stresses in the SRR are lower in the connector analyzed as part of a full-size hybrid beam compared to the isolated connector test set-up. This difference arises due to the larger flexibility of the deck in the hybrid beam, which reduces stress concentrations. As a result, the isolated test set-up is considered conservative and applicable for the design of connectors in hybrid beams, ensuring that the performance of the connectors is adequately evaluated under higher stress scenarios.
- The beam test set-up risks fatigue failure at the GFRP deck's web-to-skin junction, limiting its ability to isolate the iSRR connector's performance under high shear loads.
- The SYMMETRIC + GAP + STIFF test set-up was thus identified as the optimal approach for evaluating the fatigue performance of the iSRR connector.

6

Behavior of connectors under cyclic shear loading

This chapter presents the experimental findings on the iSRR connector subjected to shear loading under a range of environmental and loading conditions. In Chapter 5, the appropriate test set-up was established to ensure representative testing. With these considerations in place, the focus now shifts to utilizing this set-up for the experimental evaluation. Initially, the influence of the cyclic load range at a fixed, fully alternating load ratio (R = -1) is examined, as this ratio is assumed to be the most critical for a given load range. The investigation is then extended to different load ratios and environmental conditions. Key findings related to durability, stiffness degradation, and failure mechanisms are analyzed with respect to load range, load ratio, temperature, and moisture conditions. Chapter 6 provides a qualitative perspective on these results, emphasizing stiffness degradation, failure modes, and post-cyclic static performance. In Chapter 7, the same results will be reevaluated quantitatively to establish endurance (F-N) curves and predict fatigue life.

This chapter is structured into eight sections, each addressing different aspects of the experimental investigation. Section 6.1 outlines the test matrix, specimens, and instrumentation. Section 6.2 examines the cyclic behavior of the iSRR connector under fully reversed loading, while Section 6.3 explores the influence of different load ratios. Section 6.4 assesses the effect of elevated temperatures, and Section 6.5 investigates environmental aging. Section 6.6 evaluates the post-cyclic static performance, and Section 6.7 examines the residual fatigue behavior after prior cyclic loading. The findings, summarized in Section 6.8, provide a qualitative analysis of fatigue performance, setting the stage for the quantitative fatigue life assessment in Chapter 7.

6.1. Test matrix, specimens and instrumentation

A total of 18 specimens, comprising 36 connectors, are prepared and tested following the naming convention: X-YY-ZZ-E-D-C. The first letter (X) indicates the type of loading, which

Parts of this chapter have been published in Christoforidou et al.

can either be F or S for cyclic or post-cyclic static tests, respectively. The (YY) segment represents the maximum and minimum load applied during the cyclic test. For fully reversed load cases (R = -1), only a single value is displayed, while for other load ratios, both the maximum and minimum loads are indicated. For example, with an R ratio of 0.5 and a maximum load of 100 kN, the notation used would be 100_50. The letters (ZZ) denote the temperature, which can either be room temperature (RT) or elevated temperature (ET) of 55 °C. The letter (E) refers to the exposure condition: U for unaged specimens, S for submerged in water, and O for outdoor exposure. The digit (D) represents the specimens' number tested with the same parameters (X, YY, ZZ, E). Finally, since there are two connectors in each tested panel, the letter (C) indicates the location of the connector, with T for the top and B for the bottom. The various experimental parameters are presented in Table 6.1.

Table 6.1: Matrix with experimental parameters.

Loading condition	R-ratio	Max load level [kN]	Temperature	Exposure condition	No of Connectors	Section
Cyclic	-1	40	Ambient	Unaged	4	6.2 & 6.6
	-1	60	Ambient	Unaged	4	6.2 & 6.6
	-1	80	Ambient	Unaged	4	6.2 & 6.6
	-1	40	Elevated	Unaged	4	6.4 & 6.6
	-1	60	Elevated	Unaged	4	6.4 & 6.6
	-1	80	Elevated	Unaged	4	6.4 & 6.6
	-1	80	Ambient	Submerged	2	6.5
	-1	80	Ambient	Outdoors	2	6.5
	0.1	80	Ambient	Unaged	2	6.3 & 6.7
	0.1	100	Ambient	Unaged	2	6.3 & 6.7
	0.5	80	Ambient	Unaged	2	6.3 & 6.7
	0.5	100	Ambient	Unaged	2	6.3 & 6.7
Post-cyclic static (Monotonic)			Ambient	Unaged	12	6.6
			Elevated	Unaged	12	6.6

For elevated temperature experiments, the temperature is continuously monitored using temperature sensors and thermocouples for the chamber and the connectors, respectively. The tip of the temperature sensors is located close to the bolt region adjacent to the steel stiffener. In nine of the specimens (three pertaining to room temperature and six to elevated temperatures at 55 °C), two thermocouples are installed inside the SRR piece, with one thermocouple near the rod and the other near the foam, as shown in Figure 6.1. The purpose of using the thermocouples is to track the temperature rise for the specimens tested inside the temperature chamber. They are also utilized in three specimens tested under unaged ambient conditions at three distinct maximum loads with an R ratio of -1 to monitor the temperature increase due to cyclic loading. In four of the joints, the temperatures are tracked during the resin curing process to understand the resin's reactivity and monitor its gel time, i.e., when the temperature of the resin increases from 25 °C to 35 °C. The gel point of the resin is particularly important in this application since, after this point, the resin crystallizes, and no further injection can be performed.

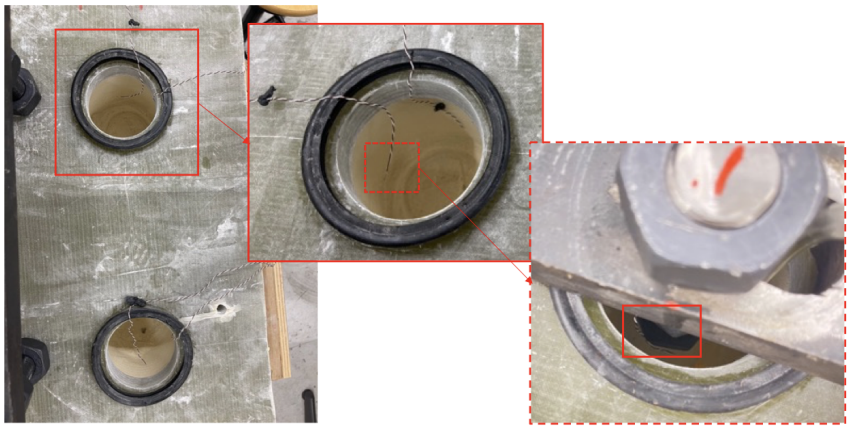

Figure 6.1: Location of thermocouples; next to bolt's head (nut) and in foam.

For the cyclic experiments, four LVDTs are placed to measure the additional displacement range increase of each connector, as shown in Figure 6.2. The placement of these LVDTs ensures accurate tracking of relative slip displacements, which remain relatively small (up to 1-2 mm) throughout the cyclic tests. Since heating the chamber and maintaining the elevated temperature has no appreciable effect on the LVDTs' performance, they are used consistently across all cyclic tests.

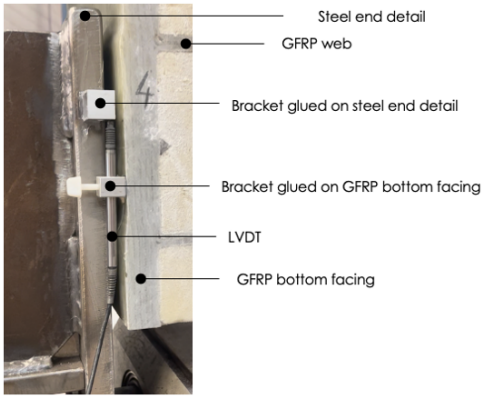

Figure 6.2: Instrumentation of specimens for measuring GFRP-steel relative slip displacement.

The specimens are installed, then the bolts are preloaded and finally the instrumentation is applied. A torque level of 900 Nm is applied for experiments tested at the low and medium load levels, while a torque of 1350 Nm is employed for the highest load level. Since all the specimens were stored in laboratory conditions, the cyclic tests at ambient temperature commence immediately once the bolts are preloaded. For the elevated temperature tests, insulation plates are then placed around the specimen, and the chamber is sealed. The interior temperature is increased to the target value at a rate of 0.1 °C/min. Once the target

temperature is achieved, it is precisely maintained within a 0.2 °C variance throughout the duration of both cyclic and static tests. To ensure uniform and stable temperature conditions within the connectors, the specimens are held at the elevated temperature for a 24-hour period before commencing the cyclic tests. Subsequently, the cyclic test proceeds until reaching a predefined number of cycles, as detailed in Section 6.2.

6.2. Cyclic behavior under fully reversed load ratio and various load ranges

Cyclic loading is applied to the specimens at three designated load range levels: low, medium, and high. These levels are defined by maximum loads of 40, 60, and 80 kN, respectively. The selection of these load levels stems from preliminary structural analyses of steel girders connected with fibre-polymer composite decks [5]. In these analyses, a load range of 62 kN is identified as the upper limit for the maximum cyclic forces exerted on connectors situated at the deck's edge.

A fully reversed load ratio (R = -1) is utilized based on its anticipated contribution to the most significant degradation rate, as indicated by Olivier et al. [21]. The cyclic load frequency is set at 4 Hz, consistent across all applied load levels. During various fatigue experiments, the temperature within the SRR piece during testing is closely monitored, ensuring that the maximum increase remains below the 10 °C limit as specified in [21].

Throughout the cyclic tests, the range (max-to-min) of the connector's shear displacement is recorded while maintaining a constant load range. The connector displacement is defined as the local differential displacement of the steel plate and the composite bottom facing close to the connector. For the sake of maintaining structurally and functionally reliable performance of hybrid bridge structures under cyclic loading, a serviceability failure criterion under long-term loading is considered in this study. The force versus number of cycles (F-N) curves are defined not as an actual failure but as an increase of the displacement range due to cyclic loading. In case of slip-resistant connectors, a slip range increase of 0.3 mm has been frequently adopted as a failure criterion [20]. This threshold is based on the assumption that connectors with a slip range increase beyond 0.3 mm may no longer provide the desired level of resistance against slip under long-term loading, potentially compromising the structural integrity and performance of the overall system.

For practical reasons and based on observations from early testing phases, the test durations are tailored to optimize data collection while ensuring efficiency. At ±60 kN load level and 25 °C, reaching the 0.3 mm displacement range increase criterion around 1.5 million cycles set a baseline for consistent termination across subsequent tests. In contrast, at ±40 kN level, where no significant displacement range trend is observed up to 1.5 million cycles, the tests are extended to 2.5 million cycles. This allowed for a more comprehensive data set, providing valuable insights into the post-cyclic behavior of the connectors. A similar approach is adopted for the connectors tested at a higher temperature. Table 6.2 presents a detailed summary of the adopted termination criteria for the cyclic experiments, which takes into account all specific load levels.

Figures 6.3a, 6.3b, 6.3c present the displacement range increase curves with standard linear axes for the ±40 kN, ±60 kN and ±80 kN load levels, respectively. For improved clarity in the early-cycle response and to highlight trends over several orders of magnitude, the

Table 6.2: Termination criteria at room temperature (25 °C).

Cyclic loading	Stop criterion
±40 kN	Cycles exceeding 2.50E+06
±60 kN	Cycles exceeding 1.50E+06
±80 kN	Displacement range increase of 0.3 mm

same data is also shown with a logarithmic x-axis in Figures 6.4a, 6.4b and 6.4c. Among all tested connectors, four reach the 0.3 mm displacement range threshold, while the others are halted at specific cycle counts.

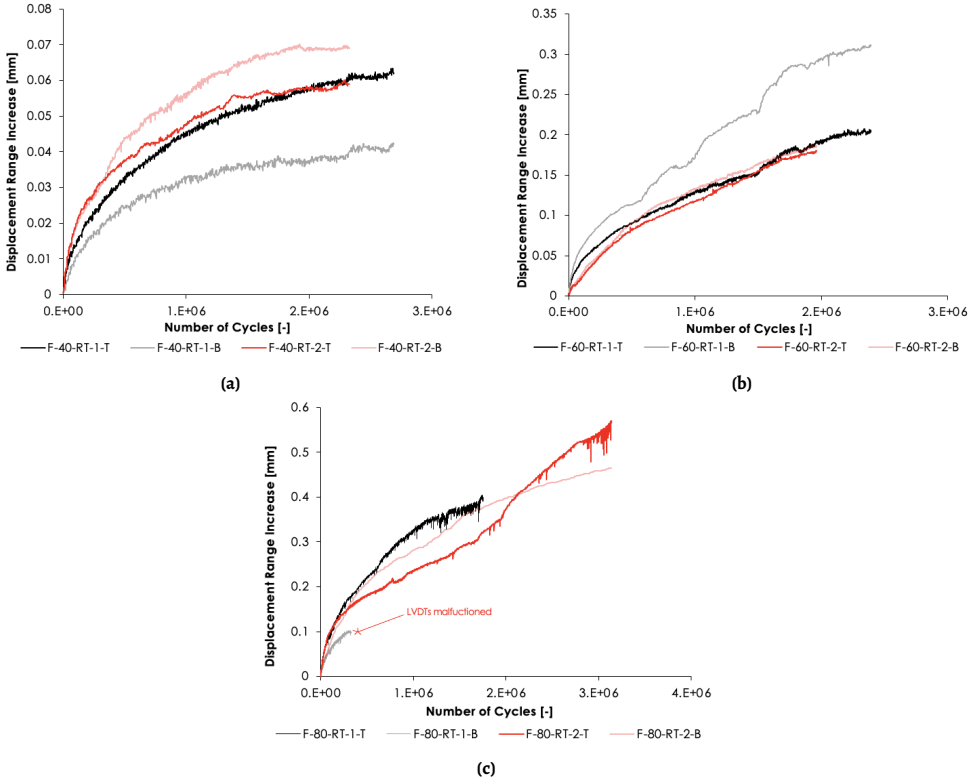

Figure 6.3: Recorded connectors' displacement range increase under room temperature: (a) ±40 kN, (b) ±60 kN, (c) ±80 kN.

Despite all connectors being produced and tested using the same methodology, some variations between individual responses are evident. This variability is inherent to fatigue testing, where achieving identical results is practically impossible. Such differences underscore the importance of conducting multiple tests to capture the range of possible behaviors and ensure a comprehensive understanding of the connectors' performance under practical conditions.

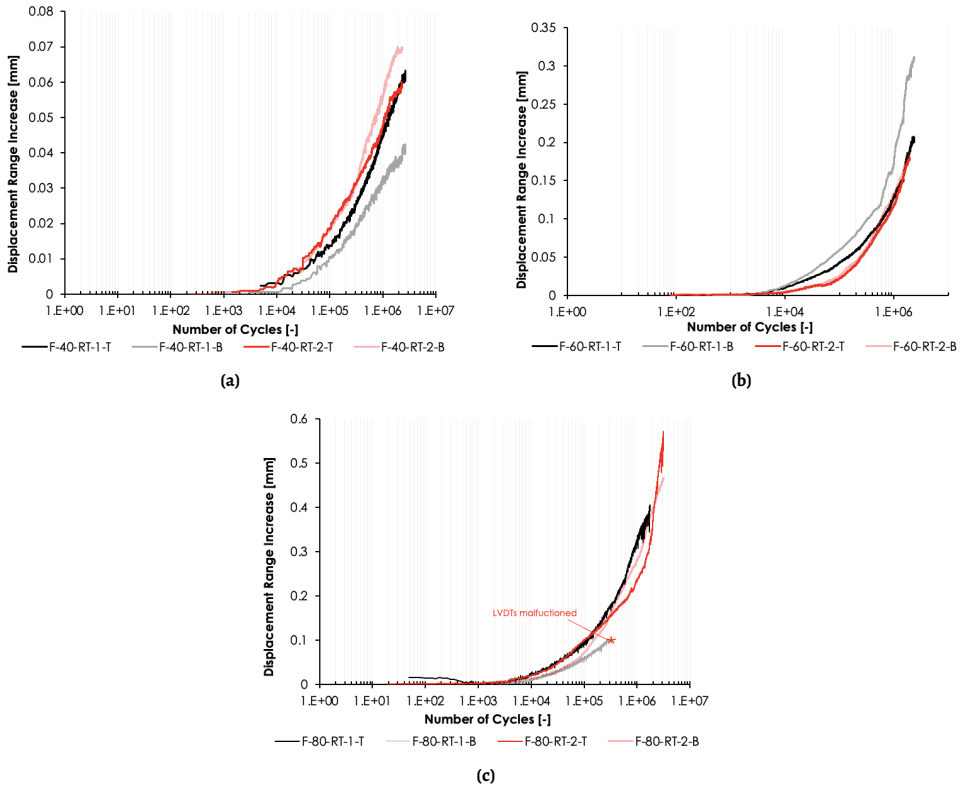

Figure 6.4: Recorded connectors' displacement range increase with number of cycles in logarithmic scale under room temperature: (a) ±40 kN, (b) ±60 kN, (c) ±80 kN.

Specifically, for the medium load level (±60 kN), it is observed that the stiffness degradation exhibits the most significant discrepancies among the tested connectors, with greater variations compared to both the ±40 kN and ±80 kN load levels. This variability could be attributed to the transitional stress state at medium loads, where the interplay between elastic and inelastic behaviors leads to less predictable fatigue responses. A more pronounced interplay between damage and plasticity could be taking place (see Section 4.2 for the dual non-linear nature of the material's fatigue response). Additionally, fatigue sensitivity at intermediate stress levels, coupled with minor specimen imperfections and temperature effects, may contribute to the observed differences.

6.3. Cyclic behavior under different load ratios

The variation of the load ratio (R value) and the maximum load is presented in Table 6.3, along with the stop criterion used. The stop criterion is again established to keep the testing time within the feasible frame of the research project. This criterion, defined in terms of the number of cycles, is introduced based on experience from tests with R = -1 (see Section 6.2). The assumption is that stiffness degradation with R ratios of 0.1 and 0.5 is less detrimental

due to the smaller total force range, therefore not leading to failure. Nevertheless, the rate of stiffness degradation is observed and compared to the results obtained with R = -1.

Table 6.3: Termination criteria for assessing the influence of different load ratios.

R ratio	Maximum load	Stop criterion	No. of connectors
0.1	80	1.50E+06 cycles[1]	2
0.1	100	1.50E+06 cycles[1]	2
0.5	80	1.50E+06 cycles[2]	2
0.5	100	1.50E+06 cycles[2]	2

[1] Tested under monotonic loading after cyclic tests (post-cyclic static loading).
[2] Tested under ±80 kN cyclic loading to failure after initial cyclic tests.

Results of displacement range increase for tests conducted at different load ratios R are presented in Figure 6.5. The inclusion of both linear, in Figure 6.5a, and logarithmic scale axes, in Figure 6.5b, is intended to help the reader clearly see and interpret these differences. The graphs compare the cyclic tests conducted at fully reversed loading $R = -1$, with tests at lower load ranges for $R = 0.1$ and $R = 0.5$. It is evident that the displacement range increase for $R = 0.5$ and $R = 0.1$ tests is significantly lower than for the alternating load ratio $R = -1$. This suggests that the load ratio strongly influences fatigue damage, with non-alternating load ratios $R = 0.1$ and $R = 0.5$ showing much less stiffness degradation. Furthermore, these results highlight that it is not the maximum load alone but rather the load range that governs the damage rate and, consequently, the fatigue life of the connectors.

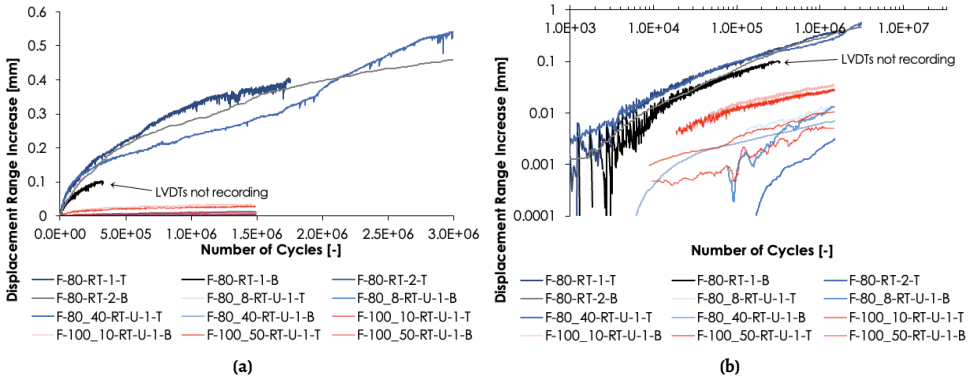

Figure 6.5: Displacement range increase of different R ratios at two different maximum load levels: (a) Linear scale axes, (b) Logarithmic scale axes.

Furthermore, Figure 6.6 presents test results with different maximum loads and load ratios but comparable load ranges. The figure includes results of cyclic tests at minimum-to-maximum loads of 10 to 100 kN, 8 to 80 kN, and -40 to +40 kN, corresponding to load ranges of 90 kN, 72 kN, and 80 kN, respectively. The displacement range increase is of comparable magnitude for the three cases, with the alternating load case exhibiting the most significant degradation. This observation partially supports the initial hypothesis that the alternating load (R = -1) is the most detrimental when considered for a given load range.

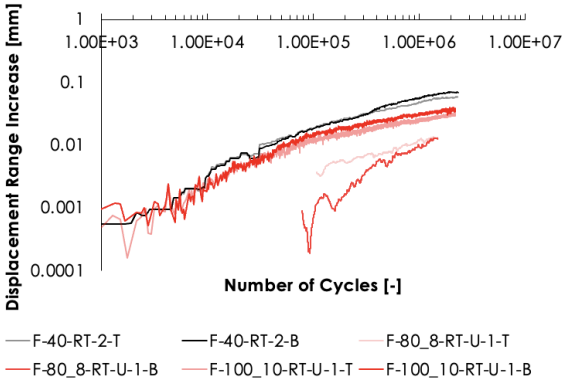

Figure 6.6: Displacement range increase of different R ratio with comparable load ratios.

6.4. Cyclic behavior under different temperatures

At elevated temperatures, a similar methodology is applied as in the room temperature experiments. However, the use of a temperature chamber is necessary, and distinct stop criteria are defined. For tests conducted at a ±80 kN load level and at 55 °C, reaching the 0.3 mm displacement range increase criterion serves as the baseline for termination. At ±60 and ±40 kN load level, where no significant displacement range trend is observed, the tests are extended to 1.0 and 2.0 million cycles, respectively, to ensure a more comprehensive dataset. The termination criteria for cyclic tests at elevated temperatures are presented in Table 6.4.

Table 6.4: Termination criteria for assessing influence of elevated temperature (55 °C).

Cyclic loading	Stop criterion
±40 kN	Cycles exceeding 2.00E+06
±60 kN	Cycles exceeding 1.00E+06
±80 kN	Displacement range increase of 0.3 mm

The comparison of the fatigue performance of the connectors tested at room and elevated temperature is approached by examining the relative stiffness. This metric is determined by dividing the load range per cycle by the respective slip range between the composite deck and the steel end detail. For comparability, stiffness values at each cycle are normalized to the initial stiffness from the first cycle, as shown in Figure 6.7.

Stiffness degradation occurs at different rates depending on the applied load at 25 °C. At ±40 kN (Figure 6.7a), stiffness degradation begins around 1.00E+04 cycles, while at ±60 kN (Figure 6.7b), the onset of degradation is earlier, at approximately 3.50E+03 cycles, and for ±80 kN (Figure 6.7c), it begins as early as 2.64E+03 cycles, as indicated by the black, vertical, dashed lines. This trend indicates that higher loads result in an earlier onset of fatigue damage, suggesting that the connectors are more sensitive to increased loading, which accelerates the degradation process.

The influence of temperature is further analyzed by comparing the results at 25 °C and 55 °C. At elevated temperatures, the onset of stiffness degradation occurs notably sooner for all load levels: around 4.40E+03 cycles for ±40 kN, 0.88E+03 cycles for ±60 kN, and 0.48E+03 cycles for ±80 kN. Additionally, the stiffness curves at 55 °C consistently lie below those at 25 °C throughout the testing period, highlighting the effect of temperature on the stiffness degradation. This demonstrates the adverse impact of elevated temperatures on the fatigue performance of the connectors, with a more pronounced effect at higher load levels.

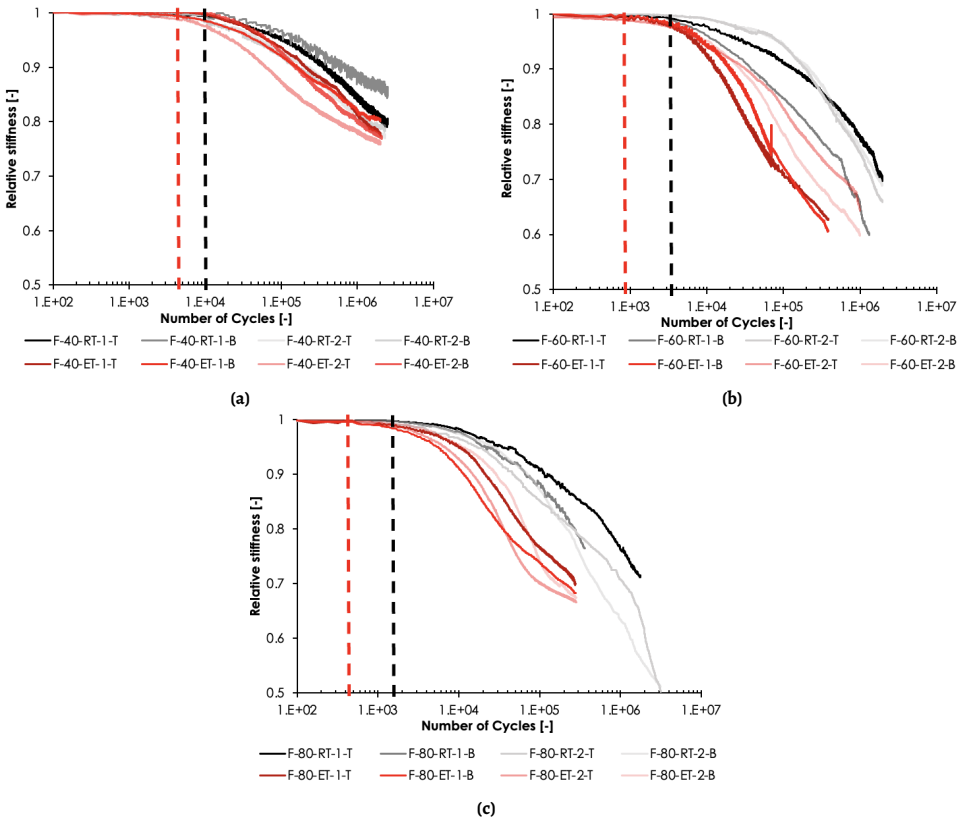

Figure 6.7: Relative stiffness of iSRR connector at different cyclic load levels at room and elevated temperature: (a) ±40 kN, (b) ±60 kN, (c) ±80 kN.

6.5. Cyclic behavior under the influence of moisture and water

The fatigue performance of the iSRR connector is evaluated following one year of environmental exposure to assess the effects of prolonged outdoor and submerged conditions. Four connectors are subjected to different environmental scenarios: two submerged in water and two exposed to outdoor conditions, each for a year, as shown in Figure 6.8. After this exposure, the connectors are tested under cyclic loading with a maximum alternating load

of ±80 kN, identified as the most detrimental condition for fatigue performance based on prior investigations. To assess the impact of environmental exposure, these results are compared with the reference case of four connectors tested at room temperature, subjected to identical force ranges. The testing matrix summarizing the conditions and corresponding stop criteria is presented in Table 6.5.

Table 6.5: Termination criteria for assessing the influence of environmental exposure.

Aging	Stop criterion	No. of connectors
No exposure	Displacement range increase of 0.3 mm[1]	4
Outdoors	Failure	2
Submerged	Failure	2

[1] Tested under monotonic loading after cyclic tests (post-cyclic static loading).

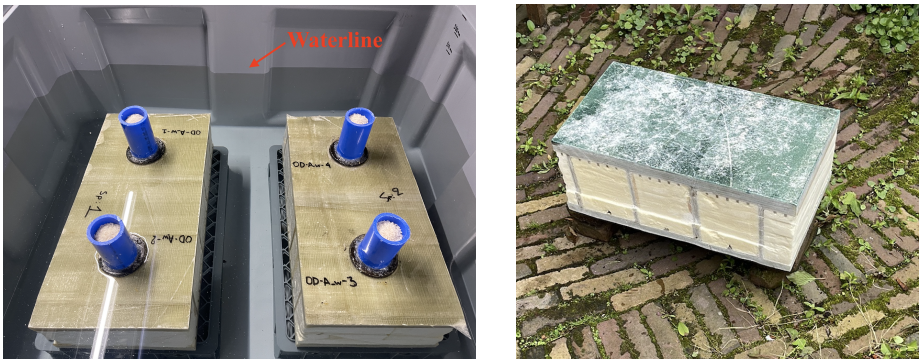

(a) (b)

Figure 6.8: iSRR connectors subjected to environmental exposure: (a) Water submerged connectors, (b) Outdoors exposure.

The relative stiffness of iSRR connectors subjected to different environmental conditions over their fatigue life is presented in Figure 6.9. The submerged connectors (red lines) exhibit rapid and pronounced stiffness degradation, reaching failure considerably earlier than both the outdoor-aged connectors and the reference specimens. This early failure suggests a critical vulnerability to submerged water exposure, likely due to mechanisms such as the swelling of the resin matrix, corrosion of the embedded steel shot, or weakening of the bond between the SRR piece and the composite component.

The connectors exposed to outdoor conditions, as shown in Figure 6.9 with blue lines, demonstrate a relative stiffness degradation profile similar to that of the reference connectors (black and grey lines) until late in the test, suggesting that typical outdoor conditions have a less significant impact on the fatigue performance compared to direct submersion.

The failure mode of the submerged connectors is characterized by debonding between the SRR piece and the GFRP facing, along with the crushing of SRR material beneath the embedded nuts, as depicted in Figures 6.10a and 6.10b for the top and bottom connector, respectively.

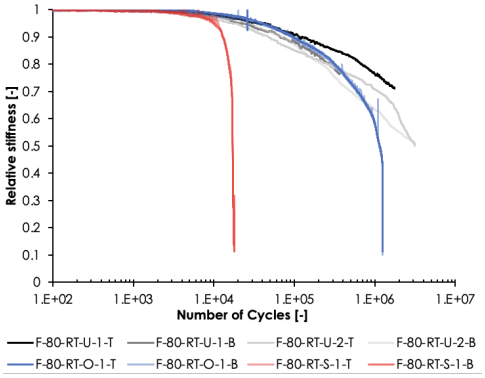

Figure 6.9: Relative stiffness of iSRR connector under different environmental exposures.



(a) (b)

Figure 6.10: Failure mode of iSRR connector under cyclic loading after water submersion: (a) F-80-RT-S-1-T, (b) F-80-RT-S-1-B.

The failure mode for the outdoor-aged connectors, similar to that of the submerged connectors, involves debonding between the SRR piece and the GFRP facing, as well as crushing of the SRR material beneath the embedded nuts. However, the extent and timing of this damage are less severe and occur much later compared to the submerged connectors, which implies that outdoor exposure does not exert the same level of deterioration on the connectors' internal bonding as direct water immersion.

Figure 6.11 shows the condition of the composite deck with iSRR connectors after one year of submersion in water. The black lines indicate the visible extent of water ingress into the composite material. Water absorption, likely affecting the interface between the SRR and the GFRP facing, potentially contributes to the observed failure modes under subsequent loading.



(a) (b)

Figure 6.11: Condition of the composite deck with iSRR connectors after one year of submersion in water: (a) Front view, (b) Behind view.

6.6. Remaining stiffness and static resistance

Once the cyclic test meets the stop criterion, the majority of the joint specimens are prepared for loading until failure under displacement-controlled monotonic loading at a constant rate of 0.01 mm/sec. The independent connector slip behavior of the two connectors in one specimen is determined by placing a pair of LVDTs on both sides of each connector, as shown in Figure 6.2. Due to the 10 mm displacement limit of the LVDTs, once the displacement capacity is reached in post-cyclic static tests, the LVDTs are readjusted, and the test resumes. The tests are executed immediately upon the completion of the cyclic test, thereby obviating the necessity for supplementary preloading. Some tests are manually terminated when at least 6 mm of relative displacement is exceeded due to lack of further displacement of the hydraulic jack.

The capability of the connectors subjected to extensive cyclic loading to still resist the Ultimate Limit State (ULS) requirements is assessed by testing them monotonically until the ultimate load at failure is reached. This approach aligns with findings by Olivier et al. [21], who reported that iSRR connectors exposed to long-term loading prior to static tests exhibited similar ultimate forces and displacement at failure relative to reference specimens subjected exclusively to static loading.

Representative force displacement curves are presented in Figure 6.12. The displacement on the X-axis represents the relative slip between the steel flange and the bottom composite facing calculated based on average measurements from both sides of the connector. Connectors that experienced failure are depicted with continuous lines, while non-failed specimens are indicated by dashed patterns. Both static tests at room and elevated temperatures are conducted once the failure or stop criteria were met during cyclic loading.

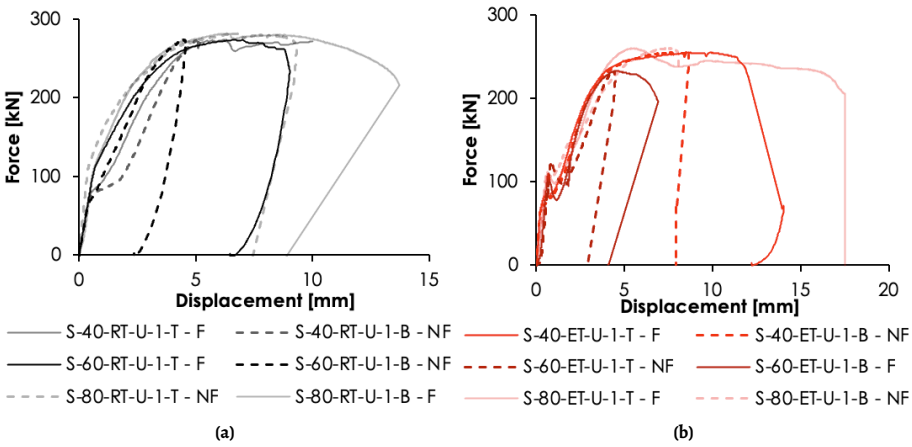

Figure 6.12: Force displacement curves of iSRR connectors under post-cyclic static loading: (a) At room temperature, (b) At elevated temperature.

The iSRR connector exhibits a two-phase linear response, initially showing a steady increase in load until their slip resistance is surpassed, followed by a secondary linear trend leading up to the maximum resistance. At room temperature, the connector reaches their peak load at an average slip of 6 mm, whereas at elevated temperatures, this is reduced to approximately 5 mm. In both cases, the peak load of most failing connectors is followed by significant ductility, with deformation capacities reaching 10-15 mm before failure. Predominantly, the nut embedded closest to the steel stiffener detaches from the SRR piece, allowing the bolt to shift several millimeters in the direction of the applied load, as illustrated in Figure 6.13c. Every test consistently exhibits bolt bending, with most cases resulting in bolt shear failure, as shown in Figure 6.13 (a, e, f). In extreme cases where exceptionally high slip at failure is observed (e.g., more than 16 mm), local crushing of the composite laminate and indications of delamination become evident, as shown in Figure 6.13d. However, these failure modes are absent in cases where failure occurs at lower slip levels. The simultaneous activation of these various dissipation mechanisms ensures significant ductility at failure, with ultimate displacements exceeding 6 mm for all connectors.

Table 6.6 and Table 6.7 summarize the static test results, highlighting initial stiffness ($k_{sc,in}$), slip resistance (F_s), ultimate load (F_{ult}) and slip at failure between the steel plate and the bottom facing of the GFRP composite deck (δ_{ult}). Variability in slip force can be primarily attributed to different torque levels during preloading. Specifically, connectors with a preload torque of 900 Nm resulted in an average slip resistance of 87.0±12.4 kN, while a torque of 1350 Nm increase the slip force to 111.1±5.7 kN. The connectors display low variation of the ultimate resistance, with coefficient of variation being 6% for both testing temperatures. Connectors tested under room temperature demonstrate a marginally higher average ultimate shear resistance compared to those tested at elevated temperature.



Figure 6.13: Damages of composite deck and SRR piece with or without bolt shear failure of iSRR connectors: (a) S-40-RT-U-2-B, (b) S-60-ET-U-1-B, (c) S-40-ET-U-1-B, (d) S-40-RT-U-2-T, (e) S-60-ET-U-1-T, (f) S-60-ET-U-2-T.

Table 6.6: Post-cyclic static results from connector experiments under room temperature.

Connectors' ID	F_s [kN]	F_{ult} [kN]	$\delta_{ult.fail}$ [mm]	$k_{sc,in}$ [kN/mm]
S-40-RT-U-1-T	84.5	273.5	5.22*	183.0
S-40-RT-U-1-B	79.3		9.99*	183.3
S-40-RT-U-2-T	70.5	241.2	18.13	346.0
S-40-RT-U-2-B	79.3		6.01*	324.8
S-60-RT-U-1-T	112.7	273.5	9.02	163.1
S-60-RT-U-1-B	75.2		4.57*	163.8
S-60-RT-U-2-T	77.9	282.1	5.39*	265.7
S-60-RT-U-2-B	96.4		5.71*	240.0
S-80-RT-U-1-T	106.9	281.4	13.71	178.6
S-80-RT-U-1-B	110.4		9.31*	245.4
Average (COV)	-	270.4 (6.2%)	-	229.4 (29.0%)

* Non failed connector

Table 6.7: Post-cyclic static results from connector experiments under elevated temperature.

Connectors' ID	F_s [kN]	F_{ult} [kN]	$\delta_{ult.fail}$ [mm]	$k_{sc,in}$ [kN/mm]
S-40-ET-U-1-T	84.8	254.9	9.3*	325.2
S-40-ET-U-1-B	77.2		14.0	305.4
S-40-ET-U-2-T	78.2	267.7	16.8	257.6
S-40-ET-U-2-B	81.9		7.0*	254.1
S-60-ET-U-1-T	109.7	232.9	6.9	231.3
S-60-ET-U-1-B	93.7		4.4*	224.5
S-60-ET-U-2-T	98.5	240.4	15.4	264.2
S-60-ET-U-2-B	92.5		5.4*	244.0
S-80-ET-U-1-T	104.7	259.8	8.1*	170.4
S-80-ET-U-1-B	108.6		12.1	187.7
S-80-ET-U-2-T	118.0	273.4	6.0*	179.9
S-80-ET-U-2-B	118.2		17.6	199.3
Average (COV)	-	254.9 (6.1%)	-	236.9 (20.4%)

* Non failed connector

Notably, there is a pronounced variation in the $k_{sc,in}$ among the samples. This variability is largely attributed to the influences of the prior cyclic tests. To better comprehend the interplay between the cyclic tests and their impact on the resulting stiffness values, Figure 6.14 is shown. This representation correlates the maximum displacement range increase, derived from the fatigue experiments, with the initial stiffness acquired during the monotonic loading. A visible interdependence emerges between these variables, as an increased displacement range accumulation corresponds to a reduction in initial stiffness. However, the trend suggests a stabilization of the retaining connector stiffness at higher displacement range increases, indicating a possible saturation effect in fatigue damage. Even the lowest retaining stiffness values appear sufficient to maintain the hybrid interaction between the deck and the steel girder, as supported by works available in literature [5, 100]. To depict this relationship, a 2nd order polynomial fitting function is chosen due to its highest R^2 value, consolidating data from both temperature tests.

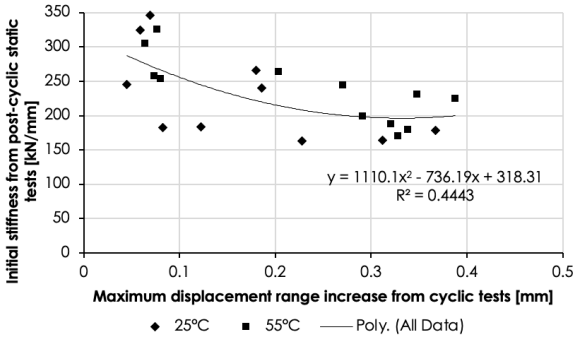

Figure 6.14: Correlation between initial stiffness of iSRR connector with the maximum displacement range increase from cyclic loading tests.

6.7. Residual fatigue behavior with fully reversed cyclic loading

The connectors tested at $R = 0.5$ exhibit minimal stiffness degradation, with an increase in displacement range limited to approximately 0.05 mm after several million loading cycles. This suggests that the connectors retain significant residual strength, prompting further tests to assess their capacity under more detrimental fatigue conditions. Following the completion of cyclic tests at a load ratio of $R = 0.5$, four iSRR connectors are evaluated for their remaining cyclic resistance under a fully reversed load ratio of $R = -1$.

The subsequent tests are conducted at a maximum load of ±80 kN with a load ratio of $R = -1$ which represents the most damaging fatigue scenario, to evaluate the ultimate failure behavior of the previously cycled connectors. Specimens, which are initially subjected to different loading conditions, from +40 to +80 kN and +50 to +100 kN, respectively are included in this investigation. These tests aim to verify whether the connectors, initially subjected to minimal damage under $R = 0.5$, exhibit similar failure modes and stiffness degradation when compared to the virgin specimens tested at $R = -1$.

The results are presented in Figure 6.15, which illustrates the stiffness degradation curves of the connectors tested under $R = -1$, alongside the reference connectors previously tested under $R = -1$ without prior cycling at $R = 0.5$. Notably, the stiffness degradation trends of the re-tested connectors align closely with those of the reference specimens, suggesting that the residual strength of the connectors is substantial even after extended cycling at $R = 0.5$. However, a key difference emerges in the final stage of testing, where the re-tested specimens exhibit actual failure at a displacement threshold, whereas the virgin specimens display a more gradual stiffness degradation. This shift in behavior between the virgin and re-tested specimens occurs beyond the adopted "apparent" failure criterion of an additional displacement range increase of 0.3 mm, highlighting that despite initial similarities in stiffness trends, the re-tested specimens eventually reach a distinct failure mode.

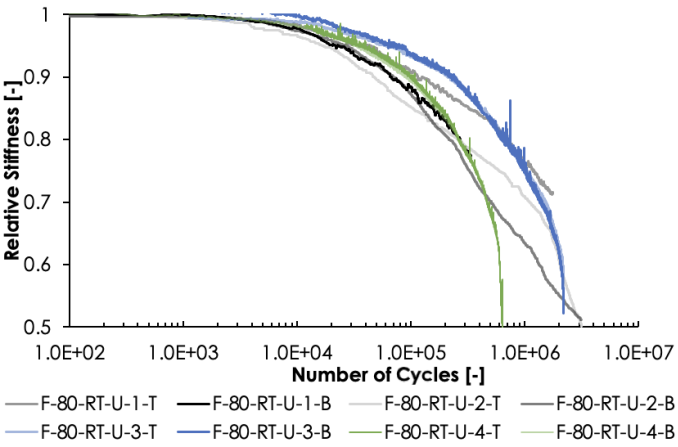

Figure 6.15: Relative stiffness of iSRR connector at fully reversed cyclic load of maximum 80 kN.

The re-tested specimens fail approximately after 2.0E+06 after reaching 0.95 mm of additional displacement range increase. In terms of failure mode, debonding between the SRR piece and the GFRP facing, along with crushing of the SRR material beneath the

embedded nuts is observed, as shown in Figure 6.16. These results offer insight into the connectors' durability under varying fatigue conditions, demonstrating their ability to endure substantial cycling without major degradation when initially tested at less severe load ratios.



Figure 6.16: Failure mode of re-tested iSRR connector subjected to fully reversed cyclic loading.

6.8. Conclusions

This chapter investigates the fatigue performance of iSRR connector embedded in a glass fibre composite deck. The study was carried out under a variety of conditions, including fully reversed cyclic loading (R = -1) with three maximum load levels: low, medium, and high, equivalent to 40, 60, and 80 kN respectively. Tests were also conducted at different load ratios (R = 0.1, and 0.5) to examine the effect of load ratio on fatigue performance. Comparisons were made between tests at room temperature and elevated temperatures (55 °C) in terms of relative stiffness degradation graphs. Additionally, the effects of environmental exposures, including submersion and outdoor aging, on the fatigue performance were evaluated. Post-cyclic static loading was applied to determine the residual ultimate resistance of the iSRR connector for hybrid steel-composite structures. From this, the following concluding remarks can be drawn:

- The stiffness degradation of connectors is found to be highly dependent on the applied load level and temperature. Higher load levels and elevated temperatures accelerated the degradation process, with the medium load level (±60 kN) showing the highest variability among tested connectors, possibly due to the transitional stress state between elastic and inelastic behaviors.

- The tests conducted at different load ratios (R-values) reveal that the load ratio significantly impacts the fatigue performance of the connectors. The connectors subjected to R = 0.5 exhibited the least detrimental fatigue behavior, indicating that positive load ratios do not compromise the fatigue resistance. Finally, it is found that the load range governs fatigue damage more than the maximum load.

- Environmental exposure significantly affects fatigue performance. Connectors submerged in water exhibit rapid and pronounced stiffness degradation compared to those exposed to outdoor conditions or reference specimens, suggesting that direct water exposure critically weakens the bond between SRR and GFRP facing.
- Regardless of the temperature and the extent of damage from cyclic loading, the resistance of the iSRR connectors varied only by about 6% around an average resistance value of 260 kN, indicating high resistance for such connectors in structural applications.
- Post-cyclic static experiments yielded two distinct slip resistances with mean values of 87 kN and 111 kN corresponding to preload torques of 900 Nm and 1350 Nm, respectively. No reduction in preload or slip resistance was observed related to cyclic loading nor related to elevated temperatures, demonstrating that the iSRR connector retains its structural integrity and does not weaken under thermal stresses.
- Residual fatigue tests on connectors initially tested under a less severe load ratio ($R = 0.5$) showed that these connectors retained substantial residual strength when subsequently tested under fully reversed loading ($R = -1$). The failure modes remained consistent, indicating that the connectors can withstand considerable fatigue without significant degradation.

The iSRR connector proved to be a resilient solution for applications demanding consistent performance for serviceability limit state, ultimate limit state checks, ductility requirements and even in thermally challenging environments. Consequently, this study demonstrates the significant potential of iSRR joints in fatigue-dominated structures, such as composite-to-steel hybrid bridges.

7

Fatigue life of connectors loaded in shear

This chapter presents the development of a fatigue life model for iSRR connectors subjected to shear loading. As discussed in Chapter 6, a 0.3 mm displacement range increase during cyclic loading could not be achieved through direct testing for connectors embedded in fibre-polymer composite deck panels under a spectrum of load levels and ratios with an exception of only ±80 kN load levels satisfying the condition. As a result, testing was carried out only up to a reasonable number of loading cycles, precluding the construction of a conventional F-N curve. To address this, the failure criterion is estimated by extrapolating in double logarithmic scale the cyclic test results toward the number of cycles where the 0.3 mm displacement range increase limit would be reached. F-N curves for room and elevated temperatures are provided, along with a comparison of the fatigue life of connectors at different R ratios and after aging, offering critical and design relevant insights into the long-term performance of the connectors.

Chapter 7 is structured into seven sections. Section 7.1 introduces the two extrapolation methods used to estimate the fatigue life of the connectors. Section 7.2 examines the influence of load levels on fatigue performance, followed by Section 7.3, which explores the effect of varying the R ratio. Section 7.4 presents an analysis of the impact of increased temperature, while Section 7.5 discusses the fatigue performance of the connectors under different aging conditions. Section 7.6 provides a discussion on the reliability and conservatism of the prediction methods, evaluating the credibility of each approach. The chapter concludes with a summary of the key findings in Section 7.7.

7.1. Extrapolation methods for F-N curve prediction

In this section, two distinct methodologies for estimating the number of cycles required to reach the 0.3 mm displacement range increase threshold are presented. The first approach utilizes linear regression analysis in a log-log scale applied to the complete dataset

Parts of this chapter have been published in Christoforidou et al. [104].

of displacement range increases. The second approach, also known as the elbow method, segments the data into distinct groups, each characterized by its own trendline, followed by separate linear regression analyses for each segment. Both methodologies are described in detail in what follows.

The first methodology, linear regression analysis, is employed to estimate the cycle count necessary to reach the 0.3 mm displacement range increase threshold by selectively analyzing a subset of the displacement range increase data. The selection of data points is a critical step, designed to ensure a satisfactory coefficient of determination (R^2). In the present study, a threshold of 0.97 for the coefficient of determination is chosen, assuming that this high R^2 leads to a robust and statistically significant fit. Specifically, data points contributing to significant deviations, especially those in the later stages of the dataset, are excluded to enhance the reliability of the model. Excluding the sub-set of data attributed to late cycles always leads to conservative results in this study because the second stage of cyclic behavior shows a lower stiffness degradation rate.

The analysis proceeds by plotting the refined dataset on a log-log scale, followed by the fitting of a trendline. This fitted model is then used for extrapolation to estimate the number of cycles required to reach the displacement range increase limit. Such a methodical selection and analysis of data points strike a balance between the precision of the trendline fitting and the representativeness of the dataset. The ultimate aim is to construct a model that reliably predicts the cycle count while maintaining the integrity and statistical significance of the data analysis.

For instance, an examination of two connectors tested on the same specimen under ±40 kN load cycles until 2.5E+06 cycles revealed maximum range increases of 0.04 and 0.06 mm, as illustrated in Figure 7.1a. When this data is plotted on logarithmic axes, a power law trendline can be fitted to estimate the number of load cycles that would result in a maximum slip limit of 0.3 mm assuming that the mechanism(s) for damage initiation and propagation do not change with time. Figure 7.1b indicates by the dashed trendline extensions that this threshold is projected to be reached after 70 to 200E+06 cycles for the top and bottom connectors, respectively.

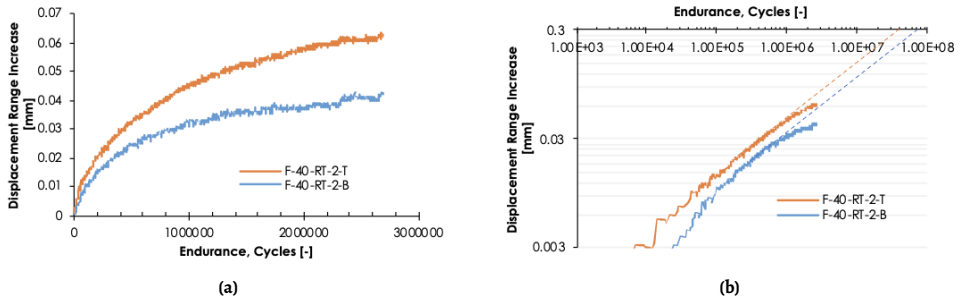

Figure 7.1: Displacement range increase of iSRR connector under loading cycles of ±40 kN at room temperature: (a) Recorded connectors' displacement range increase, (b) Projection in log-log axis.

The second method for extrapolation is the elbow method, which involves a combination of change point analysis and subsequent model fitting before performing linear regression [105]. This method is used to optimize data segmentation and improve the precision of

the regression analysis. Breakpoints within the dataset are selected to minimize the Sum of Squared Errors (SSE) for each data segment. The SSE for each cluster is computed by summing the squared distances from each data point to the centroid, which is the average of all data points within the cluster.

The selection of these breakpoints establishes the start and end points of each linear segment. This process entails iteratively adjusting breakpoints for varying numbers of segments, fitting individual linear models to each segment, and computing the SSE for each model. The optimal number of segments is determined at the point where a noticeable 'elbow' appears in the plot of SSE against the number of segments, as depicted in 7.2a. This point represents an equilibrium between model simplicity and accuracy. It's important to note that the segmentation is not merely an even division of the data range. Instead, it reflects the most statistically efficient division points within the dataset, as influenced by the natural clustering of data points. This approach ensures that each segment reliably represents a distinct pattern in the data, rather than a uniform or arbitrary division.

After segmenting the displacement range increase data, linear regression analysis (in log-log scale) is applied to each segment. The resulting trendlines provide the basis for extrapolating the estimated number of cycles needed for the displacement range to reach the specified 0.3 mm threshold. This extrapolation process, as depicted in Figure 7.2b, predicts when the displacement threshold is likely to be met for each segment.

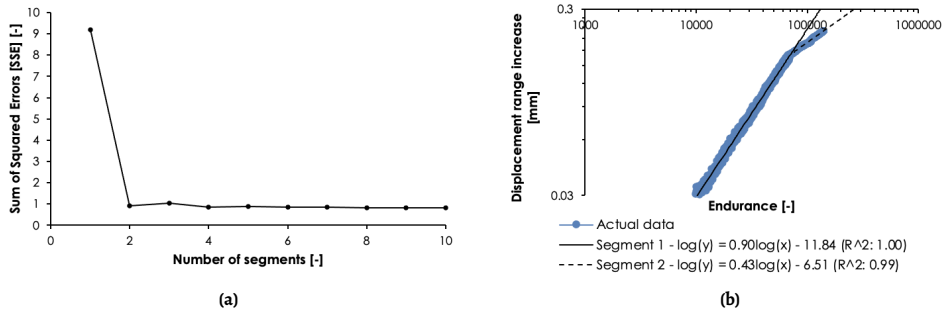

Figure 7.2: Estimating reach of failure criterion based on displacement range increase of iSRR connector: (a) Elbow method to determine optimal number of segments, (b) Segmented linear regression with projections to 0.3 mm.

For many connectors, it is observed that the displacement range increase exhibits more than one distinct slope. The specimens initially display a certain slope that decelerates during the second stage, which then sometimes even rapidly increases (third stage) after more cycles before reaching the failure criterion. The slip increase of the connectors demonstrates a fast-slow-fast trend, which mirrors the three-stage stiffness degradation trend commonly observed in composite materials [106]. This acceleration could potentially be attributed to several factors, such as the coalescence of cracks within the SRR piece, debonding between the SRR piece and the embedded nuts or the composite facing, or elongation of the hole in the bottom composite facing. However, it is important to note that these potential causes are hypothetical, and further investigation is conducted in Chapter 8 to conclusively identify the underlying mechanisms responsible for the observed acceleration.

The specimens that entered the third stage under cyclic loading were carefully examined,

and it was determined that using the highest slope among the three segments as the basis for extrapolation provides the most conservative estimate. In some cases, the initial slope is greater than that of subsequent segments, while in others, the second or third stage slope dominates. To ensure safety and reliability, the highest of the three estimated slopes is always used to predict the number of cycles required to reach failure. This conservative approach guarantees that the estimation remains on the safe side, thus minimizing the risk of overestimating the fatigue life.

The conservative nature of this approach is demonstrated in Figure 7.3, where the initial slope precedes the third stage, which accounts for the rapid increase in the displacement range. Alternatively, projecting the slope of the second stage could potentially lead to an overestimation of the number of cycles required to reach failure. Even though the 0.3 mm failure criterion was reached, the cycles obtained from extrapolating the first stage slope were employed in the construction of the *F-N* curve, taking into account the conservative nature of the initial slope extension and the goal of incorporating all the relevant data available.

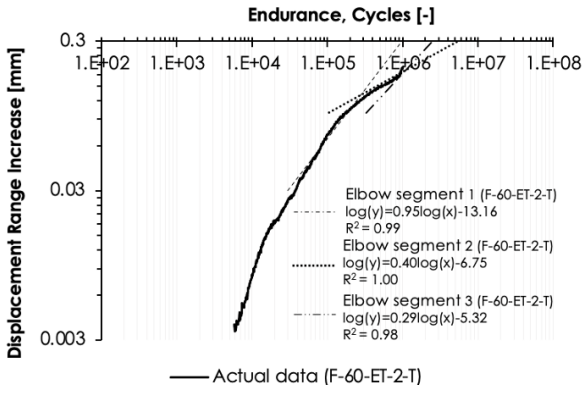

Figure 7.3: Projecting all slopes of displacement range increase of iSRR connector F-60-ET-2-T.

7.2. Influence of the load level

Figures 7.4a to 7.4c present the displacement range increase curves for the three loading cases of ±40 kN, ±60 kN and ±80 kN and for various connectors, plotted in log-log scale for clarity of trend analysis. Among all, four connectors in three different specimens achieve the 0.3 mm displacement range increase threshold, highlighting the variability in their behavior under cyclic loading conditions. In contrast, the remaining specimens are halted at pre-established cycle counts, not reaching this threshold. Additionally, the figure serves as a comparison between the linear regression and elbow segmentation methods, illustrating the process of extrapolating the number of loading cycles required to reach the failure criterion using these two distinct approaches.

For further insights, Table 7.1 presents detailed information related to this analysis and includes, in parentheses, the number of cycles at which each connector reached the 0.3 mm failure criterion. To assist the reader, it is recommended to refer to the “Parameter” column

and locate the row labeled Cycles at 0.3 mm. If a value in parentheses appears in that row, it indicates that the corresponding connector reached the 0.3 mm displacement range, and the predicted values from the two methods can be used for comparison.

Table 7.1: Estimation of cycle counts until failure criterion at room temperatures.

Connector's ID	Parameter	Linear regression $y=A\cdot x^B$	Elbow method $\log(y)=A+B\cdot\log(x)$		
			Segment 1	Segment 2	Segment 3
F-40-RT-U-1-T	A	9E-05	-9.96	-7.27	-
	B	0.446	0.50	0.30	-
	R^2	0.984	1.00	0.97	-
	Cycles at 0.3 mm	7.92E+07	4.57E+07	4.64E+08	-
F-40-RT-U-1-B	A	8E-05	-9.98	-6.69	-
	B	0.429	0.46	0.24	-
	R^2	0.972	0.98	0.81	-
	Cycles at 0.3 mm	2.01E+08	1.30E+08	1.23E+10	-
F-40-RT-U-2-T	A	3E-04	-9.82	-5.41	-
	B	0.369	0.50	0.19	-
	R^2	0.976	0.99	0.84	-
	Cycles at 0.3 mm	1.34E+08	2.62E+07	5.00E+09	-
F-40-RT-U-2-B	A	1E-04	-8.00	-4.80	-
	B	0.450	0.36	0.13	-
	R^2	0.971	0.99	0.84	-
	Cycles at 0.3 mm	5.35E+07	1.68E+08	4.44E+11	-
F-60-RT-U-1-T	A	1E-04	-9.43	-8.85	-10.10
	B	0.505	0.54	0.49	0.58
	R^2	0.995	0.98	0.99	0.94
	Cycles at 0.3 mm	7.63E+06	4.22E+06	5.76E+06	4.39E+06
F-60-RT-U-1-B	A	1E-04	-8.46	-12.34	-
	B	0.545	0.48	0.77	-
	R^2	0.982	0.99	0.98	-
	Cycles at 0.3 mm (2.14E+06)	2.43E+06	3.22E+06	1.99E+06	-
F-60-RT-U-2-T	A	1E-05	-12.46	-10.15	-10.92
	B	0.677	0.76	0.58	0.64
	R^2	0.996	0.99	0.99	0.98
	Cycles at 0.3 mm	4.13E+06	2.81E+06	4.95E+06	6.34E+06
F-60-RT-U-2-B	A	2E-05	-12.25	-8.76	-9.20
	B	0.653	0.75	0.49	0.52
	R^2	0.988	1.00	1.00	0.99
	Cycles at 0.3 mm	2.48E+06	2.54E+06	5.35E+06	4.87E+06
F-80-RT-U-1-T	A	2E-04	-9.42	-8.57	-
	B	0.540	0.61	0.54	-
	R^2	0.989	0.99	0.96	-
	Cycles at 0.3 mm (8.43E+05)	7.65E+05	7.05E+05	8.72E+05	-
F-80-RT-U-1-B	A	6E-05	-13.07	-7.81	-
	B	0.589	0.86	0.40	-
	R^2	0.986	0.99	0.96	-
	Cycles at 0.3 mm	1.77E+06	9.23E+05	1.34E+07	-
F-80-RT-U-2-T	A	4E-04	-9.83	-6.53	-
	B	0.469	0.65	0.37	-
	R^2	0.978	0.99	0.99	-
	Cycles at 0.3 mm (1.66E+06)	1.35E+06	6.00E+05	1.93E+06	-
F-80-RT-U-2-B	A	1.3E-04	-11.07	-7.85	-6.30
	B	0.553	0.73	0.48	0.36
	R^2	0.987	1.00	0.67	0.52
	Cycles at 0.3 mm (1.19E+06)	1.19E+06	7.44E+05	1.10E+06	1.26E+06

All connectors tested in this study transition through distinct stages of displacement range increase, with the majority entering a second stage characterized by slower progression. Only a limited number of connectors progress to a third stage of rapid displacement range increase, indicative of nearing ultimate failure. This section examines the effect of different load levels on the number of cycles required to transition between these stages, as summarized in Table 7.2. On average, a total of 1.6E+06 cycles is required for the connectors to enter the second stage of displacement range increase when subjected to a maximum load of 40 kN. The required number of cycles decrease by factors of 4.7 and 8 when the iSRR connectors are tested with a loading of ±60 kN and ±80 kN, respectively. This trend highlights the influence of loading conditions on the connectors' performance and their transition between different regimes of displacement range increase.

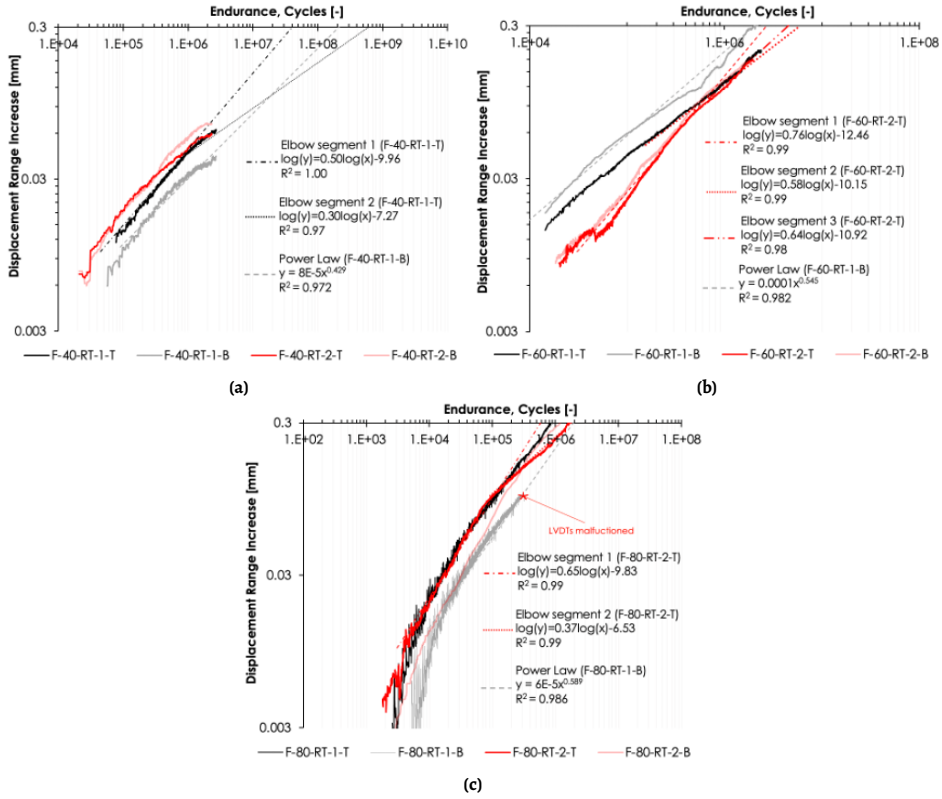

Figure 7.4: Connectors' displacement range increase in logarithmic scale axes under room temperature: (a) ±40 kN, (b) ±60 kN, (c) ±80 kN.

The extrapolated number of cycles to reach the 0.3 mm displacement range increase is used to construct the *F-N* data using both the linear regression and the elbow method. The *F-N* relationship can be approximated by a straight line on a log-log scale, in accordance with the specifications of ASTM E739 [88] and as described in Section 3.6. Employing the

twelve valid data points derived from the elbow method, regression parameters A and B are calculated to be +18.5 and -6.7, respectively, with parameter B representing the F-N curve's inverse slope parameter which is commonly referred to as m. Figure 7.5 illustrates the F-N curve based on the described statistical evaluation. A parallel analysis using linear regression instead of the elbow method i.e., without data segmentation yields closely aligned results: with A at 18.4 and B at -6.5 with m = -6.5.

Table 7.2: Cycles at intersection between stage 1 and stage 2 based on elbow approach.

Max force [kN]	End of 1st stage [Cycles]
40	1.61E+06
60	3.39E+05
80	2.01E+05

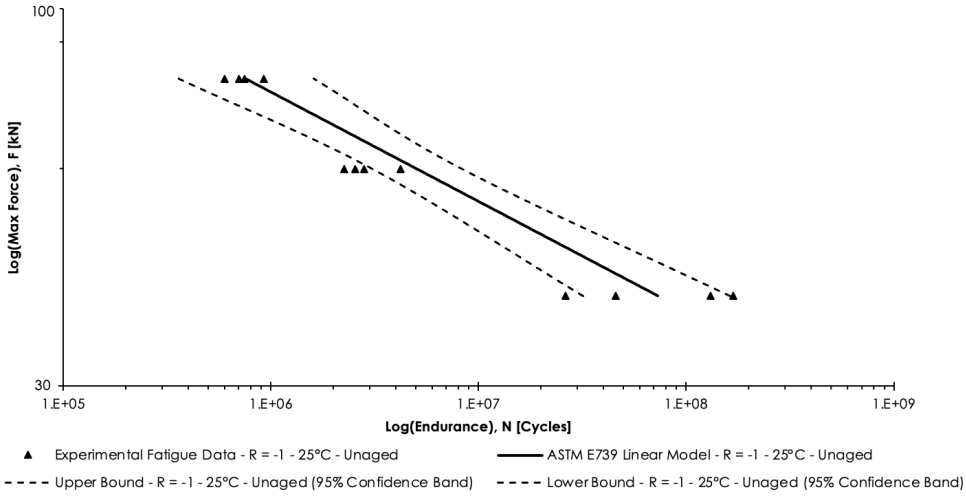

Figure 7.5: Preliminary F-N curve (R = -1) for iSRR connector at room temperature with statistical analysis based on ASTM (data collected using linear regression method).

The 95% confidence bands around the linear F-N curve are established, taking into account variations in data points, the number of tested specimens, and the force levels applied. To calculate these bands, the Fp factor, a statistical multiplier derived from the t-distribution and described in ASTM E739 [88], is used. This factor adjusts for the sample size and data scatter, ensuring a statistically robust estimation of the uncertainty in the fatigue life predictions. Table 7.3 details the 95% confidence bands for the fatigue life of the iSRR connectors under room temperature conditions based on both extrapolation methods. These confidence intervals provide a statistical estimation of the possible range of cycles to failure at specific force levels. The upper and lower bounds serve as an indicator of the reliability and variation in the projected fatigue life across different specimens and load levels.

For the ±40 kN load case, a wider spread is observed between the lower and upper bounds, particularly with the elbow method showing a diminished lower-bound prediction compared to the linear method. This suggests greater uncertainty in the fatigue performance of connectors under lower loading conditions. At ±60 kN and ±80 kN, the difference between the lower and upper bounds narrows, indicating that as the maximum applied force increases, the predictions become more reliable, and the fatigue life shows less variability. This trend aligns with typical fatigue test observations, where higher loads generally lead to more predictable failure behaviors and fewer cycles to failure.

Table 7.4 presents the average results obtained from these two analytical approaches. Notably, the average inverse slope of -6.6 from this study suggests less steep fatigue life (endurance) curve than those reported in previous research: -5.5 for pin-bearing failure of composite laminates with M16 bolted connections in a double-lap shear configuration as per [72], and -4.4 for M20 Lindapter blind-bolted connections in a single-lap shear configuration according to [25] .

Table 7.3: Confidence bands of iSRR connector at room temperature conditions based on ASTM E739.

		Average		Lower bound		Upper bound	
		Linear	Elbow	Linear	Elbow	Linear	Elbow
Model parameters	A	18.4	18.5	16.0	16.2	18.5	20.8
	B	-6.5	-6.7	-7.9	-8.0	-6.7	-5.4
Cycles at specified max Force	**40 kN**	8.46E+07	6.18E+07	3.75E+07	2.62E+07	1.91E+08	1.35E+08
	60 kN	5.99E+06	4.09E+06	3.62E+06	2.52E+06	9.93E+06	6.65E+06
	80 kN	9.18E+05	5.96E+05	4.29E+05	2.86E+05	1.96E+06	1.24E+06

Table 7.4: Average confidence bands of the two prediction methods of an iSRR connector at room temperature conditions.

		Average	Lower bound	Upper bound
Model parameters	A	18.45	16.1	19.65
	B	-6.6	-7.95	-6.05
Cycles at specified max Force	**40 kN**	7.32E+07	3.18E+07	1.63E+08
	60 kN	5.05E+06	3.07E+06	8.29E+06
	80 kN	7.57E+05	3.58E+05	1.60E+06

7.3. Influence of the load ratio

In this section, the influence of varying load ratios on the predicted fatigue life of the iSRR connectors is analyzed. In Figure 7.6, examples of the projection of the displacement range increase in log-log scale are presented for the specimens tested under three different R ratios. The number of cycles necessary to reach the 0.3 mm displacement range increase threshold criterion is extrapolated using both the linear regression and the elbow method described earlier and the results are detailed in Table 7.5.

The connectors tested at R = 0.5 show a much slower progression toward failure, compared to connectors tested at the same maximum load with load ratio of R = -1. These

connectors endure a far greater number of cycles before reaching 0.3 mm of displacement range increase, indicating a better fatigue performance under the $R = 0.5$ conditions. The displacement range increases more gradually, implying that this load ratio subjects the connectors to less severe fatigue damage. The $R = 0.1$ connectors exhibit intermediate behavior. Their displacement range increase is faster than at $R = 0.5$, but slower than for $R = -1$. This suggests that while $R = 0.1$ still leads to noticeable fatigue damage, it is less damaging than fully reversed loading but more harmful than positive loading with $R = 0.5$.

Table 7.5: Estimation of cycle counts until failure criterion with different R-ratios.

Connector's ID	Parameter	Linear regression $y=A \cdot x^B$	Elbow method $\log(y)=A+B \cdot \log(x)$		
			Segment 1	Segment 2	Segment 3
F-80_8-RT-U-1-T	A	2E-05	-10.62	-8.51	-
	B	0.454	0.44	0.29	-
	R^2	0.924	0.93	0.69	-
	Cycles at 0.3 mm	1.59E+09	1.79E+09	6.56E+10	-
F-80_8-RT-U-1-B	A	5E-08	-14.75	-15.04	-11.94
	B	0.876	0.73	0.75	0.53
	R^2	0.945	0.85	0.83	0.71
	Cycles at 0.3 mm	5.47E+07	1.13E+08	1.04E+08	5.33E+09
F-100_10-RT-U-1-T	A	9E-06	-8.83	-7.67	-7.49
	B	0.619	0.34	0.29	0.27
	R^2	0.945	1.00	0.97	0.93
	Cycles at 0.3 mm	2.00E+07	1.37E+09	5.90E+09	8.48E+09
F-100_10-RT-U-1-B	A	3E-06	-8.04	-6.67	-
	B	0.750	0.33	0.23	-
	R^2	0.964	0.99	0.76	-
	Cycles at 0.3 mm	4.60E+06	9.12E+08	1.83E+10	-
F-80_40-RT-U-1-T	A	8E-10	-12.20	-30.23	-
	B	0.947	0.40	1.67	-
	R^2	0.63	0.17	0.21	-
	Cycles at 0.3 mm	1.54E+09	1.21E+12	3.39E+07	-
F-80_40-RT-U-1-B	A	3E-05	-10.61	-9.38	-
	B	0.380	0.40	0.31	-
	R^2	0.893	0.98	0.88	-
	Cycles at 0.3 mm	3.34E+10	1.56E+10	2.78E+11	-
F-100_50-RT-U-1-T	A	1E-05	-10.80	-9.34	-
	B	0.487	0.44	0.34	-
	R^2	0.950	0.97	0.84	-
	Cycles at 0.3 mm	1.53E+09	2.57E+09	2.37E+10	-
F-100_50-RT-U-1-B	A	6E-07	-11.51	-7.15	-
	B	0.661	0.44	0.13	-
	R^2	0.720	0.76	0.30	-
	Cycles at 0.3 mm	4.20E+08	1.64E+10	2.11E+19	-

Figure 7.7 illustrates the log-log relationship between the number of cycles to 0.3 mm and the maximum applied force for three different R-values: -1, 0.1, and 0.5. All the curves start at 120 kN, which corresponds to the slip load of the iSRR connectors. This is because if the connector was subjected to a static maximum force of 120 kN, slip would occur almost immediately, and the 0.3 mm displacement range increase would be reached within the first cycle. This starting point serves to illustrate the limiting condition of the iSRR connector's performance, with lower applied forces requiring more cycles to reach the failure threshold.

The slope of the curves, plotted in Figure 7.7 demonstrate how the fatigue life decreases as the maximum applied force increases, with the load ratio influencing the rate of this

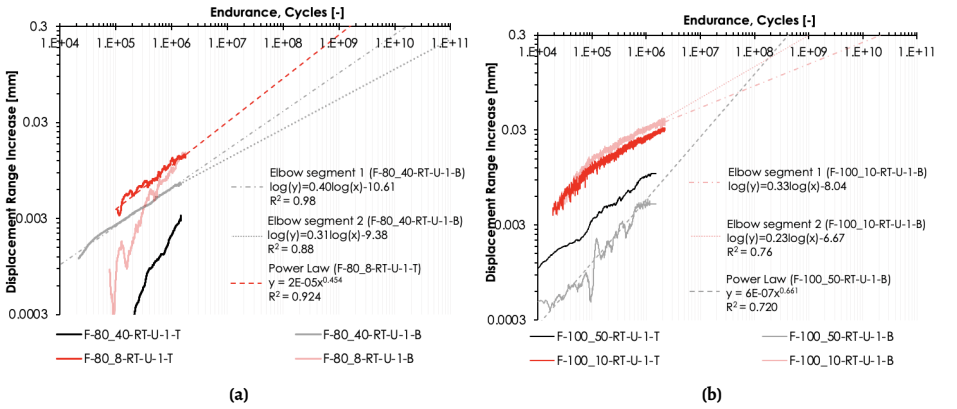

Figure 7.6: Connectors' displacement range increase in logarithmic scale axes under different R-ratios: (a) Maximum load of 80 kN, (b) Maximum load of 100 kN.

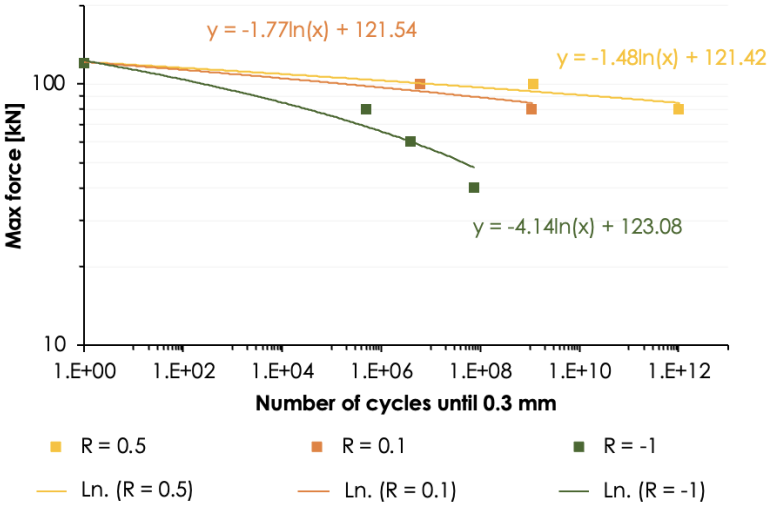

Figure 7.7: Influence of R-ratio on the fatigue life of the connectors.

reduction, indicating the influence of different load ratios on the rate of fatigue degradation. As expected, the $R = -1$ curve exhibits the steepest slope, suggesting that under fully reversed loading conditions, the connectors experience the most rapid degradation in their fatigue life. This behavior is attributed to the reversal of stress in each cycle, which intensifies fatigue damage by subjecting it to alternating compressive and tensile stresses. Additionally, the total force range in this case is higher than in other load ratios, further contributing to the increased fatigue damage.

Conversely, the curves for positive load ratios, particularly $R = 0.5$, show much gentler slopes, implying that these loading conditions impose less severe fatigue damage on the connectors. The closer the slope is to the horizontal, the greater the number of cycles

the connectors can endure before reaching the failure threshold of 0.3 mm displacement range increase. This aligns with the expectation that lower amplitude loading cycles (higher R-values) allow for an extended fatigue life.

Force range predictions and fatigue life estimations for the iSRR connector under shear loading are represented in the Constant Life Diagram (CLD) at Figure 7.8. This type of diagram is commonly used to represent the fatigue behavior of composite materials under the influence of stress range and stress ratio, where mean stress dependency cannot be neglected- such as in the case of welded steel details [107–110]. Here, it is constructed to examine the mean load level dependency of the iSRR connector subjected to shear loading.

A conventional CLD for material behavior typically includes R ratios ranging from R = 10 (compression-compression) on the left, where mean stress levels are negative, to R = -1 (fully reversed tension-compression) at the center, and further to R = 0.1 (tension-tension) on the right, where mean stress levels are most positive. However, for connectors loaded in shear, unlike bulk materials, the tension-tension and compression-compression cases are effectively equivalent. In general, the fatigue behavior remains unchanged whether the shear load is applied from one side or the other. This symmetry allows the relationship $N(F, R) = N(F, 1/R)$ to be applied, where $N(F, R)$ represents the number of cycles as a function of the maximum force or force range and the R ratio. Consequently, the CLD for iSRR connectors under shear loading is symmetrical with respect to the vertical axis at R = -1, and only the right-hand side of the diagram must be constructed.

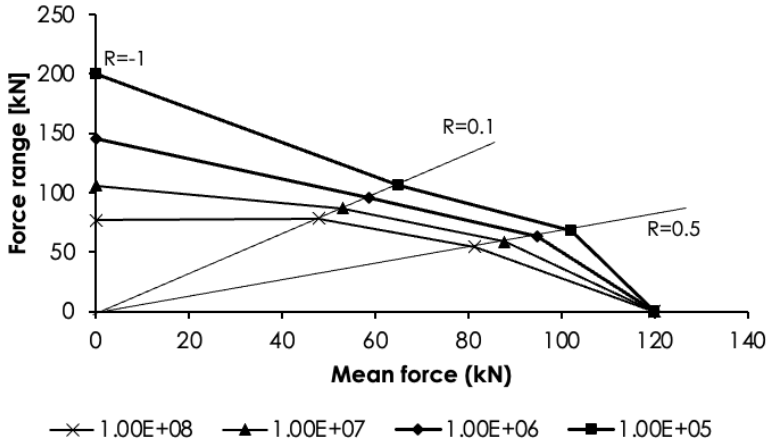

Figure 7.8: CLD of the iSRR connector under shear loading for displacement range limited to 0.3 mm.

The CLD effectively captures the relationship between the applied mean force and the force range required for the connector to survive a given number of cycles before failure. Importantly, the curves start at 120 kN, corresponding to the slip resistance of the iSRR connector. The CLD thus highlights the iSRR connector's mechanical limits and provides essential data for comparing its fatigue life across different load levels and loading scenarios.

Having collected all the results for each R-ratio, in the CLD diagram, it becomes visible that the lines in the CLD have tendency to be horizontal for a lower range of mean force

level. This indicates a potential to define a unified prediction of the fatigue behavior of the iSRR connector where mean force level would be disregarded. In Figure 7.9a, all the data are plotted irrespective of the R-ratio, allowing a statistical analysis across the entire dataset. The regression line and confidence bands are obtained for all the data to provide an overall trend. The force range is chosen as an appropriate y-axis parameter for describing the fatigue performance, considering the diversity of R-ratios applied.

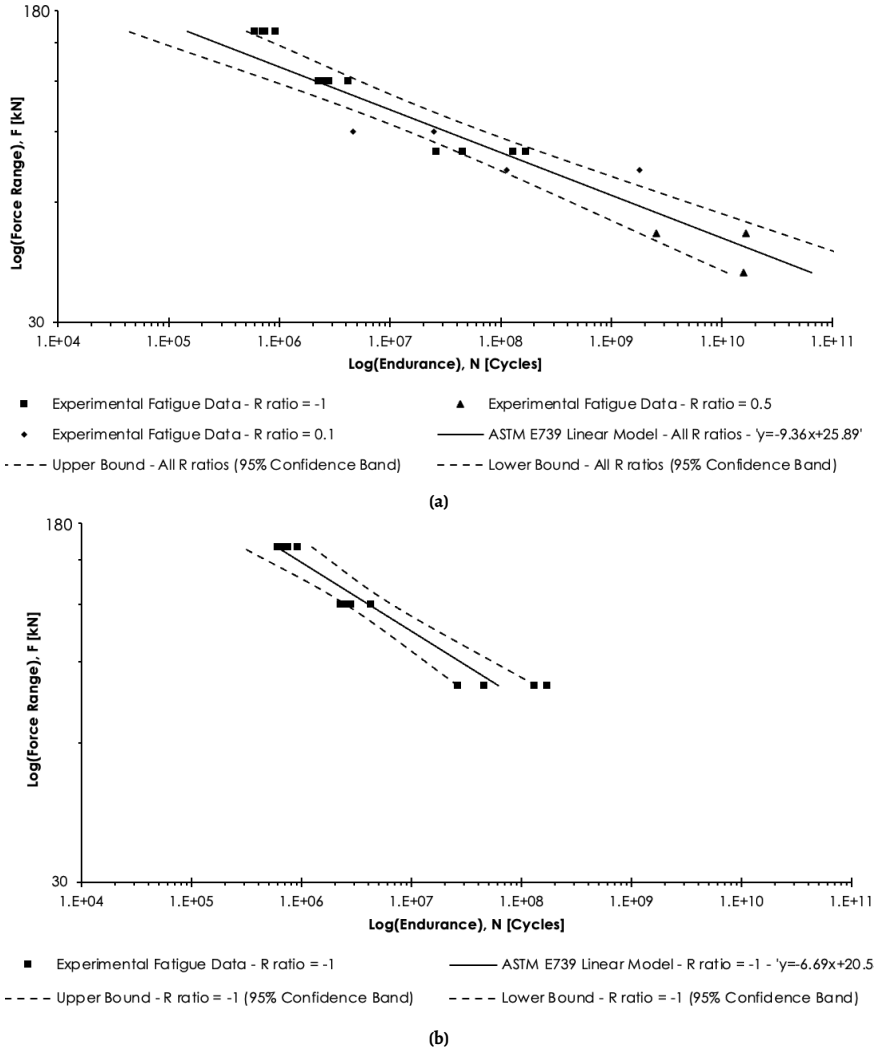

Figure 7.9: Comparison between different fatigue performance analysis: (a) All R-ratios and (b) R = -1.

The comparison between Figure 7.9a and Figure 7.9b aims to highlight the implications of incorporating multiple load ratios in the fatigue analysis, particularly in terms of improving the accuracy of fatigue life predictions. When only the R = -1 data is considered, a different

fatigue behavior emerges compared to the more comprehensive dataset. Observations from Figure 7.9b indicate that relying solely on the R = -1 dataset could result in an overprediction of the connector's resistance at higher load levels. Meanwhile, using R = -1 data alone would provide underestimated number of cycles and reduced confidence at lower load levels, owing to the variability and broader scatter of experimental results. Including data from different R-ratios provides an improved statistical basis, contributing to a more reliable estimation of the connector's fatigue performance. This highlights the advantage of considering multiple R-ratios when evaluating connector behavior under realistic service conditions.

The curves plotted in Figures 7.9a and 7.9b further demonstrate that the slope of the regression line changes significantly depending on the dataset considered. For the unified approach, so for all R-ratios, the slope is steeper at -9.36, which suggests a quicker decline in fatigue life with increasing load range compared to the -6.69 slope at R = -1. This difference reflects how an F-N curve based only on fully reversed loading may not be the most damaging condition for the highest load ranges, contrary to what was initially expected.

Finally, by creating an F-N curve that includes every R-ratio, the design and engineering procedures are simplified. Including separate F-N curves for every different R-ratio can be complicated in practical design verifications, especially when calculating fatigue life under varying conditions. Therefore, the recommendation for engineering practice is to start with the unified F-N curve for an iSRR connector as it encompasses data from all R-ratios and provides a reasonable estimation of fatigue life. If more precision is needed, separate R-ratio-specific curves could then be used for more detailed damage analysis. This approach balances simplicity with sufficient accuracy, as analysis conducted on structural level variations due to traffic loads indicated that the unified F-N curve is adequate and does not lead to overestimation of fatigue life.

7.4. Influence of temperature

The influence of elevated temperature on the fatigue performance of the iSRR connector is examined by constructing an F-N curve for connectors tested at 55 °C under fully reversed cyclic loading (R = -1). Figure 7.10 displays the displacement range increase for all tests conducted at elevated temperatures, using the log-log scale. The graph distinctly shows a linear trend in displacement range increase across all load levels until a nonlinear trend emerges in the second stage. Table 7.6 lists the average number of cycles required for this transition at each load level. Similar to the room temperature tests, iSRR connectors under lower load levels experience more cycles until the initiation of the nonlinear stage. Notably, all connectors exhibit a second stage, with the elbow method indicating that five of twelve connectors commenced to a third stage. On average, at elevated temperature, the iSRR connector requires 1.82E+05 cycles to enter the second stage under a fully reversed load of ±40 kN. This cycle count decreases by factors of 1.4 and 2.5 under load conditions of ±60 kN and ±80 kN, respectively. When these findings are compared to those in Table 7.2 for room temperature conditions, the impact of temperature on connector performance and the transition between displacement stages becomes apparent.

Similar to the experiments performed at room temperature, the two methods for extrapolating the curve along their trendlines are applied to determine the number of cycles at which the previously adopted fatigue failure criterion is reached. The number of cycles at which the projected lines reached the 0.3 mm of displacement range increase are reported

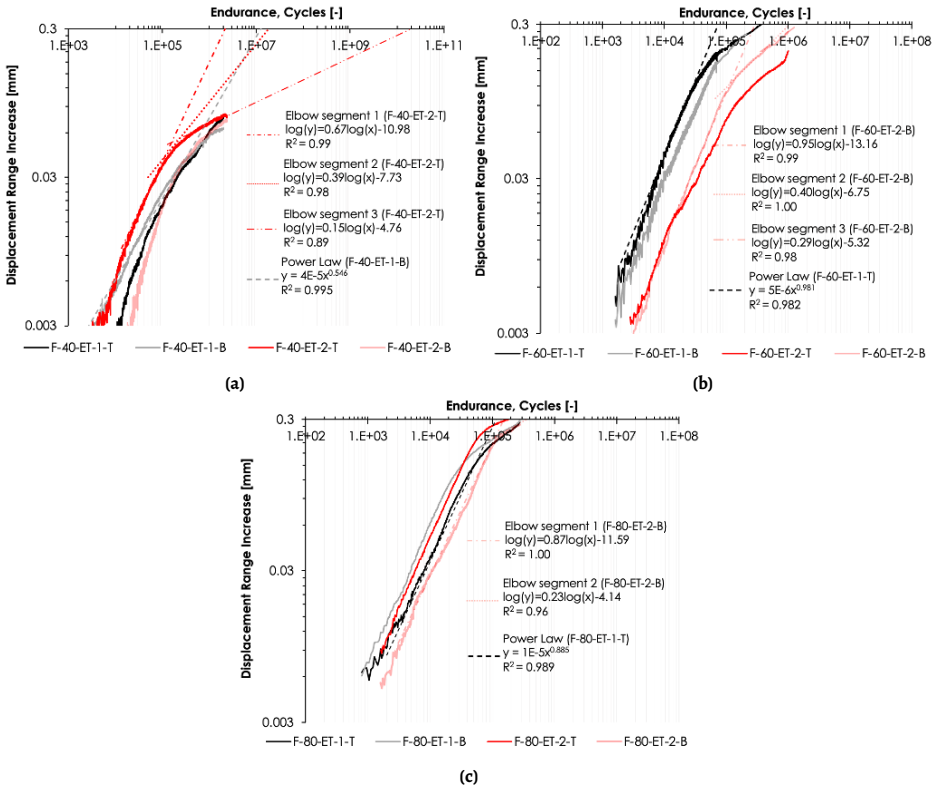

Figure 7.10: Recorded connectors' displacement range increase in logarithmic scale axes under elevated temperature: (a) ±40 kN, (b) ±60 kN, (c) ±80 kN.

Table 7.6: Cycles at intersection between stage 1 and stage 2 for connectors tested at elevated temperature.

Max force [kN]	End of 1st stage [Cycles]
40	1.82E+05
60	1.25E+05
80	7.20E+04

in Table 7.7 and are used as an input to perform the statistical evaluation that generated the *F-N* curve of the iSRR connectors at 55 °C. The actual number of cycles that reached the same criterion is also reported in parentheses in Table 7.7.

The statistical examination reveals that the *F-N* curve's slope at elevated temperatures is slightly steeper than that derived at room temperature for the same load ratio of R = -1. The twelve data points identified by the elbow method resulted in model parameters, B = -5.7 and A = +15.7, while the linear regression method yields slightly different estimates of B = -5.9 and A = +16.1. These values, along with the cycle counts for the 95% confidence

intervals pertaining to the iSRR connectors at elevated temperatures, are compiled in Table 7.8 for both analytical methods. Additionally, Table 7.9 provides the average outcomes from these two approaches.

Figure 7.11 plots the data points predicted by the elbow method and the resulted *F-N* curve and confidence bands delineated by black dashed lines for the elevated testing temperatures. For comparative purposes, the *F-N* curve at room temperature is concurrently presented, providing a visual reference against the elevated temperature data. The *F-N* curve at 55 °C exhibits a significantly reduced fatigue life across all load levels when compared to 25 °C. Notably, despite having similar slopes, the *F-N* curve at the higher temperature of 55 °C is shifted downwards, implying that the connectors tested at elevated temperatures endure substantially fewer cycles before reaching the failure criterion. This downwards shift results in consequent shift of the *F-N* curve in the horizontal direction that leads to reduction in fatigue life by a factor of approximately 10 when tested at elevated temperatures.

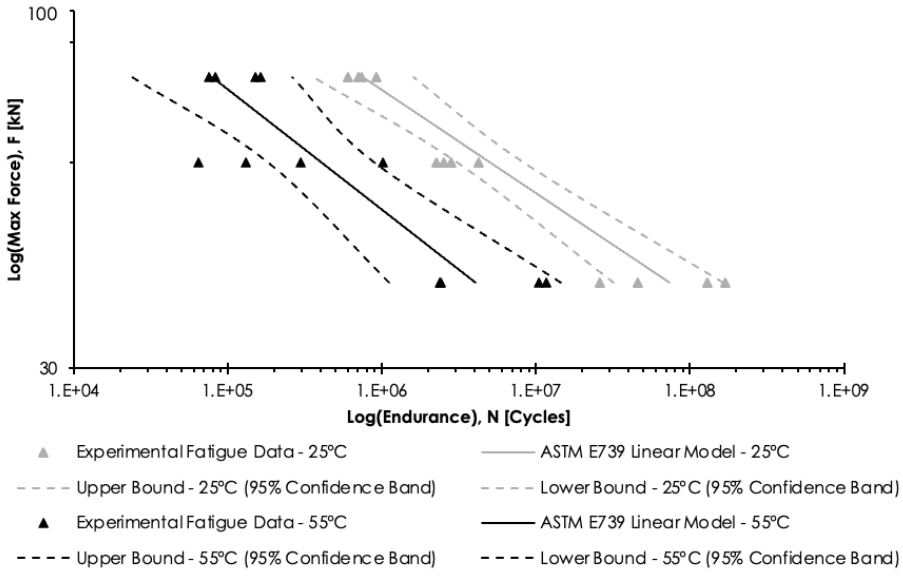

Figure 7.11: Preliminary *F-N* curve (*R* = -1) for iSRR connector under elevated and room temperature with statistical analysis based on ASTM E739.

The confidence bands at 55 °C are notably wider, indicating greater variability in fatigue life at elevated temperatures. This increased variability could stem from the accelerated degradation of the resin matrix within the connector, which is more sensitive to temperature fluctuations. The integrity of the load transfer between the steel and resin components is likely compromised at elevated temperatures, leading to an earlier onset of micro-cracking, reduced stiffness, and accelerated fatigue failure. Thus, elevated temperatures not only shorten the fatigue life but also increase the unpredictability of the connector's behavior, highlighting the need for conservative design approaches when high temperatures are expected.

Table 7.7: Estimation of cycle counts until failure criterion at elevated temperatures.

Connector's ID	Parameter	Linear regression $y=A \cdot x^B$	Elbow method $\log(y)=A+B \cdot \log(x)$		
			Segment 1	Segment 2	Segment 3
F-40-ET-U-1-T	A	3E-05	-10.74	-7.66	-
	B	0.555	0.59	0.34	-
	R^2	0.987	1.00	0.98	-
	Cycles at 0.3 mm	1.63E+07	1.04E+07	1.47E+08	-
F-40-ET-U-1-B	A	4E-05	-9.99	-6.65	-
	B	0.546	0.54	0.27	-
	R^2	0.995	0.99	0.98	-
	Cycles at 0.3 mm	1.26E+07	1.17E+07	5.95E+08	-
F-40-ET-U-2-T	A	3E-05	-10.98	-7.73	-4.76
	B	0.625	0.67	0.39	0.15
	R^2	0.988	0.99	0.98	0.89
	Cycles at 0.3 mm	2.50E+06	2.38E+06	2.28E+07	1.61E+10
F-40-ET-U-2-B	A	3E-06	-14.95	-10.88	-8.96
	B	0.762	0.95	0.61	0.45
	R^2	0.982	0.99	0.97	0.93
	Cycles at 0.3 mm	3.66E+06	1.88E+06	8.26E+06	2.73E+07
F-60-ET-U-1-T	A	5E-06	-13.18	-8.82	-6.81
	B	0.981	1.08	0.65	0.46
	R^2	0.982	0.99	0.96	0.79
	Cycles at 0.3 mm (3.24E+05)	7.41E+04	6.47E+04	1.27E+05	1.85E+05
F-60-ET-U-1-B	A	4E-06	-11.84	-6.51	-
	B	0.946	0.90	0.43	-
	R^2	0.994	1.00	0.99	-
	Cycles at 0.3 mm (3.24E+05)	1.23E+05	1.31E+05	2.63E+05	-
F-60-ET-U-2-T	A	1E-05	-10.30	-5.54	-9.16
	B	0.772	0.66	0.28	0.54
	R^2	0.998	0.98	0.99	0.90
	Cycles at 0.3 mm	6.28E+05	1.01E+06	6.45E+06	2.25E+06
F-60-ET-U-2-B	A	1E-06	-13.16	-6.75	-5.32
	B	0.990	0.95	0.40	0.29
	R^2	0.995	0.99	1.00	0.98
	Cycles at 0.3 mm	3.40E+05	2.96E+05	1.01E+06	1.70E+06
F-80-ET-U-1-T	A	1E-05	-7.92	-4.58	-
	B	0.885	0.56	0.27	-
	R^2	0.989	0.99	1.00	-
	Cycles at 0.3 mm (2.50E+05)	1.15E+05	1.50E+05	2.49E+05	-
F-80-ET-U-1-B	A	3E-05	-7.62	-3.31	-
	B	0.807	0.57	0.13	-
	R^2	0.976	1.00	0.55	-
	Cycles at 0.3 mm (1.98E+05)	9.05E+04	8.27E+04	3.21E+05	-
F-80-ET-U-2-T	A	1E-05	-11.23	-4.56	-
	B	0.894	0.89	0.28	-
	R^2	0.996	1.00	0.97	-
	Cycles at 0.3 mm (1.74E+05)	1.01E+05	7.49E+04	1.41E+05	-
F-80-ET-U-2-B	A	1E-05	-11.59	-4.14	-
	B	0.827	0.87	0.23	-
	R^2	0.997	1.00	0.96	-
	Cycles at 0.3 mm	2.59E+05	1.64E+05	4.02E+05	-

Based on Figure 7.11, the mid-load level (±60 kN) once again demonstrates the highest variation among the experimental results, with a noticeable spread in endurance values compared to the lower (±40 kN) and higher (±80 kN) load levels. This variability is evident at both room temperature (25 °C) and elevated temperature (55 °C) conditions. Moreover, some experimental data points fall outside the 95% confidence bands for both temperature scenarios, indicating greater uncertainty and scatter in fatigue performance at this load level. The data suggests that the fatigue response at ±60 kN is less predictable, which could be attributed to the transitional behavior between purely elastic and inelastic damage modes that typically occurs at intermediate stress levels.

Table 7.8: Confidence bands of iSRR connector at elevated temperature conditions based on ASTM E739.

		Average		**Lower bound**		**Upper bound**	
		Linear	Elbow	Linear	Elbow	Linear	Elbow
Model parameters	***A***	16.1	15.7	12.2	14.9	20.0	24.1
	B (slope)	-5.9	-5.7	-8.1	-10.1	-3.7	-4.8
Cycles at specified max Force	**40 kN**	4.81E+06	4.02E+06	1.30E+06	1.11E+06	1.78E+07	1.45E+07
	60 kN	4.46E+05	4.03E+05	1.98E+05	1.82E+05	1.01E+06	8.94E+05
	80 kN	8.26E+04	7.89E+04	2.43E+04	2.37E+04	2.81E+05	2.62E+05

Table 7.9: Average confidence bands of the two prediction methods of an iSRR connector at elevated temperature conditions.

		Average	**Lower bound**	**Upper bound**
Model parameters	***A***	15.9	13.5	22.0
	B	-5.8	-9.1	-4.3
Cycles at specified max Force	**40 kN**	4.42E+06	1.20E+06	1.62E+07
	60 kN	4.25E+05	1.90E+05	9.49E+05
	80 kN	8.08E+04	2.40E+04	2.72E+05

The degradation in the fatigue performance of the iSRR connector at elevated temperatures, particularly at 55 °C, can be closely linked to the behavior of the SRR material, composed of UPE+PU resin and steel balls. Material-level tensile tests conducted on the SRR at 55 °C, presented in Section 3.6, revealed accelerated stiffness degradation and a reduction in endurance, phenomena that are reflected in the fatigue behavior of the connectors under shear loading.

At 55 °C, the iSRR connectors show a considerable decrease in fatigue life and a faster progression to failure compared to room temperature conditions. This correlates with the observed behavior of the SRR material, where stiffness degradation occurs more rapidly under elevated temperatures. The F-N curve at 55 °C displays a steeper slope and a downward shift, suggesting that the thermal sensitivity of the SRR material is a significant factor driving the connector's reduced performance.

While the material-level tests are conducted under tensile loading, and the connectors are tested under shear loading, the influence of elevated temperatures on the UPE+PU resin matrix and its interface with the steel balls is evident in both cases. The accelerated

degradation mechanisms observed at the material level provide insight into the overall fatigue behavior of the iSRR connectors. The faster accumulation of damage, linked to the thermal response of the SRR material, necessitates careful consideration when predicting the long-term durability of the connectors in environments where elevated temperatures are anticipated.

7.5. Influence of environmental exposure

In this section, the results of the fatigue life of iSRR connectors subjected to one year of environmental aging are presented. Two connectors were submerged in water, and two were exposed to outdoor conditions for a year. Each of the aged connectors are tested under a cyclic load of ±80 kN, as this load condition gives the maximum load range. Given the limited number of specimens, the available data are sparse, yet they offer useful insights into the potential degradation of the connectors over time. The projected cycles to the 0.3 mm displacement range increase as the adopted failure criterion are shown in Figure 7.12 and Table 7.10.

More specifically, Figure 7.12 displays the displacement range increase of iSRR connectors tested at a consistent load level of ±80 kN, with the different colors representing connectors subjected to distinct environmental conditions. The lines with different shades of black correspond to the connectors aged outdoors for a year, the shades of red lines indicate the connectors submerged in water for the same duration, and the blue lines show the reference connectors tested at room temperature without any aging, shown earlier in Figure 7.4.

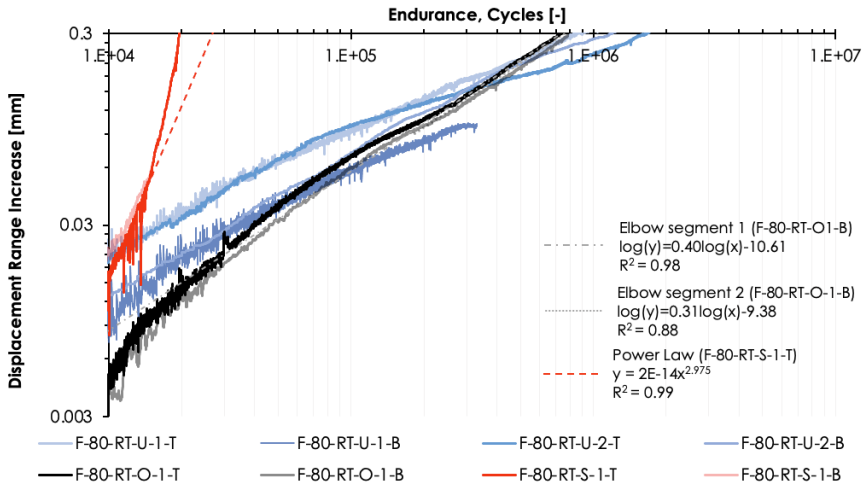

Figure 7.12: Displacement range increase of iSRR connector in logarithmic scale axes under different environmental exposure conditions.

Interestingly, the connectors aged outdoors exhibit a displacement range increase that is very similar to the reference connectors tested at room temperature. This suggests that the outdoor exposure, while slightly affecting the connector performance, did not drastically

reduce fatigue resistance compared to the non-aged connectors. Both blue and the black lines show a more gradual increase in displacement range compared to the submerged connectors. However, between the reference (blue) and the outdoor-aged (black) connectors, the reference connectors seem to perform slightly better, displaying a slightly slower rate of displacement range increase, indicating a marginally greater resistance to fatigue.

On the other hand, the submerged (red) connectors display the fastest displacement range increase, indicating accelerated stiffness degradation and earlier failure compared to both the outdoor-aged and the reference connectors. This implies that water exposure has a more detrimental impact on the fatigue performance of the connectors, leading to a significant reduction in fatigue life. The submerged connectors reach the 0.3 mm failure criterion much earlier, around 2.0E+4 cycles, whereas the outdoor-aged connectors and the reference connectors demonstrate a more gradual progression, reaching the 0.3 mm failure criterion closer to 7.5E+05 cycles, as shown in parentheses in Table 7.10.

Table 7.10: Estimation of cycle counts until failure criterion with different environmental exposure conditions.

Connector's ID	Parameter	Linear regression $y=A\cdot x^B$	Elbow method $\log(y)=A+B\cdot\log(x)$		
			Segment 1	Segment 2	Segment 3
F-80-RT-S-1-T	A	2E-14	-35.79	-18.83	-41.23
	B	2.975	3.51	1.59	4.00
	R^2	0.990	0.93	0.84	0.97
	Cycles at 0.3 mm (1.95E+04)	2.69E+04	1.92E+04	6.31E+04	2.19E+04
F-80-RT-S-1-B	A	3E-09	-62.23	-73.29	-
	B	1.728	6.17	7.29	-
	R^2	0.741	1.00	1.00	-
	Cycles at 0.3 mm (1.96E+04)	4.26E+04	2.02E+04	1.98E+04	-
F-80-RT-O-1-T	A	5E-06	-12.09	-12.35	-
	B	0.821	0.81	0.83	-
	R^2	0.998	0.99	1.00	-
	Cycles at 0.3 mm (7.30E+05)	8.46E+05	7.10E+05	7.33E+05	-
F-80-RT-O-1-B	A	1E-06	-12.42	-12.71	-
	B	0.924	0.83	0.85	-
	R^2	0.996	0.99	1.00	-
	Cycles at 0.3 mm (7.99E+05)	6.61E+05	7.80E+05	8.11E+05	-

These results highlight that outdoor exposure has a less drastic effect on the fatigue performance compared to submersion. Importantly, considering the intended application of these connectors in bridge structures, where they will always be in non-submerged conditions, the outdoor exposure results are particularly relevant. The study involving submerged conditions was conducted to evaluate the worst-case scenario, ensuring comprehensive safety margins. Given the promising results observed in the outdoor-aged connectors, it is evident that the iSRR connectors exhibit sufficient resilience for bridge environments, where continuous exposure to atmospheric moisture is expected, but continuous submersion is not. These findings support the reliability of the connectors under realistic field conditions, highlighting their suitability for practical use in infrastructure subjected to typical outdoor aging factors.

7.6. Reliability and conservatism in prediction methods

In this study, two methods are used to estimate the number of cycles required for each connector to reach a 0.3 mm displacement failure criterion: linear regression and the elbow method. The actual number of cycles for each connector, obtained from experimental testing, is compared with the cycles estimated by both methods in Table 7.11. Only the cases where the displacement range increase of 0.3 mm was reached in the experiments are considered. The linear regression method generally produces higher cycle predictions than the elbow method, suggesting that linear regression may be less conservative in predicting a longer service life before failure. This is evident in cases like connector F-80-RT-U-2-T, where linear regression estimates 1.35E+06 cycles compared to the elbow method's 6.00E+05 cycles. Such differences indicate that the elbow method tends to underestimate the actual number of cycles, although in some instances, it provides reasonable estimates, as seen with F-80-RT-O-1-B, where the elbow method predicts 7.80E+05 cycles, closely matching the actual 7.99E+05 cycles.

The reliability of these methods is better understood by evaluating the ratios R_i, which are defined as the ratio of the actual number of cycles to the estimated number of cycles. Ideally, an R_i value of 1 indicates a perfect prediction. On average, the linear regression method performs closer to the actual values, with a mean R_i of 1.58. This indicates that the linear regression method in average underestimates the number of cycles by a factor 1/1.58=0.63, i.e. 37% overestimation. In contrast, the elbow method results in a higher mean R_i of 2.48, meaning it underestimates the actual cycles by approximately 55%, making it a more conservative approach.

Figure 7.13 illustrated the relationship between the estimated and actual number of cycles, providing a visual assessment of the accuracy and reliability of each method. A power-law relationship is observed, with a fitting equation of $y = 1.58 \cdot x$ with $R^2 = 0.957$ for the linear regression method. The high R^2 indicates that this method has a strong correlation with the actual data, with predictions closely aligned with experimental results. The near-linear trend in the log-log scale suggests that linear regression offers reliable estimates of fatigue life.

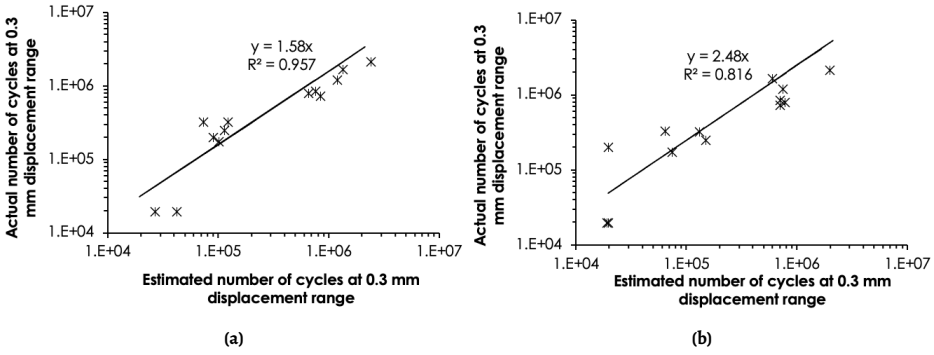

Figure 7.13: Comparison of actual data and extrapolated cycles at 0.3 mm displacement range increase: (a) Linear regression method, (b) Elbow method.

Table 7.11: Comparison of actual data and extrapolated cycles at 0.3 mm displacement range increase.

Connector's ID	Actual Data	Linear Regression	R_i	Elbow	R_i
F-60-RT-U-1-B	2.14E+06	2.43E+06	0.88	1.99E+06	1.08
F-80-RT-U-1-T	8.43E+05	7.65E+05	1.10	7.05E+05	1.20
F-80-RT-U-2-T	1.66E+06	1.35E+06	1.23	6.00E+05	2.76
F-80-RT-U-2-B	1.19E+06	1.19E+06	1.00	7.44E+05	1.60
F-60-ET-U-1-T	3.24E+05	7.41E+04	4.38	6.47E+04	5.02
F-60-ET-U-1-B	3.24E+05	1.23E+05	2.64	1.31E+05	2.47
F-80-ET-U-1-T	2.50E+05	1.15E+05	2.18	1.50E+05	1.66
F-80-ET-U-1-B	1.98E+05	9.05E+04	2.19	8.27E+04	2.40
F-80-ET-U-2-T	1.74E+05	1.01E+05	1.71	7.49E+04	2.32
F-80-RT-S-1-T	1.95E+04	2.69E+04	0.73	1.92E+04	1.02
F-80-RT-S-1-B	1.96E+04	4.26E+04	0.46	1.98E+04	0.99
F-80-RT-O-1-T	7.30E+05	8.46E+05	0.86	7.10E+05	1.03
F-80-RT-O-1-B	7.99E+05	6.61E+04	1.21	7.80E+05	1.02
Model factor (Mean ratio between actual and estimated cycles, R)			1.58		2.48

In contrast, the elbow plot shows a slightly lower R^2 value of 0.816, suggesting that the elbow method has a weaker correlation compared to linear regression. The fitting equation, $y = 2.48 \cdot x$, indicates that while the elbow method generally follows a similar trend, it tends to provide more conservative estimates.

Although absolute accuracy remains challenging in predictive modeling, these methodologies offer robust estimates that address different design priorities. Engineers can use these methods to predict the connectors' fatigue life. Thus, for reliable life predictions, backed by a strong correlation with experimental data, the linear regression method is suggested while the elbow method can be employed when a more conservative, risk-averse approach is warranted.

7.7. Conclusions

In this chapter a methodology to predict the fatigue shear behavior of the iSRR connector using experimental data is developed and validated. The approach to extrapolate the displacement range increase to a defined threshold prioritizes conservative estimates to ensure safety and reliability in the predicted fatigue life of the connectors. Two distinct methods, the linear regression analysis and the elbow method, were utilized, and consistent results were observed across both approaches. Additionally, the methods were compared against experimental data for the 0.3 mm displacement range increase was actually reached. This validation demonstrated that predictions based on partial data were well-aligned with dataset of experimental results. Although absolute accuracy is impractical in predictive modeling, the methodologies provide credible lower and/or upper-bound estimates, ensuring a reliable and conservative assessment of the iSRR connector's fatigue life. The following key conclusions are drawn:

- A final overall F-N curve was established, incorporating data from all load ratios, providing a comprehensive fatigue life prediction for the iSRR connectors. The R

= -1 curve, representing fully reversed loading, exhibited the most rapid fatigue degradation and serves as a conservative lower bound, particularly at lower load levels. However, at higher load levels, other load ratios, especially $R = 0.5$, demonstrated significantly better fatigue performance. The preliminary $F\text{-}N$ curve at room temperature was derived using a displacement range increase of 0.3 mm as the failure criterion, yielding a slope with $m = 6.7$. The iSRR connectors exhibited remarkable fatigue resistance, with no failure observed at low and medium load levels after 2.5E+06 and 1.5E+06 cycles, respectively, while high load levels reached the failure criterion after approximately 1.2E+06 cycles. These findings support the suitability of iSRR connectors for structural applications subjected to cyclic loading, offering high fatigue tolerance under typical conditions.

- When the temperature was increased to 55 °C, a reduction in the fatigue performance of the iSRR connector was noted. The slope of the $F\text{-}N$ curve decreased to $m = 5.7$, indicating that elevated temperatures have a detrimental effect on the fatigue strength. The reduced slope and downward shift of the $F\text{-}N$ curve imply that connectors subjected to higher temperatures endure fewer cycles before reaching the failure threshold. This highlights the thermal sensitivity of the resin-steel interface and suggests that, while the iSRR connectors exhibit good fatigue performance at ambient temperatures, additional considerations must be made for elevated temperature environments.

- The influence of one-year environmental aging was evaluated for iSRR connectors submerged in water and those exposed to outdoor conditions. The submerged connectors demonstrated accelerated stiffness degradation, reaching the failure criterion much earlier (around 2×10^4 cycles) compared to the outdoor-aged and reference connectors (approximately 7.5×10^5 cycles). This highlights the significant detrimental effect of prolonged water exposure. However, the connectors aged outdoors showed a performance comparable to that of the reference connectors tested at room temperature, suggesting that outdoor exposure had minimal impact on their fatigue resistance. Given that the intended application for these connectors is in bridge structures that will always be in non-submerged conditions, the observed outdoor-aged performance is promising and supports their reliability in realistic field conditions.

- The linear regression and elbow methods provide valuable yet distinct predictions for the number of cycles to failure criterion: linear regression offers reliability more closely aligned with experimental data, while the elbow method ensures conservative estimates, most suitable for safety-critical applications.

IV

Analysis and Prediction of Fatigue Behavior of iSRR Connector

8

Damage mechanisms of iSRR connector

The cyclic behavior of the iSRR connector is characterized by a cumulative increase in displacement range over repeated loading cycles, without a clearly defined failure initiation point. Understanding the underlying damage mechanisms is crucial for predicting long-term performance and improving the connector's fatigue resistance. This chapter investigates these mechanisms through numerical simulations conducted in ABAQUS®, focusing on the progressive deterioration of the connection under cyclic shear loading. The objective is to identify and quantify the contributions of different failure modes to the overall stiffness degradation observed in experimental tests. Unlike previous analyses, this study does not account for environmental factors such as temperature variations or moisture exposure.

This chapter is structured into six sections. Section 8.1 identifies the primary damage mechanisms influencing the cyclic behavior of the iSRR connector, categorizing them based on their contribution to stiffness degradation and displacement range increase. Section 8.2 outlines the numerical modeling approach, detailing the FE set-up, material properties, and boundary conditions used to simulate these mechanisms. Section 8.3 presents the numerical results while Section 8.4 analyzes the impact of individual and combined damage mechanisms on connector performance. Section 8.5 validates the numerical models against experimental data, incorporating findings from cyclic and creep experiments to assess the accuracy of the simulations. Finally, Section 8.6 summarizes the key conclusions, highlighting their implications on the fatigue performance.

8.1. Decomposition of damage mechanisms of the connector

To understand the potential damage mechanisms that may occur during cyclic loading of an iSRR connector, one must first thoroughly comprehend the mechanisms of load transfer during the application of shear cyclic loading. In practical scenarios, loads are typically introduced by wheel traffic, conveyed through the GFRP top facing, down to the webs, and

then to the bottom facing. The load is then transmitted to the SRR material, through the bolt rod, and finally to the steel girder.

In contrast, during the laboratory cyclic loading experiments, a reverse loading protocol is applied, where the load is applied to the steel plates and then transferred through the structure in reverse order. This reversed approach in experimental set-ups is used to enumerate the possible damage mechanisms. A detailed view of the possible damage mechanisms is shown in Figure 8.1. It should be noted that the level of bearing stresses around the composites hole are considered minimal and therefore no fatigue damage is considered to take place in the facing, as confirmed by inspecting connectors specimens after the tests. Additionally, preliminary analyses highlighted the negligible effect of the foam on the accumulation of displacement range and therefore is excluded. Finally, the five potential damage mechanisms (DM) considered are:

1. **DM1**: Interface between nuts and SRR. The preloading of bolts transmits load to the SRR. This interface is susceptible to tensile (mode I) failure.

2. **DM2**: Stiffness degradation in SRR. The stiffness of the SRR material, especially in the compression region confined by composite facing, can diminish, potentially leading to an increased displacement range.

3. **DM3**: Longitudinal cracks in SRR. Following stiffness degradation, cracks may develop and split the SRR injection body, predominantly perpendicular to the load direction.

4. **DM4**: Interface between SRR and GFRP. The transfer of load from SRR to the GFRP interface can induce tensile cracks (mode I), intensifying fatigue degradation in a similar fashion as DM1.

5. **DM5**: Interface involving bolt rod and bolt head with SRR. The load transfer from the bolt head and rod to the SRR, through their interface, is prone to tensile (mode I) cracking, which may further contribute to fatigue degradation.

8.2. Description of numerical analysis

The FE model set-up follows a similar approach to that used in Chapter 5, which was developed to design the experimental set-up. This chapter builds upon that foundation, with specific modifications introduced to capture the damage mechanisms of the iSRR connector. For a detailed description of the general modeling approach, readers are referred to Section 5.6, while key alterations relevant to this study are outlined below.

The FE models represent half of the GFRP deck, including the embedded iSRR bolted connector, and one steel end detail composed of a steel plate with two stiffeners. The iSRR connection is explicitly modeled, incorporating embedded bolts, nuts, and washers while omitting the threaded sections. To maintain a representative mechanical response, the bolt rods are modeled using their minor diameter of 23 mm rather than their major or pitch diameter. This follows the methodology described by Pavlovic [93] and ensures an accurate representation of an M27 bolt under cyclic loading.

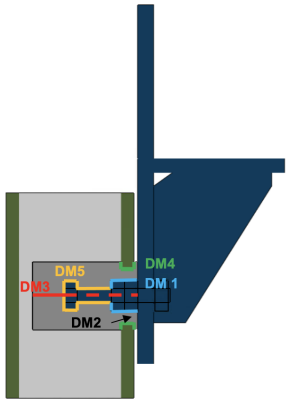

Figure 8.1: Possible damage mechanisms in iSRR connection.

Defining the interaction properties between the SRR material and associated components like the bolt, nuts, washer, and GFRP facing is crucial and the main difference from the FE model described in Section 5.6. Considering that the SRR material exhibits cracks or debonding during fatigue testing, several models are developed to simulate all potential damage mechanisms independently and in combination. The reference model assumes an undamaged SRR block and interfaces, employing an elastic modulus (E) of 16.2 GPa and tie constraints at every interface. To simulate the stiffness degradation in SRR, additional models incorporating a 50% reduction in the elastic modulus across the entire SRR volume are employed. For the representation of potential interface damage, tie constraints are removed from candidate interfaces and replaced by a contact interaction utilizing a friction coefficient of 0.2. The SRR material and at its contact interfaces, including the GFRP bottom facing, bolt rod, nuts, and head are considered as the candidate interfaces to represent damage mechanisms DM1, DM4 and DM5. The modeling of longitudinal cracks within the SRR material follows the same approach on the embedded splitting crack. By altering these interface conditions, the simulations adeptly depict various internal and external crack development scenarios. Furthermore, a tie constraint is strategically implemented between the washers and steel plate to accurately mimic the real-world clamping effect attributable to preloading.

8.3. Numerical results

Taking into account the five damage mechanisms delineated previously, a total of 32 FE models are analyzed to thoroughly investigate these phenomena. This suite of models includes a diverse array of configurations: five models isolate each damage mechanism individually; ten models explore pairs of damage mechanisms in combination; another ten models examine interactions among three damage mechanisms; five models are dedicated to assessing the effects of four combined damage mechanisms. Additionally, one comprehensive model incorporates all five damage mechanisms to gauge their collective impact. Completing this set is a reference model, which incorporates none of the identified damage mechanisms,

serving as a reference for comparison.

The force-displacement curves for the five models, each exclusively representing a distinct damage mechanism, are presented in Figure 8.2. This figure also includes the force-displacement curve of the reference model for comparative analysis. The displacement values reported in these graphs represent the relative displacement between the bottom facing of the composite deck and the steel plate at the connector level. This approach is designed to replicate the relative displacement measurements captured by the LVDTs in the experimental set-ups. These graphs facilitate the calculation of the displacement range increase, which can be determined by subtracting the displacement of the reference model from the displacement observed in the models with the introduced damage mechanisms, at a specified load level. The final displacement range increase should be adjusted based on the load ratio.

Although all material properties serving as input for the model are linear, some combinations of damage mechanisms exhibit nonlinear behavior. This nonlinearity arises from the incorporation of contact interactions at damaged interfaces, leading to geometrically nonlinear effects. Consequently, the results are represented in the form of load-displacement curves to capture such behavior accurately. This also implies that the displacement range increase, as evaluated through the proposed modeling procedure, is not necessarily proportional to the applied load level, as would be expected in a purely linear (both materially and geometrically) model.

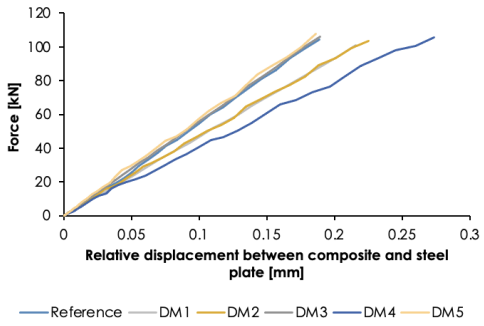

Figure 8.2: Force displacement graph of models that isolate every damage mechanism individually and reference model.

8.4. Influence of single and combined damage components

After conducting simulations with all 32 models, a "heat map" is presented in Figure 8.3, illustrating the outcomes of these simulations. This heat map specifically visualizes the increase in displacement range, a value derived by calculating the difference between the displacement in the reference model and that in each model encompassing various damage mechanism combinations. This analysis is conducted at a maximum load level of +80 kN, under a load ratio of R = -1, assuming equivalent damage when the load is reversed to -80 kN. Notably, the results indicate that the most significant single damage mechanism contributing to the increase in displacement range is DM4 i.e., damage at the GFRP to SRR

interface with 0.368 mm displacement range increase. Conversely, the data suggest that cracks within the SRR, and debonding at the interface between the SRR and the bolt, have a minimal impact on displacement range increase.

		DM1 + DM2	DM1 + DM3	DM2 + DM3	DM1 + DM4	DM2 + DM4	DM3 + DM4	DM1 + DM2 + DM3 + DM4
DM1	0.132	0.304	0.201	0.371	0.394	0.554	0.397	0.566
DM2	0.077	0.304	0.371	0.082	0.554	0.504	0.507	0.566
DM3	0.006	0.371	0.201	0.082	0.397	0.507	0.369	0.566
DM4	0.368	0.554	0.397	0.507	0.394	0.504	0.369	0.566
DM5	0.000	0.323	0.424	0.091	0.395	0.502	0.371	0.566
DM1+DM5	0.155	0.323	0.424	0.444	0.395	0.559	0.400	0.566
DM2+DM5	0.091	0.323	0.444	0.091	0.559	0.502	0.507	0.566
DM3+DM5	0.005	0.444	0.424	0.091	0.400	0.507	0.371	0.566
DM4+DM5	0.368	0.559	0.400	0.507	0.395	0.502	0.371	0.566

Figure 8.3: Heat map of every damage mechanism and possible combintations at ±80 kN.

Figure 8.4 presents maximum principal stress distributions in the SRR piece of the iSRR connector under a load of 80 kN, with different damage mechanisms (DM1-DM5) modeled. Comparing the models to the undamaged configuration, in Figure 8.4a, provides insights into how different damage mechanisms impact stress distribution. In DM1, a crack is embedded at the interface between the nuts and SRR, resulting in a reduction of peak stress values and indicating a more distributed load transfer with reduced stiffness at the interface compared to the fully tied condition.

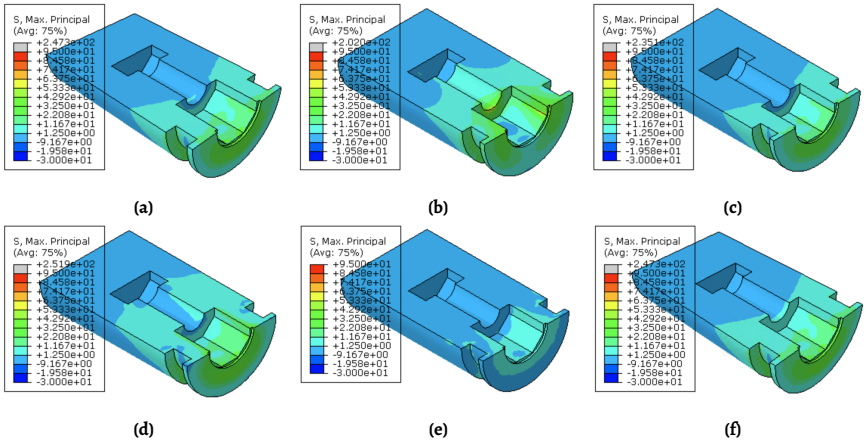

Figure 8.4: Maximum principal stresses in SRR piece at 80 kN with different damage components: (a) Tie, (b) DM1, (c) DM2, (d) DM3, (e) DM4, (f) DM5.

For DM2 (Figure 8.4c), which models stiffness degradation in the SRR material, the results indicate a lower peak stress and a more evenly distributed load, signifying that stiffness reduction results in increased compliance. DM3, involving longitudinal cracks in the SRR and presented in Figure 8.4d, leads to significant stress redistribution, which may reduce peak stresses but could potentially introduce fatigue issues over time. In DM4

(Figure 8.4e), a crack at the interface between SRR and GFRP results in reduced stress concentration, suggesting that allowing some movement at this interface can mitigate damage accumulation by redistributing stresses. Finally, in DM5, introducing a crack at the bolt rod and bolt head interface with SRR has almost negligible influence, as shown in (Figure 8.4f).

Overall, these models demonstrate how different damage mechanisms can alter the stress distribution in the iSRR connector. Introducing cracks and allowing specific interfaces to experience movement generally results in a more compliant system with lower stress peaks. Understanding the effects of each damage mechanism is crucial for optimizing the design and ensuring the reliability of the connector under cyclic loading conditions.

8.5. Model validation

The numerical analysis presented here enables the estimation of both upper and lower bounds for the initial and fully degraded stiffness of the connectors. This is achieved by incorporating tie constraints for the upper bound and introducing cracks at the interfaces along with a reduction in SRR stiffness as the lower bound. The connectors that actually failed under ±80 kN reached an average displacement range increase equal to 0.95 mm, as shown in Figure 8.5. From the performed analysis, the calculated displacement range increase is smaller than the contributions of every damage mechanism combination as shown in Figure 8.3. This suggests the presence of additional failure mechanisms not accounted for in the current analysis.

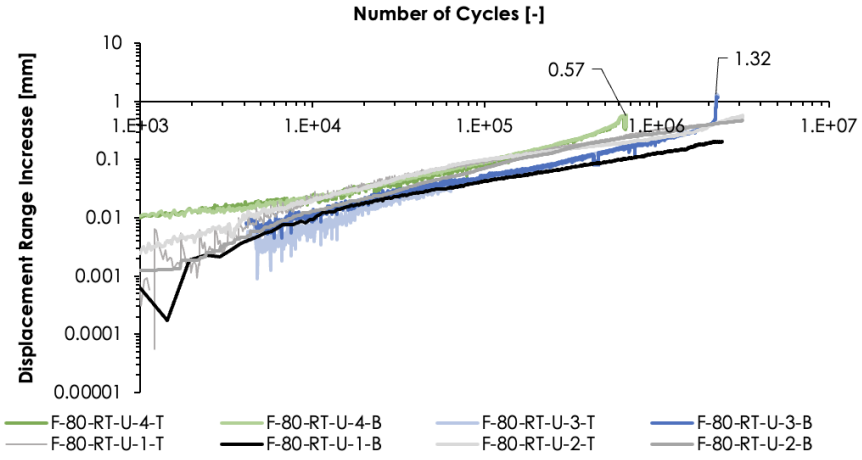

Figure 8.5: Displacement range increase during ±80 kN cyclic testing.

A plausible explanation for this disparity could be the accumulation of plastic strain in the iSRR connector, a phenomenon that might be better understood through creep experiments. Supporting this hypothesis, Olivier et al. have conducted experiments where iSRR connectors were subjected to a sustained load of 40 kN, and the resultant creep displacements were monitored over a period of two months. These creep displacement results are depicted in Figure 8.6 [21].

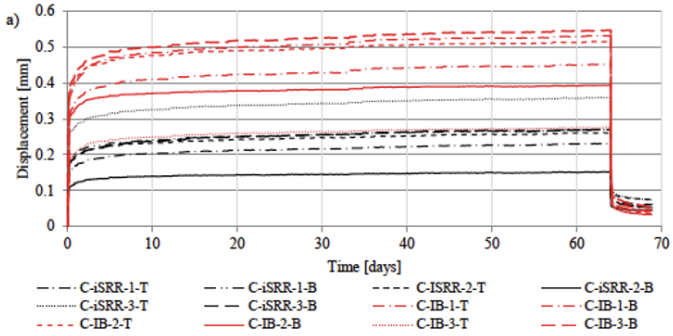

Figure 8.6: Elastic and creep displacement as well as the recovery phase during 2 months of sustained 40kN tensile shear loading [21].

In an initial estimation for a connector subjected to cyclic loading at ±80 kN, it is reasonable to assume that the mean force acting quasi-permanently to each side of the SRR injection piece approximates ±40 kN. Consequently, for the experiments conducted at ±80 kN, as shown in Figure 8.5, the creep displacements from Figure 8.6 are applicable for analysis. For instance, the experimental set-ups F-80-RT-2-T and F-80-RT-2-B were subjected to 3.13E+06 cycles at a frequency of 4 Hz, translating to a total test duration of 9 days. This implies that the connectors experienced 4.5 days of sustained loading at 40 kN and another 4.5 days at -40 kN. By applying the creep displacement data from Figure 8.6 to these conditions, an additional creep displacement of approximately 0.44 mm can be inferred as attributable to the creep phenomenon.

Another approach to validate the numerical results is by focusing on comparing the initial experimental stiffness (linear regime) of the force displacement graph with the one obtained numerically. In the FE software two points are selected to obtain the vertical displacement and the one displacement is subtracted by the other to be comparable with the displacement of the LVDTs. Figure 8.7 illustrates the impact of different interaction models on system performance, particularly focusing on the initial stiffness of the connector.

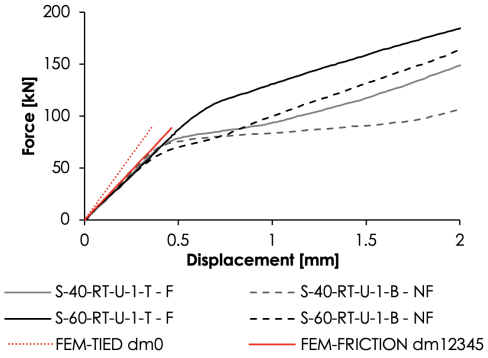

Figure 8.7: Comparative force-displacement responses of iSRR connector.

The numerical model representing the undamaged connector (tied constraints on all candidate crack interfaces), which prevents any slip or damage initiation in the SRR material, shows a stiffer response compared to post cyclic quasi-static tests on damaged connector specimens. Such relation is to be expected. Conversely, the model introducing all candidate cracks is well-capturing the lower bound of stiffness observed in the post-cyclic static experiments. The experimental curves, particularly for the S-60-RT-U-1 series, exhibit less compliant behavior as displacement increases, reflecting potential initiation of damage mechanisms not captured by the purely elastic numerical models. This emphasizes that the initial stiffness behavior is useful for estimating the early-phase response, while subsequent deviations highlight areas where additional damage models could improve prediction accuracy.

8.6. Conclusions

This chapter focused on investigating the damage components affecting the iSRR connector under cyclic loading conditions, aiming to understand how different interaction properties influence stiffness degradation. A total of 32 FE models were analyzed to isolate and combine the five identified damage components. Results provided insights into stress distribution, displacement range increase, and stiffness changes, enabling the development of more predictable connector designs for fatigue applications. In line of these, the following conclusions can be drawn:

- Damage occurring at the GFRP-SRR interface was found to contribute up to a 50% increase in displacement range, making it the most influential component compared to other damage mechanisms.
- The numerical analyses enabled the estimation of the upper and lower bounds for both initial and fully degraded connector's displacement range under cyclic loading. This was achieved by either maintaining tie constraints to represent an undamaged state or converting them to contact interactions to simulate crack formation at critical interfaces. Notably, the crack embedded model corresponded closely to the lower bound of connectors' stiffness observed in post-fatigue static experiments. The absolute difference in connector deformation between the lower and upper bounds at a load level of ±80 kN was quantified as 0.57 mm.
- Discrepancies between experimental observations and model predictions with respect to the absolute displacement range increases, notably the increased slip at ±80 kN, suggest that additional failure mechanisms, such as creep and plastic deformation, are present. Based on data from literature, creep was estimated to contribute an additional displacement of 0.44 mm, leading to a total displacement range increase of 1.01 mm.
- Although the stiffness degradation of the SRR alone did not significantly increase slip, combining this degradation with damage at the GFRP-SRR interface resulted in 90% of the maximum observed increase in displacement range (0.57 mm).

9

Computational prediction of steel reinforced resin behavior

This chapter presents the FE-based prediction and validation of SRR behavior under cyclic loading. The chapter begins by introducing a micro-mechanical model to ensure that using a simplified phenomenological model based on CDM principals is valid and reflects the underlying physics of the material's failure. The developed CDM model, implemented via a custom subroutine, is validated against experimental data, demonstrating its ability to predict stiffness degradation and failure modes under both compression and tension conditions. The subroutine is applied beyond coupon-scale experiments to model the behavior of iSRR connectors embedded in GFRP decks, highlighting its applicability to complex 3D structures.

The chapter is structured into seven sections. Section 9.1 introduces the micro-mechanical modeling of SRR material through finite element simulations of a Representative Volume Element (RVE), capturing the material's local heterogeneity. Section 9.2 presents the physical motivation and empirical calibration behind the CDM approach. Section 9.3 describes the FE model set-up used for implementing the subroutine, while Section 9.4 details the subroutine's implementation within the software. Section 9.5 then evaluates the cyclic response of SRR material under compression and tension, validating the CDM-based model against experimental results and observed failure modes. Section 9.6 applies the model to the iSRR connector embedded in a GFRP deck, demonstrating the subroutine's ability to capture damage evolution in 3D geometries. Finally, Section 9.7 summarizes the key findings and insights from the computational analyses.

9.1. Micro-mechanical modeling of SRR material

Heterogeneous materials like SRR, composed of steel balls embedded in a resin matrix, exhibit distinct properties and interact at a microscopic scale. Micro-mechanical modeling typically involves numerical simulation of a RVE, which captures these complex interactions

Parts of this chapter have been published in Christoforidou et al. [91].

and reflects the material's local heterogeneity. This method reveals specific micro-structural details responsible for non-linear material behavior, providing valuable insights into SRR stiffness, interfacial strength, and failure mechanisms. Similar micro-mechanical approaches have been applied in thermal studies of highly filled composites, where particle contact and interface properties were shown to significantly influence material behavior [111].

This section validates the behavior of a fine-scale finite element model, consisting of limited amount of steel balls and resin interacting within a microscopically small structure, against the unconfined and confined compressive experimental static behavior of SRR, as discussed in Chapter 4. The use of a periodic hexagonal packing follows common micro-mechanical modeling strategies for particulate composites, where idealized arrangements enable efficient analysis of stress distribution and interfacial effects. Prior studies have shown that hexagonal packing can reliably reproduce the macroscopic stiffness and local stress behavior of composites with circular inclusions [112]. Bayat and Aghdam [113] demonstrated that hexagonal RVE more reliably capture local stress distributions and yield behavior in fibrous composites compared to square arrangements, further validating this choice. While the current model uses this idealized structure, real SRR material likely exhibits non-uniform packing. As demonstrated in [114, 115] such particle clustering can significantly reduce failure strain, increase local stress concentrations and promote early interface damage. This suggests that although the present model is representative for average conditions, future work could incorporate spatial randomness to assess the influence of clustering on damage evolution more comprehensively.

A three-dimensional periodic hexagonal arrangement of the steel balls within the resin matrix is modeled, representing a cubic RVE with dimensions of 3 x 3 x 3 mm, as shown in Figure 9.1. The steel balls, each 1 mm in diameter, are arranged with a global particle volume fraction of 75%, consistent with experimentally observed compaction levels [75]. The mesh model uses geometrically versatile linear tetrahedron elements with four nodes (C3D4) for both steel balls and resin, with a global mesh size of 0.05 mm. This mesh size, determined through a sensitivity study, is adequate to represent the micro-structural interactions and SRR's response under static loading.

The modeled components are assigned two distinct material properties. The steel balls have isotropic elasto-plastic properties (E = 210 GPa, ν = 0.3), with the nominal stress-strain relationship for plasticity assuming 355 MPa as onset of yielding followed by linear hardening towards 480 MPa with 20% plastic strain [116]. The resin is also modeled as elasto-plastic (E = 3 GPa, ν = 0.35), with stress-strain data assuming ideal elasto-plastic behavior with yield limit of 70 MPa as lower bound estimate of resin strength incorporating various imperfections and stress concentrations on level scale smaller than the one modeled here. A ductile damage material model is applied to the resin, accounting for post-peak behavior through modulus reduction, with initiation and damage evolution parameters derived iteratively to match micro-mechanical stress-strain curves with experimental results.

The damage initiation criterion is defined by the equivalent plastic strain at the onset of damage, $\bar{\epsilon}_0^{pl} = 0.025$, dependent on stress triaxiality (θ). For this quasi-static analysis, strain rate effects are neglected due to slow load application. The equivalent plastic strain at fracture, $\bar{\epsilon}_f^{pl} = 0.2$, is based on findings by M.P. Nijgh [47] for $\theta = 1/3$ (uniaxial tension), with an exponential dependency on triaxiality. A mode-independent damage evolution law

with exponential softening is implemented. The equivalent plastic displacement at failure, $\overline{u}_f^{pl} = 0.01$, is determined by multiplying the characteristic element length that equals 0.05 mm in this study, by the plastic strain accumulated during the damage process.

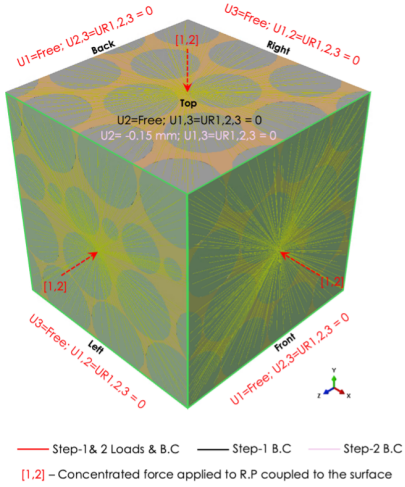

Figure 9.1: FE model of the zoomed-in SRR material system.

To account for the interactions between different component surfaces, a general contact formulation with multiple contact pairs is defined. All contact pairs between resin matrix and steel balls, as well as between the adjacent steel balls, are automatically determined and reassessed during the analysis. A finite-sliding approach using a penalty method enforces tangential contact constraints according to Coulomb friction. The friction coefficient is set at 0.2 between steel balls and 0.4 between steel balls and resin, with 'hard' pressure over-closure for normal behavior.

Surface-based cohesive behavior between steel balls and resin is modeled with a bilinear traction-separation law for interface constitutive behavior, relating normal and shear stresses to their separations. A quadratic traction failure criterion evaluates damage initiation, assuming for simplicity equal normal and shear maximum traction of 16 MPa in this study. Mixed-mode energy-based linear softening is applied to model cohesive stiffness degradation, using the Benzeggagh-Kenane fracture criterion (exponent 2). Fracture energy parameters are determined iteratively by comparing the meso-level cylinder compressive experiments to the micro-mechanics model, and are set equal to $G_{.I} = 0.1$ N/mm and $G_{.II} = G_{.III} = 0.2$ N/mm. As it can be noticed a number of model parameters related to constituent material and interface behavior are either assumed, simplified or phenomenologically calibrated by comparing the results to meso-level experiments. The aim here is to show potential of such a model and use it to better understand physical behavior of the SRR material. Therefore, such approximate approach in determining the parameters within the bounds of physically acceptable ranges is deemed appropriate for the aim of this study. More elaborate modeling focusing on the potential of such micro-mechanical model to optimize and completely characterize the material behavior. e.g. for multi/axial stress states or aging, can be conducted in future.

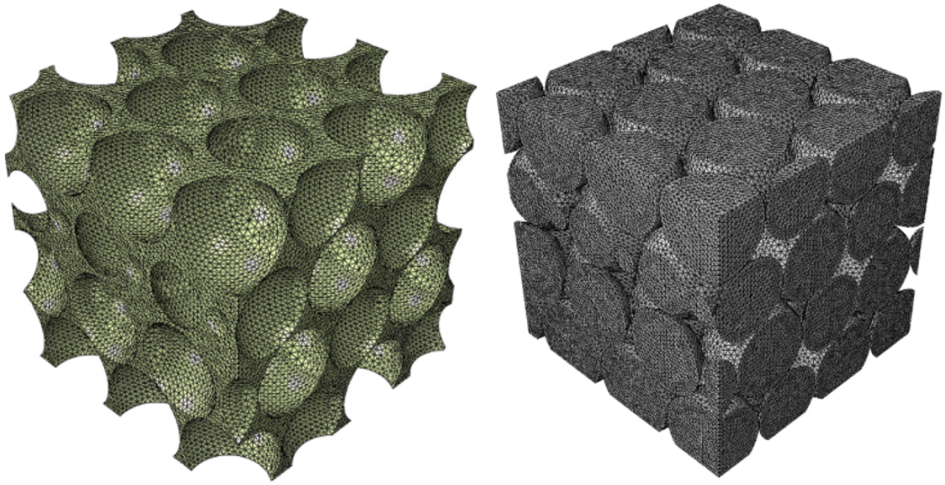

(a) (b)

Figure 9.2: Mesh applied in both parts: (a) Resin, (b) Steel balls.

The analysis of the micro-mechanical SRR model under confinement is performed in two sequential steps, as shown in Figure 9.1. In Step 1, confinement is applied compressively to reference points on the cube's side faces, kinematically coupled to the corresponding surfaces. In Step 2, confinement remains constant, and a compressive displacement of 0.15 mm is applied to the top and bottom faces. ABAQUS®/Explicit solver is utilized to resolve complex non-linear material and interface behavior, large deformations and multiple complex contact interactions (steel balls sliding on each other). Inertial effects are minimized using mass scaling with a time increment of 0.005 s for both the confinement (can also be understood as preloading) and the load application steps of the analysis. A smooth time-dependent load amplitude function is used with an artificial time period of 100 and 300 s, respectively. The FE model without confinement includes a single step where imposed displacement is applied.

Using the defined material and interface parameters in the fine-scale FE model, stiffness, Poisson's ratio, and failure progression are analyzed to correlate the compressive behavior across varied geometries. The stress-strain diagram in Figure 9.3 shows that the initial stiffness of the micro-mechanics model closely aligns with the experimental data, exhibiting a Young's modulus of 11.7 GPa. This agreement highlights the accuracy of the FE model in capturing the initial linear response of SRR material under compressive loading, contributing to a reliable understanding of its behavior.

Points A, B and C indicated in the stress-strain diagram in Figure 9.4 show the progression of damage at the interface between the steel balls and the resin. Notably, points B and C confirm the hypothesis in Chapter 4 concerning the development of micro-cracks and localized interface damage in post-peak region. While the micro-mechanics model cannot fully capture the post-peak behavior due to convergence limitations, it provides valuable insights addressing the modeling objectives.

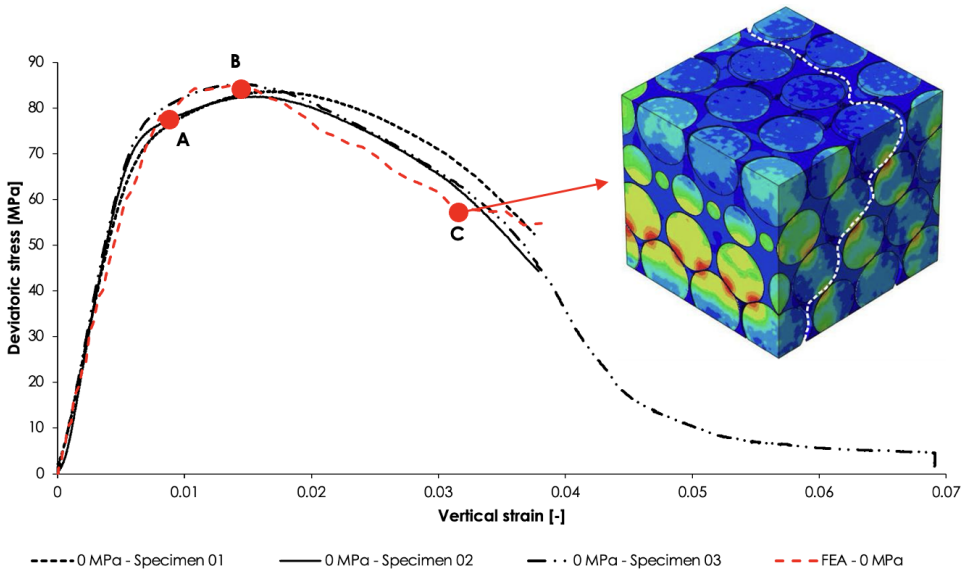

Figure 9.3: Compressive behavior of SRR as predicted by the micro-mechanics model.

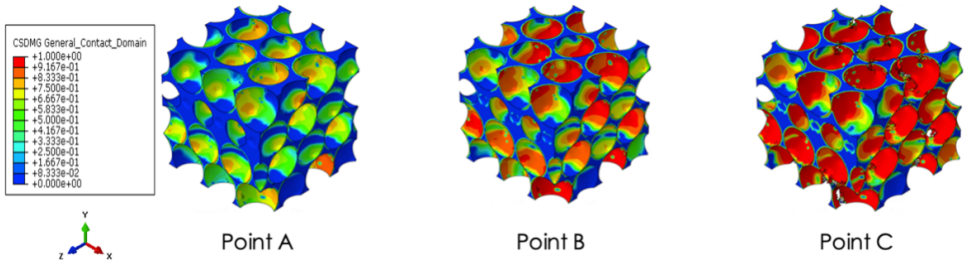

Figure 9.4: Degradation of interface between steel balls and resin at various points on the stress-strain curve.

To thoroughly examine and understand the effects of elevated confinement, the existing FE model is analyzed under increased confinement levels of 10, 20 and 30 MPa, similar to the experiments presented Chapter 4. The stress-strain diagram of the micro-mechanical prediction along with the corresponding experimental results under elevated confinement, are presented in Figure 9.5. The predicted Young's modulus values for 10, 20 and 30 MPa of confinement correspond to 10.4, 10.88 and 12.39 GPa, respectively. These values conform closely to the experimental values presented in Chapter 4.

To assess the interface damage, two points are identified for each confinement level. Points A1, A2 and A3 indicate comparable levels of interface damage at the onset of non-linearity. Similarly, points B1, B2, B3 demonstrate consistent damage levels. This suggests that higher confinement delays the initiation of non-linearity, resulting in higher ultimate stress. The transition from the elastic region to the plateau is driven by progressive interface damage. Regions A1, A2, A3 mark the onset and gradual progression of damage ($D > 0$) until its full development ($D = 1$) near the beginning of the plateau at a certain point in the

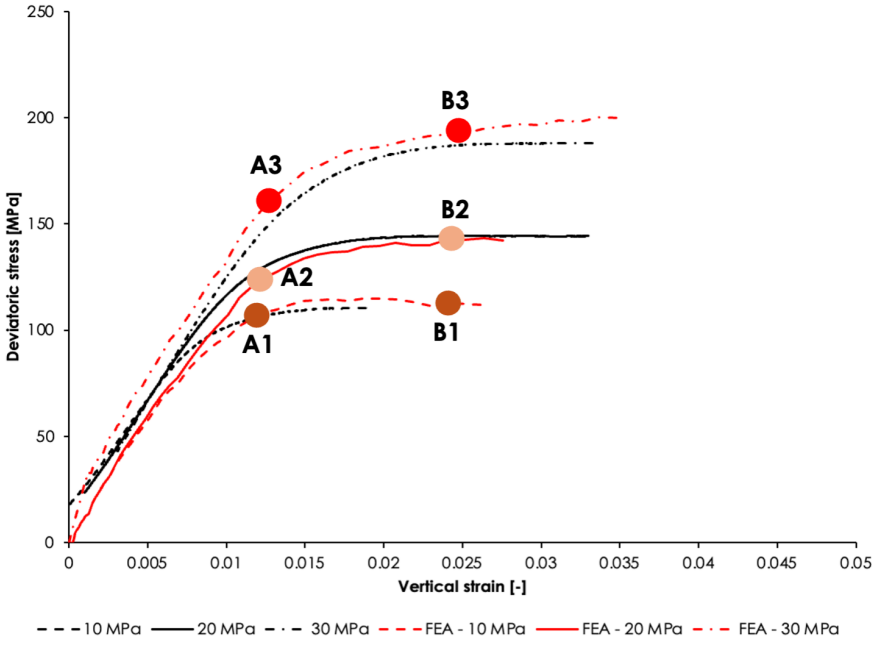

Figure 9.5: Triaxial compressive behavior of micro-mechanical FE model against the experimental results.

interface. The plateau region corresponds to the full progression of interface damage in regions between the balls and the resin, as depicted in Figure 9.6. The presence of confinement slows the damage evolution, promoting a smooth non-linear response and plateau formation.

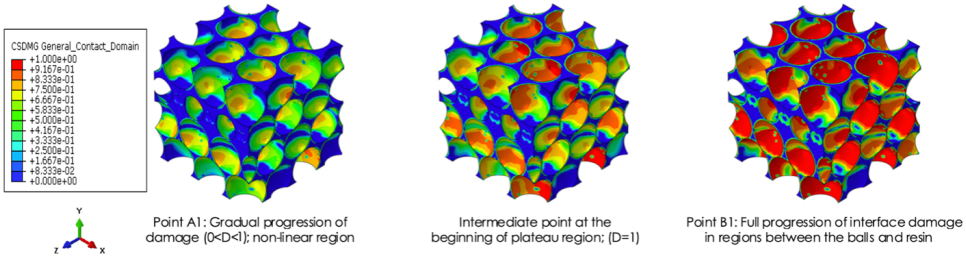

Figure 9.6: Degradation of interface between steel balls and resin at various points on the stress-strain curve.

The results presented above demonstrate that the micro-mechanical FE model is well able to predict the uniaxial and triaxial compressive behavior observed in the cylindrical steel-reinforced resin experimental campaign. With the fine-scale model validated for compressive scenarios, additional simulations are conducted without confinement to study the tensile behavior. This study is used to further validate this model based on the Poisson's ratio derived from indirect tensile splitting tests, as discussed in Chapter 3. The stress-strain response of the RVE under tensile loading is illustrated in Figure 9.7.

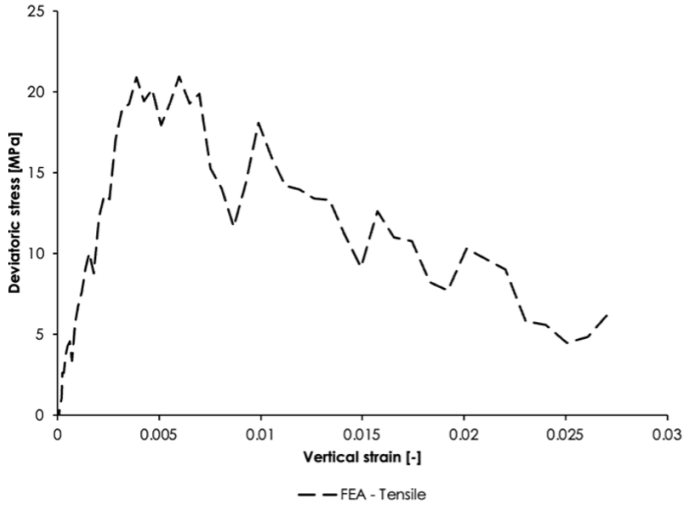

Figure 9.7: Tensile behavior of SRR as predicted by the micro-mechanics model.

The tensile strength is significantly lower than the compressive strength, exhibiting a reduction of approximately 75%. This pronounced decrease is primarily attributed to the absence of contact between the steel balls under tensile loading, which forces the resin to carry the entire load. As a result, the initial stiffness drops to 5.2 GPa. This change in the load transfer mechanism not only affects stiffness but also leads to a noticeable alteration in the material's Poisson's ratio.

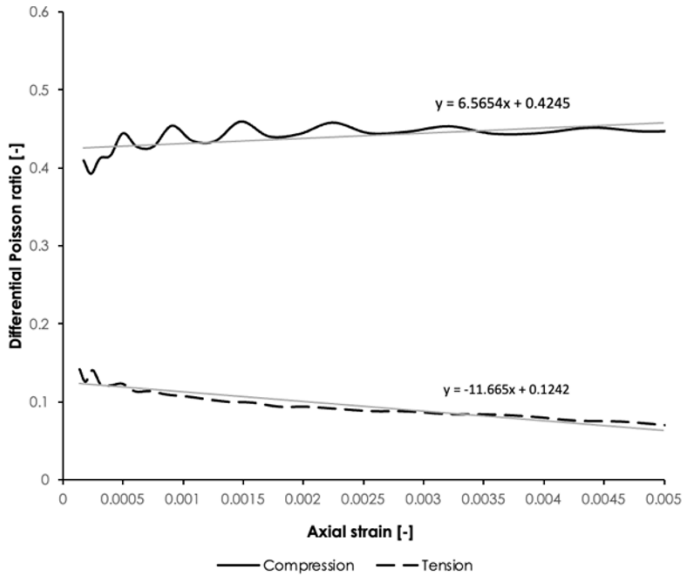

Figure 9.8: Differential Poisson's ratio response of micro-mechanics model with no confinement.

Figure 9.8 presents the differential Poisson's ratio versus axial strain for both compressive and tensile loading conditions. The differential Poisson's ratio, particularly in the tensile case, shows a value of approximately 0.124, which closely resembles to the experimental results from the indirect tensile splitting tests [75]. Under compression, the initial Poisson's ratio is significantly higher, around 0.425, reflecting the pronounced lateral expansion caused by confinement and particle interaction within the granular structure as axial strain begins to develop.

Figure 9.9 provides a fair comparison of the deformed configurations in tension (Figure 9.9a) and compression (Figure 9.9b) under a 0.1 mm applied displacement, with deformations magnified five-fold for clarity. These visualizations reveal the distinct failure mechanisms under different loading modes. Under tensile loading (Figure 9.9a), the resin matrix undergoes brittle fracture along axial planes, with limited lateral contraction. Under compression (Figure 9.9b), failure is more distributed, primarily governed by progressive debonding between the resin and the steel particles, accompanied by pronounced lateral bulging. These contrasting behaviors confirm the asymmetric mechanical response of SRR and reinforce the importance of using distinct material parameters for tension and compression in numerical modeling.

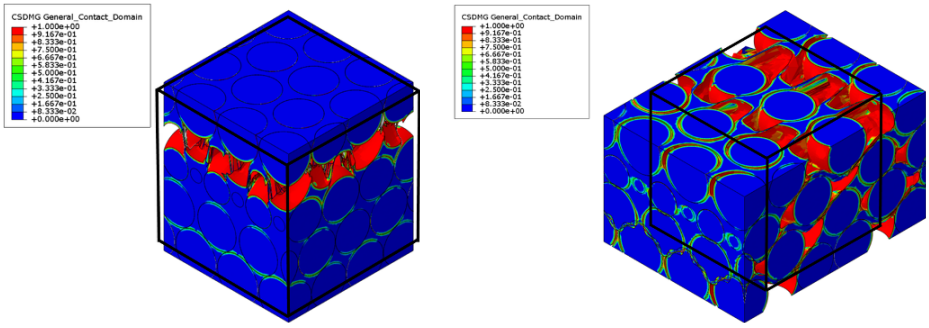

Figure 9.9: Five-times exaggerated deformed shapes of micro-mechanics model under tensile and compressive loading at 0.1 mm applied displacement (black lines represent the undeformed cube): (a) Tension, (b) Compression.

9

9.2. Continuum Damage Mechanics approach

The micro-mechanical modeling described above serves as a foundation for understanding and simulating the fatigue behavior of SRR material. It provides insight into the fundamental failure mechanisms of SRR, such as interface debonding, resin cracking, and particle sliding under compression. By understanding that these are the mechanisms that contribute to stiffness degradation at different phases, it becomes possible to derive a phenomenological model based on existing CDM principles. In other words, understanding SRR failure at the micro-level is crucial as it verifies that the empirical approach used in CDM can sufficiently well predict the meso-level behavior of SRR material in complex structures. The CDM model described below relies on stiffness degradation curves, calibrated from experimental data, to predict material behavior under cyclic loading.

More specifically, the model focuses on tracking stiffness degradation under cyclic loading. For a given stress level, like the fatigue tests in compression and tension presented in Chapters 3 and 4, stiffness degradation curves are derived from experimental fatigue data. These curves represent how stiffness decreases per stress cycles at specific stress levels and can be approximated by a fitting curve represented by the parameters a, b and c. In Figure 9.10 the compression experiment on SRR material at 56.50 MPa is displayed together with the empirical fitting curve. The parameters used in this example are $a = 8$, $b = 2$ and $c = 0.4$ and they define the form of the stiffness degradation curve, expressed as in the formula given below.

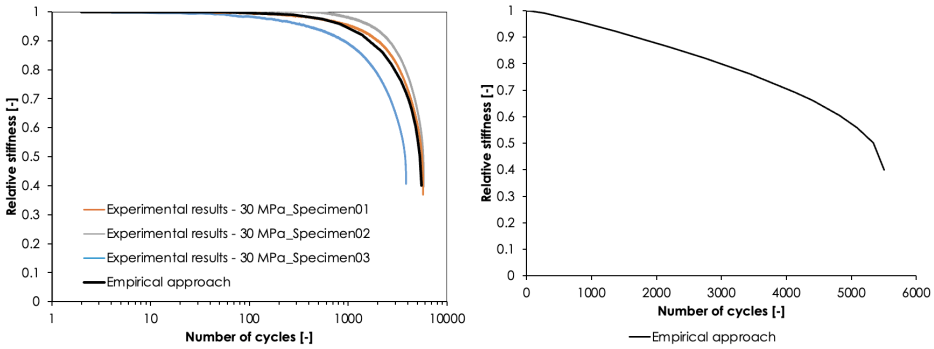

Figure 9.10: Experimental results vs. fitting curve for describing stiffness degradation of SRR material under cyclic compression at stress level of 56.50 MPa: (a) Number of cycles in log scale, (b) Number of cycles in linear scale.

$$\frac{E}{E_0} = \left(1 - \left(\frac{log(nr)}{log(nr_{max})}\right)^{a}\right)^{\left(\frac{1}{b}\right)} \cdot (1 - c) + c \tag{9.1}$$

where E is the current stiffness and E_0 is the initial stiffness. This definition allows to quantify the progressive degradation of stiffness as damage accumulates during cyclic loading. Here, a, b and c are calibrated from experimental data at different stress levels and allow for interpolation and extrapolation to stress levels not directly tested. This enables a generalized prediction of stiffness degradation over a range of constant and uniform cyclic loading conditions like the ones in simple cylinder experiments in Chapter 4.

Once the stiffness degradation is computed the damage variable D can be defined as:

$$D = 1 - \frac{E}{E_0} \tag{9.2}$$

To allow accumulation of damage for various stress states in variable and non uniform conditions (like SRR connector), dD/dN, the incremental change in damage D is calculated with respect to the number of cycles n. The rate dD/dN is computed using the finite difference approximation:

$$\frac{dD}{dN} = \frac{D_i - D_{i-1}}{n_i - n_{i-1}} \tag{9.3}$$

where D_i is the damage at the current cycle n_i and D_{i-1} is the damage at the previous cycle n_{i-1}. Figure 9.11 illustrates this rate of stiffness degradation (dD/dN) for SRR material under compression at a stress level of 56.50 MPa. The rate of damage is presented in two different scales: a logarithmic scale in Figure 9.11a and a linear scale in Figure 9.11b. These visualizations provide insights into how the damage rate evolves throughout the fatigue life of the material. In Figure 9.11a, the logarithmic scale on the x-axis allows for a clearer view of the damage rate behavior across a wide range of cycles. At the initial stages of loading (up to approximately 10 cycles), the rate of damage is very low, near to zero. This corresponds to the material undergoing minor damage with no significant changes in stiffness. As the number of cycles increases (between 10 and 1000 cycles), there is a gradual rise in the damage rate. This region is assumed to correlate to the onset of micro-mechanical damage mechanisms, such as resin cracking and interface debonding, which begin to accumulate more noticeably.

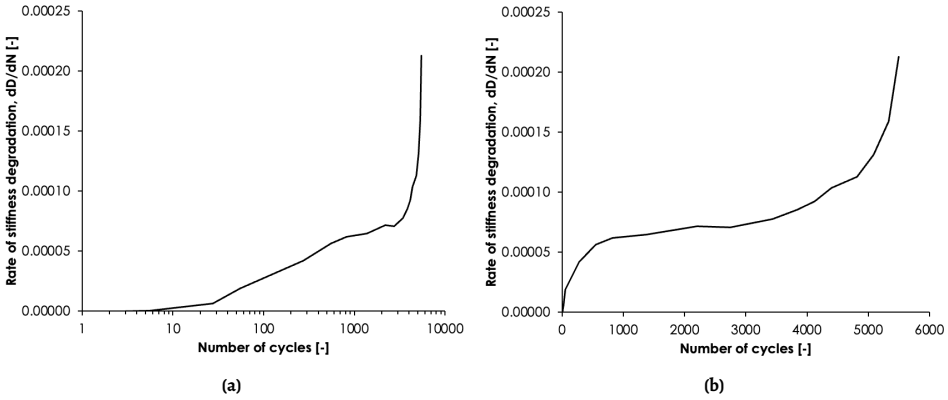

Figure 9.11: Damage rate following the fitting curve of stiffness degradation at 56.5 MPa cyclic compressive stress: (a) Number of cycles in log scale, (b) Number of cycles in linear scale.

For the SRR material under compression at a stress level of 56.50 MPa an inflection point occurs between 1000 and 2000 cycles. Beyond this point, the damage rate begins to increase more significantly. This suggests that damage accumulation has reached a stage where micro-cracks are propagating and interacting with each other, accelerating the stiffness degradation process. As the material approaches failure (beyond 3000 cycles), the damage rate increases sharply, indicating rapid damage progression and imminent failure.

In Figure 9.11b, the linear scale on the x-axis provides a different perspective, focusing on the damage rate progression over a more localized range of cycles. The initial low damage rate is more apparent in this representation, showing a near-zero slope for at the very first cycles. Between approximately 500 and 2000 cycles, the damage rate remains relatively steady, indicating a period where damage accumulation occurs at a consistent, although slow, rate. This phase likely corresponds to the stable propagation of micro-cracks and minor stiffness degradation.

As the number of cycles continues to increase, the damage rate exhibits a more noticeable upward trend, particularly beyond 3000 cycles. The linear scale highlights the sharp increase in damage rate near the end of the fatigue life, emphasizing the transition from stable

damage accumulation to rapid failure. This behavior is characteristic of fatigue damage mechanisms, where localized failures (e.g., crack growth) lead to a cascading effect, causing the material to deteriorate rapidly.

To describe the damage rate not solely dependent on the applied stress level but also on the current level of accumulated damage, Figure 9.12 is constructed. The figure shows the relationship between the rate of stiffness degradation (dD/dN) and the current level of damage D obtained still under constant compressive cyclic loading corresponding to 56.5 MPa. This graph is derived by combining two separate curves: one for damage D as a function of the number of cycles N and another for the rate of damage dD/dN as a function of N. By eliminating the explicit dependence on N, we obtain a direct relationship dD/dN and D for a given stress range as driving parameter for damage progression. This approach allows to understand how the damage rate evolves solely with the accumulation of damage, not only directly dependent of the number of cycles.

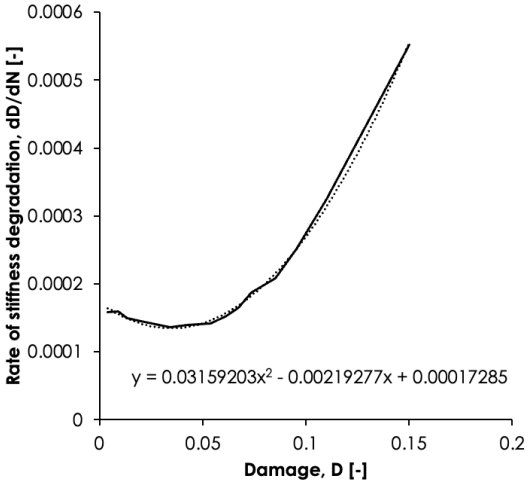

Figure 9.12: Rate of stiffness degradation as a function of damage at constant cyclic loading for a compressive stress of 56.5 MPa.

Based on this, a damage evolution law to track the accumulation of damage at each material point can be obtained. These parameters control the rate of damage accumulation. Once the data is plotted, an appropriate function is used to describe the trend. In this case, a second-order polynomial function is fitted to the data to capture the nonlinear behavior of the damage rate. The polynomial equation describing the curve is given by:

$$\frac{dD}{dN} = \alpha(\sigma) \cdot D^2 + \beta(\sigma) \cdot D + \gamma(\sigma) \tag{9.4}$$

where $\alpha(\sigma)$, $\beta(\sigma)$ and $\gamma(\sigma)$ are determined by fitting experimental data for $\frac{dD}{dN}$ at different stress states. For each tested stress level, a polynomial function is used to fit the $\frac{dD}{dN}$ versus D curve, providing fitted values for α, β and γ. The use of this function allows for interpolation and extrapolation of the damage rate for different levels of damage and stress conditions.

The calibrated model is designed to function beyond coupon-scale experiments. In mechanically loaded structures, different regions experience varying stress states due to complex loading conditions. Not only does the stress field vary within an arbitrary component, but the stress state also changes with the number of cycles as the stiffness of neighboring points degrades. This approach allows each material point to respond to its unique stress level and damage state. Stiffness degradation evolves locally for each point, for each step of the incremental analysis, influenced by the current level of cyclic stress σ and accumulated damage D. This capability enables the model to capture the effects of localized damage and predict how damage propagates in a 3D structure.

In this model, crack initiation and propagation are coupled. In that respect, the crack is not modeled as an infinitely thin surface, like in fracture mechanics approach. Contrary, following the CDM, the crack is modeled as a surface of finite thickness, defined by finite elements with extensively degraded stiffness to simulate the damaged region. The stiffness degradation is assumed immediately for all elements but largely dependent on the cyclic stress (stress range) experienced at each location. Considering an arbitrary large body with non-uniform stress filed, in regions where stresses are high, stiffness degradation will be rapid. In other regions the stiffness degradation (the accumulation of it) will be negligible. Crack formation occurs when damage at a material point exceeds a predefined threshold, such as 5, 10 , 20% or any other value that would emerge from cyclic material tests with uniform and constant stress ranges. Once this threshold is reached, the affected material point can no longer carry load, causing stress redistribution to neighboring regions. This redistribution increases stress levels in surrounding areas, accelerating damage accumulation and initiating a chain reaction that leads to crack growth. Rather than treating crack initiation and propagation as distinct phases, this approach views them as a continuous progression. Damage evolves naturally, with crack propagation emerging as a direct outcome of localized damage reaching critical thresholds.

9.3. FE model set-up for subroutine implementation

The FE models replicate the actual geometries used in the experimental tests for the disk, cylinder, and iSRR connector to ensure reliable simulation of cyclic behavior and stress concentrations. These models maintain the same dimensions as the physical specimens, faithfully capturing the conditions observed in the experiments. The SRR material within these models is assigned an elastic modulus of 16 GPa and a Poisson's ratio of 0.13. Additionally, the SRR material behavior incorporates a user-defined field material model with DEPVAR assignments to account for the internal state variables necessary for the phenomenological damage subroutine. This ensures that both the elastic properties and the damage evolution are captured during the simulation.

In both disk (Figure 9.13a) and cylinder (Figure 9.13b) models, the bottom face is fully constrained, and a compressive load is applied through a reference point on the top face, which is coupled to a steel plate that uniformly introduces the load into the specimen. Both models incorporate steel plates on the top and bottom surfaces to replicate the experimental loading and support conditions. For the cylinder model, this set-up reliably reproduces the diagonal shear failure planes that develop under uniaxial compression loading. For the disk model, the plates ensure uniform loading across the specimen height, leading to the development of tensile stresses along the vertical plane and subsequent crack propagation.

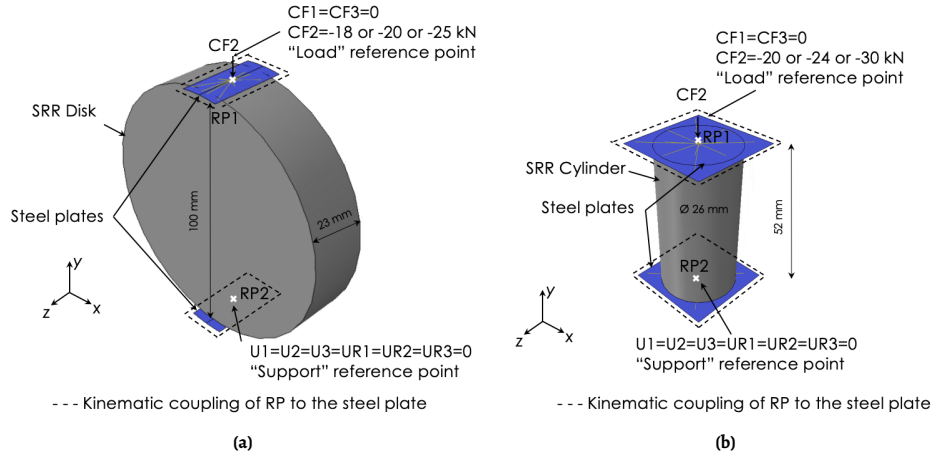

Figure 9.13: Finite element model set-ups with boundary conditions and loading configuration: (a) Disk specimen with steel plates, and (b) Cylinder specimen with steel plates .

The modeling approach adopted for simulating the cyclic behavior of SRR material in ABAQUS® requires careful consideration of stress concentrations inherent in the specimen geometry. Unlike specimens designed for uniform stress distribution, such as the dog-bone specimens used in tensile tests with regions of constant cross-section, the disk, cylinder, and iSRR connector configurations inherently exhibit stress concentration-driven failure planes. In disks, these concentrations arise along the splitting plane due to indirect tensile stresses as consequence of Poisson's effects, while in cylinders, they develop along diagonal shear planes under compression. In the iSRR connector, the SRR material experiences complex stress states influenced by the interaction with surrounding components. Because the phenomenological damage approach in the subroutine is calibrated based on these failure mechanisms, capturing the localized stress concentrations is essential for reliable damage prediction.

To achieve this, the FE models for the disk, cylinder, and the critical SRR region in the iSRR connector are constructed using the same linear hexahedral elements (C3D8R) with a consistent mesh size of 1.5 mm (Figure 9.14). In the disk model (Figure 9.14a) and the cylinder model (Figure 9.14b), the SRR material is discretized with hex elements, while the top and bottom steel plates are meshed using 2.0 mm S4R shell elements. These plates are used to apply and transfer the compressive load uniformly, replicating the experimental conditions. In the iSRR connector model (Figure 9.14c), the region near the shear interface is refined with a 1.5 mm mesh, while the remaining SRR volume is assigned a coarser 3.0 mm mesh to reduce computational cost.

This consistent mesh type and sizing in critical regions ensure that stress concentrations are reliably resolved and that damage evolution is reliably represented. Since the CDM-based subroutine is sensitive to local stress gradients, the accuracy of the results is inherently mesh-dependent. Consistency in both element type and mesh size across all FE models is therefore essential to ensure that the calibrated phenomenological model behaves as predicted in different geometries and under varying boundary and load conditions. It

is important to note that this simulation framework is in an early stage of development at TU Delft and that further refinement is anticipated, particularly in addressing stress concentration effects and calibration limitations in non-uniform stress field conditions.

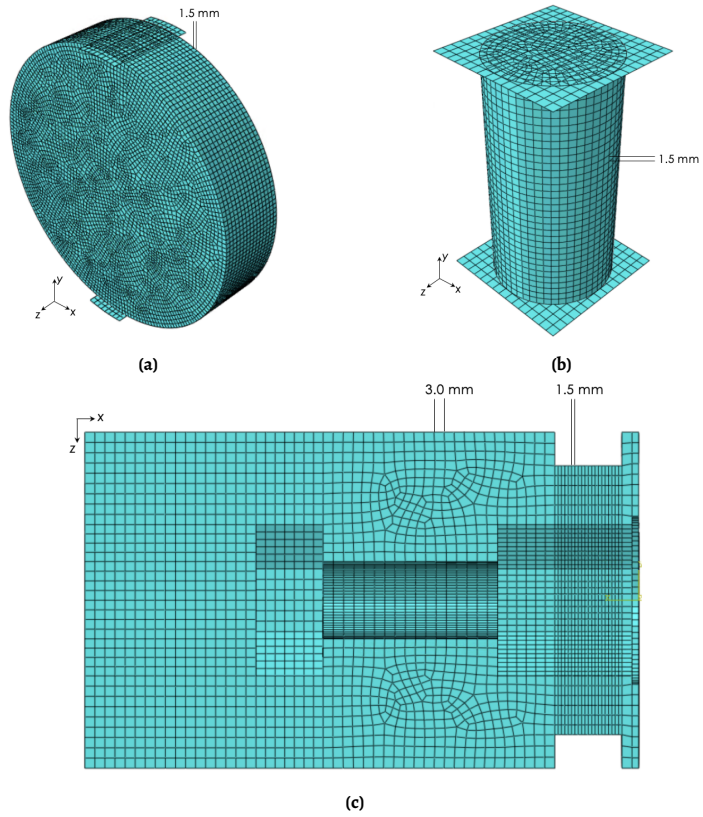

Figure 9.14: Finite element meshing for the models used in the CDM framework: (a) Disk specimen with 1.5 mm C3D8R elements in the SRR and 2.0 mm S4R shell elements in the steel plates, (b) Cylinder specimen with the same mesh configuration, (c) iSRR connector with refined mesh (1.5 mm) around the shear interface and coarser mesh (3.0 mm) elsewhere in the SRR domain.

The boundary conditions and model setup for the iSRR connector are similar to those described in Chapter 8, with several key modifications introduced. First, the loading is applied as a force to represent the cyclic amplitude, whereas in Chapter 8, the load was applied as a displacement through the same reference point. Second, the SRR material in the iSRR connector employs a user-defined field material behavior with the appropriate DEPVAR assignments to define the number of internal state variables for the user-defined material [29]. Additionally, while earlier simulations in other chapters used tetrahedral elements to handle complex geometries, the models in this chapter uniformly adopt linear hexahedral elements (1.5 mm) for the critical SRR regions. This switch ensures consistency with the damage model calibration and improves the accuracy of stress gradient representation, which is essential for reliable predictions. All interfaces between the SRR material

and connected components, such as the GFRP deck, bolts, and nuts, are constrained using tie interactions, consistent with the tie model approach detailed in Chapter 8.

Finally, all the FE models consist of two distinct loading stages: the initial loading stage, where the load is gradually applied, and the "quasi-cyclic" loading stage, where a constant load amplitude is simulated. For a representative model, the total step time is 3000 s, with the load smoothly increasing to its maximum value within the first 500 s and remaining constant thereafter, as illustrated in Figure 9.15, where the smooth transition to the maximum load and the subsequent cyclic loading stage are clearly depicted. This approach ensures the simulations reliably replicate experimental conditions and capture damage progression reliably.

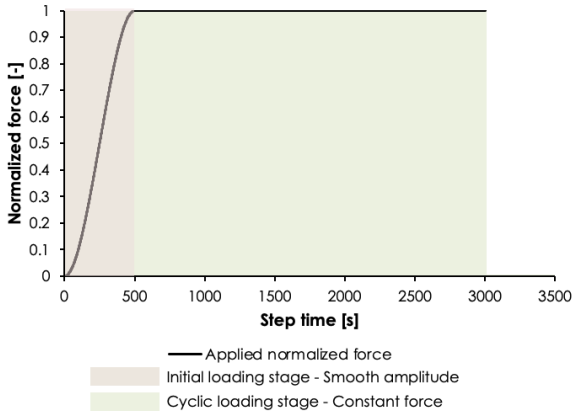

Figure 9.15: Applied amplitude with smooth and constant loading.

9.4. Implementation of CDM fatigue model using subroutine

The cyclic mechanical behavior of SRR material is modeled using a custom subroutine developed within the ABAQUS®/Explicit framework. This subroutine, called VUSDFLD, defines user-specific field variables at each material point. These variables can be calculated based on a function of time, strain, stress, or other material point quantities. Once defined, the field variables can be assigned to any chosen parameter and used to perform various calculations, set limits, or control specific aspects of the material behavior during the simulation. In this work, they are used to simulate damage evolution, stiffness degradation, and failure under cyclic loading. After the analysis is complete, all results related to these field variables are stored and can be accessed within ABAQUS® for further evaluation. The methodology followed in this work represents the nonlinear response of SRR material to cyclic stresses and strains and ensures that damage accumulation aligns with experimental observations.

The implementation of the subroutine follows an approach that integrates several computational processes. At first, stress and strain tensors from the previous increment are retrieved using the utility routine, VGETVRM. These tensors are critical for evaluating the material state at each integration point. Using the retrieved data, the principal stresses and

strains are calculated through the VSPRINC function, which identifies the governing tensile or compressive behavior. Further on, a subroutine is developed which enables modeling the cyclic damage evolution in the SRR material. It computes incremental damage based on the stress and strain history at each integration point, at each increment of explicit dynamic analysis.

The finite element analysis consists of two distinct loading stages: the initial loading stage and the cyclic loading stage. These stages are characterized based on the load amplitude and are defined programmatically within the subroutine using the $t_{p_{load}}$ parameter, which determines the transition between the two stages.

During the initial loading stage, the load is gradually applied using a smooth step function, controlled by the parameter $t_{p_{load}}$. This gradual increase in load minimizes numerical instabilities related to unwanted inertial effects using explicit solver for quasi-static problems. Throughout this stage, the principal stresses and strains are evaluated, and the dominant tensile and compressive values are identified. These values are stored as state variables for each material point. Although the stresses and strains are recorded, no damage is applied during the initial loading stage. This phase serves to bring the model to the deformation and stress stage that corresponds to maximum load in a cycle of fatigue loading for the subsequent cyclic loading stage.

Once the maximum load is reached and the $stepTime$ exceeds the $t_{p_{load}}$ parameter, the simulation continues under the assumption that the cyclic loading is taking place. In this phase, the maximum load amplitude is maintained, providing the information in each increment of the dynamic explicit solution about the stress state in the model that corresponds to the maximum load level in a load cycle. Assumption is taken here that if the unloading would take place, as it happens in each cycle in physical tests, then the stresses would revert back to zero. Thus, the stress range in each cycle can be estimated by stress due to maximum load only. There is key advantage in such assumption. It enables utilization of robust explicit solver that solves complex systems with contact interactions and damage over hundreds of thousands of increments within few minutes or hours on modern computes without facing the usual convergence or inertial issues. Each increment in the analysis is used therefore for one cycle jump of a specified size without necessity to alter the load that would have huge computation costs to fight back the issues of inertial effects. This assumption is only completely correct for cyclic loading with load ratio of $R = 0$ and in case that no residual deformation evolves during the cyclic loading but only damage.

Therefore, the methodology at this stage of development is only suitable for simulating constant load amplitudes of non-reversed load with only damage evolving in the material and interface and without plasticity. Such limitations are close to the type of behavior examined in this thesis when considering cyclic load experiments of $R = 0.1$. At each increment of the "quasi-cyclic" part of the analysis ($stepTime > t_{p_{load}}$) damage accumulation and stiffness degradation based on a CDM model are calculated to evaluate damage D in the material at each integration point in the part of the model representing SRR material.

At the beginning of the cyclic stage, some parameters are initialized to guide the damage calculations. The ultimate allowable stress ($\sigma_{ult} = 10.00$ or -85.00 MPa for tension and compression respectively) and an initial damage value ($D_0 = 0.001$) serve as reference points for determining the damage progression. A threshold value ($D_{th} = 0.15$ or $D_{th} = 0.60$ for tension and compression respectively) are also set to govern at which level the material

would rapidly lose stiffness and be deleted.

During the simulation, the principal stresses and strains are extracted for each element at maximum load. The routine identifies the governing tensile and compressive behaviors by computing the maximum and minimum principal stress and strain components. The maximum tensile strain ($e_{t,max}$) and compressive strain ($e_{c,max}$) are critical for evaluating the corresponding damage rates. Similarly, the principal stresses are used to calculate the normalized stress (σ/σ_{ult}), which directly influences the empirical damage model.

Damage evolution is governed by an empirical relationship that links damage accumulation to the stress state at each material point using the relationship below:

$$\frac{dD}{dN} = a \cdot D^2 + b \cdot D + c \tag{9.5}$$

where a, b and c are empirical coefficients derived from experimental calibration. These coefficients are determined separately for tensile and compressive behaviors. The subroutine at the current stage of implementation, does not select which calibration to apply; instead, the user explicitly chooses whether to simulate tension-based or compression-based behavior depending on the specific simulation objective. This flexibility allows for tailored modeling of SRR's fatigue behavior under the desired loading conditions. These coefficients ensure that the damage rate reflects the nonlinear response of the SRR material under cyclic loading. The damage increment (dD) is then calculated as the product of the damage rate and the cycle step size (dN), and it is added to the cumulative damage from previous cycles.

As the simulation progresses, the stress and strain tensors are recalculated at each increment, and the principal components are evaluated to determine the governing tensile or compressive response. Based on the stress level at each material point, the subroutine calculates the corresponding damage and applies it incrementally. This damage reduces the effective stiffness of the material, which is modeled as:

$$E_{\text{residual}} = (1 - D) \cdot E_0 \tag{9.6}$$

where E_0 is the initial elastic modulus. This reduction in stiffness reflects the material's progressive degradation under cyclic loading.

Field and state variables defined through this subroutine are updated in each increment of dynamic explicit analysis to store the cumulative damage and associated parameters for each element, ensuring consistent tracking of damage progression across simulation increments. Each increment of the analysis is set to correspond to certain cycle jump. If "i" is an integer number that represents the number of analysis increment, then the cycle jump per increment is defined as dN/di. In the first increment of the quasi-cyclic loading phase, the cycle jump per increment dN/di is set to 1 to prevent excessive damage accumulation. For the subsequent increments, the step size is set to the predefined fixed value dN/di which can be larger or lower than 1 depending on the global load level applied and total expected number of cycles, allowing efficient simulation while maintaining a reliable damage progression. The aimed number of increments in a typical analysis would be between 200.000 and 1.000.000 which enables analysis of very low stress levels in simulated components aimed at high number of cycles.

9.5. Meso-scale modeling of SRR material under cyclic tension and compression loading

The cyclic tension and compression experiments on SRR material, described in Chapter 3 and 4 respectively, provide the basis for validating the developed subroutine. To generate the stiffness degradation curves and validate the numerical simulations, results are exported from the ABAQUS®/Explicit model. During the simulation, several quantities are stored as state variables for post-processing. The applied displacement of the cylinder or disk is recorded at each increment of the analysis. Additionally, the reaction force is exported, providing the necessary data to calculate the applied stress. The number of increments performed during the simulation is also tracked. This information is crucial for determining the corresponding number of cycles, which is calculated based on a predefined cycle jump factor (dN/di).

From the exported data, stress, strain, and stiffness are determined. The strain ϵ is computed from the recorded displacements divided by the height of the specimen. The stress σ is derived from the reaction force and the cross-sectional area of the coupon. Once stress and strain are calculated, the stiffness E is obtained as their ratio.

This process allows for the generation of stiffness degradation curves, which represent the progressive loss of stiffness under cyclic loading. Figures 9.18a to 9.18c show the normalized stiffness degradation curves from uniaxial compression tests under three load levels: -20 kN, -24 kN, and -30 kN. The experimental data are used to calibrate the parameters of the subroutine, which is then employed to generate the numerical stiffness degradation curves shown in red.

For each load level, the subroutine reliably replicates the experimentally observed stiffness degradation. The numerical predictions closely match the experimental data across the entire loading history, demonstrating the ability of the subroutine to capture the cyclic behavior of SRR material under different levels of cyclic compression loading.

Figure 9.17 presents the prediction of stress range versus the number of cycles ($log(N)$) for SRR material under indirect tensile loading conditions. The black data points represent the experimental results, while the red crosses correspond to the predictions from the FE models using the developed subroutine. The FE predictions closely match the experimental data across the entire range of stress levels, capturing the fatigue life for different stress ranges. This agreement demonstrates that the subroutine effectively models the stiffness degradation and damage accumulation in tensile splitting experiments.

The failure modes observed in cyclic compression tests provide important insights into the damage mechanisms of SRR material. Figure 9.18 compares the numerical and experimental results, showing similar failure patterns: a cone-shaped failure in the FE simulation (Figure 9.18a) and a clepsydra-shaped failure in the physical test (Figure 9.18b).

In both cases, the failure involves the cylinder splitting into fragments with a conical or hourglass shape. This pattern is characterized by localized crushing at the top and bottom edges of the specimen, with cracks propagating diagonally toward the center. The cone failure seen in the simulation captures this process effectively, illustrating the regions of high compressive stress and the subsequent material degradation. Likewise, the clepsydra failure observed in the experiments reflects the brittle nature of SRR material under compression, where cracks propagate along shear planes, causing the cylinder to split into multiple pieces.

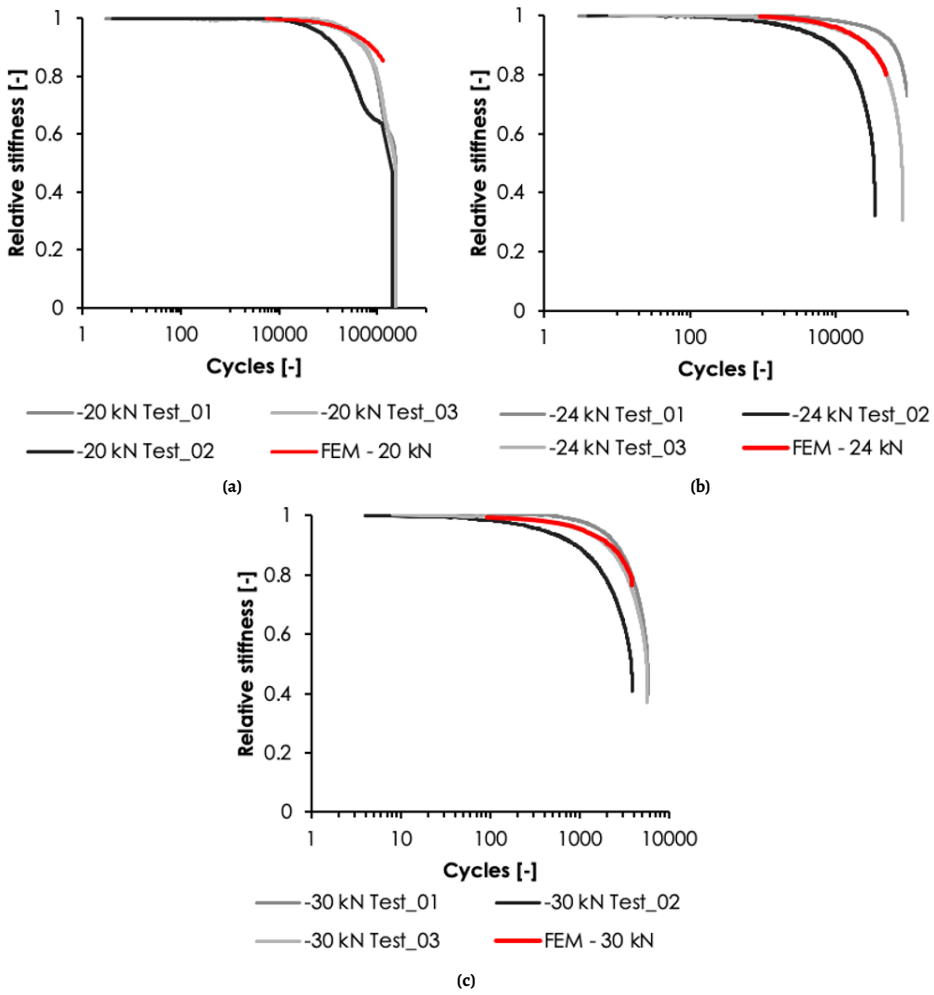

Figure 9.16: Numerical normalized stiffness values for SRR material under uniaxial compression over their fatigue life: (a) Minimum load of -20 kN, (b) Minimum load of -24 kN, (c) Minimum load of -30 kN.

The similarities between the simulated cone failure and the experimental clepsydra failure suggest that the numerical model reliably replicates the key damage mechanisms occurring during cyclic compression. Both failure modes indicate significant stiffness degradation and localized crushing leading to sudden failure. These consistent results validate the subroutine's potential to predict the complex failure behavior of SRR material under cyclic loading.

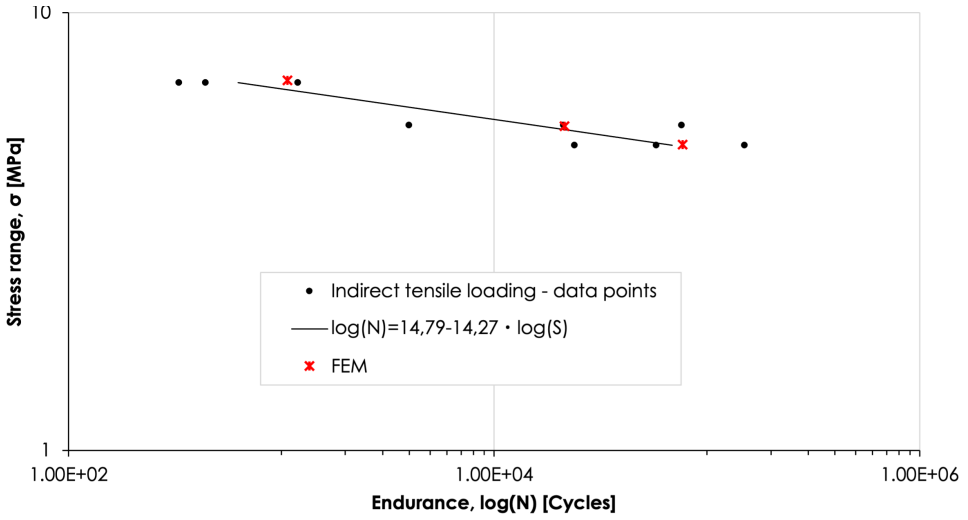

Figure 9.17: Prediction of stress versus number of cycles under tension of SRR material.

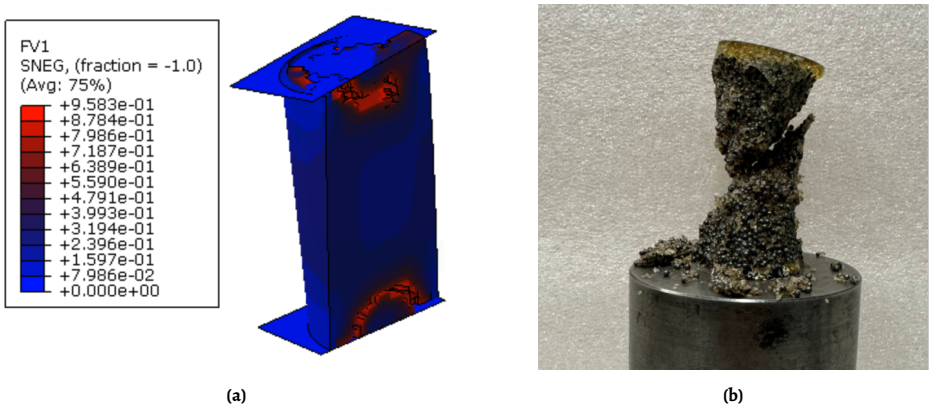

Figure 9.18: Numerical versus experimental results of cyclic loading under uniaxial compression: (a) Cone failure during FE simulation, (b) Clepsydra failure during test.

For the disk geometry, the failure modes obtained through indirect tensile splitting cyclic tests and FE simulation are depicted in Figure 9.19. In the numerical analysis (Figure 9.19a), the tensile splitting failure manifests as a vertical crack propagating through the SRR material, driven by the tensile stresses acting along the diameter normal to the direction of loading. This failure mode corresponds closely to the experimental results (Figure 9.19b), where the specimen fractures along a similar path. The subroutine successfully captures the progressive crack initiation and propagation observed during the cyclic tests, validating its ability to model tensile damage mechanisms reliably.

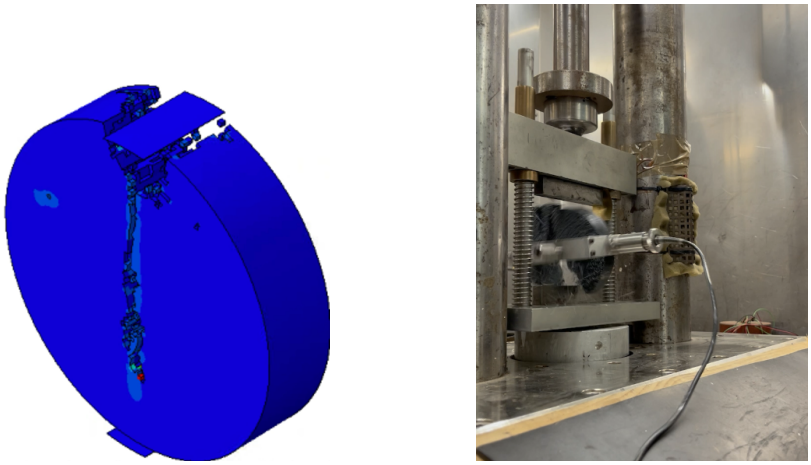

(a) (b)

Figure 9.19: Numerical versus experimental results of cyclic loading under tension: (a) Tensile splitting failure during FE simulation, (b) Tensile splitting failure during experiments.

9.6. Connector-level cyclic FE model and discussion

The aim here is to test the ability of the developed CDM model and the implemented subroutine to simulate the cyclic response of the iSRR connector embedded in an GFRP deck, showcasing the damage evolution in 3D structural components beyond simple coupon-scale experiments. Initially, the SRR material is meshed using 1.5 mm hex elements in the load-transferring region (the SRR surrounded by the facing), while the rest of the SRR uses a mesh size of approximately 3 mm. This inconsistent meshing approach presents challenges in meaningfully capturing fatigue behavior and crack propagation at the current stage of development of the CDM model and subroutine. In areas with larger elements, stress concentrations average over a greater volume, reducing their magnitude and thus delaying damage development. As a result, the predicted fatigue life appears artificially extended, with no significant increase in displacement range until a critical point when a sudden crack forms, as presented in Figures 9.21a, 9.21b and 9.21c. Once these larger elements fail, stresses redistribute to neighboring smaller elements, which then fail almost immediately because of the numerically induced larger stress concentrations, causing rapid crack propagation. These findings underline the current limitations of mixing mesh sizes, as it distorts stress redistribution and prevents the CDM model from capturing gradual stiffness degradation effectively.

Using a consistent mesh size throughout the SRR part of the model in the stress concentration region produces more consistent crack growth along the probable crack path. With finer and uniformly sized elements, stress gradients are captured more reliably, enabling proper incremental damage evolution and stable crack propagation, as illustrated in Figures 9.21a - 9.21d. The displacement range increases progressively as damage accumulates, indicating a more gradual loss of stiffness.

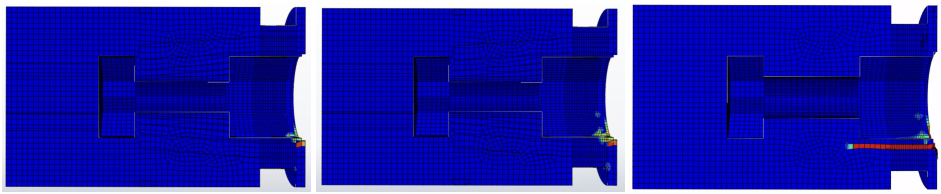

Figure 9.20: Crack propagation in SRR material with inconsistent mesh observed over progressive cycles: (a) 1st cycle, (b) 2.07E+09 cycle, (c) 2.08E+09 cycle.

However, this approach also leads to failure at a lower number of cycles compared to the inconsistent mesh size model. This earlier failure happens because the consistent finer mesh resolves localized stress concentrations with a higher magnitude, allowing the CDM model to identify critical damage thresholds sooner. While damage develops earlier, the model produces a more reliable outcome by capturing the material's behavior under cyclic loading, including more refined stress redistribution and more steady crack growth. This highlights the importance of mesh consistency in applying the CDM model, particularly for simulating fatigue damage and crack propagation mechanisms.

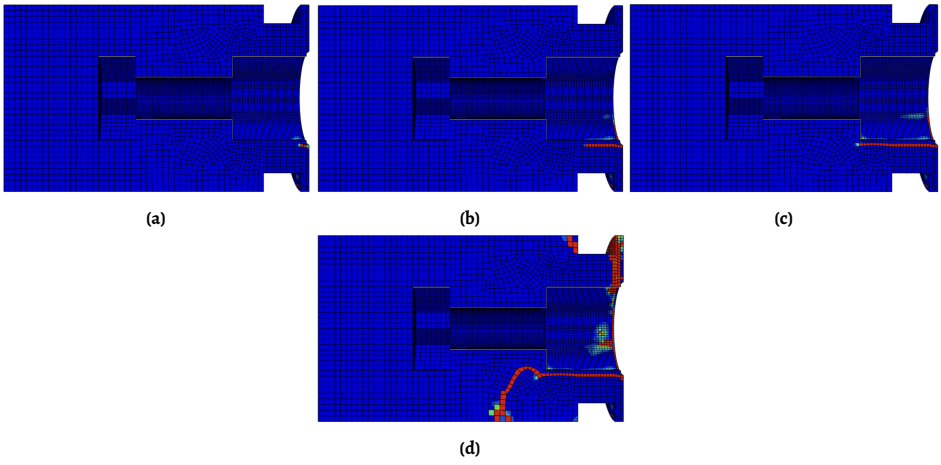

Figure 9.21: Crack propagation in SRR material with consistent mesh observed over progressive cycles; (a) 5.24E+04 cycle, (b) 6.99E+04 cycle, (c) 8.74E+04 cycle, (d) 1.03E+06 cycle.

The coupon cylinder model under uniaxial compression serves as the calibration basis for the CDM model, using a consistent mesh size of 1.5 mm. In this simpler geometry, stress states are relatively uniform, dominated by axial compression with diagonal shear planes forming as the primary failure mode. The CDM model performs well in this scenario, successfully capturing gradual damage accumulation and crack progression along predictable paths and number of cycles to failure similar as in the coupon cylinder experiments.

In contrast, the iSRR connector model introduces more complex stress states due to its geometry and loading conditions, including stress concentrations at component interfaces.

The more uniform stress distribution in the cylinder model facilitates straightforward calibration of damage parameters ("a", "b", and "c"), whereas the connector model requires finer resolution to capture localized stress redistribution reliably.

Additionally, in the cylinder model, lateral stresses provide a confinement effect that delays damage initiation and promotes a more uniform failure progression. The iSRR connector model, however, exhibits significant sensitivity to mesh size due to the interplay of axial, radial, and shear stresses. This sensitivity is particularly evident with inconsistent mesh sizes, where abrupt failures occur as stresses redistribute from larger to smaller elements. By using a consistent mesh size, the connector model achieves more gradual damage accumulation, better aligning with the behavior observed in the cylinder tests.

Hex elements provide a computationally efficient approach for modeling the iSRR connector and cylindrical specimens, particularly in regions with uniform stress distributions. However, they face challenges in maintaining consistent element sizes in areas with complex geometries or high stress concentrations, as demonstrated in the mixed mesh size results that distort the CDM model's accuracy. Tetrahedral (tet) elements offer a viable alternative for meshing complex geometries, providing more consistent element sizing and better stress resolution in challenging regions. Despite potential drawbacks, such as lower accuracy for the same element count and higher computational cost, tet elements excel at capturing stress concentrations and damage evolution in areas prone to crack initiation and propagation, making them a promising choice for future studies.

9.7. Conclusions

In this chapter, micro-mechanical modeling was developed to better understand fundamental SRR material behavior under confined and unconfined conditions. Model reveals that non-linear behavior up to ultimate stress is mainly governed by damage at the resin matrix to steel balls' interface. Such finding is confirmed in modeling also for triaxial stress states with confinement stress up to 35% of the original compressive strength of the material. Given that damage and not plasticity is governing early stages of nonlinear material behavior, a motive was given to engage in developing CDM based model for studying fatigue behavior of the SRR material and the iSRR connector.

A prediction method was developed in this study that effectively captures the progressive stiffness degradation of SRR under both tensile and compressive cyclic loading scenarios, using a CDM model. The model recalculates damage at each material point during every calculation step of explicit dynamic solution of the FE analysis, providing an incremental representation of the material's fatigue behavior. By continuously updating the stress and damage distributions, the approach enables the identification of regions with localized damage increments and stress concentrations, which ultimately lead to failure. Element-level damage calculations allow the model to pinpoint areas experiencing higher stress, where damage accumulates more rapidly, to predict crack path and related fatigue life. Through the implementation of a subroutine in ABAQUS®, this methodology incrementally updates damage at each time step, allowing the simulation to proceed until the stiffness degradation threshold is reached. Modeling with this approach was cross-validated with coupon-level material experiments (cylinder in compression and disk under tensile splitting loading) and connector-level cyclic tests (under shear loading).

The results underscore the critical role of mesh consistency in fatigue modeling, partic-

ularly when using a CDM approach. A uniform mesh size enables reliable stress resolution, stable crack propagation, and realistic fatigue life predictions. In contrast, inconsistent mesh sizes distort stress redistribution patterns, leading to unrealistic and abrupt failures. The comparison with the cylinder model highlights the importance of calibrating the CDM model under consistent and representative conditions to ensure reliable predictions for complex geometries like the iSRR connector.

Future work should include mesh sensitivity analyses to identify optimal element sizes for different connector regions. Mitigation measures that may lead to reduced mesh sensitivity can be in direction of exploring the use of tetrahedral elements in areas with complex geometries which offer a promising path to achieve consistent element sizing. These steps will ensure that the CDM model captures the gradual stiffness degradation and fatigue behavior of the SRR material, aligning simulation results with experimental observations and real-world structural behavior.

V

Epilogue

10

Conclusions and recommendations

10.1. Conclusions

This dissertation aims to advance the understanding and application of shear connection technology for hybrid bridges. It focuses on a novel bolted connector, the injected Steel Reinforced Resin (iSRR) connector. The research combines experimental, computational, and analytical methods to characterize the connector's fatigue behavior. This comprehensive evaluation contributes to bridge engineering, especially for fibre-polymer composite-to-steel hybrid systems.

A key aspect of the research is the experimental investigation of the iSRR connector and its core material, SRR, under cyclic loading. The research provides new knowledge for fatigue characterization of such hybrid connections by developing an experimental set-up and computational model that provided opportunity to establish endurance criterion for the novel connectors. The finite element (FE) analyses, from material-level to connector-scale simulations and full-size bridge predictions, provide framework for better understanding of underlying damage mechanisms and real world behavior of the connectors. A phenomenological model based on Continuum Damage Mechanics (CDM) principles is developed to model fatigue on the material and on the component level. This approach offers a novel perspective for understanding degradation mechanisms.

The results from this work highlight several key findings, summarized in the following points:

- Material-level tests conducted on SRR with an 80% volume fraction of steel shot using unsaturated polyester polyurethane resin proved that the performance is pressure dependent in static and fatigue. Applying a confining pressure of 30 MPa, corresponding to approximately 35% of the original unconfined compressive strength (85 MPa), results in a strength increase of over 120%, raising the compressive strength to 190 MPa. Micro-mechanics FE models reveal that the Poisson's ratio of the SRR material differs from 0.13 in tension to 0.43 in compression. These valuable insights into the mechanical behavior of SRR under varying loading conditions provide essential test data for predicting the fatigue performance of iSRR connectors.

- Incremental cyclic compressive tests on SRR material reveal that fracture is governed by the coupled mechanisms of plastic deformation and damage evolution. Experimental results demonstrate that plastic strain reaches 4% at a total ultimate strain of 5%. The tests further show a concurrent progression of damage, characterized by a reduction in stiffness, which is directly correlated with the accumulation of plastic strain. When applied in the iSRR connector within a GFRP deck subjected to cyclic shear loading, both plastic deformation and damage are expected to interact under the combined effects of external shear load. This interaction leads to a gradual decline in the connector's stiffness and an increase in slip, ultimately driving the degradation of the connector's structural performance.
- Gradual damage evolution, up to 60% before total fracture, is observed in cyclic fatigue tests of SRR material in compression. In contrast, the development of damage in cyclic tensile splitting tests is limited to 10% before the final fracture stage. This indicates that the CDM must account for different damage evolution mechanisms under compression versus tension. Tests conducted at different stress levels in tension and compression reveal similar shape of stiffness degradation curves which is favorable for implementation of CDM approaches for predicting fatigue damage.
- In the examined shear connector, cyclic damage is primarily governed by debonding of the SRR injection from the large hole in the lower facing of the GFRP composite deck and local compressive damage of the SRR in front of the embedded bolt and nut. At the highest load level of ±80 kN, corresponding to approximately 30% of the static strength, these two mechanisms lead to actual failure of the connector at ambient and increased temperature. Notably, a rapid increase in additional displacement, leading to failure, is observed after a displacement range of 0.95 mm is reached. However, at lower load levels (±40 kN and ±60 kN, corresponding to approximately 15% and 22% of the static resistance, respectively) the experiments mainly show a gradual increase in shear displacement range, without actual failure after 2.0E+06 cycles.
- A fatigue life prediction model was developed for the iSRR connector, using an increase in the displacement range of 0.3 mm during cyclic loading as the failure criterion. The fatigue endurance of the iSRR connector follows an F-N curve with a slope of 6.7 under alternating load conditions (R = -1), which was found to be the most critical loading scenario. The estimated number of cycles to reach the defined failure criterion for load ratios of R = 0.1 and R = 0.5 is 134 times and 68 times longer, respectively, compared to the similar load range with R = -1.
- A temperature of 55 °C reduces the estimated number of cycles to reach the defined failure criterion by a factor of 10. Aging in outdoors and submerged conditions leads to a reduction of fatigue life by factors of 2 and 60, respectively. The damage over the service life should consider a portion of load cycles acting at high temperature, assuming the impact of airborne moisture as a baseline.
- A CDM is presented that effectively captures the fatigue behavior of SRR material under both compression and tension by representing the progressive degradation of material stiffness. The model uses empirical relationships calibrated from experimental data to account for damage accumulation as a function of stress cycles,

providing insights into the fatigue endurance of SRR. When calibrated using indirect tensile splitting tests, the model predicts a significantly shorter fatigue life compared to experimental observations for the iSRR connector. Conversely, when calibrated using compressive test data, the model reaches the failure criterion of 0.3 mm additional displacement range at a much higher number of cycles, aligning more closely with experimental results. Importantly, failure patterns observed in all material and iSRR connector models remain consistent with experimental findings.

10.2. Recommendations for future research

In view of the findings presented in this thesis, a set of recommendations is outlined to further advance the experimental, numerical, and engineering aspects of this research. The key points for future work could focus on: (i) long-term durability studies to assess environmental effects on SRR material and iSRR connectors, (ii) enhanced fatigue modeling incorporating plasticity effects and R-ratio dependence, and (iii) structural integration to facilitate large-scale implementation in infrastructure applications. These aspects are important for improving the reliability and applicability of the proposed connection technology and are summarized as follows:

- Future research should extend aging tests beyond one year, incorporating extreme conditions such as freeze-thaw cycles, while also investigating micro-structural and chemical degradation mechanisms like resin aging and steel particle corrosion. Additionally, studying creep-fatigue interactions will be essential to model long-term structural degradation in bridges under sustained and cyclic loads.
- Further development of the subroutine is needed to improve fatigue life predictions across different R-ratios, accounting for both stiffness degradation and plasticity effects. Since fatigue damage in SRR material is influenced by both factors, refining the plasticity formulation within the subroutine will improve predictions of cumulative damage and failure under varying loading conditions. Additionally, a twin-model approach could be explored specifically for alternating R-ratios, allowing the separation of damage contributions under reversing load conditions and improving the robustness of fatigue predictions.
- Future studies should explore real-world applications through full-size bridge testing and real-time performance monitoring under traffic loads, while also working toward standardized design guidelines for GFRP-to-steel hybrid bridges. Additionally, a comprehensive life-cycle cost analysis should be conducted to compare the economic and durability benefits of iSRR connectors against traditional bolted or welded connections.

Acronyms

CDM Continuum Damage Mechanics. ix, xi, 53, 141, 148, 152, 155–157, 160–163, 167, 168

CLD Constant Life Diagram. 119

DIC Digital Image Correlation. 34–38

FE Finite Element. viii, ix, 13, 14, 34–37, 70–73, 133–135, 139–141, 143–146, 152, 153, 155, 158–161, 163, 167

GFRP Glass Fiber Reinforced Polymer. viii, xi, 4–9, 11, 14, 18, 20–25, 65, 67–74, 76–81, 84–87, 89, 93, 100, 101, 103, 106, 108, 133–136, 138, 140, 141, 155, 160, 168, 169

iSRR injected Steel Reinforced Resin. vii, xi, 5–11, 13–16, 24–26, 50, 65–70, 75–80, 82, 84–87, 89, 91, 99–112, 114–117, 119–123, 125–127, 129, 130, 133–135, 137–141, 152–154, 160, 162, 163, 167–169, 183

LVDTs Linear Variable Displacement Transducers. 31, 36, 39, 50, 51, 57, 58, 93, 102, 136, 139

RVE Representative Volume Element. 141, 142, 146

RWS Rijkswaterstaat. xi, 6, 10, 82, 183

SRR Steel Reinforced Resin. vii–ix, xi, 6–8, 10, 11, 13–20, 24, 25, 29–47, 49–61, 65–67, 69, 70, 72–76, 78–81, 84–89, 92, 94, 100, 101, 103, 104, 106, 108, 111, 125, 126, 133–145, 147–150, 152–164, 167–169

SSE Sum of Squared Errors. 111

UD unidirectional. 9, 72

ULS Ultimate Limit State. 102

UTM Universal Testing Machine. 31

Bibliography

[1] Eurocode 2: design of concrete structures-part 1–1: general rules and rules for buildings. *British Standard Institution, London*, 668:659–668, 2005. Available at https://eurocodes.jrc.ec.europa.eu/.

[2] H. Snijder and B. Hesselink. Repair, strengthening and upgrading of steel bridges in the netherlands. In *39th IABSE Symposium in Vancouver 2017: Engineering the Future: Engineering the Future*, pages 1177–1184. International Association for Bridge and Structural Engineering, 2018.

[3] R. Leidraad. Sturen op prestaties van systemen, 2010.

[4] J. Arnoldussen, P. Groot, J. I. Halman, and R. v. Zwet. Innovatie in de bouw: opgaven en kansen. 2017.

[5] K. Gribnau. Shear force in bolted connections for hybrid steel-frp bridges. Msc thesis, Delft University of Technology, Delft, Netherlands, 2021. https://resolver.tudelft.nl/uuid:a6250270-77b4-4ee3-9495-fc1aeac84813 (Available at TU Delft Repository).

[6] C. J. van Halen MSc and H. R. te Riele MSc. Product service systems, ecological and economic basics. 1999.

[7] Z. Shehu and A. Akintoye. Construction programme management theory and practice: Contextual and pragmatic approach. *International Journal of Project Management*, 27(7):703–716, 2009. https://doi.org/10.1016/j.ijproman.2009.02.005.

[8] D. Malschaert. Fracture mechanics: Application on orthotropic steel decks. 2020. https://resolver.tudelft.nl/uuid:9cef6563-5e27-41a7-9b72-69c9036dd3d2 (Available at TU Delft Repository).

[9] F. Toutlemonde and J. Resplendino. *Designing and Building with Ultra-High Performance Fibre-Reinforced Concrete (UHPFRC): State of the Art and Development*. Wiley-ISTE, 2010.

[10] R. Ranade. *Advanced cementitious composite development for resilient and sustainable infrastructure*. PhD thesis, University of Michigan, 2014.

[11] M. Sams. Broadway bridge case study: Bridge deck application of fiber-reinforced polymer. *Transportation Research Record: Journal of the Transportation Research Board*, (CD 11-S), 2005. https://doi.org/10.3141/trr.11s.wtk80rg438125v44.

[12] B. Castanie, C. Bouvet, and M. Ginot. Review of composite sandwich structure in aeronautic applications. *Composites Part C: Open Access*, 1:100004, 2020. https://doi.org/10.1016/j.jcomc.2020.100004.

[13] W. Shawkat, H. Honickman, and A. Fam. Investigation of a novel composite cladding wall panel in flexure. *Journal of composite materials*, 42(3):315–330, 2008. https://doi.org/10.1177/0021998307087965.

[14] A.-H. Zureick, B. Shih, and E. Munley. Fiber-reinforced polymeric bridge decks. *Structural Engineering Review*, 3(7):257–266, 1995.

[15] T. Keller. *Use of fibre reinforced polymers in bridge construction*. 2003.

[16] A. P. Vassilopoulos and T. Keller. *Fatigue of fiber-reinforced composites*. Springer Science & Business Media, 2011. https://doi.org/10.1007/978-1-84996-181-3.

[17] K.-T. Park, S.-H. Kim, Y.-H. Lee, and Y.-K. Hwang. Degree of composite action verification of bolted gfrp bridge deck-to-girder connection system. *Composite structures*, 72(3):393–400, 2006. https://doi.org/10.1016/j.compstruct.2005.01.010.

[18] P. Smith and K. Pascoe. Fatigue of bolted joints in (0/90) cfrp laminates. *Composites science and technology*, 29(1):45–69, 1987. https://doi.org/10.1016/0266-3538(87)90036-4.

[19] M. Heshmati. *Durability and long-term performance of adhesively bonded FRP/steel joints*. Chalmers Tekniska Hogskola (Sweden), 2017.

[20] F. Moon, D. Eckel, and J. Gillespie Jr. Shear stud connections for the development of composite action between steel girders and fiber-reinforced polymer bridge decks. *Journal of Structural Engineering*, 128(6):762–770, 2002. https://doi.org/10.1061/(ASCE)0733-9445(2002)128:6(762).

[21] G. Olivier, F. Csillag, E. Tromp, and M. Pavlović. Conventional vs. reinforced resin injected connectors' behaviour in static, fatigue and creep experiments on slip-resistant steel-frp joints. *Engineering Structures*, 236:112089, 2021. https://doi.org/10.1016/j.engstruct.2021.112089.

[22] M. Nijgh. New materials for injected bolted connections. Msc thesis, Delft University of Technology, Delft, Netherlands, 2017. https://resolver.tudelft.nl/uuid:089a5c6f-3c28-4c58-9b5a-34138bf2be86 (Available at TU Delft Repository).

[23] Airblast-Abrasives B.V. High carbon steel shot & grit: Technical data sheet. https://airblast.com/wp-content/uploads/2024/11/Steel-shot.pdf, 2024. Accessed: 2025-05-26.

[24] F. Csillag and M. Pavlović. Push-out behaviour of demountable injected vs. blind-bolted connectors in frp decks. *Composite Structures*, 270:114043, 2021. https://doi.org/10.1016/j.compstruct.2021.114043.

[25] G. Olivier, F. Csillag, E. Tromp, and M. Pavlović. Static, fatigue and creep performance of blind-bolted connectors in shear experiments on steel-frp joints. *Engineering Structures*, 230:111713, 2021. https://doi.org/10.1016/j.engstruct.2020.111713.

[26] FiberCore Europe. FiberCore ® Technology. https://www.fibercore-europe.com/en/. Accessed: 2025-05-26.

[27] CUR. Cur96: Cur recommendation 96: Fibre reinforced polymers in civil load bearing structures, 2003.

[28] M. Koetsier. Virtual fatigue verification of glass fibre-reinforced polymer components for civil engineering applications. Msc thesis, Delft University of Technology, 2021. https://resolver.tudelft.nl/uuid:048f4aa4-9cbe-47d1-823d-9aee861861e7 (Available at TU Delft Repository).

[29] Abaqus-Inc. Abaqus user manual, version 6.14. *Dassault Systémes Simulia Corp: Rhode Island, USA*, 2014.

[30] P. Zuo and A. P. Vassilopoulos. Review of fatigue of bulk structural adhesives and thick adhesive joints. *International Materials Reviews*, 66(5):313–338, 2021. https://doi.org/10.1080/09506608.2020.1845110.

[31] T. H. Courtney and J. Wulff. Matrix-limited fatigue properties in fibre composite materials. *Journal of Materials Science*, 1:383–388, 1966. https://doi.org/10.1007/BF00549937.

[32] G. Tao and Z. Xia. Biaxial fatigue behavior of an epoxy polymer with mean stress effect. *International Journal of Fatigue*, 31(4):678–685, 2009. https://doi.org/10.1016/j.ijfatigue.2008.03.025.

[33] W. Broughton. *Review of Durability Test Methods and Standards for Assessing Long Term Performance of Adhesive Joints: Report No. 1.* Nat. Phys. Lab., 1997.

[34] E. Hagerup. Flexural fatigue testing of polyesters. *Journal of Applied Polymer Science*, 7(3):1093–1116, 1963. https://doi.org/10.1002/app.1963.070070324.

[35] R. Hertzberg and J. Manson. Environment, frequency and temperature effects on fatigue in engineering plastics. *Fatigue: Environment and Temperature Effects*, pages 231–240, 1983. https://doi.org/10.1007/978-1-4899-1736-2_13.

[36] L. J. Broutman and S. K. Gaggar. Fatigue behavior of epoxy and polyester resins. *International Journal of Polymeric Materials*, 1(4):295–316, 1972. https://doi.org/10.1080/00914037208075291.

[37] J. Brunbauer and G. Pinter. Effects of mean stress and fibre volume content on the fatigue-induced damage mechanisms in cfrp. *international Journal of Fatigue*, 75:28–38, 2015. https://doi.org/10.1016/j.ijfatigue.2015.01.014.

[38] I. Constable, J. Williams, and D. Burns. Fatigue and cyclic thermal softening of thermoplastics. *Journal of Mechanical Engineering Science*, 12(1):20–29, 1970.

[39] F. M. Ramírez, M. F. de Moura, R. D. Moreira, and F. G. Silva. A review on the environmental degradation effects on fatigue behaviour of adhesively bonded joints. *Fatigue & Fracture of Engineering Materials & Structures*, 43(7):1307–1326, 2020. https://doi.org/10.1111/ffe.13239.

[40] F. Ascione, L. Granata, L. Guadagno, and C. Naddeo. Hygrothermal durability of epoxy adhesives used in civil structural applications. *Composite Structures*, 265:113591, 2021. https://doi.org/10.1016/j.compstruct.2021.113591.

[41] F. Ascione, L. Granata, and A. Lombardi. The influence of the hygrothermal aging on the strength and stiffness of adhesives used for civil engineering applications with pultruded profiles: an experimental and numerical investigation. *The Journal of Adhesion*, 98(12):1733–1771, 2022. https://doi.org/10.1080/00218464.2021.1936507.

[42] M. Savvilotidou, A. P. Vassilopoulos, M. Frigione, and T. Keller. Development of physical and mechanical properties of a cold-curing structural adhesive in a wet bridge environment. *Construction and Building Materials*, 144:115–124, 2017. https://doi.org/10.1016/j.conbuildmat.2017.03.145.

[43] S. Gantayat, D. Rout, and S. K. Swain. Carbon nanomaterial–reinforced epoxy composites: a review. *Polymer-Plastics Technology and Engineering*, 57(1):1–16, 2018. https://doi.org/10.1080/03602559.2017.1298802.

[44] D. R. Bortz, C. Merino, and I. Martin-Gullon. Carbon nanofibers enhance the fracture toughness and fatigue performance of a structural epoxy system. *Composites Science and Technology*, 71(1):31–38, 2011. https://doi.org/10.1016/j.compscitech.2010.09.015.

[45] T. Adachi, M. Osaki, W. Araki, and S.-C. Kwon. Fracture toughness of nano-and micro-spherical silica-particle-filled epoxy composites. *Acta Materialia*, 56(9):2101–2109, 2008. https://doi.org/10.1016/j.actamat.2008.01.002.

[46] C. Manjunatha, A. Taylor, A. Kinloch, and S. Sprenger. The effect of rubber micro-particles and silica nano-particles on the tensile fatigue behaviour of a glass-fibre epoxy composite. *Journal of Materials Science*, 44:342–345, 2009. https://doi.org/10.1007/s10853-008-3092-1.

[47] M. Nijgh. *A multi-scale approach towards reusable steel-concrete composite floor systems*. Msc thesis, Delft University of Technology, 2021. https://resolver.tudelft.nl/uuid:983b06e7-c30b-465c-a032-2439a7e9863f (Available at TU Delft Repository).

[48] M. P. Nijgh, H. Xin, and M. Veljkovic. Non-linear hybrid homogenization method for steel-reinforced resin. *Construction and Building Materials*, 182:324–333, 2018. https://doi.org/10.1016/j.conbuildmat.2018.06.111.

[49] B. Pedrosa, L. Buecking, and M. Veljkovic. Steel-reinforced resin for bolted shear connectors: Confined behaviour under quasi-static cyclic loading. *Engineering Structures*, 256:114023, 2022. https://doi.org/10.1016/j.engstruct.2022.114023.

[50] F. Csillag. Demountable deck-to-girder connection of frp-steel hybrid bridges. Msc thesis, Delft University of Technology, Delft, Netherlands, 2018.

[51] G. Olivier, F. Csillag, A. Christoforidou, L. Tromp, M. Veltkamp, and M. Pavlovic. Feasibility of bolted connectors in hybrid frp-steel structures. *Construction and Building Materials*, 383:131100, 2023. https://doi.org/10.1016/j.conbuildmat.2023.131100.

[52] A. Talaat, A. Emad, A. Tarek, M. Masbouba, A. Essam, and M. Kohail. Factors affecting the results of concrete compression testing: A review. *Ain Shams Engineering Journal*, 12(1):205–221, 2021. https://doi.org/10.1016/j.asej.2020.07.015.

[53] S. Erkens, X. Liu, A. Scarpas, A. Molenaar, and J. Blaauwendraad. Asphalt concrete response: experimental determination and finite element implementation. In *Proceedings, Ninth International Conference on Asphalt Pavements, Copenhagen, Denmark, August*, volume 17, pages 3–6, 2002.

[54] Z. Bieniawski and I. Hawkes. Suggested methods for determining tensile strength of rock materials. *International Journal of Rock Mechanics and Mining Sciences*, 15(3):99–103, 1978.

[55] H. Kupfer, H. K. Hilsdorf, and H. Rusch. Behavior of concrete under biaxial stresses. In *Journal proceedings*, volume 66, pages 656–666, 1969. https://doi.org/10.1061/JMCEA3.0001789.

[56] J. C. Lim and T. Ozbakkaloglu. Design model for frp-confined normal-and high-strength concrete square and rectangular columns. *Magazine of Concrete Research*, 66(20):1020–1035, 2014. https://doi.org/10.1680/macr.14.00059.

[57] A. Zhou and T. Keller. Joining techniques for fiber reinforced polymer composite bridge deck systems. *Composite Structures*, 69(3):336–345, 2005. https://doi.org/10.1016/j.compstruct.2004.07.016.

[58] V. Mara and R. Haghani. Review of frp decks: Structural and in-service performance. In *Proceedings of the Institution of Civil Engineers-Bridge Engineering*, volume 168, pages 308–329. Thomas Telford Ltd, 2015. https://doi.org/10.1680/bren.14.00009.

[59] A. Temeles, T. Cousins, and J. Lesko. Composite plate and tube bridge deck design: Evaluation in the troutville, virginia weigh station test bed. In *Proc., 3rd Int. Conf. on Advanced Composite Materials in Bridges and Structures, ACMBS*, volume 3, pages 801–808, 2000.

[60] S. Satasivam and Y. Bai. Mechanical performance of bolted modular gfrp composite sandwich structures using standard and blind bolts. *Composite Structures*, 117:59–70, 2014. https://doi.org/10.1016/j.compstruct.2014.06.011.

[61] H. W. Gürtler. Composite action of frp bridge decks adhesively bonded to steel main girders. Technical report, EPFL, 2005.

[62] M. Schollmayer and T. Keller. Modeling of through-thickness stress state in adhesive joints connecting pultruded frp bridge decks and steel girders. *Composite structures*, 90(1):67–75, 2009. https://doi.org/10.1016/j.compstruct.2009.02.007.

[63] X. Jiang, M. Kolstein, and F. Bijlaard. Experimental and numerical study on mechanical behavior of an adhesively-bonded joint of frp–steel composite bridge under shear loading. *Composite structures*, 108:387–399, 2014. https://doi.org/10.1016/j.compstruct.2022.115743.

[64] G. Turvey and P. Wang. Failure of pultruded grp single-bolt tension joints under hot–wet conditions. *Composite structures*, 77(4):514–520, 2007. https://doi.org/10.1016/j.compstruct.2005.08.024.

[65] C. Wu, Y. Bai, and J. Toby Mottram. Effect of elevated temperatures on the mechanical performance of pultruded frp joints with a single ordinary or blind bolt. *Journal of Composites for Construction*, 20(2):04015045, 2016. https://doi.org/10.1061/(ASCE)CC.1943-5614.0000608.

[66] C. Xue, M. Yu, B. Yang, T. Wang, M. Saafi, and J. Ye. Experimental and numerical study on tensile properties of bolted gfrp joints at high and low temperatures. *Composite Structures*, 293:115743, 2022. https://doi.org/10.1016/j.compstruct.2022.115743.

[67] L. Liu, X. Wang, Z. Wu, and T. Keller. Tension-tension fatigue behavior of ductile adhesively-bonded frp joints. *Composite Structures*, 268:113925, 2021. https://doi.org/10.1016/j.compstruct.2021.113925.

[68] I. Ashcroft, D. Hughes, S. Shaw, M. A. Wahab, and A. Crocombe. Effect of temperature on the quasi-static strength and fatigue resistance of bonded composite double lap joints. *The Journal of Adhesion*, 75(1):61–88, 2001. https://doi.org/10.1080/00218460108029594.

[69] M. Heshmati, R. Haghani, and M. Al-Emrani. Environmental durability of adhesively bonded frp/steel joints in civil engineering applications: State of the art. *Composites Part B: Engineering*, 81:259–275, 2015. https://doi.org/10.1016/j.compositesb.2015.07.014.

[70] T. Keller and H. Gürtler. Quasi-static and fatigue performance of a cellular frp bridge deck adhesively bonded to steel girders. *Composite Structures*, 70(4):484–496, 2005. https://doi.org/10.1016/j.compstruct.2004.09.028.

[71] J. F. Davalos, A. Chen, and B. Zou. Stiffness and strength evaluations of a shear connection system for frp bridge decks to steel girders. *Journal of Composites for Construction*, 15(3):441–450, 2011. https://doi.org/10.1061/(ASCE)CC.1943-5614.0000162.

[72] A. Van Wingerde, D. Van Delft, and E. Knudsen. Fatigue behaviour of bolted connections in pultruded frp profiles. *Plastics, rubber and composites*, 32(2):71–76, 2003. https://doi.org/10.1179/146580103225009103.

[73] B. Zafari, J. Qureshi, J. T. Mottram, and R. Rusev. Static and fatigue performance of resin injected bolts for a slip and fatigue resistant connection in frp bridge engineering. In *Structures*, volume 7, pages 71–84. Elsevier, 2016. https://doi.org/10.1016/j.istruc.2016.05.004.

[74] W. Feng, P. He, and M. Pavlovic. Combined dic and fea method for analysing debonding crack propagation in fatigue experiments on wrapped composite joints. *Composite Structures*, 297:115977, 2022. https://doi.org/10.1016/j.compstruct.2022.115977.

[75] A. Christoforidou, R. Verleg, and M. Pavlovic. Static, fatigue and hygroscopic performance of steel-reinforced resins under various temperatures. *Construction and Building Materials*, 403:133079, 2023. https://doi.org/10.1016/j.conbuildmat.2023.133079.

[76] A. Afshar, M. Alkhader, C. S. Korach, and F.-P. Chiang. Effect of long-term exposure to marine environments on the flexural properties of carbon fiber vinylester composites. *Composite Structures*, 126:72–77, 2015. https://doi.org/10.1016/j.compstruct.2015.02.008.

[77] T. J. Hsu and L. J. Lee. Physical properties of transfer-molded polyurethane-polyester interpenetrating polymeric network. *Journal of applied polymer science*, 33(3):793–807, 1987. https://doi.org/10.1002/app.1987.070330310.

[78] S. Damani and L. J. Lee. The resin-fiber interface in polyurethane and polyurethane-unsaturated polyester hybrid. *Polymer composites*, 11(3):174–183, 1990. https://doi.org/10.1002/pc.750110306.

[79] AOC Resins. *Product Data Sheet: Atlac® 430 Epoxy Bisphenol A Vinylester Resin*, 2018. Accessed: 2025-05-26. Technical documentation provided by Aliancys (now AOC) for Atlac 430 resin.

[80] AOC Resins. *Technical Data Sheet: Daron® 8151 Resin (Marketed as AQR 1025/B25)*, 2021. Accessed: 2025-05-26. Supplied by AOC as technical documentation for resin used in SRR fabrication.

[81] Resoltech. *Technical Data Sheet: 1080S Epoxy Infusion System (with Hardeners 1083, 1084, 1086)*, 2020. Datasheet version V4, published 15.02.2020. Accessed: 2025-05-27.

[82] G. Cerni, E. Bocci, F. Cardone, and A. Corradini. Correlation between asphalt mixture stiffness determined through static and dynamic indirect tensile tests. *Arabian Journal for Science and Engineering*, 42(3):1295–1303, 2017. https://doi.org/10.1007/s13369-016-2380-3.

[83] T. Ma, N. Peng, Z. Zhu, Q. Zhang, C. Yang, and J. Zhao. Brazilian tensile strength of anisotropic rocks: review and new insights. *Energies*, 11(2):304, 2018. https://doi.org/10.3390/en11020304.

[84] A. ASTM. C496/c496m-17 standard test method for splitting tensile strength of cylindrical concrete specimens. In *American Society for Testing and Materials*, 2017. https://doi.org/10.1520/C0496_C0496M-17.

[85] C. EN et al. Bituminous mixtures–test methods for hot mix asphalt–part 26: Stiffness. *European committee for standardization Brussels*, 2012.

[86] Y. Belrhiti, J. Dupre, O. Pop, A. Germaneau, P. Doumalin, M. Huger, and T. Chotard. Combination of brazilian test and digital image correlation for mechanical characterization of refractory materials. *Journal of the European Ceramic Society*, 37(5):2285–2293, 2017. https://doi.org/10.1016/j.jeurceramsoc.2016.12.032.

[87] R. A. Stirling, D. J. Simpson, and C. T. Davie. The application of digital image correlation to brazilian testing of sandstone. *International Journal of Rock Mechanics and Mining Sciences*, 60:1–11, 2013. https://doi.org/10.1016/j.ijrmms.2012.12.026.

[88] ASTM. E739 10 standard practice for statistical analysis of linear or linearized stress-life in: Annual book of astm standards. In *American Society for Testing and Materials*, 1980.

[89] G. Xiao and M. Shanahan. Water absorption and desorption in an epoxy resin with degradation. *Journal of Polymer Science Part B: Polymer Physics*, 35(16):2659–2670, 1997. https://doi.org/10.1002/(SICI)1099-0488(19971130)35:16<2659::AID-POLB9>3.0.CO;2-K.

[90] X. Yin, Y. Liu, Y. Miao, and G. Xian. Water absorption, hydrothermal expansion, and thermomechanical properties of a vinylester resin for fiber-reinforced polymer composites subjected to water or alkaline solution immersion. *Polymers*, 11(3):505, 2019.

[91] A. Christoforidou, A. Baskar, E. Kane, and M. Pavlovic. Compressive behaviour and micromechanical modelling of steel-reinforced resin under monotonic and cyclic loading. *Composites Science and Technology*, page 111387, 2025.

[92] E. C. for Standardization. Eurocode 4: Design of composite steel and concrete structures - part 1-1: General rules and rules for buildings, 2004. Available at https://eurocodes.jrc.ec.europa.eu/.

[93] M. Pavlović, Z. Marković, M. Veljković, and D. Buđevac. Bolted shear connectors vs. headed studs behaviour in push-out tests. *Journal of Constructional Steel Research*, 88:134–149, 2013. https://doi.org/10.1016/j.jcsr.2013.05.003.

[94] B. Egan, C. McCarthy, M. McCarthy, P. Gray, and R. Frizzell. Modelling a single-bolt countersunk composite joint using implicit and explicit finite element analysis. *Computational Materials Science*, 64:203–208, 2012. https://doi.org/10.1016/j.commatsci.2012.02.008.

[95] W. Liu, F. Yu, Z. He, and G. Qing. A progressive damage model introducing temperature field for bolted composite joint with preload. *Modelling and Simulation in*

Materials Science and Engineering, 27(6):065011, 2019. https://doi.org/10.1088/1361-651X/ab230f.

[96] H. Tuwair, M. Hopkins, J. Volz, M. A. ElGawady, M. Mohamed, K. Chandrashekhara, and V. Birman. Evaluation of sandwich panels with various polyurethane foam-cores and ribs. *Composites Part B: Engineering*, 79:262–276, 2015. https://doi.org/10.1016/j.compositesb.2015.04.023.

[97] G. Pearce, A. Johnson, A. Hellier, and R. Thomson. A study of dynamic pull-through failure of composite bolted joints using the stacked-shell finite element approach. *Composite Structures*, 118:86–93, 2014. https://doi.org/10.1016/j.compstruct.2014.07.016.

[98] A. Du, Y. Liu, H. Xin, and Y. Zuo. Progressive damage analysis of pfrp double-lap bolted joints using explicit finite element method. *Composite Structures*, 152:860–869, 2016. https://doi.org/10.1016/j.compstruct.2016.06.028.

[99] G. Turvey. Bolted joints in pultruded glass fibre reinforced polymer (gfrp) composites. In *Composite Joints and Connections*, pages 77–111. Elsevier, 2011. https://doi.org/10.1533/9780857094926.1.77.

[100] J. Swinnen. Modelling the mechanical performance of bolted deck-to-girder connections in frp-steel hybrid bridges. Msc thesis, Delft University of Technology, Delft, Netherlands, 2020. https://resolver.tudelft.nl/uuid:07a2c6fd-7bfe-46ac-b9b6-a3cd253caa72 (Available at TU Delft Repository).

[101] Z. Haodong. Thermal behavior of frp bridge decks under environmental loads. Msc thesis, Delft University of Technology, 2021. https://resolver.tudelft.nl/uuid:6b446c67-059e-4b4d-88e2-aa90c11bbf58 (Available at TU Delft Repository).

[102] M. Poulton, W. Sebastian, and J. T. Mottram. Dic study of strain concentrations and damage within web-flange junctions of pultruded gfrp bridge decking. *Composites Part A: Applied Science and Manufacturing*, 179:108011, 2024. https://doi.org/10.1016/j.compositesa.2024.108011.

[103] M. Poulton, W. Sebastian, J. Mottram, and L. Kawashita. Non-linear finite element modelling of damage within web-flange junctions of pultruded gfrp bridge decking. *Composites Part A: Applied Science and Manufacturing*, 191:108666, 2025. https://doi.org/10.1016/j.compositesa.2024.108666.

[104] A. Christoforidou and M. Pavlovic. Fatigue performance of composite-steel injected connectors at room and elevated temperatures. *Engineering Structures*, 315:118421, 2024. https://doi.org/10.1016/j.engstruct.2024.118421.

[105] M. A. Syakur, B. K. Khotimah, E. Rochman, and B. D. Satoto. Integration k-means clustering method and elbow method for identification of the best customer profile cluster. In *IOP conference series: materials science and engineering*, volume 336, page 012017. IOP Publishing, 2018. https://doi.org/10.1088/1757-899X/336/1/012017.

[106] J. Gao, P. Zhu, Y. Yuan, Z. Wu, and R. Xu. Strength and stiffness degradation modeling and fatigue life prediction of composite materials based on a unified fatigue damage model. *Engineering Failure Analysis*, 137:106290, 2022. https://doi.org/10.1016/j.engfailanal.2022.106290.

[107] T. P. Philippidis and A. P. Vassilopoulos. Complex stress state effect on fatigue life of grp laminates.: part i, experimental. *International journal of fatigue*, 24(8):813–823, 2002. https://doi.org/10.1016/S0142-1123(02)00003-8.

[108] J. F. Mandell, D. D. Samborsky, L. Wang, and N. K. Wahl. New fatigue data for wind turbine blade materials. *J. Sol. Energy Eng.*, 125(4):506–514, 2003. https://doi.org/10.1115/1.1624089.

[109] H. J. Sutherland and J. F. Mandell. Optimized constant-life diagram for the analysis of fiberglass composites used in wind turbine blades. 2005. https://doi.org/10.1115/1.2047589.

[110] A. P. Vassilopoulos, B. D. Manshadi, and T. Keller. Influence of the constant life diagram formulation on the fatigue life prediction of composite materials. *International journal of fatigue*, 32(4):659–669, 2010. https://doi.org/10.1016/j.ijfatigue.2009.09.008.

[111] R. Zong, B. Liu, S. Wang, X. Jia, S. Li, and X. Huai. Numerical simulation of heat transfer of highly filled composites with spherical alumina fillers. *Composites Science and Technology*, page 111064, 2025. https://doi.org/10.1016/j.compscitech.2025.111064.

[112] S. Li. General unit cells for micromechanical analyses of unidirectional composites. *Composites Part A: applied science and manufacturing*, 32(6):815–826, 2001. https://doi.org/10.1016/S1359-835X(00)00182-2.

[113] M. Bayat and M. Aghdam. A micromechanics based analysis of hollow fiber composites using dqem. *Composites Part B: Engineering*, 43(8):2921–2929, 2012. https://doi.org/10.1016/j.compositesb.2012.06.021.

[114] J. Segurado and J. LLorca. Computational micromechanics of composites: the effect of particle spatial distribution. *Mechanics of materials*, 38(8-10):873–883, 2006. https://doi.org/10.1016/j.mechmat.2005.06.026.

[115] L. Mishnaevsky Jr, K. Derrien, and D. Baptiste. Effect of microstructure of particle reinforced composites on the damage evolution: probabilistic and numerical analysis. *Composites Science and Technology*, 64(12):1805–1818, 2004. https://doi.org/10.1016/j.compscitech.2004.01.013.

[116] H. Xin and M. Veljkovic. Residual stress effects on fatigue crack growth rate of mild steel s355 exposed to air and seawater environments. *Materials & Design*, 193:108732, 2020. https://doi.org/10.1016/j.matdes.2020.108732.

Acknowledgements

This was the very first part of the thesis I wrote. One day in my office, I felt the urge to thank someone, and that moment sparked the idea: even if I had nothing else written, I'd start with the people who mattered. I began keeping a separate file of acknowledgments, long before my first paper, and it grew quietly alongside my work. Revisiting it while finalizing the thesis reminded me that I must have done something right. I formed bonds stronger than the iSRR connectors I tested, and writing this section is what I feel most proud of. I know almost every thesis says something like this, but please know I mean it: this achievement wouldn't have been possible without you.

At first I would like to acknowledge my supervisors. Dear **Marko**, you kept believing in me even during the times when I had completely lost hope. You saw something in me when I couldn't, and you never stopped encouraging me to see it too. Pursuing a PhD was, in large part, because I enjoyed working with you so much. Your guidance went far beyond teaching me how to think critically and outside of the box. Every bit of scientific progress I've made is because of you. There were days during my PhD when I walked into the lab feeling genuinely proud. From doubting myself during my very first quarter as an MSc student to working passionately in the lab as a PhD candidate. I have to admit, every time those moments of pride come, my first thought is how grateful I feel to you. If I've ever made you feel even a little proud, I hope you've given yourself some credit for it. Because, I always do! Dear **Milan**, you have the unique ability to make my brain freeze with a single question. I didn't feel I had "made it" when I published my first paper, but when I answered a hard question from you. I believe I couldn't have a better promotor to help me in battling my insecurities and to propel me to my utmost capabilities. Thank you also for involving me in events like Eurosteel and the DOSSA award, giving me a slice of fame within the steel community.

I would also like to sincerely thank the independent members of my doctoral committee: Prof. dr. **M.A.N. Hendriks**, Dr. **V.A. Popovich**, Em. prof. dr. **J.T. Mottram**, Prof. dr. **M. Schäfer**, and Prof. dr. ir. **H.E.J.G. Schlangen**. Thank you for taking the time to read my thesis, for your thoughtful comments, and for your willingness to participate in the defence. I am especially grateful to Em. prof. dr. **Mottram** for his detailed feedback, which significantly strengthened the quality and clarity of this dissertation. His insights helped shape the final version of this work and made it more professional and complete.

My gratitude also goes to the user committee of my PhD project. I begin by acknowledging RWS for providing the necessary funding that made the experimental research possible, and in particular, I thank **Johan** for his support. These experiments could not have been conducted without the in-kind contributions from AOC Resins and FiberCore Europe, for which I am truly grateful. **Ron**, thank you for all the resin experiments and for welcoming me to the Zwolle factory. **Fruzsina** and **Liesbeth**, I sincerely appreciated your suggestions. And **Martijn**, thank you for continuously opening the doors to your facilities and for ensuring I always had the decks I needed.

Thanks go to my dear officemates. **Florentia**, you taught me one of the most important

lessons during my PhD, gratitude. You've always made a point to recognize those who helped you, and working with you reminded me to do the same. This acknowledgment section wouldn't be that lengthy without your influence. I hope you go further than you ever imagined, and I'm sure many will support you knowing that you'll never forget to give them credit. **Trayana**, watching you tackle every challenge with calm and precision has always inspired me. You made me think, more than once, that academia could be a stress-free place. There's no barrier you can't cross, and that's not just a feeling, it's a fact.

I want to thank everyone from our lab, who supported me both practical and emotional. Specifically, **Giorgo St.**, you've always been my emotional ally. Not only you helped with experiments, you even knew how I felt just by looking at me. Together with **Fani, Thaleia and Kleio**, you made this place feel like home. **Marco**, thank you for trusting me, training me, and eventually giving me the permission to use the equipment in the pavement lab independently. You have no idea how much that boosted my self-esteem. I still remember in July 2021, you were so eager to see where I was working, and when you realized I wasn't wearing the proper face mask for injection, you immediately ran to get me one. Honestly, I think I should also thank you for saving my life that day. **Ruben**, even though your expertise was in timber, you never hesitated to help me with my work. You carried heavy decks, helped install them, and even supported me in setting up the custom-made temperature chamber. **Fred**, thank you for helping me start or stop countless experiments along the way. That night that you send me the right LUA script, you managed to save both my testing campaign and my sanity. **Kees**, thank you for fixing the MP3 system every time I asked. Even if it was just one button, you did it with a smile. **John, Derek**, thank you for every time you cut something for me. **Louis** thank you for the nice figure you made. Lastly, **Sergio**, thank you for listening, navigating chaos, and holding the lab together.

To my colleagues from the composites research group: **Mathieu**, thank you for all your help, from gluing optical fibers to unraveling numerical headaches. In May 2023, you texted me that I was doubting myself while others were intimidated by my full potential. That message came at exactly the right time and gave me the push I needed. **Pei**, I followed your journey from 2019 to your PhD defense in 2023, and I want to thank you for keeping me inspired throughout. Most of my regular meetings took place right after **Weikang** had finished his. Your progress, drive, and results consistently motivated me and at times, even intimidated me.

I want to extend my thanks to everyone in the ES and faculty PhD councils for your time, dedication, and the sense of community you helped build. In particular, I'd like to thank **Enxhi, Giuli, Yuanchen, Michele, Giorgio, Ali, Shozab, Luuk, Roberto, Till, Lisa**, and **Entela** for your commitment, your efforts, and your collaboration. And Prof. dr. **G. Bertotti**, thank you for always having time for PhDs in need of direction.

I also want to thank my psychiatrist, **Grigoris**, whose support made an immeasurable difference when things felt overwhelming. When we discovered that I was experiencing performance anxiety, he not only gave me tools to manage it, but also a sense of relief. He once joked that the day of my defence would bear his last name, and in many ways, it will. That small moment of care helped me more than he probably knows.

My gratitude also goes to the students I have supervised. Especially, to **Job ter Kuile** for being the most independent student I have ever had and to **Jelco Köhlenberg** for never jumping into conclusions without a proper investigation. Finally, I want to thank **Eric**

Barelts for being the first who explored the fatigue performance of preloaded bolts in oversized holes. Most importantly, I want to thank him for our interactions that provided me with invaluable lessons on the dynamics of supervision and the importance of patience and understanding in collaborative engagements.

The list should also include one last person to whom I was not sure where to put because of his different roles in my life. **Abishek** started as one of my students, then he became a colleague to finally end up being a true friend of mine and someone that I can rely on so much that I could not consider defending my PhD without him next to me. So, Abishek you get your own category but most importantly you get my sincere and most heartfelt thank you. My appreciation started from when you were carrying decks, gluing fibers, producing and testing connectors, organizing trips to India for me and actually this list never stops. There has been times before we started our collaboration that I felt lonely but once you joined my project and ever since I felt part of a team, the A team! You are an asset for anyone you work for. I hope you will grow big, and have your own team. And I truly wish that it will be consisting of many people like you, although one Abishek is more than enough.

Moving on, I want to thank my friends, the people who remind me that I did something right in this life, simply because I found them. Starting with **Thanasis** who is the longest-standing friendship I have in the Netherlands. I've learned so much from you, going back to our university days in Greece. What I'm most thankful for, though, is that through you I learned how meaningful and supportive a deep friendship between a woman and a man can be. You've been there without me even needing to ask. Through emotional spirals, delusional rants, and everything in between. You didn't just survive my breakdowns; you helped fix them with care and practical suggestions. I couldn't imagine defending without you by my side, and I hope that we'll share many more milestones together. At least that's my plan.

Sometimes I think that if I ever become the best version of myself, I'll turn into my friend **Elissavet**, whose creativity and drive I deeply admire. I never realized how much I needed to be heard until I met you. Of all the things you have done for me, I cannot thank you enough for encouraging me to open up. You listened, understood, gave advice, and brought new hobbies into my life. Now that this book is printed, let me tell you one last thing: "Ελισσαβάκι μου, όντως μπόρεσα!", and I did it because you lifted me up when I was down.

The start of my PhD began with moving in with my friend **Ioanna**. Those early years were some of the nicest and least stressful, mostly thanks to you. Thank you for giving me a social life even during curfews and lockdowns. For the drinks, the board games, the singing, the secret gatherings, and endless talks in our living room. I look up to the way you live your life. That is the purest thought I have when I think of you.

The last years of my PhD I've spent living with **Tom**, the most easy-going housemate someone could have. I still laugh remembering you teasing me late at night when I was in front of the laptop: "Τι λένε τα computers και οι αριθμοί;». I hope I answered to you after briefly reading this dissertation. Θωμάκο you are one of the most important people in my life. I'm grateful I met you, and even more grateful you happened to like me. You once promised to stay in the Netherlands at least until I finished my PhD and that's the best gift you could've given me. And imagine, I use your AirFryer almost every day. But I guess for every gift you've given me, I should also thank **Vania** for falling in love with you and keeping you here.

I also want to thank **Giorgo Ts**. for his parental friendship. Although very close to the end of my PhD you got bored of being our parent and went on to make the cutest kid of your own. **Konstantina**, thank you for making everything you do seem so easy and doable. Delivering a baby in ten minutes is like delivering a thesis without a mental breakdown. I couldn't manage either.

Alessandro, thank you for every dinner that you cooked for me, every ride to the supermarket, every compliment you gracefully gave me and every hug you offered me.

Arun and **Diana**, thank you for your genuine care. You always made time to listen, to check in, and to offer thoughtful advice when I needed it most. I'm grateful for your calm presence and kindness. I also owe my thanks to my friend **Edo**, not just for convincing me to sign up for the gym (which was an achievement on its own), but for your friendship that brought me comfort and ease. This circle of friends would not be complete without **Francesca**, the loudest and most energetic person I know. Fra, I'm sure we'll still be singing karaoke with our deodorants in hand even when we're old and grumpy. Thank you for every memory we've shared across the Netherlands, India, Spain, and Italy. Greece is next.

My forever best friends since school, **Ismini, Aristi, Christina, Eirini** and **Niki**. I only wish we lived closer, but even one Zoom call with you brings me warmth until we meet again. In another perfect life, we're rich neighbors meeting every night to play card games and make jokes to Christina that we only hang out with her to visit her pool.

Giuseppe, thank you for making the waiting time from delivering the first draft until the day of the defence feel so joyful. Falling in love with you was the perfect ending to this long chapter and was even more exciting than completing my PhD.

Finally, I want to express my deepest gratitude to my family. More specifically, to my cousin **Giannis**, who every single time I was presenting somewhere, publishing something or getting some small recognition he would be there to text me or call me to tell me how much proud of me he is.

Two things instantly come to my mind when I think of my **dad**. First is the image of him reading a book. Well, the one you are holding now, μπαμπά, is the one you contributed to the most, through all your support over the years. Second is the thought that he is the man who can fix anything he touches. Quite a pity that you touched this book only once it was printed and cannot be fixed now. But that's okay. You're still the most amazing, calm, and wise person I know.

Frida, my younger sister who has managed to far exceed me on every stage in life. I used to think your greatest skill was copying me. But it turns out, you've just been outpacing me all along. Φριντούλι μου, the thought that you are now creating your own family together with **Tasos** gives me pride and a bit of anxiety, but mostly pride. Your growth pushed me to reflect on my own life and confront what I needed. Since I can recall my existence I have lived next to you and I know this is the main reason why I am always trying to improve.

Mum, I know there were moments during my PhD that made you cry because of how I was doing, and that is a thought that weighs heavily on me. You were there through my lowest points with nothing but patience and love. Μανούλα μου, you were the one person I could always turn to, even when everything else felt unbearable. Thank you for being my source of strength and for holding on, even when I was rude to you. You wanted me to do a PhD even before I started wanting it too, so it goes without a doubt that this thesis is dedicated to you, with all my love and gratitude.

Curriculum Vitæ

Angeliki Christoforidou

23-04-1994 Born in Thessaloniki, Greece

Academic experience

2012–2017 Diploma of Civil Engineering
Aristotle University of Thessaloniki, Greece
Thesis: Generation of artificial accelerograms using stochastic methods
Supervisor: Dr. G. Stefanou

2017–2020 Master of Science in Civil Engineering
Delft University of Technology, the Netherlands
Thesis: New joints of GFRP tower with a steel support structure for offshore wind turbines
Supervisor: Dr. M. Pavlovic

2020 Researcher
Delft University of Technology, the Netherlands
Project: Adhesively bonded examples for the new technical specification for the design of composite structures
Supervisor: Dr. M. Pavlovic

2020–2024 Ph.D. researcher
Delft University of Technology, the Netherlands
Thesis: Fatigue performance of injected bolted connections for composite decks in highway bridges
Promotor: Prof. dr. M. Veljkovic
Copromotor: Dr. M. Pavlovic

Publications

Journal publications

1. **Christoforidou, A.**, Baskar, A., Kane, E., & Pavlovic, M. (2025). Compressive behaviour and micromechanical modelling of steel-reinforced resin under monotonic and cyclic loading. *Composites Science and Technology, 111387*.

2. **Christoforidou, A.**, & Pavlovic, M. (2024). Fatigue performance of injected steel reinforced resin connectors for FRP-steel joints at room and elevated temperatures. *Engineering Structures, 315*,118421.

3. **Christoforidou, A.**, Verleg, R., & Pavlovic, M. (2023). Static, fatigue and hygroscopic performance of steel-reinforced resins under various temperatures. *Construction and Building Materials, 403*, 133079.

4. Olivier, G., Csillag, F., **Christoforidou, A.**, Tromp, L., Veltkamp, M., & Pavlovic, M. (2023). Feasibility of bolted connectors in hybrid FRP-steel structures. *Construction and Building Materials, 383*, 131100.

5. Kavoura, F., **Christoforidou, A.**, Pavlovic, M., & Veljkovic, M. (2022). Mechanical properties of demountable shear connectors under different confined conditions for reusable hybrid decks. *Steel and Composite Structures, 43*(4), 419.

Conference publications

1. **Christoforidou, A.**, Baskar, A., & Pavlovic, M. (2025). Fatigue and hygroscopic performance of injected bolted connectors in GFRP sandwich web core panels. In *Proceedings of the 12th International Conference on FRP composites in Civil Engineering, CICE 2025*. Lisbon, Portugal.

2. **Christoforidou, A.**, Baskar, A., & Pavlovic, M. (2024). Numerical prediction of iSRR fatigue performance based on cyclic compressive tests on SRR. In *Proceedings of the Bridge Engineering Institute (BEI-2024)*. Las Vegas, USA.

3. **Christoforidou, A.**, Baskar, A., & Pavlovic, M. (2024). Static, quasistatic and fatigue behaviour of steel-resin composite material. In *Proceedings of 21st European Conference on Composite Materials (ECCM21)*. Nantes, France.

4. **Christoforidou, A.**, Baskar, A., Barelts, E., Kavoura, F., & Pavlovic, M. (2023). Fatigue performance of preloaded bolted connection with oversized holes. In *Proceedings of the 10th Eurosteel conference (Eurosteel 2023)*. Amsterdam, the Netherlands. ce papers 6.3-4 (pp. 1287–1292).

5. **Christoforidou, A.**, Veltkamp, M., Csillag, F., Tromp, L., & Pavlovic, M. (2023). Fatigue performance of injected steel reinforced resin connectors in GFRP sandwich web core panles. In *Proceedings of the 11th International Conference on FRP composites in Civil Engineering, CICE 2023*. Rio de Janeiro, Brazil.

6. Karpenko, O., Peeters, T., **Christoforidou, A.**, & Pavlovic, M. (2023). Fatigue of web core composite bridge decks: An experimental and numerical study. In *Proceedings of the 11th International Conference on FRP composites in Civil Engineering, CICE 2023*. Rio de Janeiro, Brazil.

7. Pavlovic, M., **Christoforidou, A.**, & Keller, T. (2022). Adhesive joint design methods and examples. In *Proceedings of the 20th European Conference on Composite Materials: Composites Meet Sustainability, ECCM 2022*. Lausanne, Switzerland (Vol. 5, pp. 615-622).

8. **Christoforidou, A.**, Kavoura, F., Pavlovic, M., & Veljkovic, M. (2021). Mechanical performance of injected steel-reinforced resin connectors under different confined conditions for reusable composite structures. In *Proceedings of the 9th International Conference on Composite Construction in Steel and Concrete*. Stromberg, Germany. ce papers 6.1 (pp. 694–705).

Awards

1. Best Paper Award presented to **Christoforidou, A.** for the outstanding paper, poster, and pitch presentation on: *Shear and wheel loading on bolted connectors for composite bridge decks*. Awarded at the *IABSE Young Engineers Colloquium 2023*, Ghent, Belgium, November 24, 2023.

2. Best MSc Thesis Award (1st Prize in the 'Master' category) presented to **Christoforidou, A.** for the thesis: *New joints of GFRP tower with a steel support structure for offshore wind turbines. An experimental and numerical approach*. Issued by *Bouwen met Staal*, Amsterdam, the Netherlands, October 2020.

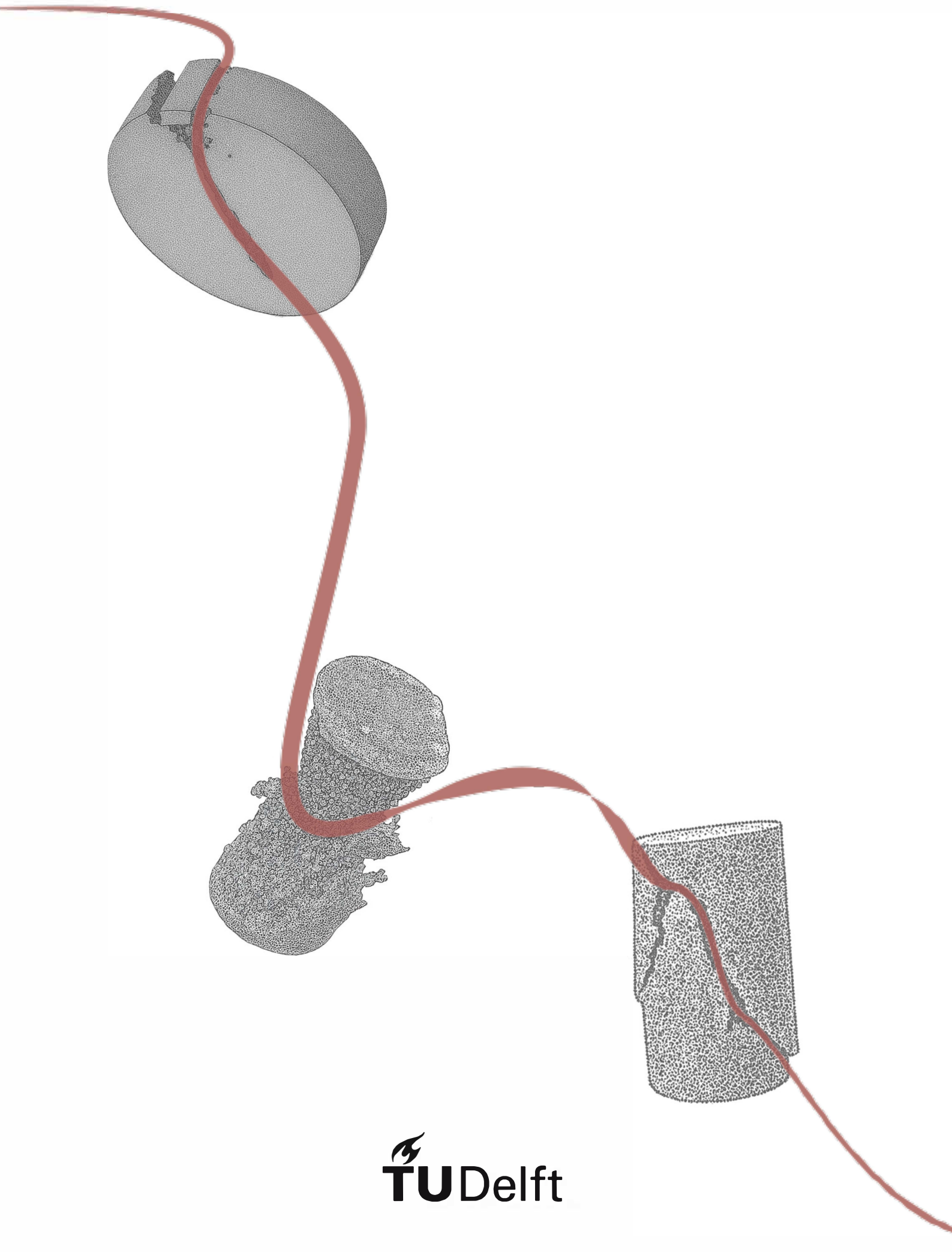

TU Delft